Development ofPerovskite Solar Cells Using Electrodeposition

Mirella Al Katrib

THÈSE

Pour obtenir le grade de

DOCTEUR DE L'UNIVERSITE GRENOBLE ALPES

Spécialité : **Matériaux, Mécanique, Génie civil, Électrochimie**

Arrêté ministériel : 25 mai 2016

Présentée par

Mirella AL KATRIB

Thèse dirigée par **Emilie PLANES**, Université de Savoie Mont-Blanc et co-encadrée par **Lara PERRIN,** Maître de conférences, Université de Savoie Mont-Blanc

préparée au sein du **Laboratoire d'Électrochimie et Physico-chimie des Matériaux et des Interfaces**
dans **l'École Doctorale I-MEP2 – Ingénierie – Matériaux, Mécanique, Environnement, Énergétique, Procédés, Production**

Cellules solaires pérovskites réalisées par électrodéposition

Development of Perovskite Solar Cells Using Electrodeposition

Thèse soutenue publiquement le **31 Janvier 2022**,
devant le jury composé de :

Madame Emilie PLANES
MAITRE DE CONFERENCES HDR, Université Savoie Mont Blanc, Directrice de thèse
Madame Fannie ALLOIN
DIRECTRICE DE RECHERCHE, CNRS délégation Alpes, Présidente
Madame Emmanuelle DELEPORTE
PROFESSEURE DES UNIVERSITES, ENS Paris-Saclay, Rapportrice
Monsieur Nicolas MERCIER
PROFESSEUR DES UNIVERSITES, Université d'Angers, Rapporteur
Monsieur Jean-François GUILLEMOLES
DIRECTEUR DE RECHERCHE, CNRS délégation Île-de-France Sud, Examinateur
Monsieur Yann BULTEL
PROFESSEUR DES UNIVERSITES, Grenoble INP, Examinateur

Acknowledgments

After finishing my master's internship at IEM – Montpellier, I had the opportunity to pursue my passion in research by starting this thesis on materials for photovoltaic application at the laboratory of electrochemistry and physico-chemistry of materials and interfaces LEPMI, team GUIDE, located within the national institute of solar energy INES. During my doctoral thesis, I became familiar with the different thin film deposition techniques, and the different characterizations necessary to understand the chemical structure, the optical properties and the morphology of the prepared layers. I was able to conduct various research operations through data analysis, preparation of presentations to report writing. I also gained in responsibility and autonomy, and was able to supervise several student projects. I would therefore like to thank this team who put their confidence in me to join their laboratory.

I would like to start by thanking my thesis director, Ms. Emilie PLANES, who guided me through these three years. She was always available for help, and gave me the courage I needed to develop my work. I would also like to thank my supervisor Ms. Lara PERRIN for her continuous presence, for her positivity and motivation. I had the pleasure to work with two successful women, who helped me gain the scientific knowledge and the confidence I have today.

In addition, I would like to thank all the jury members for agreeing to review this work , and for their fruitful discussion during my defense. My thanks therefore go to Ms. Emmanuelle DELEPORTE and Mr. Nicolas MERCIER who agreed to be this work's reviewers, to Mr. Jean-François GUILLEMEOLES and Mr. Yann BULTEL who agreed to be the examiners, and to Ms. Fannie ALLOIN who agreed to be the jury President.

When I first started my thesis with the GUIDE team at the LEPMI laboratory, I was immediately welcomed as a member of this team. They certainly became my family in France, and for that I thank every one of them: Mr. Lionel FLANDIN, our team chief, who was always present and encouraging, Mr. Nicolas CHARVIN for his everyday support, Mr. Gilles DE-MOOR for his unconditional help, Ms. Marjorie ESNAULT for her motherly love, Mr. Johann RAVAUX for his presence and his friendship, Mr. Ali NOURDINE for his help in the laboratory, Mr. Julien GIBOZ, Ms. Florence DUBELLEY and Mr. Christophe CARRAL for their tips and encouragements, in addition to Mr. Sylvain CARRIER, Mr. Patrice MELE, Ms. Corine BAS, Mr. David BROWN and Ms. Sylvie NEYERTZ.

I also had the pleasure to share this experience with other PhD students, and post-docs in the GUIDE team. I would like to thank the ones that finished before I do and could not be present during my defense but certainly showed all their support: Zeinab and Manon for their support, Quentin and Marwen for their daily tips , Donia and Marie for their kindness and beautiful hearts. A special thank you to Thibault who was not only a colleague but a friend and was always ready to answer my questions and help me. I would also like to thank the current PhD students and post-docs: Mylène, Saman, Camille, Noémie, Méryll and Lucie. An individual thank you to my colleague and friend Rachel with whom I shared a lot of memories during these three years. Most importantly, a big thank you for my office colleagues, my two friends and neighbors who became my sisters, Marwa and Cynthia, for

their daily support, for sharing all the ups and downs with me and for their unconditional love.

During my thesis, I had the opportunity to supervise many projects and internships. Therefore, I would like to thank Mathilde and Sarah who did a great work during their project, and offered me important results related to the carbon paste. I also want to thank the sweetest intern Diana for her support even after she finished her work, and most importantly a big thank you to the amazing intern Lucile for the important work she offered to support my thesis. I also had the opportunity to meet other colleagues at INES-CEA, that worked on perovskites, and with whom I was able to discuss my work, and for that I would like to thank them.

When I moved from Lebanon to France, a beautiful Lebanese community welcomed me in Chambéry, they helped me settle down and became like a family to me. The first big thank you goes to Pia who was and still is like a sister to me, she was always there for me, always ready to help, and was also my mentor in the perovskite field. I would also like to thank all my Lebanese friends for their help and support: Karine, Hassan S., Malek, Ali Saied, Ibrahim, Mabelle, Marianne, Abbas, Ali Isber, Ali Choumen, Hussein, Kassem, Jamal, Mohammad, Louai, Hassan H., Tarek, Rita, Rim, Farah and all the other Lebanese in Chambéry. I also want to thank Ms. Rima BURGOS for all her support, she welcomed me as a friend to her family and was always ready to help.

Many of my Lebanese best friends also moved to France, and therefore shared with me my experience. I will start with a big thank you to the closest people to my heart, Roudy and Stephanie, for their daily support and their amazing friendship. I would also like to thank Marleine for being the sweetest mentor and friend, Yana for her big heart and her daily motivation, and Grace for her help whenever I needed it. One special person I would like to thank is Joe, my angel friend who never stopped supporting me with his motivation and prayer. I want to thank each and every one of my friends for their support, even the ones I did not mention by name.

Three years ago, I had to leave my country and adapt to a new culture and a new lifestyle to pursue my dreams. It was a beautiful experience, but the hardest part was being far from my family. Distance might have separated us, but they always remained next to me, closer than ever, and for that I will always be grateful. The biggest thank you goes to my parents, for the education they offered me, and their unconditional love and support. I am forever grateful to them because they helped me become the successful woman I am today. A big thank you to my mother for all her prayers, and for her daily support and motivation. I would also like to thank my four sisters, each and every one of them: Layal for her motherly love, Michella my soulmate sister, Melissa for all her motivation and Marina my sweetheart. Having them in my life is a blessing, and they all helped me evolve in my life and during my thesis.

Last but not least, I would like to thank God for all the beautiful opportunities he offered me in life, for all the daily miracles he blessed me with and for all the angels he put in my path.

"Cast all your anxieties on him, because he cares for you" ~ ***1 Peter 5:7***

Table of contents

Glossary

5-AVA	5-Aminovaleric acid
5-AVAI	5-Ammonium valeric acid iodide
CBM	Conduction band minimum
CdTe	Cadmium Telluride
CE	Counter electrode
CIGS	Copper indium gallium selenide
CIS	Cadmium indium selenide
Cp	Carbon paste
DMF	Dimethylformamide
DMSO	Dimethyl sulfoxide
DOC	Diesel oxidation catalyst
DSSC	Dye sensitized solar cell
ED	Electrodeposition
ETL	Electron transport layer
ETM	Electron transport material
EtOH	Ethanol
FA	Formamidinium
FABr	Formamidinium bromide $CH(NH_2)_2Br$
$FAPbI_3$	Formamidinium lead iodide $CH(NH_2)_2PbI_3$
FET	Field-effect transistor
FF	Fill factor
FTO	Fluorine doped tin oxide
GaAs	Gallium arsenide
HOMO	Highest occupied molecular orbital
HTL	Hole transport layer
HTM	Hole transport material
I_{max}	Maximum PL spectral intensity
IPA	Isopropanol
ITO	Indium tin oxide
J_{sc}	Short-circuit current density
LED	Light emitting diode
Li-TFSI	Bis(trifluoromethane) sulfonamide lithium salt
LUMO	Lowest unoccupied molecular orbit
MA	Methylammonium
MACl	Methylammonium chloride CH_3NH_3Cl
MAI	Methylammonium iodide CH_3NH_3I
$MAPbI_3$	Methylammonium lead iodide $CH_3NH_3PbI_3$
NF	Nanofiber
NREL	National Renewable Energy Laboratory
OPV	Organic PV

P3HT	Poly(3-hexylthiophene)
PCBM	[6,6]-phenyl-C_{61}-butyric acid methyl ester
PCE	Power conversion efficiency
PEDOT:PSS	Poly(3,4-ethylenedioxythiophene) polystyrene sulfonate
PK	Perovskite
PL	Photoluminescence
PSC	Perovskite solar cell
PTAA	Poly[bis(4-phenyl)(2,4,6-trimethylphenyl)amine]
PV	Photovoltaic
QD	Quantum dot
QDSC	Quantum dots solar cell
R.H.	Relative humidity
RE	Reference electrode
R_s	Series resistance
R_{sh}	Shunt resistance
SCE	Saturated calomel electrode
SEM	scanning electron microscopy
Si	Silicium
SnO_2	Tin(IV) oxide
Spiro-OMeTAD	2,2',7,7'-Tetrakis[N,N-di(4-methoxyphenyl)amino]-9,9'-spirobifluorene
TBP	4-tert-butylpyridine
TCO	Transparent conductive oxide
TDP	Tetragonal distortion parameter
TiO_2	Titanium dioxide
TiO_{2c}	Compact TiO_2
TiO_{2m}	Mesoporous TiO_2
TWC	Three-way catalyst
UV-Vis	Ultraviolet–visible spectroscopy
VBM	Valance band maximum
V_{oc}	Open circuit voltage
WE	Working electrode
XRD	X-ray diffraction
λ_{max}	Wavelength at maximum emission intensity

General Introduction

Photovoltaic energy is considered today as the most useful natural energy source[1]. To date, different types of solar technologies are industrially available, and the attempts in research and development to improve their potential are continuing. While a number of different materials with different efficiencies can achieve photovoltaic solar energy conversion, so far, no particular material or combination is cheap enough to compete with large-scale fossil fuel-generated electricity[2]. Nowadays, Si-based cells are the most marketed, and they produce high solar conversion efficiencies[3]. However, expensive high temperature and high vacuum processes are adopted in order to elaborate pure Si[4]. Another active material called perovskite, newly emerged in the solar community. It has attracted major attention worldwide because of its outstanding photovoltaic performance, easy fabrication process, small band-gaps, high extinction coefficients, and high carrier mobility. As they are capable of generating a power conversion efficiency approaching that of the leading Silicon solar cells[5–7] and that their cost is lower, perovskite solar cells (PSCs) are considered the future of the photovoltaic technology. The enormous potential of PSCs reigns in their efficiency rise from 3.8% to 25.2% within a decade, and it is continuously rising to date[8]. The record conversion efficiency was achieved in April 2021, by researchers at South Korea's Ulsan National Institute of Science and Technology (UNIST) and the Swiss Federal Institute of Technology Lausanne (EPFL). In addition to their rapidly increased efficiency, PSCs are characterized by their flexibility in material growth and architecture.

Usually in PSCs, the perovskite active layer is sandwiched between an electron transport layer (ETL) and a hole transport layer (HTL). Transport layers must exhibit good properties, such as good thermal stability, non-toxicity and must be resistive towards external degrading factors[9]. Hence, the layers sandwiching the perovskite play a critical role in improving the power conversion efficiency and managing the device's stability. The choice of the nature of the perovskite is also a key for good performances. $MAPbI_3$ is the most common hybrid halide perovskite for photovoltaic applications but it is known for its unstable nature[10,11]. Chemical engineering by substitution of cations or anions, or even using double ions, was demonstrated to be an effective strategy to further enhance the optoelectronic properties of $MAPbI_3$[12–14]. When it comes to contact electrodes, metallic contact cathodes are usually used because of their good conductivity. They present however many drawbacks such as the high cost, complexity of deposition and the impact they leave on the stability of the PSCs. As an alternative, carbon-based electrodes have been widely applied in PSCs because they resolve the issues confronted with metallic electrodes. They are known for their good conductivity, processing flexibility, high chemical inertness, and low cost, which makes them compatible with up-scalable techniques, signifying their solid potential for mass-production[15].

Furthermore, one of the most important factors to determine the performance of PSCs is the quality of the elaborated active layer. Most film properties like its crystallinity, morphology and uniformity depend on the fabrication method chosen to deposit it. Spin coating has been the most commonly used perovskite deposition method. However, it requires work in inert environment (glove box), which increases its cost, enables the deposition only on small surfaces, and requires some toxic additives to maintain the stability of the perovskite[16]. There is a need to look up for other deposition methods, more ecofriendly, at lower costs, applicable for large-scale production of PSCs. The

electrodeposition method has been recently started to be explored as an efficient alternative for perovskite fabrication. This technique is low cost, forms smooth and uniform layers, could be applied for large scale devices and most importantly is elaborated in ambient atmosphere. There have been several attempts over the past years to optimize the electrodeposited perovskite layer and adjust its crystallization on dissimilar layers. All sub-techniques started by electrodepositing an initial layer (PbO, PbO_2 or PbI_2) followed by one or several conversions of the as-deposited layer[16–31].

In this work, we decided to further investigate the electrodeposition of perovskite. Pouncing from electrodeposited PbO_2 to perovskite was the most efficient and simple route, whether by direct conversion or two-step conversion with simple immersion of the electrodeposited film in a conversion solution. In this way, there will be no need to work in inert atmosphere, and no need to spin-coat the conversion solution on the electrodeposited layer. Although it was applied before, the electrodeposition of PbI_2 turns out to be not practical and hard to achieve, hence the choice of PbO_2 as a starting material. In addition, trying to electrodeposit mixed perovskites such as $MAPbI_{3-x}Cl_x$ and $MA_{1-y}FA_yPbI_{3-x}Br_x$ can also enhance the performance and stability of perovskite.

After studying the state of the art concerning this subject in the first chapter, we here present in chapter 2 our first article which concerns the optimization of the electrodeposition of simple $MAPbI_3$. In particular, two different conversion routes were compared. The effects on the morphology, the chemical and the optical properties of the perovskite film of both the substrate nature and the conversion route were also investigated. Finally, the photovoltaic performances of the elaborated perovskite layers were compared in a carbon-based PSC. This first study allowed us to define the most suitable way for the electrodeposition of perovskite. In the following a similar procedure will be adopted.

Chapter 3 consists of our second article, where chlorine was infiltrated in $MAPbI_3$ scaffold, prepared using electrodeposition, to enhance its performance and stability. This article will be the first to ever investigate the electrodeposition of $MAPbI_{3-x}Cl_x$. The effect of the Cl ratio used in the conversion bath on the perovskite properties was studied. Then, the prepared $MAPbI_{3-x}Cl_x$ perovskite films were tested in solar devices and their performance was compared to that of $MAPbI_3$. Finally, the stability of these electrodeposited perovskites was evaluated under mild aging conditions during 500h.

An identical procedure was followed in chapter 4, presented in a third article, where another mixed perovskite is prepared using electrodeposition, being $MA_{1-y}FA_yPbI_{3-x}Br_x$. This study is one of its kind, since this double mixed perovskite was never developed using electrodeposition before. As in chapter 3, the effect of the FA and Br ratios infiltrated in the perovskite lattice on the properties of the perovskite was investigated. Solar devices using these materials were developed and their performances and stabilities were compared to those elaborated using electrodeposited $MAPbI_3$.

Since the architecture of the solar device has a key role on its photovoltaic performance, we investigate in chapter 5 the options for the choice of the different transport layers, the contact electrodes and the structure of the solar cell. The optimization of the active layer was studied, and different solar devices with different architectures were compared.

Chapter I: State of the Art

I. General Introduction

Since the industrial revolution, the emission of many gases such as carbon dioxide increases, causing global warming. This phenomenon raised the surface temperature of earth by 0.6°C, and future predictions indicate an increase of about 1.4°C, to 5.8°C if nothing is done. This can cause catastrophes like glacier melting, sea level rise, droughts and floods, which leads to serious disruptions to agriculture and natural ecosystems. Therefore, reducing such emissions is necessary, which can be achieved by using renewable energy technologies instead of many traditional energy application[32]. Along the growing concerns about environmental conservation, the petroleum crisis incites a continuous increase in renewable energy demand[33]. Among the alternative energy sources, wind, water and bio-energy are all used sources, derived from solar power in one way or another. However, the electrical energy from photovoltaic panels (PV) is nowadays considered the most useful natural energy source. In fact, the sun provides each day 10 000 times the energy needed on the planet[1]. This energy source is free, abundant, produces no greenhouse gases, and is distributed over the earth[34,35], thus the remarkable improvement of technologies channeling solar powers. Many governments and companies consider photovoltaics (PV) as the future of energy production and the European union energy council states that it will become the most important alternative renewable energy source until 2040[35].

II. Photovoltaic Cells

II.1. Introduction

The idea of converting light into chemical fuel or electric power started when the French scientist Edmond Becquerel discovered the photoelectric effect in 1939[36]. Ever since, researchers and engineers focused on catching this free energy to convert it into a valuable and crucial resource that is electrical power, or use it for fuel generation such as hydrogen[37,38]. Photovoltaic effect is based on the phenomena of a photon falling on a semi-conductor, imparting enough energy to some electrons to raise their energy level and thus become free, creating electron-hole pairs. This effect can set up an electric potential difference across the interface of two different materials, which in turn is used to drive a current through a circuit[39,40] . This leads to direct conversion of sunlight into electricity. Photovoltaic devices are rough and simple in design requiring very little maintenance and their biggest advantage being their construction as stand-alone systems to give outputs from microwatts to megawatts. Hence, the demand for photovoltaics is increasing every year with their vast array of applications. They are used for power source, remote buildings, water pumping, solar home systems, satellites and space vehicles, communications, and for even megawatt-scale power plants[41].

Presently, various types of solar cells are industrially available, and the strive for research and development is continuing to improve these devices[1]. While photovoltaic solar energy conversion can be achieved by different materials inducing variable efficiencies, no particular material or combination so far is cheap enough to compete with large-scale fossil fuel- generated electricity[2]. The growth of such technology depends on materials,

architectures and manufacturing processes development, and the goal will always be maximum power at minimum cost.

All solar cells require a light absorbing material, present within the cell structure to absorb photons and generate free electrons via the photovoltaic effect. Through the years, many materials were used, the most common being silicon in its amorphous and crystalline forms, but other materials (organic, inorganic or hybrid) can be used and opened the way to thin films photovoltaic cells[40,42].

II.2. Photovoltaic Cells' History: the three generations

Through the years, the photovoltaic cell has been developed. As Becquerel observed in 1839: “electrical currents appear from a light induced chemical reaction”. Similar effects were observed by William Grylls Adams and Richard Evans Day in selenium in 1876, several decades later[43]. This photoelectric effect observed, it was necessary to wait 1905 so that an imminent scientist proposes an explanation to this effect by introducing the concept of "photon": Albert Einstein receives the Nobel prize of physics in 1921 for this work. In the early 20th century, Planck demonstrated the quantum nature of light and Wilson proposed the quantum theory of solids in 1930. A decade later, Mott and Schottky developed the theory of solid-state rectifier. Bardeen, Bratttain and Schockley invented the transistor nine years later. In 1954, the silicon solar cell was developed by the researchers of the Bell laboratory (Chapin, Fuller, Pearson and Prince), with an efficiency of 6%[44,45]. The same year, Reynolds *et al.* developed solar cells based on cadmium sulphide, and theses solar cells were used on an orbiting satellite (Vanguard 1) for the first time in 1958[46].

Concerning the evolution of solar cells along the years, the first generation of solar cells are based on Si wafers. Si-single crystals and bulk polycrystalline Si wafers were first used[47]. Nowadays, these cells are marketed and produce high solar conversion efficiencies according to the wafer quality and the development procedure. The world record efficiency for a silicon cell was established by Amonix, reaching 27.6% under 92x concentration[3]. Polycrystalline Si was also developed by high cost and advanced technological steps, to better increase their solar conversion efficiency[47]. However, expensive high temperature and high vacuum processes are adapted for the silicon to be extremely pure[4].

The research works continued leading to the development of the second generation solar cells, based on thin film technology. Various materials such as amorphous silicon (a-Si), cadmium indium selenide (CIS), Cadmium Telluride (CdTe) or thin silicon films on indium tin oxide (t-Si) are used in this technology[48]. Thanks to materials savings, their low temperature processes and their high level of automation in mass production, manufacturing costs could be reduced, in addition to the fact that this technology has been developed on flexible substrates[49]. Thus, this second generation solar is taking on an important role in the field of energy conversion, gaining new applications such as the integration into textiles. After using material combinations of CIGS cells (Cu/In/Ga/Se) as well as the III/V semiconductors like GaAs, thin film solar cells have achieved a solar conversion efficiency of 23.35% [50], a world record achieved by Solar Frontier using

$Cu(In,Ga)(S,Se)_2$. Unfortunately, this technology is expensive (due to the rarity of indium), it possess limited stability and its manufacture is difficult, hence a small market share[51].

The aforementioned photovoltaic technologies seemed to develop to a stage where the amount of the active materials dominated the costs. It is therefore imperative that photovoltaics evolve into a more economical form, hence the third generation of solar cells focused on high-efficiency thin-film technology[52]. It combines several innovative solar cell technologies: organic, inorganic or hybrid. The four main types of nanotechnology-based-solar cells that have emerged over the past few decades are full organic PV solar cells (OPVs), dye sensitized solar cells (DSSCs), quantum dots solar cells (QDSCs), and hybrid perovskite solar cells (PSCs). These technologies have stood out in recent years in terms of efficiency, technological advancement and novel PV applications[53].

First, organic semiconductor polymers were introduced in solar devices because of their advantages: they are cheap, light weight, flexible and made into large areas by roll-to-roll processing. In the 1950's, two groups lead by Gutmann and Kallman measured the photo-electromotive forces of several organic semiconductors on inorganic substrates, which reached 1V[54,55]. These promising results sparked the interest of researchers on OPVs, having the possibility to tailor the organic molecular structure to enhance the photocurrent[2]. However, thirty years later, the continuous development of existing technologies still makes it difficult for OPVs to compete with traditional systems such as silicon solar cells in terms of efficiency and reliability[56]. The major drawback is that the conventional architecture typically used for solar cells fabrication requires a high vacuum to deposit the top metal electrode, which is not suitable for roll-to-roll processing[56]. Despite these difficulties, OPVs offer unique commercial properties based on mechanical flexibility, transparency and processing of arbitrary shape processing. This is a real promising alternative for certain applications, where the main selling point is the addition of functionality to already existing features. Prominent examples of these applications include portable/flexible/wearable electronics and building integrated photovoltaics[57]. Currently, the record value for organic solar cells is 17.5% in the NREL chart (information on the device area is not specified), and in 2021, Wurfel *et al*. were able to develop a 1 cm^2 organic solar cell with a certified efficiency of 15.2% [58].

In addition to OPVs, dye-sensitized solar cells (DSSC) are one of the most promising and cost-effective PV technologies today due to their low-cost materials and simple manufacturing process. They are also an alternative to traditional silicon based solar cells. Their era began in 1991, when Oregan and Gratzel built the first dye sensitized nanocrystalline solar cells, achieving a power conversion efficiency of 7.1%[59]. This simple structure and low cost technology generated a lot of interest, and the efficiency of these cells reached 13% by a team of EPFL in 2014[60]. Although the increase in their efficiency over the years has not reached the performance of traditional systems, DSSCs have several elements of interest. The devices can be developed using TiO_2 semiconductor commonly used as a paint base in pigment industry, and the dye sensitizer extracted from a variety of natural resources with minimum costs[61]. They can be processed at room temperature and can be easily fabricated using low-cost solution based procedures, such as inkjet or screen printing[62–64]. They are also compatible with conventional roll-to-roll techniques[65],

a continuous and low-cost manufacturing method. As a result, DSSCs can be printed on flexible substrates[66,67], textiles and paper[68,69], enabling their application in the field of portable electronics. DSSC devices are also semitransparent and can be developed in different colors. These features, along with the aforementioned flexibility, make them compatible with architectural elements other than the roof and are therefore extremely attractive in the field of building integrated photovoltaics[70]. In addition, DSSCs offer high performance in darker conditions (in the dawn and dusk or in cloudy weather), and in indoor conditions under artificial light, making them an excellent choice for indoor applications like windows and sunroof[4,61].

Based on the DSSC's structure, quantum dot (QD) was introduced as a replacement of dye due to its excellent opto-electronic properties[71]. QDs are nano-scale particles of semiconductor, whose physical and chemical properties are size-dependent due to quantum physical effects. One of the remarkable characteristics of QDs is their tunable band gap, since the absorption bands can be optimally adjusted to the wavelengths of the irradiating light. They also present many advantages such as narrow emission spectrum, good photostability, broad excitation spectra, high extinction coefficient and multiple exciton generation[72,73]. Therefore, researchers have been able to fabricate high-performance solar devices, using QDs such as CdSe and $CsPbX_3$[74]. In 2020, scientists at Australia's University of Queensland have set a new world record for a quantum dot solar cell. The group has developed a 0.1 cm^2 device from perovskite and measured power conversion efficiency at 16.6% with negligible hysteresis[75]. However, the current state research still does not allow for the development of a quantum dot module[47].

In addition to all the mentioned third-generation solar-devices, perovskite-based solar cells (PSCs), originated from DSSCs architecture, have attracted increasing attention worldwide owing to their outstanding photovoltaic performance[76], their easy fabrication process, small band-gaps, high extinction coefficients, and high carrier mobility[5–7]. Their cost being lower than Si solar cells, PSCs are considered the future of the PV technology as they are now capable of generating a power conversion efficiency approaching that of the leading Silicon solar cells. The enormous potential of PSCs is indisputable since their efficiency has risen from 3.8% to 25.2% within a decade, and it is continuously rising to date[77]. In addition to their rapidly increased efficiency, the emergence of these solar cells revolutionized the field because of their flexibility in material growth and architecture[78].

III. Perovskites

III.1. Introduction

The term "perovskites" designates a wide class of oxides with the chemical formula ABX_3 where A and B are two cations of different sizes and X is an anion that bonds to them. They usually have cubic or orthorhombic structure, and feature exceptional physical properties, such as ferroelectric, magnetic and electronic conductivity. The name perovskites derived from the mineral calcium titanate, $CaTiO_3$, discovered in 1839 by G. Rose and later named after Lev A. Perovski who was a Russian mineralogist. At first, perovskites where ABO_3 minerals such as $SrTiO_3$ discovered in 1982 or $BaTiO_3$, a mineral that is hardly present in its pure form in nature. Other than the titanates, silicate perovskites exist such as iron magnesium silicates $(Mg,Fe)SiO_3$, abundantly present in the

Earth's lower cloak, stabilized by the high conditions of pressure and temperature[79]. In 1946, P.W. Bridgman was awarded the Nobel Prize in Physics, when he first found $MgSiO_3$ on the Earth's surface as inclusions in the Tenham meteorite, which was named 'bridgmanite' in 2014 in its honor[80]. A wide variety of oxides termed after the B site ion is also present such as cobaltates, chromates, ferrites and manganites. Nowadays, the attention is increasing more for halide-based perovskites. The first publications about such perovskites date before 1985[81], where in the chemical formula ABX_3, X stands for a halogen such as F, Cl, Br or I, and A and B could be mono or divalent cations[79].

III.2. Crystallography

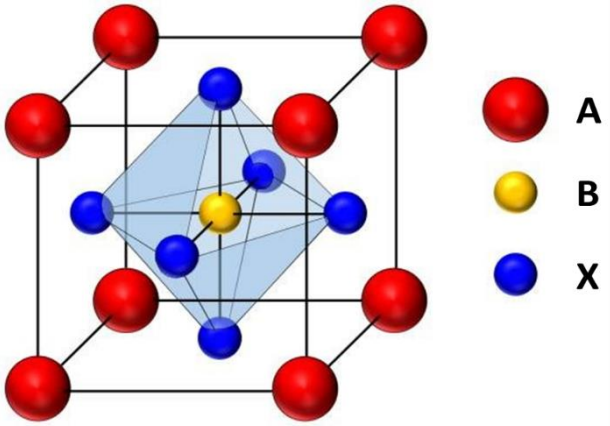

Figure 1: The 3D perovskite cubic structure, with general formula ABX_3. The BX_6 octahedron is highlighted by blue shades[82]

In the cubic lattice unit cell presented in Figure 1, A represents the eight cations at the corner of the cubic lattice, B is another cation (mainly metal) of different size that resides in the center, and the six centers of the cube's faces contain the anion X. Several derivatives of this ABX_3 structure has also been developed and investigated such as $A_3B_2X_9$, $A_2BB'X_6$ and A_2BX_6[83]. The presented 3D crystal structure system is the most common one. This structure is also distinguished by its flexibility, where the A site for example, can be occupied by a mixture of divalent or trivalent cations, granted that they have equivalent diameters[79]. This adaptability engenders a wide variation of properties that will be discussed in the upcoming part.

III.3. Properties

Another advantage of the perovskite is that it can be present in a hybrid form, meaning it can be constituted of organic and inorganic compounds. A hybrid material combines both good properties of organic and inorganic semiconductors. Inorganic semiconductors are widely exploited due to their important optical, electric or magnetic properties, leading to high-performance and stable devices. They require though difficult synthesis techniques, such as high vacuum or high temperature, which raises their fabrication cost. In contrast, organic materials sustain from poor properties and performance, yet they are easy to produce, versatile for various applications and economical. Hence, the hybrid organic-inorganic nature of some materials can offer high quality materials, easily elaborated, at rather low cost. More specifically, when talking about hybrid perovskites, one can focus on its plethora of advantages[84]. It offers remarkable optical and charge-transport properties such as high external quantum efficiency[85,86], excellent light absorption coefficient[87,88], long charge carrier diffusion length[7,89], and long lifetime[90,91].

The most common example is the methylammonium lead iodide ($CH_3NH_3PbI_3$), also called $MAPbI_3$. In this perovskite, $CH_3NH_3^+$ resides in the A cation site, the divalent metal Pb^{2+} in the B cation site, and I^- as the halide anion in the X site. In the optical point of view, the valance band maximum (VBM),conduction band minimum (CBM) and band gap for $MAPbI_3$ were estimated to be -5.43 eV, -3.93 eV and 1.5 eV, respectively[92]. Due to its low temperature solution genesis (~100°C), this material can be elaborated on a wide range of substrates and using various deposition techniques such as spin-coating, drop-casting, spraying, slot-die coating, etc. This offers an important economic advantage and facilitates the incorporation of this material in different devices[82].

III.4. Applications

Due to its unique properties and low-cost solution process ability, perovskites are found to be an outstanding candidate for many applications. To start, it has been demonstrated that perovskite-type oxides could be valuable alternatives to conventionally used Three-Way Catalysts TWC compositions and can be suitable for a wide range of automotive applications, ranging from TWC to Diesel Oxidation Catalysts (DOC), from NO_x Storage Reduction catalysts (NSR) to soot combustion catalysts[93]. The catalytic activity of perovskites was first published by G. Parravano in 1953, that used $La_{0.65}Sr_{0.35}MnO_3$ as a catalyst for the oxidation of carbon monoxide[94]. In 1971, $LaCoO_3$ perovskite-type oxide was proposed as an economic substitute for noble metal-based exhaust after treatment catalysts[95]. Over the past several years, a lot of research focused on understanding and improving the catalytic properties of perovskite-type oxides in automotive applications[93].

In addition to their catalytic activity, perovskites have been extensively recognized as third generation photocatalysts due to their unique traits such as high chemical/thermal stability, excellent electronic conductivity, and their ability to photogenerate and separate charges. Their photocatalytic properties were mainly used for the removal of deleterious gases, organic contaminants, heavy metals and radionuclides[96].

Furthermore, perovskites offer unique optoelectronic and ferroelectric properties. The dielectric properties of para- and ferroelectric perovskites were mapped by G. Rupprecht and R. O. Bell in 1964, laying the foundations for multiferroic materials[97]. These properties engendered the widespread use of high-performance perovskites in memories, sensors, microelectronics, piezoelectric actuators, energy harvesting and storage systems, mechanical processing, ultrasonic energy converters as well as optical and other related devices.

Many of the interesting electronic and optical properties of halide perovskites such as high optical absorption coefficient, direct energy band gap, large oscillator strength, long carrier lifetime and high quantum efficiency are particularly attractive for light emitting devices[98–101]. The first exhibition of perovskite material-based light emitting device LED was demonstrated in 1994 by the IBM research labs[102]. On the other hand, lasers are the youngest member of the family of perovskite optoelectronic devices. Perovskite lasers have entered the field with the vision to create low-cost, solution processed laser diodes[98,103]. Due to their ability to absorb incident radiations over broad wavelength range with excellent optoelectronic transfer efficiency, organometal trihalide perovskites marked a shift in the engineering of low-cost, yet high-performance photodetectors[104,105].

Oxide and hybrid perovskite materials are also used in field-effect transistors, which are among the essential elements in modern electronics[106].

Most importantly, the unique properties and low-cost solution process ability of perovskites made them great candidates for photovoltaic applications. Since the first application of perovskites in solar devices by Kojima *et al.* in 2009[107], hybrid perovskites have become the star materials in the photovoltaic field during the past decade. The publication on high efficiency perovskite solar cells by Kim *et al.* in 2012 further increased the research on these materials[92]. Nowadays, Web-of-Science documents more than 4500 articles under the keyword "perovskite solar cell" [108] (Figure 2).

Perovskite based optoelectronic devices exhibit great potential in commercial applications; they still suffer however from several disadvantages. In fact, the poor quality of perovskite polycrystalline film and unfavorable phase transition can largely affect the charge carrier dynamics, which will influence the optoelectronic performance of devices. Other than that, perovskites suffer from poor stability when exposed to moisture, high temperature, and light[83]. Despite these drawbacks, perovskites are still emerging as serious alternatives for photovoltaic application, and researchers are studying their improvement to overcome the confronted problems.

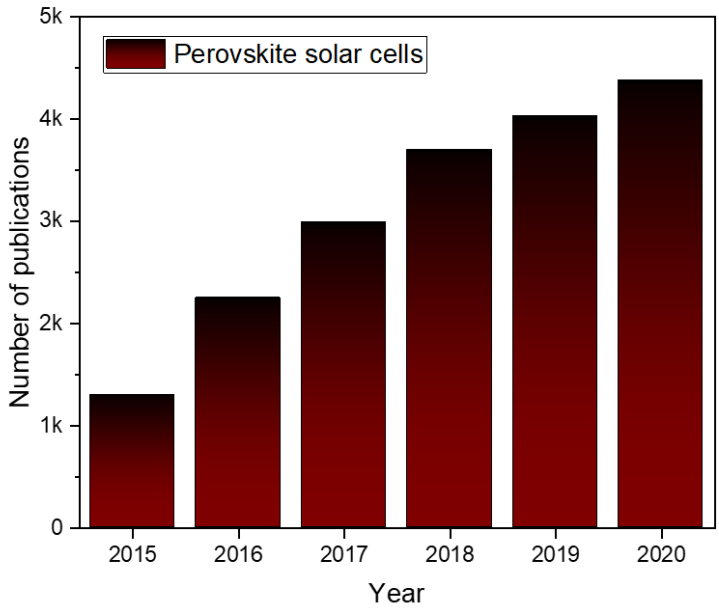

Figure 2: Number of published articles by keyword search: "perovskite solar cells" from 2015 to 2020. Source: ISI Web of Science, Thomson Reuters. [108]

IV. Perovskite Photovoltaic Cells

IV.1. Introduction

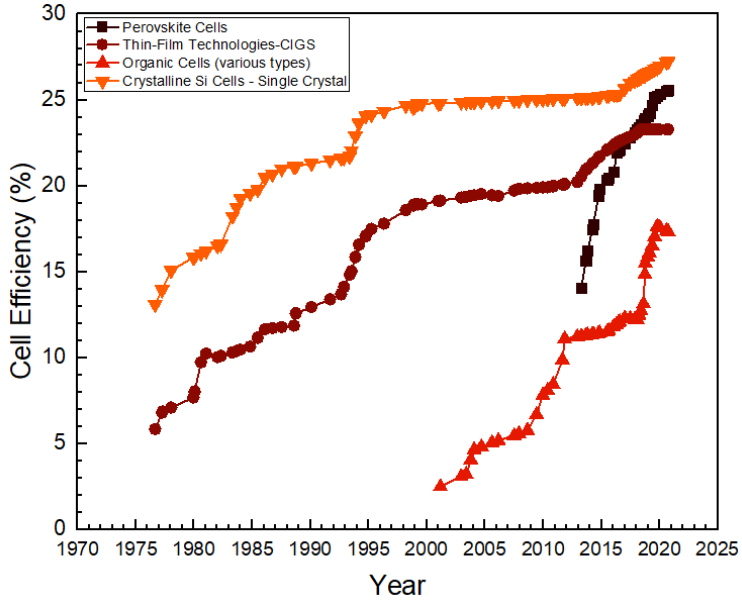

Figure 3: NREL – Best research cells efficiency[8]

As previously explained, perovskites generally exhibit good physical properties such as magnetic, ferroelectric, and two-dimensional electronic conductivity. Their excellent optical and electronic properties make them attractive candidates for many optoelectronic and electronic devices such as light emitting diodes (LEDs), lasers, photodetectors, memory devices, and field-effect transistors (FETs)[84]. Specifically, they offer excellent optical and charge-transport properties such as high external quantum efficiency, high absorption coefficient value, long charge carrier diffusion length, and long lifetime. In fact, their defect states are unique since they exist within the valence band and conduction band or they appear as shallow traps; the carrier can then be easily de-trapped from these states. The free charge carrier lifetime of perovskites is on the order of nanoseconds, indicating a slowing charge recombination within them. This makes halide perovskites ideal candidates for absorption in photovoltaic devices[109]. In 2009, Kojima *et al.* elaborated the first perovskite-based solar cell with a PCE of 3.8%[107]. This discovery received little attention because of its stability issues, including instant dissolution of the perovskite in a liquid electrolyte. Later in 2012, the first solid-state PSC with an efficiency of 9.7% and long-term stability of 500 h was reported by Kim *et al.*[92]. Just two years after, PSCs yields quickly reached 18% (Figure 3)[8]. This PSC technology was then selected as one of the biggest scientific breakthroughs of 2013 by the editors of Science and Nature[110,111] They are currently seen as promising materials for low-cost, high-efficiency solar cells. The emergence of these solar cells revolutionized the field not only because of their rapidly increased efficiency, but also because of flexibility in material growth and architecture. The commercialization of solar-cells is also being explored in term of efficiency and material cost. Although in 2021 silicon-based solar cells are dominating with large power conversion-efficiency of 25-26%, perovskite solar cells are considered an alternative since their PCE reached 25.6%[112]. This record has been obtained for a single

junction perovskite solar cell by researchers at South Korea's Ulsan National Institute of Science and Technology (UNIST) and the Swiss Federal Institute of Technology Lausanne (EPFL) in April 2021. These results slightly exceed the previous record of 25.2% achieved in February 2021 by scientists at the Massachusetts Institute of Technology (MIT), and the previous UNIST's result of 25.17% achieved in November 2020[113].

IV.2. PSC Architecture

One of the performance deciding factors in the evolution of the PSCs is the advancements in device architecture. In 2009, the perovskite was first used as a liquid electrolyte in a dye-sensitized solar cell (DSSC). However, this configuration did not bring great attention due to the low efficiency (3.8%) and unstable nature of the device, since it was elaborated using a liquid electrolyte[107]. This liquid electrolyte was replaced later by a solid state perovskite, which not only improved the device efficiency (10%) but exhibited successful operation for 500 h also[92].

In general, a typical PSC is composed of five components: (i) a metal-based cathode, (ii) a Hole transport layer (HTL), (iii) an active layer as an absorber material (being the perovskite here) (iv), an Electron transport layer (ETL) and (v) a Transparent Conductive Oxide(TCO). The structure of PSCs is either of n-i-p or p-i-n configuration. The perovskite layer sandwiched between ETL in the bottom and HTL at the top is the n-i-p structure. In the p-i-n structure, the perovskite is sandwiched between ETL at the top and HTL in the bottom (Figure 4)[109]. The function of HTL is to collect holes from the absorber layer and transport them towards the cathode and block electrons, and the function of ETL is to collect electrons from the absorber layer and transport them towards anode and block holes. Transport layers must exhibit good properties, such as good thermal stability, non-toxicity and must be resistive towards external degrading factors[9]. Hence, the layers sandwiching the perovskite play a critical role in improving the power conversion efficiency and managing air stability.

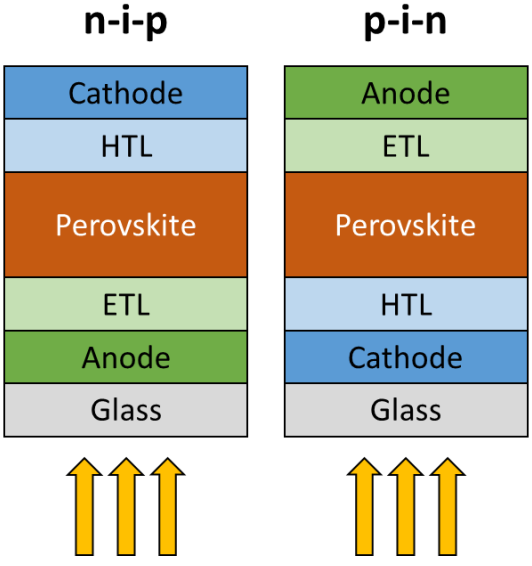

Figure 4: Scheme representation of a n-i-p and p-i-n structure for a PSC

In a perfect n-i-p structure, electrons are transferred through the ETL to the TCO substrate and the holes from the HTL to the metal electrodes such as Au or Ag. Particularly, in order

to have an ideal scenario and realize efficient hole and electron transport and extraction, the highest occupied molecular orbital (HOMO) of HTMs should be greater than valence band maximum (VBM) of perovskite materials. The lowest unoccupied molecular orbit (LUMO) of ETMs should be additionally lower than the conduction band minimum (CBM) of perovskite materials, as shown in Figure 5[114–117]. In other words, for any material to function as a HTM, it must have its HOMO slightly higher than that of the perovskite absorber layer; for a material to be used as an ETM, it must have its HOMO and LUMO levels higher than that of the perovskite absorber layer[77].

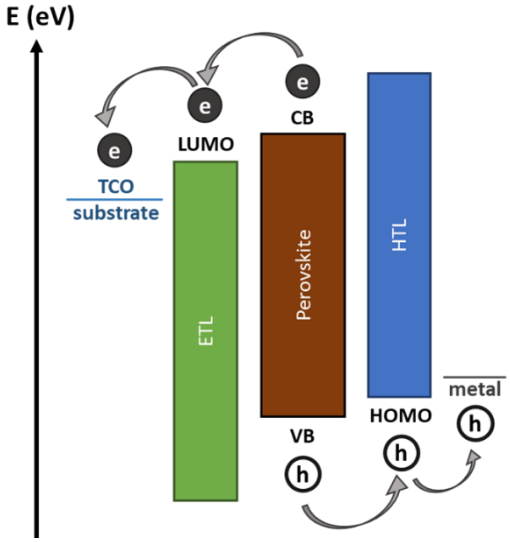

Figure 5: Energy diagram of PSC with n-i-p structure showing the alignments of the LUMO and HOMO layers.

Concerning the transport layers, in addition to a good energy alignment (Figure 6), in a n-i-p structure, ETMs must have high transmittance in UV–visible region so that all the photons pass through it, and are largely absorbed by the absorber layer. Various ETMs could be used for a PSC such as TiO_2, SnO_2, SiO_2, PCBM, ZnO, etc. SnO_2 and TiO_2 are considered the best ETM candidates. SnO_2 has been well considered in many state-of-the-art PSCs due to its high mobility and wide bandgap. It suffers however from degradation in high temperature, and the main concern with its application as an ETL is that it presents a much lower conduction band compared to perovskite, which may result in a voltage loss of PSCs[118]. On the other hand, TiO_2 can typically be used as ETL in planar heterojunction solar cells due to its suitable band alignment with perovskite absorber layer and good transparency for visible light[119]. The main concern in its application as ETL is that it suffers from low electron mobility, limiting the overall device performance. Consequently, using mesoporous TiO_2 was considered to enhance the electron transport properties since the porous network of TiO_2 scaffold can be totally filled in this case[22]. This feature of good pore filling and full coverage enhances the interface between the ETL and the active layer and thus limits the recombination of the excitons if they were to travel more than their diffusion length before dissociation[120].

In an inverted PSCs (p-i-n), the typical ETM is PCBM, a fullerene derivative that tends to passivate the perovskite surface with a significant suppression of hysteresis and recombination losses[121]. However, the PCBM/metal contact is not optimal for electron extraction due to the energy level mismatch[122,123]. Therefore, interface engineering is usually carried out between the PCBM and metal contact by inserting additional layers,

such as ZnO. The additional ZnO layer not only improves the energy level alignment at the cathode, but also blocks the reactions in air between the metal electrode and the perovskite components[124–126].

A wide range of potential HTLs has been explored over the past decade, from organic small molecules such as spiro-OMeTAD, to polymers such as P3HT, to inorganic compounds such as CuI, NiO_x, CuSCN, with the inclusion of various additives. The importance of HTMs comes with their ability to boost the performance of the solar cell by preventing charge recombination. In fact, it was experimentally demonstrated that the proper HTM inhibits back electron transfer, which would increase the fill factor (FF) of the solar cell, and its open circuit voltage (V_{oc}). On the other hand, a hole conductor is not necessarily required in a PSC since a number of them have been developed without HTMs, with a carbon –based contact. However, PSCs with HTMs display higher efficiencies, which makes HTMs critical for elaborating efficient perovskite solar cells. Although a large variety of HTMs is undergoing intense research being one of the most crucial part of PSCs, the fundamental impact of the HTM on the charge collection and the charge transfer at the interfaces of devices remains partially understood[114–117].

P3HT is a commonly used HTM in organic solar cells with a relatively high hole mobility and great stability. This polymer is a dopant-free HTM and thus could be a suitable choice for stable PSCs[127]. However, the most widely used solid-state materials as HTL in high efficiency PSCs are Spiro-OMeTAD and PTAA[128,129], since they proved to offer great performances in solar devices. However, the pristine spiro-OMeTAD possesses an inherent low hole mobility and poor conductivity due to its triangular pyramid configuration and large intermolecular distance. Appropriate doping can be therefore applied to resolve this problem. The common p-type dopants to the spiro-OMeTAD are bis(trifluoromethane) sulfonamide lithium salt (Li-TFSI) and 4-*tert*-butylpyridine (TBP). It is observed that lithium salt helps in oxidation process of spiro-OMeTAD whereas TBP improves conductivity of active layer by dissolving in perovskite layer[130]. However, the added dopants are usually hygroscopic and would thus decompose the perovskite film that is sensitive to moisture. Even though they are the most commonly used HTMs, both spiro-OMeTAD and PTAA have properties that inhibit their optimal functioning as HTLs, which include sub-optimal conductivity, significant recombination at the perovskite/HTL interface and stability issues linked to dopant hydrophilicity and reactivity[129].

Also considering some inorganic compounds as good matching HTMs, nickel oxide (NiO_x) was selected as a good candidate. It is an stable inorganic material with a suitable HOMO level for hole extraction and electron blocking properties in perovskite-related applications[131] . NiO_x is also a suitable candidate due to its high optical transmittance, sufficient conductivity and chemical stability. In addition, NiO_x HTMs can be easily elaborated via solution from corresponding precursors at low temperatures[132].

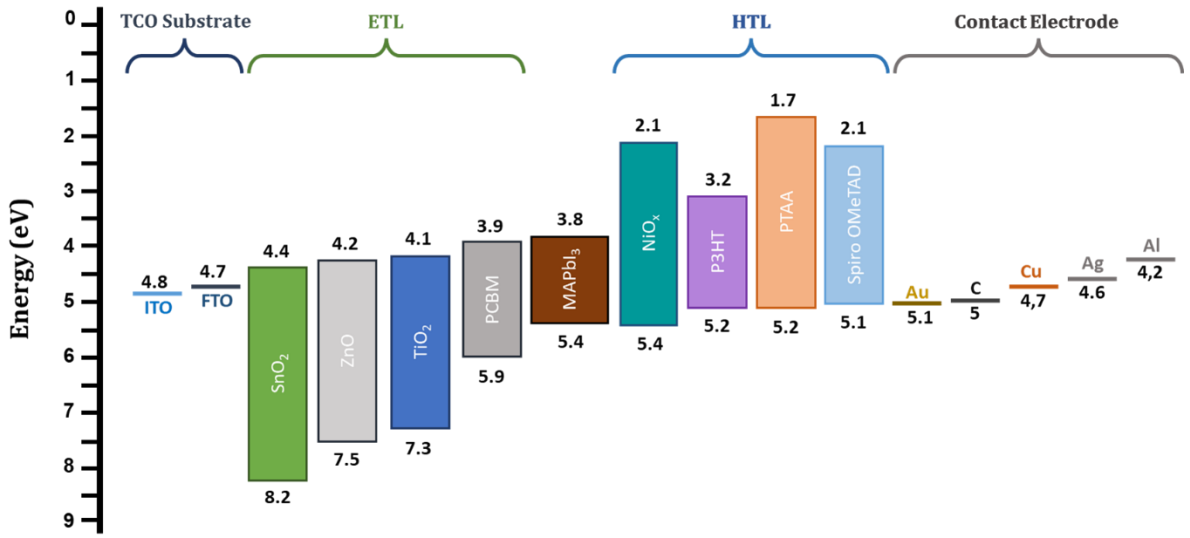

Figure 6: Energy diagrams of the different typical layers used in a PSC

For the choice of contact anode and cathode, transparent FTO and ITO are typically used as anodes in n-i-p PSCs, coupled with metal cathodes like Al, Ag, Ni and mainly Au. The roles are reversed when developing a p-i-n structure[133]. However, the good conductivity of contact metal cathodes comes with many drawbacks such as high cost, complexity of deposition and the impact they leave on the stability of the PSCs. The processing of rare earth metal requires complex vacuum-based techniques, which is another problem. Therefore, there is an urgent need to replace the precious metal cathode for this high-efficiency photovoltaic device. Thus, carbon-based electrodes have been widely applied in PSCs because they solve the problems faced by metal/HTM-based PSCs[134]. Available in abundance on earth, carbon is also known for its good conductivity, flexibility in processing and electro-chemical activity which makes it compatible with scale-up techniques, which means it has great potential for mass-production[135]. Carbon is the most important material in the world. Its importance also lies in its high chemical inertness and water resistance[15] due to its hydrophobic nature that promotes less absorption of moisture into the cell, thus improving cell life[135]. In addition, carbon electrodes can extract photogenerated holes on their own, making them an attractive choice for contact electrodes in HTM-free PSC. Thus, PSCs could be developed without the need to use expensive and unstable HTMs, a smart solution to reduce the cost and enhance the stability[15,135]. Carbon black and graphite are mainly used to elaborate the counter electrodes in conventional carbon-based PSCs. These materials require high processing temperatures to burn off the organic binder[136,137], which hinders the large-scale production in solar cells. However, carbon electrodes in PSCs can be prepared by high- or low-temperature curing. A typical high-temperature carbon-based cell is elaborated by deposition of mesoscopic selective electrode layers, which are usually printable, followed by a high-temperature pyrolysis of the organic binders and solvents in them at around 400-500°C. This means that the perovskite precursor solution can be only added afterwards[62,64]. In contrast, in low-temperature carbon-based cells, the electrode layer is developed at temperatures below the irreversible perovskite degradation, which allows the deposition of perovskite before the counter electrode. Commercial carbon paste can be found that offer several advantages such as high conductivity, low cost, low-temperature process (100 °C), and good stability[138,139].

IV.3. PSC Active layer

Organic–inorganic halide perovskite materials (e.g., $MAPbI_3$, $FAPbI_3$) have been intensively studied for photovoltaic application, mainly processed using spin-coating (allowing its fabrication together with its deposition in one step). Lead halide based perovskites have shown high solar energy conversion efficiencies (25%) but toxicity issues with these materials need to be addressed. Therefore, major concerns for the commercialization of perovskite photovoltaic technology include lead toxicity, long-term stability, hysteresis, and optimal bandgap. Therefore, there is still need to explore alternative materials[140]. Lead-free perovskites have emerged as viable substitutes in PSCs to ensure clean and green photovoltaic technology, as they possess a suitable band gap. Substitution of lead with Sn, Ge, Bi, Sb, Cu and other potential candidates have resulted in efficiencies of up to 9%, but their stability in air needs further improvements. The use of additives has a significant effect on their efficiency and stability. In addition, engineering the elemental composition of $MAPbI_3$ and $FAPbI_3$ has been proposed to address the following concerns. Incorporation of cations such as diethylammonium, phenylethyl ammonium, phenylethyl ammonium iodide, etc., mixed cations with different compositions at the A-site, or mixed anions at the B-site has been reported with engineered bandgaps having significant efficiency and stability[141]. Among the best certified power conversion efficiencies reported by National Renewable Energy Laboratory on perovskite-based solar cells, a large portion is based on mixed perovskites (e.g., $MAPbI_{1-x}Br_x$, $FA_{0.85}MA_{0.15}PbI_{2.55}Br_{0.45}$, $Cs_{0.1}FA_{0.75}MA_{0.15}PbI_{2.49}Br_{0.51}$)[140].

As previously mentioned, highly efficient perovskite solar cells are composed of perovskites that have an ABX_3 three-dimensional (3D) structure and are commonly composed of an organic/inorganic monovalent cation A (e.g., methylammonium (MA); formamidinium (FA); Cs^+; Rb^+), a divalent metal cation B (e.g., Pb^{2+}; Sn^{2+}), and halide anion moiety X_3 (e.g., I^-; Br^-; Cl^-). From the beginning of PSC developments, methylammonium lead iodide perovskite ($MAPbI_3$) has been intensively used as light harvesting material[5,92,107,142,143]. Perovskite compositions with single ions occupying each of A, B, and X sites (e.g., $MAPbI_3$, $FAPbI_3$) are denoted as "simple perovskites" and has been intensively studied. In earlier studies, perovskites with mixed halides including small quantities of chlorine atoms in the X_3 moiety of $MAPbI_3$ (i.e., $MAPbI_{3-x}Cl_x$) were employed[144,145], but to this day, researchers still tend to use high contents of iodine-based perovskite deposition recipes for photovoltaic applications[146–150]. However, the future trends for PSC technology is focusing more on mixed perovskites. Hence, the benefits of employing mixed cations and halides in perovskite materials need to be investigated more, such as higher performance, increased stability, enhanced carriers charge transport, enabling band gap tuning, less pronounced hysteresis. In addition, a thorough understanding of fundamental aspects of Pb-based mixed cations and halides may lead to alternative Pb-free perovskites. Before starting to describe more complex mixed cation perovskite systems, the understanding on structure–property relationship of simple perovskite systems needs to be outlined (e.g., $MAPbI_3$ and $FAPbI_3$).

IV.3.a. Simple Perovskites

$MAPbI_3$ is the most common hybrid halide perovskite for photovoltaic applications and therefore its fundamental properties were studied intensively[151–153]. At room

temperature, the ionic radii of Pb^{2+} = 0.132 nm, I^- = 0.206 nm, and MA^+ = 0.18 nm suggesting the tetragonal phase, which was confirmed experimentally by $MAPbI_3$ single crystal X-ray diffraction data[14]. A wide range of band gaps values between 1.5 and 1.61 eV have been reported for $MAPbI_3$ [13,153–155] with the band gaps values generally higher for polycrystalline films possibly due to quantum confinement[13,14]. However, the optimal band gap for a single-junction solar cell is between 1.1 and 1.4 eV on the basis of the Shockley–Queisser limit[45]. The modification of the $MAPbI_3$ structure is thus well-considered. In addition, $MAPbI_3$ is known for its unstable nature[10,11]. As a matter of fact, it has been reported that perovskites have a naturally soft structure, also called "plastic"[156], that influences on the optoelectronic properties of the material, such as its energy levels, bandgap, and balanced/imbalanced charge transport[157,158]. Furthermore, $MAPbI_3$ undergoes a phase transition from the tetragonal to cubic phase at ~54 °C, a temperature that is usually surpassed during typical solar cell elaboration[159]. Therefore, it is imperative to discover perovskites insensitive to composition instabilities under stress conditions. For certification, solar modules must be successfully operative in the temperature range between −40°C and +85°C[160].

Chemical compositional engineering, like substitution of MA^+ by other cations such as FA^+, Cs^+ or Rb^+, was demonstrated to be an effective strategy to further enhance the optoelectronic properties of $MAPbI_3$, as evidenced by reported certified efficiencies[12–14]. In contrast to $MAPbI_3$, $FAPbI_3$ was reported to not manifest phase transition in a wide temperature range going from 25°C to 150 °C[161,162]. However, the best PCE reported for $FAPbI_3$ perovskite solar cells is lower than the $MAPbI_3$-based ones. FA^+ possesses a larger ionic radius compared to MA^+, so $FAPbI_3$ perovskites are expected to have a smaller band gap compared to $MAPbI_3$ (between 1.47 and 1.55 eV)[163]. Consequently, higher PCE would be expected for $FAPbI_3$ solar cells as light harvesting range extends further into the near-infrared. Comparative works have shown that $FAPbI_3$ devices offer higher J_{sc} than $MAPbI_3$, confirming the ability of extended light-absorption of $FAPbI_3$ perovskites. However, a major loss in the PCE comes from the poor FF[164]. Several studies proposed that this limitation is associated with the phase instability of the pure $FAPbI_3$ in ambient conditions. In fact, $FAPbI_3$ possess two polymorphs: a photoinactive hexagonal δ-$FAPbI_3$ perovskite formed at ambient temperature (delta or yellow phase), and a photoactive trigonal α-$FAPbI_3$ perovskite formed at higher temperatures (~125–165 °C) (alpha or black phase)[165,166]. After α-$FAPbI_3$ is formed, a slow phase transformation to δ-$FAPbI_3$ is reported when kept at room temperature, which leads to unstable device operation.

IV.3.b. Mixed A cations: Binary (FA/MA)PbI_3 System.

Perturbing the A cation size can influence the optical properties by deforming the BX_6 octahedron network. A larger cation (e.g., FA^+ = 0.19–0.22 nm) or smaller cation (e.g., Cs^+ = 0.167 nm, Rb^+ = 0.152 nm) causes the lattice to expand or contract leading to the change of B–X bond length, which has been shown to influence the band gap[14]. The first mixed cation perovskite was reported by Pellet *et al.*, who described the bandgap tunability of $MA_xFA_{1-x}PbI_3$-based solar cells by varying the ratio of MA to FA[167]. The mixed perovskites were here first developed by dipping a PbI_2 film in premixed $MA_xFA_{1-x}I$ – IPA conversion solution. The $MA_{0.6}FA_{0.4}PbI_3$ composition resulted in the best PCE of 13.4% with a band gap of 1.53 eV, similar to that of pure $FAPbI_3$ perovskite. Over the years, several studies

have been published showing better $MA_xFA_{1-x}PbI_3$ film quality, higher film coverage, fewer pinholes, higher crystal quality, and larger grain sizes with smaller roughness within[168–172]. Inverted structure was also employed[173,174], and several studies used perovskite deposition techniques other than spin-coating, such as doctor blading[175], chemical vapor deposition[176] and low-pressure vapor assisted solution process[177].

In fact, the incorporation of MA^+ into the $FAPbI_3$ structure gives in a much more stable $MA_xFA_{1-x}PbI_3$ perovskite structure, which was further investigated by Binek *et al.*[178]. The incorporation of a smaller cation (MA^+) with a large dipole moment exhibits a stronger interaction with the PbI_6 octahedra, which stabilizes the 3D arrangement of α-$FAPbI_3$ with little lattice shrinkage or changes in optical properties. The phase transition behavior as a function of $FA_xMA_{1-x}PbI_3$ composition and temperature was studied experimentally by Weber *et al*.[179]. At 300 K, $FA_xMA_{1-x}PbI_3$ with $0.2 \leq x \leq 1$ revealed a cubic structure. However, the tetragonal phase was observed for $MAPbI_3$ and $FA_{0.1}MA_{0.9}PbI_3$ perovskites. UV−visible measurements on $FA_xMA_{1-x}PbI_3$ revealed a linear decrease in the optical band gap with increase in the FA content from $0.2 \leq x \leq 1$. Huang *et al.* synthesized a series of perovskite single crystals with mixed organic cations $FA_{1-x}MA_xPbI_3$[171]. The mixed organic cations improve the stability of the cubic phase, and the carrier lifetime of $FA_{1-x}MA_xPbI_3$ was significantly improved compared with the $MAPbI_3$ form. $FA_{0.85}MA_{0.15}PbI_3$ single crystal exhibited higher electron/hole mobilities than $FA_{0.15}MA_{0.85}PbI_3$. In addition, the $FA_{0.85}MA_{0.15}PbI_3$ single crystal presented lower dark current hysteresis than the $FA_{0.15}MA_{0.85}PbI_3$ single crystal, which was reversed when stored in a high humidity condition. Recently, Pauporte *et al.* investigated the key effects of the additive methylammonium chloride (MACl) on the growth of $FA_{1-x}MA_xPbI_3$ perovskite layers. They described the reproducible synthesis of mixed organic cation halide perovskite films using methyl ammonium chloride as an additive in a large amount and a rather low-concentration precursor solution compared with other high-efficiency PSC works. The optimum amount of this additive was found to be 48 mol%. The perovskite compound had a low bandgap, very large grains and was optimized to be free of parasitic phases. Importantly, they were able to determine the actual methylammonium fraction in the $FA_{1-x}MA_xPbI_3$ perovskite photovoltaic films. A small amount of MA ($x \sim 0.06$) is analyzed as the best for the entropic stabilization of the $FA_{1-x}MA_xPbI_3$ compound. This results in a high PCE up to 22.15% and an excellent stability of the prepared solar cells.

IV.3.c. Mixed X anions: Binary MAPb(I/Cl/Br) or FAPb(I/Cl/Br) Systems

Several reports described and summarized the new optoelectronic properties of mixed perovskites when mixed halide ions are incorporated in perovskites[154,155,172,180–182]. The structure−property relationship was studied in several published papers for MAPb(I/Cl), FAPb(I/Cl), MAPb(I/Br), FAPb(I/Br), MAPb(Br/Cl), CsPb(I/Br), CsPb(Br/Cl), CsPb(I/Cl), MAPb(I/Br/Cl).

IV.3.c.1. Binary MAPb(I/Cl) or FAPb(I/Cl) Systems

The MAPb(I/Cl) material system is by far one of the most studied binary mixed perovskite[181,183–185]. From earlier reports, the synthesis of $MAPbI_3$ consists mainly on employing PbI_2 and MAI precursors, generally in equimolar ratio of PbI_2:MAI (i.e., 1:1), if one-step method is extensively used (using spin-coating). The first deposition approach

employing $PbCl_2$ and 3-fold excess of MAI (i.e., 1:3) was reported by Lee *et al.*[144]. Although Cl incorporation has been reported to improve optoelectronic properties, since the diffusion lengths for electron in $MAPbI_3$ increases by 10 times in $MAPbI_{3-x}Cl_x$[7,186], the controversial question whether Cl can in fact be incorporated into the crystal lattice of $MAPbI_3$ is still not completely settled. Reported studies show contradicting results regarding detection or absence of Cl in $MAPbI_{3-x}Cl_x$ perovskite. Many studies confirmed the presence of Cl in $MAPbI_{3-x}Cl_x$ using several characterizations. However, there are also studies concluding that Cl is absent in the final perovskite films, because its proportion is below the detection limit of the instruments[187–189]. Many hypotheses have been argued regarding the elaboration of the $MAPbI_{3-x}Cl_x$ perovskite. It has been suggested that Cl incorporation yields low miscibility with iodine as a result of the larger difference in ionic radii[155,190,191],and that $MAPbI_{3-x}Cl_x$ phase is metastable or possess higher formation energies[189]. $MAPbI_{3-x}Cl_x$ and $MAPbI_3$ perovskites show very similar UV–visible and XRD patterns indicating no or a very small amount of Cl can be incorporated[144,155,189]. In addition, large variations in the post-annealing temperature is employed for the perovskite crystallization, for example a large range covering 90 – 120 °C for 45 – 120 min[144,192–194] can be reported when using in the one-step spin-coating method. The fine-tuning of annealing temperature and time plays an important role for the delicate incorporation of Cl into the perovskite crystal lattice. Li *et al.*[195] used the two-step method (see paragraph IV.4) to elaborate $MAPbI_{3-x}Cl_x$ films, and their XRD data showed that the (110) and (220) diffraction peaks shift as the $PbCl_2$ concentration increases. The shift is small but not negligible and could be detected since it is above the instrumental sensitivity. The UV– visible of perovskite films show that when increasing $PbCl_2$:PbI_2 ratio, the absorption edge shifts toward a shorter wavelength. Zhang *et al.* synthesized single-crystalline nanofibers (NFs) of $MAPbI_{3-x}Cl_x$ perovskites in the tetragonal phase at room temperature with the Cl content between $0 \leq x \leq 0.75$[196]. They suggested that I ions are not substituted by Cl ions along the [001] direction of single-crystalline NFs, but along the [100] or [010] directions within the crystal ab-plane. Luo *et al.* developed $MAPbI_{3-x}Cl_x$ perovskites under vacuum conditions by coevaporation of MAI and $PbCl_2$ sources[197]. Interestingly, upon subsequent post-annealing treatments, they observed that a phase transition from tetragonal to a cubic phase takes place in $MAPbI_{3-x}Cl_x$ perovskites, which also remained stable after the cooling at room temperature. Kim *et al.* studied the function of MACl additive in $FAPbI_3$-based perovskite and detected that MACl successfully induces an intermediate to the pure $FAPbI_3$ α-phase without annealing.

Based on extensive analytical measurements, researchers showed that the incorporation of Cl ions into the perovskite crystal lattice is feasible only in a small quantity (<1 at. %), but sufficient to induce new material properties[195]. As an alternative, Cl-based additives might help facilitate Cl-incorporation into the perovskite lattice. HCl[198,199], NH_4Cl[200], $CaCl_2$[201] ,and TPPCl[202] additives were reported to play an important role in the formation of high quality films as well as enhancement of device stability.

IV.3.c.2. Binary MAPb(I/Br) or FAPb(I/Br) Systems

The substitution of I^- by Br^- ions has been widely demonstrated to effectively tune the band gap of perovskites[203], contrary to the MAPb(I/Cl) material system. Noh *et al.* were the first to demonstrate the photovoltaic properties of mixed $MAPbI_{3-x}Br_x$ by reporting

an efficiency of 12.3%[203]. In their study, a low Br content (<10%) gave the best initial efficiency due to a lower band gap, but higher Br contents (>20%) offered a better stability to high-humidity (RH 55%). This was correlated with a tetragonal to pseudocubic structural transition (at x = 0.13) due to the smaller ionic radius of Br. A year later, Jeon *et al.* used the solvent-engineering method, to deposit a uniform and dense perovskite films of $MAPbI_{3-x}Br_x$ (x = 0.10−0.15), achieving a certified PCE of 16.2%[204]. Brivio *et al.* identified the two most stable configurations being $MAPbIBr_2$ and $MAPbI_{0.5}Br_{2.5}$[205]. Although under storage conditions the MAPb(I/Br) system exhibits enhanced stability, it has been reported that material degradation and phase segregation take place when the material is exposed to light. In 2016, Misra *et al.* performed photochemical stability tests on $MAPbI_{3-x}Br_x$ encapsulated films (x = 0.11, 0.16, 0.22, 1) under accelerated stressing conditions using concentrated sunlight (100 suns)[206]. They observed that $MAPbBr_3$ was the most stable composition exhibiting no degradation, whereas increasing iodine incorporation leads to accelerated photochemical degradation with PbI_2 as a final remaining product. No degradation was recorded for $MAPbI_{3-x}Br_x$ under shelf-storage conditions, and degradation was observed to occur only under illumination conditions. More recently, in 2021, Singh *et al.* investigated the effects of various crystalline structures of $MAPbI_{3-x}Br_x$ (x = 0, 1, 2, and 3) perovskites on the optical, charge transport, and photovoltaic properties. The light absorption and morphological properties of the perovskite films were adjusted by varying the I^-/Br^- ratio content. The optimized PSCs using $MAPbI_3$, $MAPbI_2Br$, $MAPbIBr_2$, and $MAPbBr_3$ perovskites offered high PCEs of 29.8, 23.7, 21.5, and 19.9%, respectively, under an indoor LED light source at 1000 lux. The cell containing $MAPbBr_3$ demonstrated a V_{oc} of 1.15 V, which is superior to all previously reported values for PSCs under indoor light conditions. The variation in crystal structure was shown to have a remarkable impact upon the electrical conductivity, trap density, recombination loss, and operational stability of the solar devices. Overall, it was concluded that the pure crystalline phase of the $MAPbI_3$ and $MAPbBr_3$ perovskites is more efficient and stable for photovoltaic applications than the pseudo cubic $MAPbI_2Br$ and $MAPbIBr_2$ perovskites.

Similarly, mixed halide $FAPbI_{3-x}Br_x$ perovskites were also investigated with x varying from 0 to 1[207,208]. Interestingly, both reports described that they were unable to form crystalline phases of $FAPbI_{3-x}Br_x$ perovskites with bromide contents in the range $0.3 < x < 0.5$. Rehman *et al.* used the term “amorphous”, implying that the crystalline order is too short in the length scale detectable by XRD[207].

IV.3.d. Simultaneous Mixed A-cations and Mixed X-anions: (FA/MA)Pb(I/Br) System

More complex mixed-perovskite systems were also investigated, where the double (MA/FA)[209,210], (Cs/MA)[211], (Cs/ FA)[212], triple (Cs/FA/MA)[213], and even quadruple (Rb/Cs/FA/MA)[214] mixed cations are generally followed by the mixed (I/Br), e.g., (Rb/Cs/FA/MA)Pb(I/Br). These newly developed material systems were reported to show even higher stability and efficiencies[214,215].

One of the most studied mixed cations-anions perovskite is $MA_xFA_{1-x}Pb(I_yBr_{1-y})_3$. The interest of researchers in this material started after the initial works by Jeon *et al.*[209] and Yang *et al.*[210] on the simultaneous FA^+/MA^+ cation mixed and I^-/Br^- halide mixed perovskites. Jacobsson *et al.* explored the compositional space spanned by $MAPbI_3$, $MAPbBr_3$, $FAPbI_3$ and $FAPbBr_3$. They provided the entire compositional space of $MA_xFA_{1-x}Pb(I_yBr_{1-y})_3$ experimentally. In their work, a total of 49 different perovskite compositions

were made by independently varying the MA/FA and the I/Br-ratio. The optical and crystallographic properties of these perovskites were investigated and their performance was tested in PSCs. XRD data indicated that the spin-coated MA-rich perovskites are highly textured and probably have a tetragonal unit cell, whereas the FA-rich perovskites have a cubic structure and form films with more random crystal orientations. An increased amount of bromide increases the band gap, whereas an increased amount of FA decreases the band gap but to a smaller extent. An empirical relation between the band gap and the perovskite composition was derived based on absorption data. XRD data also showed that PbI_2, but not $PbBr_2$, is found in the mixed perovskites, which shows that $PbBr_2$ more readily forms the perovskites than PbI_2. Complete solar cell devices were made with all the 49 investigated perovskite compositions, and a small change in the composition had a huge effect on the device performance, since the efficiencies vary over a broad range. The lowest efficiencies are found for mixed perovskites with a high bromide content, and the highest efficiencies are found for devices where $1/6^{th}$ of the iodine is replaced by bromide and where $2/3^{rd}$ of the MA is replaced by FA. The efficiencies of those devices were up to 20.7%, which at the time of testing was higher than the highest certified efficiency found in the record tables from NREL.

IV.4. Perovskite Deposition Techniques

One of the most important factors to determine the performance of PSCs is the quality of the elaborated active layer. The various properties of the film like its crystallinity, morphology and uniformity depend on the fabrication method chosen to deposit it. The processing technique must give complete film coverage over the substrate, since incomplete film coverage can engender shunt paths by creating direct contact between ETLs and HTLs. In addition, the incident light may not be totally absorbed by the active layer if it does not have full coverage as the photons might pass through it directly[77]. To date, several methods have been established to fabricate a good quality of perovskite film that can be synthesized using a variety of low-temperature processes due to its low activation energy.

Hybrid perovskite materials proved their worth in the research community due to their easy manufacturing, remarkable electronic properties and great photovoltaic performances. This initiated the idea of successful commercialization of the PSCs. So far in laboratories, spin coating is the commonly used technique for research purposes. However, this method cannot be adopted to fabricate large-scale PSC, hence the need to look up new methods for large scale production of PSCs.

IV.4.a. Single-step deposition

This technique is simple and low cost so it has been the most commonly used perovskite deposition method. In this technique, the organic and inorganic components are mixed together in a specific polar solvent like DMF, DMSO, GBL, DMAc, and NMP[204,216–219], which results in a precursor solution. This solution is then generally spin-coated over the substrate, and a uniform and crystallized layer of perovskite is formed. The formation of a uniform layer is due to strong ionic interaction among halogen anions and metal cations, coupled with the evaporation of the solvent during the spinning. After the precursor solution is spin-coated over the substrate, annealing is applied at temperatures ranging between 80 °C and 150 °C[209,220,221] (Figure 7). However, simple spin coating never gives

uniform and homogeneous layer over a large area, since the uniformity of the perovskite layer depends on the thickness of the substrate layer[222]. Although this deposition technique is easy to execute since it requires simple processing steps, it forms a non-uniform layer with pinholes due to slow crystallization. To overcome the uncontrollable growth of perovskite resulting in variable morphologies for obtained crystals, a two-step sequential deposition technique was proposed by Mitzi *et al.*[223].

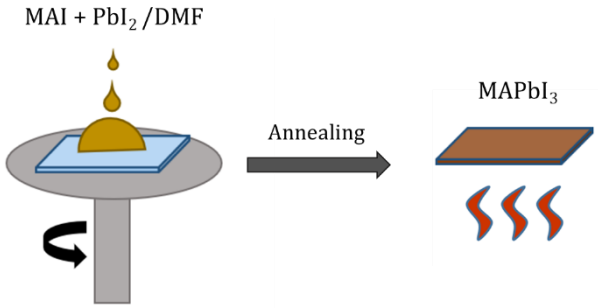

Figure 7: The schematic representation of the One-step deposition method

IV.4.b. Two-step sequential deposition

The two-step solution deposition method was first developed by Mitzi *et al.*, where they first spin coated a PbI_2 film on nanoporous TiO_2 [223]. The layer was then converted into perovskite by reaction with MAI solution, whether by spin coating the solution of MAI over the PbI_2 layer, or dip coating the PbI_2 film in MAI solution (Figure 8). When MAI solution is spin-coated over the PbI_2 film, the quality of the formed perovskite layer is determined by the spinning speed and spinning time[224]. In the case of dip coating, the dipping time and dipping concentration adopt the major impact. It was discovered by Im *et al.* that in this case, the grain size reduces with the increase of the MAI concentration[225].

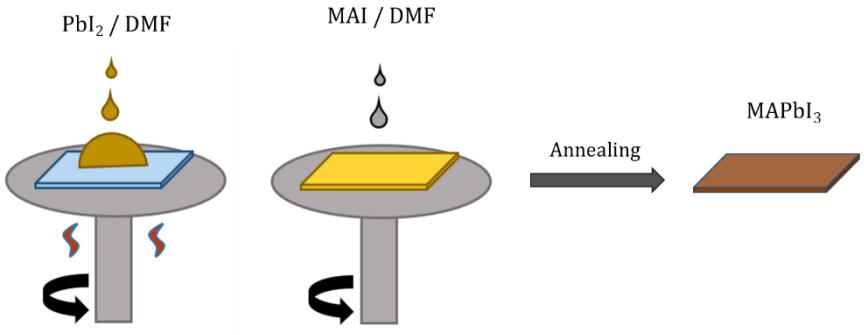

Figure 8: The schematic representation of the Two-step deposition method

Although this method produces better film comparing to the one-step deposition method, it does show several disadvantages. On one hand, as the grain size increases, the surface roughness also increases, which indicates a larger grain size leading to high leakage current and high surface recombination loss. On the other hand, a smooth film with small grains suffers from small carrier lifetime and short diffusion length. Hence, a compromise composition has to be chosen. Another drawback is confronted in the case of partial conversion of PbI_2, specifically in planar structure. A large ratio of residual PbI_2 can reduce the light absorption and hinder the carrier transport which further reduces the

performance of the PSCs[226,227]. In order to deal with these problems, solvent engineering techniques were applied: either by rapid deposition crystallization or by Lewis base adduct method.

In rapid deposition crystallization, after the perovskite layer is deposited over the substrate, an antisolvent is dripped within a short time delay. Various antisolvents could be used such as chlorobenzene, benzonitrile, ethanol, benzene, xylene, methanol, ethylene glycol, toluene, and acetonitrile. This technique increases the growth rate and nucleation of the film, which creates a uniform film with larger grain crystals[228].

The Lewis base adduct method of lead (II) iodide was proposed in 2015 by Ahn *et al.* . Spin coating a DMF solution containing PbI_2, DMSO and MAI in equimolar concentration forms transparent adduct film. During the spinning, diethyl ether is added so that DMF gets completely removed and the formation of 1:1:1 adduct film takes place. In order to eliminate the volatile DMSO from adduct, the film is heated at 65 °C for 1 min and gets converted into dark brown. The PSCs fabricated by this method gave a PCE of 19.7%[229].

Another modified version of the two-step deposition could be elaborated by a vapor assisted solution processing. In 2014, Qi Chen *et al.* developed a novel low-temperature vapor assisted process to deposit perovskite film. A PbI_2 layer is first spin-coated on the substrate, then MAI was incorporated via vapor deposition, at 150 °C in an inert environment. The obtained film was uniform, fully covered with micro-grains, with minimal roughness and a complete precursor transformation[230].

IV.4.c. Thermal vacuum-assisted evaporation

The first vacuum-deposited film was developed by Snaith *et al.* by coevaporation of the organic and inorganic components[145]. They prepared $CH_3NH_3PbI_{3-x}Cl_x$ by evaporating simultaneously MAI and $PbCl_2$ precursors from separate sources at 10^{-5} mbar with an as-deposited molar ratio of 4:1 (Figure 9). Vapor deposited film came out to be exceptionally uniform with excellent crystalline features than the spin coated ones, leading to a PCE of 15.4% (vs. 8.6% for same batch spin-coated cells). Recently in 2021, Feng *et al.* were able to develop an in-vacuum low-temperature annealing process to fabricate high-density formamidine-based mixed perovskite films using PbI_2, CsI and FAI. At an optimized annealing temperature, the efficiency of the resulting PSC reached 21.32%, the highest value for a PSC fabricated using vacuum deposition[231].

Although this technique proved its ability to elaborate different types of perovskites, it still needs an elevated level of vacuum, which rises its cost and prevents its application on large scales.

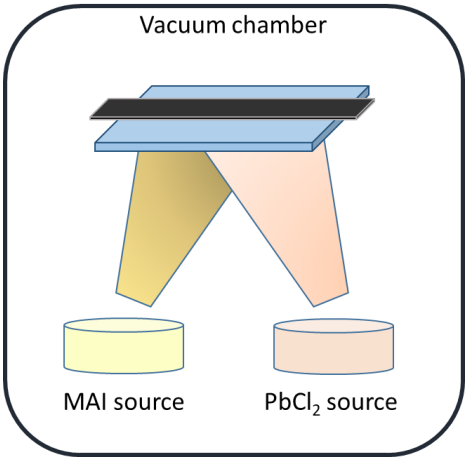

Figure 9: The schematic representation of a vacuum-assisted evaporation deposition method

IV.4.d. Drop casting

Drop casting of the perovskite precursor solution over the substrate is a low cost, productive method for the fabrication of PSC modules, enabling large scale production (automatable process). It is executed by simply pouring the perovskite precursor solution over the substrate scaffold followed by heating to remove excess solvent (Figure 10). Mei *et al.* were the first to use drop casting to elaborates PSCs in 2014[228]. The perovskite layer was directly deposited on m-ZrO_2 and m-TiO_2 double mesoporous scaffold layer (allowing an adequate diffusion of the casted drop on a surface larger than 1 cm^2), with 5-AVA as an additive in the precursor solution, which enhanced pore filling and low defect concentration. In 2015, Nie *et al.* used a solution-based hot casting method to fabricate pinhole-free uniform perovskite layers[232]. The elaborated PSC offered an efficiency of 18% in planar architecture. However, the PCE reached by this method is still much lower than that attained by the conventional spin coating method, and attempts to produce larger area with subcells connections did not help to maintain high efficiency levels[233].

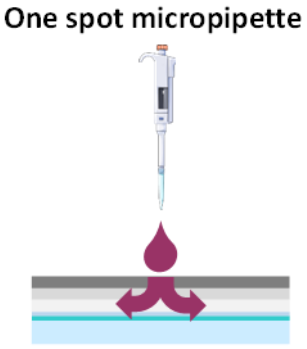

Figure 10: The schematic representation of a drop-casting deposition method

IV.4.e. Inject printing

Inkjet printing technology is the digitalized form of the conventional printing process where desired patterns are controlled by computers. This process eliminates the requirement of a particular material or substrate shape, which is a great advantage of this method[224]. It is a low cost scalable technique that uses efficiently the material, while

providing high-resolution printing[234]. This method was first used by Wei *et al.* in 2014, where the first planar PSC was developed with inkjet printing and had precise control over the interface. Over the years, this method has proved to be capable of producing stable and durable PSCs with good production scalability[77]. In 2021, Gao *et al.* developed a PSC using inkjet printing, with effective area of 120 cm^2 and a PCE as high as 16.78%, the highest reported so far[235].

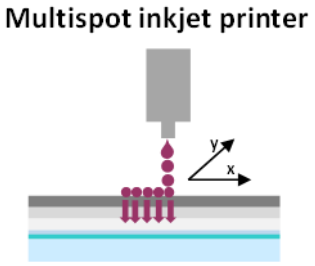

Figure 11: The schematic representation of an inkjet printing deposition method

IV.4.f. Doctor blade and Slot-die coating

The doctor blade technique consist of simply applying a fixed amount of perovskite precursor solution over a substrate, then swipe linearly using a blade with a high speed motion (Figure 12). This technique is appropriate for large scale production of PSCs since it is low cost, simple to execute, has high productivity and is compatible with roll-to-roll fabrication. During doctor-blading, the substrate is usually kept at high temperatures. The heated substrate and the application of an airflow enhances the solvent evaporation rate and promotes nucleation and crystal growth, which allows the fabrication of pinhole-free, uniform, and smooth films[236]. By regulating the concentration of precursor solution, the gap between the blade and the substrate, and the speed movement of the blade, one can control the crystallization and the thickness of the film in this method. Deng *et al.* were the first group to use this technique to develop PSCs with a 15.1% efficiency. One of the remarkable advantages about this technique is that it requires a comparatively lesser amount of precursor solution as compared to conventional spin coating techniques[237,238]. Many works have been carried out using this process to fabricate PSCs with large areas with optimized PCE[239,240].

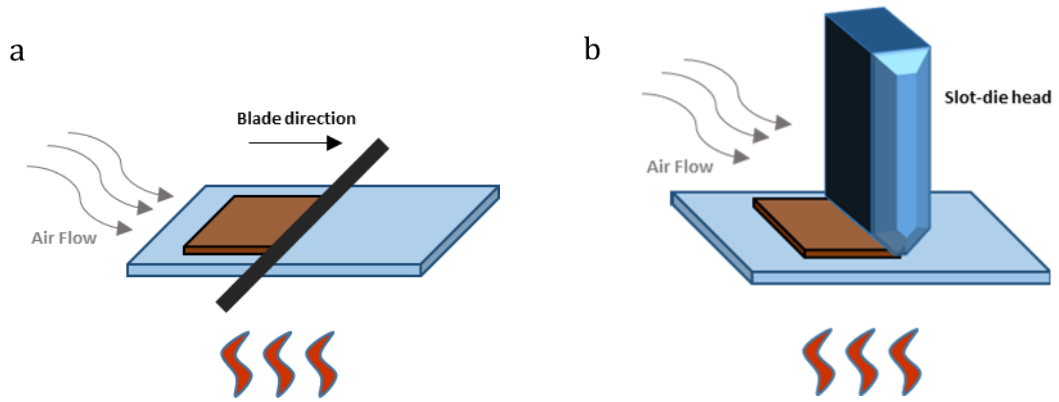

Figure 12: The schematic representation of a) the Doctor blade deposition method and b) the slot-die deposition method

Similar to the doctor blade coating technique, slot die-coating is another method where the blade is supplied with an ink reservoir which spreads the precursor solution over the substrate. Although the film quality attained in this technique is better than the one obtained with doctor-blading, the amount of precursor solution required in slot die coating is much larger. Verhees *et al.* was able to use this technique along with laser patterning to fabricate a large area panel of dimensions 170 cm^2 and attained PCE of 10%[241].

IV.4.g. Electrodeposition

The electrodeposition method was very recently explored as an efficient alternative for perovskite fabrication[28]. This technique is low cost, forms smooth and uniform layers, could be elaborated for large scale devices and most importantly could be realized in ambient atmosphere[28]. There have been several attempts over the past years to optimize the electrodeposited perovskite layer and adjust its crystallization on dissimilar layers. All sub-techniques started by electrodepositing an initial layer (PbO, PbO_2 or PbI_2) followed by one or several conversions of the as-deposited layer[16–31](Figure 13). Pouncing from electrodeposited PbO_2 to perovskite was the most efficient and simple route. Chen *et al.* were able to elaborate a carbon-based solar device with a simple $MAPbI_3$ perovskite. They used a two-step conversion method by film-immersion in conversion baths, and were able to develop a carbon-based solar device with a 10% PCE[22].

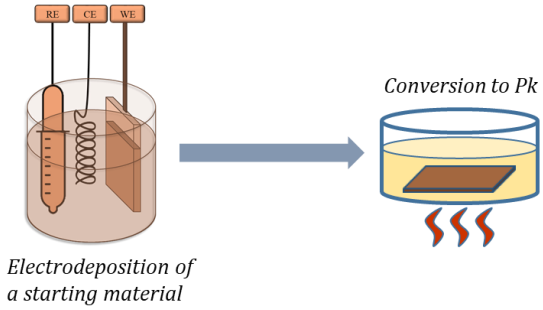

Figure 13: The schematic representation of one way to elaborate perovskites using electrodeposition

V. Focus on the electrodeposition of Perovskite

V.1. Introduction

Using PbO or PbO_2 as starting material in a two-step deposition process was evaluated to be an efficient technique for elaborating perovskite solar cells. This is not possible with spin-coating method, since spin-coating PbO as starting material onto a mesoporous or planar substrate initiates inter-diffusion reaction with methylammonium halide, resulting in unwanted material. On one hand, conventional spin-coating of large scale, uniform, smooth and flat thin films of perovskite imposes significant challenges, although these properties are required for efficient charge transfer[16]. On the other hand, a substitute technique such as electrodeposition was proven to be environmentally friendlier, reproducible and does not require high temperature treatment or vacuum environment[242]. Hence, electrodeposition represents an efficient approach to vary film thickness and surface profile of the deposited thin films. It also allows the formation of a variety of layers for photovoltaic application using PbO, PbO_2, PbI_2, Pb or PbS as a starting

material to grow perovskite film. Electrodeposition is a bottom-up technique used for uniform deposition of thin layer, with minimum wastage of useful material attained with precise control of the deposition parameters. The control of the thermodynamic deposition parameters also allows the control of the film thickness and the enhancement of smooth surface profile[242]. In nearly all designs, a three-electrode system is used for electrodeposition composed of a counter electrode, a working electrode and a reference electrode, placed in the electrolyte that can be reused several times and thus reduce production price. There have been several attempts over the past years to optimize the electrodeposited perovskite layer and adjust its crystallization on dissimilar layers. All sub-techniques started by electrodepositing an initial layer (PbO, PbO_2 or PbI_2) followed by one or several conversions of the as-deposited layer[16–31]. Uniformly electrodeposited thin film of perovskite improves power conversion efficiency of devices by careful control of the deposition potential, concentration of the electrolytic solution and deposition time[243]. Precise optimization of the deposited thin film is mandatory to efficiently harvest the incident photons from wider spectral wavelength, generating then more photo-induced charge carriers, which improves the device performance[28]. To this moment, the effect of the different parameters used in the electrodeposition on the perovskite layer, the impact of the substrate nature, and the conversion route has not been fully understood.

V.2. State of the art: Electrodeposition of perovskite

The first attempt to develop a perovskite layer using electrodeposition was in 2014 by Cui *et al.*[20]. They started with the electrodeposition of PbO as a starting material in a single compartment cell, where a mesoporous TiO_2 coated-FTO glass was used as a working electrode and a Pt wire as a counter electrode. The deposition bath consisted of aqueous solution of 2 mM $Pb(NO_3)_2$ and 0.2 M H_2O_2. The obtained PbO layer was then exposed to iodine vapor to obtain a PbI_2 film. The conversion of PbI_2 into $MAPbI_3$ was carried out using two different methods: solid-solid or solid-liquid interdiffusion reaction for the perovskite. In the solid-solid interdiffusion reaction for the perovskite, MAI solution (40 mg in 1ml IPA) was spin-coated on the PbI_2 film at 6000 rpm for 30s at room temperature, and dried at 100 °C for one hour. In the case of the solid-liquid interdiffusion reaction for the perovskite, the PbI_2 film was immersed in the MAI solution (10 mg in 1ml IPA) at room temperature for 5 minutes, and dried at 70 °C for 10 minutes. Solar devices with the architecture $FTO/TiO_{2m}/MAPbI_3/Spiro\text{-}OMeTAD_{doped}/Au$ were developed for efficiency tests. When using the solid-solid interdiffusion reaction, the most efficient PSC gave a short-circuit photocurrent density (J_{sc}) of 19.81 $mA.cm^{-2}$, an open-circuit voltage (V_{oc}) of 0.91 V, and a fill factor (FF) of 69% to yield a power conversion efficiency (PCE) of 12.5%. For the solid-liquid interdiffusion reaction, they obtained a PSC having a J_{sc} of 18.86 $mA.cm^{-2}$, a V_{oc} of 0.78 V, a FF of 61%, and a PCE of 9.0%. The active surface was not specified.

One year later, Chen *et al.* electrodeposited PbO_2 on mesoporous TiO_2 to elaborate perovskite layers[22]. They used an electrolyte containing 0.1M $Pb(CH_3COO)_2$, 0.2M $NaNO_3$ and 0.1M HNO_3, which was very stable and could be reused many times. The electrodeposition was conducted at room temperature in a standard three-electrode system with TiO_2 scaffold as a working electrode, Pt gauze as a counter electrode and

Ag/AgCl as reference electrode. The deposition potential and duration ranged from 1.4 V to 2.6 V (vs. Ag/AgCl) and 5s to 60s, respectively. The electrodeposited PbO_2 was then converted to PbI_2 in HI bath, and then the obtained PbI_2 was converted to $MAPbI_3$ by immersion for 15 min in MAI bath heated at 100 °C to improve crystallization. For the optimization of the quality of the obtained perovskite layer, the concentration of the HI solution used in the first conversion step was variated. Decreasing the HI concentration offered bigger PbI_2 crystals, and bigger $MAPbI_3$ grains since a direct grain size relation was detected between PbI_2 and $MAPbI_3$. This also engenders a variation in the absorption of the perovskite since a red shift was detected for low HI concentrations. To evaluate the performance of the developed perovskite layer, an HTL-free PSC was elaborated with the following architecture: FTO/TiO_{2m}/$MAPbI_3$/C. The carbon electrode was printed and then heated at 100°C for 2h to improve the interface contact with the $MAPbI_3$ layer. The PCE tests showed that the PCE increase when the grain size decrease (HI concentration increase) until a certain limit (1.25M). The average PCE was of 8%, the best PSC offering a PCE of 10.19%, for a 0.07 cm^2 of active surface, and 4.5% for a 4 cm^2 PSC.

In the same year, Huang *et al.* electrodeposited PbO on compact TiO_2 using Pt as a counter-electrode[16]. The deposition bath consisted of an aqueous solution of 2 mM $Pb(CH_3COO)_2$, 1.5 M dimethyl sulfoxide (DMSO) and 200 mM H_2O_2. The electrodeposition was carried out at 70 °C with a potential of around 1.3 V. To convert to $MAPbI_3$, MAI was spin coated on the obtained PbO film then heated at 150 °C for 1 h under N_2 atmosphere for solid-solid interdiffusion reaction. FTO/TiO_{2c}/$MAPbI_3$/Spiro-$OMeTAD_{doped}$/Au PSCs were elaborated using the obtained perovskite film as an active layer, and offered a PCE of 14% for 0.04 cm^2. Although this method gives performant PSCs, it does not solve neither the spin-coating problem, nor the inert atmosphere.

Also in 2015, Hill *et al.* developed a perovskite film using electrodeposition with a PbI_2 film as a starting material[31]. FTO coated glass or single crystal gold substrates were used as the working electrode. The counter electrode was a high surface area platinum coiled wire, and an Ag/AgCl as reference electrode. The electrodeposition solution was prepared by dissolving lead nitrate and sodium nitrate in deionized (DI) water, adjusting the pH to 2 with nitric acid, and subsequently combining this with a solution of iodine dissolved in ethanol for final concentrations of 5 mM lead nitrate, 10 mM iodine, and 100 mM sodium nitrate in 66% ethanol. Iodine begins to be reduced at about +0.3 V vs Ag/AgCl and lead ions are reduced to lead metal at about −0.4 V vs Ag/AgCl. Therefore, PbI_2 can be electrodeposited in the potential range of −0.3 to +0.3 V vs Ag/AgCl. Some tests were done at 0 V vs. Ag/AgCl until 0.5 C/cm^2 of charge were passed. Conversion to $MAPbI_3$ was carried out by exposure to MAI vapor in inert atmosphere. The orientation of electrodeposited PbI_2 was studied with respect to the orientation of the Au plane, but the obtained perovskite layer was not tested in a solar device.

The electrodeposition of perovskite proving to give interesting results, attempts to further understand the mechanism of this method increased with the years. In 2016, Koza *et al.* that already worked on the electrodeposition of epitaxial PbI_2 and its conversion to textured $MAPbI_3$ perovskite with Hill, investigated the electrodeposition of either textured or epitaxial PbO_2 on textured Au or single crystal Au[18]. PbO_2 was electrodeposited from a solution of 0.1 M $Pb(NO_3)_2$ and 5 M NaOH in deionized water at

50 °C. Films were deposited at a potential of 0.2 V on Au sputtered glass and Au single crystals and at 0.25 V on Pt-sputtered quartz crystals, $Ag/AgCl/KCl_{sat}$ being the reference electrode. Conversion of PbO_2 into $MAPbI_3$ was performed by immersion in 0.1M MAI-IPA solution. For comparison, PbI_2 was spin coated then converted the same way. The mass variation with conversion time and temperature was checked, along with many characterizations, to understand the relation between PbO_2 orientation and $MAPbI_3$, and the effect of temperature conversion. No PSC was elaborated to verify the photovoltaic performance of the developed perovskite layer.

During the same year, Popov *et al.* electrodeposited PbO_2 films on FTO using an electrodeposition bath containing 0.10 M lead(II) acetate trihydrate and 1.00 M sodium acetate[23]. The solution was prepared by first dissolving sodium acetate, followed by initial pH adjustment to 5.6–5.8. Next, lead (II) acetate trihydrate was dissolved, followed by final pH adjustment to 5.5. ED was performed without stirring at ambient temperature with a three-electrode arrangement. FTO slides (5.0 × 2.5 cm^2) acted as working electrodes, with the active deposition area being 10 cm^2 (4.0 × 2.5 cm^2). A cylinder-shaped platinum net was used as the counter electrode and an Ag/AgCl/KCl (3 M) electrode as the reference electrode. Electrodeposition was done galvanostatically at a current density of 0.25 $mA.cm^{-2}$. PbO_2 was then converted into PbI_2 with HI vapor then into $MAPbI_3$ with MAI vapor. The PbO_2 layer was characterized, and its thickness variation was checked on different areas of substrate and when rotating it during electrodeposition. However, the study did not implicate the elaborated layer in a photovoltaic application.

In 2017, a second attempt was performed by Kosta *et al.* to develop $MAPbI_3$ films using electrodeposited PbI_2, this time in ionic liquid[19]. For this purpose, a three-electrode electrochemical cell was used: Ti-Pt mesh as CE and a Pt wire as the pseudo-RE, and glass/ FTO/c-TiO_2 (2.5 cm^2) as the WE. The PYR14TFSI based electrolyte consisted of a 0.008 M $Pb(TFSI)_2$ and 0.01 M I_2 solution, deareated before (10 minutes) and during the electrochemical experiments. Electrodeposition was performed potentiostatically at -0.65 V until a charge density of -0.14C/cm^2 was reached. Conversion of PbI_2 in nperovskite was carried out in MAI-IPA-hexane (6 mg/ml) for a certain period and rinsed with isopropanol. Different amounts of hexane (0-50% v/v) and duration times (5–30 min) were investigated. They studied the variation of the grain size using SEM, the PCE variation when changing hexane concentration, and the variation of crystallography (XRD) and PCE (J-V) when increasing the conversion time (the PSC having an active surface of 0.07 cm^2). For a $FTO/TiO2_c/MAPbI_3/Spiro\text{-}OMeTAD_{doped}/Au$ solar device, the best PCE reached was 9% when using 5% hexane.

The same year, Li *et al.* also developed a PSC using electrodeposited perovskite with PbI_2 as a starting layer[21]. The electrodeposition of PbI_2 was elaborated on TiO_{2m} with a three-electrode system: Pt foil as CE and a saturated calomel electrode (SCE). The electrolyte consisted of 10mM lead nitrate, 20mM iodine, and 100mM sodium nitrate in deionized water/ethanol (1:2 by volume) with the pH of 2 adjusted by nitric acid. Obtained PbI_2 films were then dipped in 10 $mg.ml^{-1}$ MAI-IPA solution to convert to $MAPbI_3$. The chemical and crystal structure, the morphology and the optical properties of the PbI_2 and $MAPbI_3$ films were compared when changing the deposition time. The best PSC (0.1 cm^2) offered a PCE of 6.6% for 50 min deposition, having the architecture $FTO/TiO_{2m}/MAPbI_3/Spiro\text{-}OMeTAD_{doped}/Au$.

Zanca *et al.* decided in 2018 to investigate more the effect of the conversion solutions' concentration and the conversion time on the obtained films[29]. They electrodeposited PbO_2 in a three-electrode system: ITO PET as the WE, graphite as the CE and saturated calomel electrode (SCE, E = +0.24 V/SHE) as the RE. The electrolytic solution of 0.1 M lead(II) acetate trihydrate, 0.2 M sodium nitrate, 0.1 M nitric acid was used for the electrodepositions. PbO_2 samples were obtained by two consecutive steps: potentiostatic (for 0.15 C/cm^2) and galvanostatic (for 75s), at room temperature while stirring. Conversion of PbO_2 to PbI_2 was carried out by dipping in varying hydroiodic acid (57% wt) from 1.25M to 0.001M in ethanol at room temperature. PbI_2 was then converted to $MAPbI_3$ by dipping in a 6-10 mg/ml MAI-IPA solution for 1-2 hour. However, the obtained films were not tested in solar devices.

In 2019, Lee *et al.* developed a new path to obtain $MAPbI_3$ from electrodeposited PbO_2[17]. First, PbO_2 was electrodeposited on the NiO/ITO or textured Si/ITO substrate using a three-electrode system (NiO/ITO substrate, Pt foil, and a saturated calomel electrode (SCE)). A 2mM $Pb(NO_3)_2$ aqueous solution was used as the electrolyte and was kept at 50 °C using a water bath. The pH of the solution was fixed at 4.8. The deposition potential ranged from 0.9 to 1.7 V (vs. SCE), and the deposition time ranged from 100 to 300 s with stirring at 250 rpm. After the deposition, the PbO_2 films were rinsed and annealed at 150 °C for 10 min on a hot plate. They were then converted into PbO by purging with H_2/Ar and annealing, and finally converted to $MAPbI_3$ by MAI vapor exposure. This work focused on the study of the effect of deposition potential and conversion time, the effect of substrate nature (planar or textured), and the effect of deposition technique (constant or pulsed potential). No photovoltaic application was tested.

The interest of researchers to further develop the electrodeposition of perovskites kept on increasing. In 2020, six different articles studied the electrodeposition of perovskite films. Abdy and Heydari worked published two papers of work on this subject[24,27]. The first one was a brief review on the perovskite synthesis method. Then they electrodeposited perovskite by three different methods: two-step solution deposition (spin-coating PbI_2, then spin-coating MAI), solvent engineering (spin-coating of one mixture solution), and electrodeposition (eletrodeposition of PbO_2, then conversion to PbI_2 by HI vapor in glass boat, and finally conversion to $MAPbI_3$ by MAI vapor in glass boat). The morphology and crystal properties of the obtained films were then compared. In their second publication, they prepared $MAPbBr_3$ via direct transformation of electrodeposited PbO_2 for photodetector application, which was the first work on the electrodeposition of $MAPbBr_3$. In the electrodeposition bath, sodium acetate was dissolved in deionized water and the pH of the solution was adjusted to about 5.6–5.8. Lead(II) acetate was added followed by adjusting the pH of the solution to 5.5. For improving the adhesion of electrodeposited PbO_2 to the TiO_2 substrate, NaF was added to the solution. Adjustments of pH were done using 5 M acetic acid and 3 M sodium hydroxide. The resulting electrolyte solution contained 0.1 M lead(II) acetate ($Pb(CH_3COO)_2 \cdot 3H_2O$), 1 M sodium acetate ($NaCH_3COO$), and 0.04 M sodium fluoride (NaF). PbO_2 deposition was carried out at room temperature, without stirring, using a galvanostat instrument and a three-electrode cell (TiO_2 on FTO substrate (WE), platinum (CE), and Ag/AgCl/KCl (RE)) with a current density of 0.32 mA.cm^{-2} for 200 s. PbO_2 films were converted into perovskite with the MABr powder in a solid–solid transformation

process in a 0.7 bar vacuum system and heating at 170 °C for 2 h. The morphology and optical properties of the films electrodeposited for 200 s and 300 s were then compared.

In that same year, Liu *et al.* developed a perovskite layer by electrodeposition of Pb on the substrate, then conversion to $MAPbI_3$ by electrodeposition of MAI[25]. As a first step, the electrodeposition of Pb layer was carried out in a nitrogen-protected two-electrode cell (Pt sheet and mp-TiO_2 substrate). The deposition bath was a solution of 10 mM PbI_2, 1.3 M NaI, and 0.7 M ethylene glycol tertiary butylether dissolved in dimethyl sulfoxide. Deposition was performed at a constant applied potential difference of -2 V for 240, 260, 280, and 300 s, respectively. Then, conversion into $MAPbI_3$ was carried out by depositing MAI onto the as-prepared Pb layer. The reaction was performed in a 10 mg/mL MAI solution in isopropanol. A square-wave pulse potential difference (f=5 Hz) was introduced with a +2 V first half-wave amplitude and a -2 V second half-wave amplitude to carry out electrodeposition. Deposition was separately carried out for 120, 140, 160, and 180 s. The performance of the elaborated perovskite film was then tested in a c-TiO_2/mp-TiO_2/$MAPbI_3$/Spiro-OMeTAD/Au solar device (0.04 cm^2), and the best PCE reached was of 14.3%.

Yadav *et al.* also studied the electrodeposition of $MAPbI_3$, while investigating the effect of the potential gradient on the morphology and crystallography of the obtained layer[26]. In this study, PbO_2 was electrodeposited on 1.5 cm × 1.5 cm and 7.5 cm × 2.5 cm ITO substrate at 0.27, 0.3, 0.4, and 0.5 V for 254 s in 0.1 M $Pb(NO_3)_2$ in 5 M NaOH using Ag/AgCl and a graphite rod as the reference and counter electrodes, respectively. The solution of 0.1 M $Pb(NO_3)_2$ in 5 M NaOH was prepared by dissolving lead nitrate in 5 M NaOH at 50 °C for 1 h under stirring. The subsequent conversion to $MAPbI_3$ was carried out by dipping the PbO_2 film in a 0.1 M MAI solution in isopropanol at 50 °C. In addition to the density gradient, the stability, fluorescence and photochemical properties of the layers was studied. The elaborated perovskite was however not tested in a PSC.

No doubt this method has risen the interest of the researchers, since also in 2020, Lv *et al.* were the first group to develop a mixed perovskite via electrodeposition[30]. They studied the preparation of all-inorganic $CsPbI_{2-x}Br_{1+x}$ perovskite solar cells based on electrodeposited PbO_2 film. The main electrolyte was a mixture of 0.1 M $Pb(CH_3COO)_2$, 0.2 M $NaNO_3$ and 0.1 M HNO_3 (The electrodes being a TiO_2 film, a Pt sheet and a saturated Ag/AgCl). The active area of the TiO_2 working electrode was 1.5 × 2 cm^2. The deposition current was set to 0.01 A, while the deposition time was 15 s. The obtained PbO_2 layers were immersed in the 0.05 M HI ethanol solution at room temperature. The immersion time was related to the film thickness of PbO_2. The PbI_2 layer was rinsed afterwards in ethanol. A methanol solution containing 0.05 M CsBr was spin-coated onto the PbI_2 film at 2000 rpm for 20 s to form the $CsPbI_{2-x}Br_{1+x}$ inorganic perovskite layer, for several times (1–8 times) to form a high-quality layer, while DMF was used as an additive. The concentration of DMF ranged from 0.5 v% to 4.0 v%. Then, the samples were heated to 350 °C for 30 s on a hotplate. When testing the performance of the obtained perovskite layers, a PCE of 6.87% was obtained for small cells (0.25 cm^2) and 2.84% for large size cells (1.5 cm^2) using the c-TiO_2/m-TiO_2/$CsPbI_{2-x}Br_{1+x}$/C structure. Although their attempt was innovative, the as-mentioned procedure did not exclude the need for spin-coating, hence the low efficiencies for larger cells.

In addition to the method described above, Wang *et al.* developed a perovskite under atmospheric conditions by electrodepositing Pb then converting it to $CsPbBr_3$ perovskite under a positive bias in a CsBr solution[244]. The first step was the deposition of Pb onto TiO_{2m} with 0.02 M PbI_2 solution in IPA. The second step was the conversion of Pb into $CsPbBr_3$ perovskite under a positive bias in a methanol solution of CsBr (15 $mg{\cdot}mL^{-1}$). The as-prepared samples were then annealed at 250 °C for 10 min. They used this perovskite in a PSC having the architecture FTO/TiO_{2m}/$CsPbBr_3$/Spiro-OMeTAD/Au and achieved a PCE of 7.86%, with a V_{oc} of 1.43 V, a J_{sc} of 8.85 $mA.cm^{-2}$, and a FF of 0.62 (the active surface was not indicated). The unencapsulated perovskite showed remarkable stability, where the cell maintained ~99.7% of its original PCE even after 150 days of storage in air (40–50 RH % and RT) under natural light.

Recently in 2021, Wang *et al.* studied the electrodeposition of perovskite on textured c-Si solar cells, with a perspective of application in tandem solar devices[245]. They first electrodeposited Pb in sodium iodide and PbI_2 -IPA solution, at a bias voltage going from −1 to −6 V and for a deposition time of 300 s . Then the conversion to $MAPbI_3$ was carried out in MAI-IPA solution by applying a symmetric square-wave pulse voltage set at the positive pulse voltage for 100 ms and then at the negative pulse voltage for 100 ms in one cycle, the amplitude set at 1−6 V and the conversion time was 400s. The elaborated perovskite was however not tested in a solar device.

Most recently, Gozaldadeh *et al.* elaborated $FAPbI_{3-x}Br_x$ perovskite by depositing PbS as a starting layer[246]. A three-step deposition method was employed to produce the perovskite film. Initially a PbS layer was coated on substrates via chemical bath deposition method (but electrodeposition method could also be affordable perspective). The deposition bath contained an aqueous solution consisting of $Pb(CH_3COO)_2$. $3H_2O$, thiourea $SC(NH2)_2$, NaOH and triethanolamine. The deposition was performed at room temperature. Afterward, the PbS layers and iodine chips were put inside a petri dish at different temperatures to chemically convert PbS to PbI_2. Next, PbI_2 films were exposed to a FAI:MACl:MABr solution (85:10:10 $mg.ml^{-1}$) and then spun at 5000 rpm for 30 s. After two step annealing at 150 °C and 100 °C for 30 min per each, the conversion of PbI_2 to perovskite film was completed. They tested this perovskite layer in a PSC (FTO/TiO_{2c}/TiO_{2m}/perovskite/Spiro-OMeTAD/Au) and reached a PCE of 11.35% with corresponding photocurrent of 21.43 $mA.cm^{-2}$ and open circuit voltage of 0.918 V, but the active surface was not mentioned.

V.3. Existing chemical reactions for $MAPbI_3$ perovskite synthesis using an initial electrodeposition step

Electrodeposited film	Reaction for the conversion in PK
PbO	$CH_3NH_3I \rightarrow CH_3NH_2 + HI$ $PbO + 2\ HI \rightarrow PbI_2 + H_2O$ $PbI_2 + CH_3NH_3I \rightarrow CH_3NH_3PbI_3$
PbO_2	$PbO_2 + 5\ MAI \rightarrow 4\ CH_3NH_2\ (g) + 2\ H_2O + I_2 + CH_3NH_3PbI_3$
PbO_2 via PbI_2	$PbO_2 + 4\ HI \rightarrow PbI_2 + 2\ H_2O + I_2$ $PbI_2 + CH_3NH_3I \rightarrow CH_3NH_3PbI_3$
PbI_2	$PbI_2 + CH_3NH_3I \rightarrow CH_3NH_3PbI_3$
Pb	$Pb^{2+} + CH_3NH_3^{+} + 3I^{-} \rightarrow CH_3NH_3PbI_3$
PbS	$PbS + I_2 \rightarrow PbI_2 + S$ $PbI_2 + CH_3NH_3I \rightarrow CH_3NH_3PbI_3$

V.4. Overview table on electrodeposited perovskite in literature

	Deposited compound	Substrate	Bath composition	Deposition T°C	Deposition conditions	Deposition parameters	Route to PK	PSC
2014 Cui	PbO	TiO_{2m}	Aqueous 2 mM $Pb(NO_3)_2$ 0.2 M H_2O_2	-	-	-	· Exposed to iodine vapor to obtain PbI_2 · Converted to $MAPbI_3$ by spin coating MAI (1) · Converted to $MAPbI_3$ by immersion in MAI (2)	FTO/TiO_{2m}/$MAPbI_3$/Spiro-OMeTAD/Au PCE 12.5% device 1 PCE 9% device 2
2015 Chen	PbO_2	TiO_{2m}	Aqueous 0.1M $Pb(CH_3COO)_2$ 0.2M $NaNO_3$ & 0.1M HNO_3	Room T°C	-	1.4V to 2.6V vs Ag/AgCl 5s to 60s	· Conversion to PbI_2 in HI bath · Conversion to $MAPbI_3$ in MAI bath	FTO/TiO_{2m}/MAPI/C Best PCE 10.19% (0.07 cm^2)
2015 Hill	PbI_2	Single crystal Au	In 66% ethanol 5 mM $Pb(NO_3)_2$ 10mM I_2 & 100mM $NaNO_3$	-	-	Potential range of −0.3 to +0.3 V vs Ag/AgCl	Exposure to MAI vapor in inert atmosphere	-
2015 Huang	PbO	TiO_{2c}	Aqueous 2 mM $Pb(CH_3COO)_2$ 1.5M DMSO & 0.2M H_2O_2	70 °C	-	1.3 V vs Ag/AgCl	Spin coating of MAI and solid-solid interdiffusion reaction at 150 °C for 1 h under N_2	FTO/TiO_{2c}/$MAPbI_3$/Spiro-OMeTAD/Au PCE 14% (0.04 cm^2)
2016 Koza	PbO_2	Textured or single crystal Au	Aqueous 0.1 M $Pb(NO_3)_2$ 5 M NaOH	50 °C	-	0.2 V on Au and at 0.25 V vs Ag/AgCl on Pt-sputtered	Immersion in 0.1M MAI-IPA solution	
2016 Popov	PbO_2	FTO	Aqueous pH 5.5 0.10 M $Pb(CH_3COO)_2$ 1.00 M $NaCH_3COO$	Ambiant	Without stirring	Galvanostatically at a current density of 0.25 $mA.cm^{-2}$	· To PbI_2 with HI vapor · To $MAPbI_3$ with MAI vapor	
2017 Kosta	PbI_2	FTO/TiO_{2c}	PYR14TFSI based 0.008 M Pb (TFSI)2 0.01 M I_2 DW/ethanol (1:2) pH 2 10mM $Pb(NO_3)_2$ 20mM I_2 & 100mM $NaNO_3$	-	Deaerated before and during ED	Potentiostatically at -0.65 V until a charge density of -0.14 C/cm^2	Conversion in MAI-IPA-hexane (6 mg/ml)	FTO/TiO_{2c}/$MAPbI_3$/Spiro-OMeTAD/Au Best PCE 9% for 5% Hex (0.07 cm^2)
2017 Li	PbI_2	TiO_{2m}		-	-	-	Immersion in 10 mg/mL MAI-IPA	FTO/TiO_{2c}/$MAPbI_3$/Spiro-OMeTAD/Au Best PCE 6.6% for 50 min ED (0.1 cm^2)
2018 Zanca	PbO_2	ITO	0.1 M $Pb(CH_3COO)_2$ 0.2 M $NaNO_3$ 0.1 M nitric acid	Room T°C	Stirring	Potentiostatic for 0.15 C/cm^2 Galvanostatic for 75s	· To PbI_2 by dipping in varying HI-EtOH from 1.25M to 0.001M · To $MAPbI_3$ by dipping in a 6-10 mg/ml MAI-IPA solution for 1-2 hour	-
2019 Lee	PbO_2	NiO/ITO Textured Si/ITO	Aqueous pH 4.8 2 mM $Pb(NO_3)_2$	50 °C using a water bath	Stirring	Potential from 0.9 to 1.7 V (vs. SCE), deposition time from 100 to 300 s	· To PbO by purging with H_2/Ar and annealing · To $MAPbI_3$ by MAI vapor exposure	-
2020 Abdy	PbO_2	FTO TiO_{2c} TiO_{2m}	Aqueous pH 5.5 0.1 M $Pb(CH_3COO)_2$ 1 M $NaCH_3COO$ & 0.04 M NaF	Room T°C	Without stirring	Current density of 0.32 $mA.cm^{-2}$ for 200s	· To PbI_2 by HI vapor in glass boat · To $MAPbI_3$ by MAI vapor in glass boat	-
2020 Heydari	PbO_2	FTO	Aqueous pH 5.5 0.1 M $Pb(CH_3COO)_2$ 1 M $NaCH_3COO$ & 0.04 M NaF	-	-	-	To $MAPbBr_3$ with the MABr powder in a solid–solid transformation process in vacuum and heating at 170 °C for 2 h	-
2020 Liu	Pb	TiO_{2m}	In DMSO 10 mM PbI_2 1.3 M NaI & 0.7 M ETB	-	-	Potential of -2 V for 240, 260, 280, and 300 s	To $MAPbI_3$ by depositing MAI, in a 10 mg/mL MAI-IPA solution, square-wave pulse potential: -2V and +2V, for 120, 140, 160, and 180 s	TiO_{2m}/$MAPbI_3$/Spiro-OMeTAD/Au Best PCE 14.3% (0.04 cm^2)
2020 Lv	PbO_2	FTO/TiO_{2m}	Aqueous 0.1 M $Pb(CH_3COO)_2$ 0.2 M $NaNO_3$ & 0.1 M HNO_3	-	-	Deposition current 0.01A Deposition time 15 s	· To PbI_2 in 0.05M HI solution · To PK by spin coating CsBr several times and heating	$TiO_{2c,m}$/$CsPbI_{3-x}Br_{x-m}$/C PCE of 6.87% is obtained for small cells (0.25 cm^2) and 2.84% for large size cells (1.5 cm^2)
2020 Yadav	PbO_2	ITO	Aqueous 0.1 M $Pb(NO_3)_2$ 5 M NaOH	-	-	Potential of 0.27, 0.3, 0.4, and 0.5 V for 254s	To $MAPbI_3$ by dipping in 0.1M MAI-IPA solution at 50°C	-
2020 Wang	Pb	TiO_{2m}	0.02 M PbI_2 - IPA	Ambiant	-	-	To $CsPbBr_3$ under a positive bias in CsBr- methanol (15 mg:mL−1), then 250°C for 10 min	FTO/TiO_{2m}/$CsPbBr_3$/Spiro-OMeTAD/Au PCE 7.86%
2021 Wang	Pb	Textured c-Si	NAI and PbI_2 -IPA	-	-	Bias voltage going from −1 to −6 V, for 300 s	To $MAPbI_3$ by a symmetric square-wave pulse voltage (100 ms), at 1–6 V and for 400s	-
2021 Gozaldadeh	PbS	TiO_{2m}	Pb$(CH_3COO)_2$.3H_2O SC$(NH_2)_2$ NaOH & TEA	-	-	-	Convert PbS to PbI_2 by mixing with I_2 chips Convert to $FAPbI_{3-x}Br_x$ by spin coating FAI:MACl:MABr solution	FTO/$TiO_{2c,m}$/$FAPbI_{3-x}Br_x$/Spiro-OMeTAD/Au PCE 11.35%

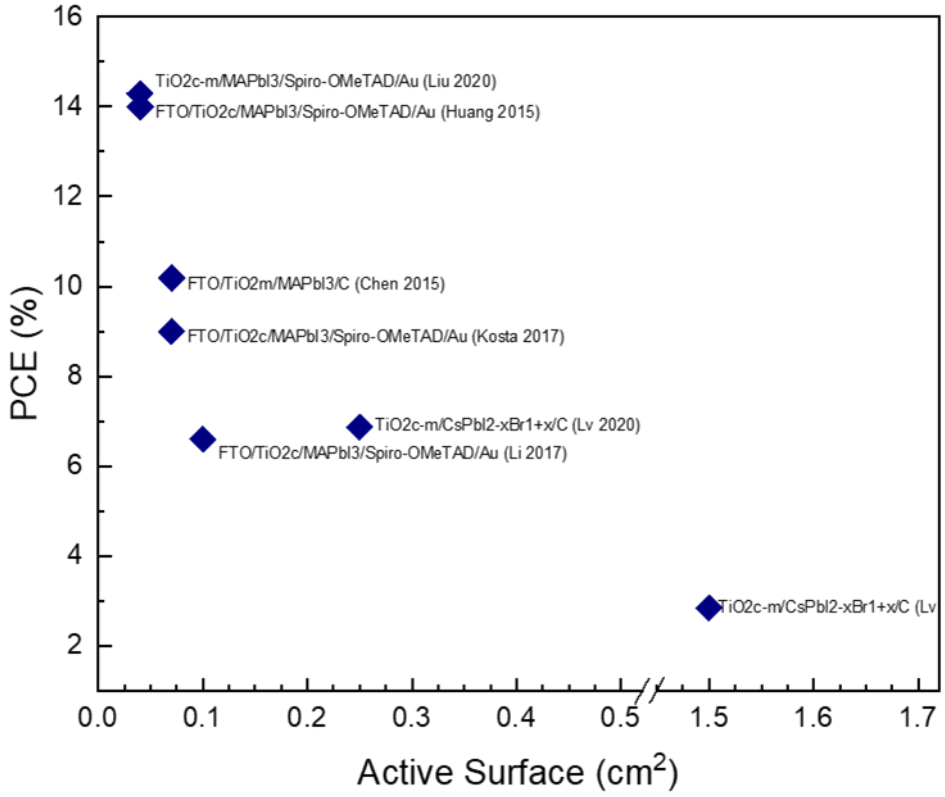
TiO2c-m/MAPbI3/Spiro-OMeTAD/Au (Liu 2020)
FTO/TiO2c/MAPbI3/Spiro-OMeTAD/Au (Huang 2015)
FTO/TiO2m/MAPbI3/C (Chen 2015)
FTO/TiO2c/MAPbI3/Spiro-OMeTAD/Au (Kosta 2017)
TiO2c-m/CsPbI2-xBr1+x/C (Lv 2020)
FTO/TiO2c/MAPbI3/Spiro-OMeTAD/Au (Li 2017)
TiO2c-m/CsPbI2-xBr1+x/C (Lv
PCE (%)
Active Surface (cm2)
16
14
12
10
8
6
4
2
0.0
0.1
0.2
0.3
0.4
0.5
1.5
1.6
1.7

VI. General Conclusion and Outlook

Through the years, many materials have been used in photovoltaic devices like silicon, inorganic materials originating for the II-IV and III-V groups, organic molecules and polymers, and hybrid perovskites. Although silicon-based solar devices are the most common and commercialized nowadays, having the world record efficiency of 27.6%[3], expensive high temperature and high vacuum processes are needed for the silicon to be extremely pure, which elevates the commercialization cost. Contrarily, perovskite solar cells have revolutionized the field because of outstanding photovoltaic performance, approaching that of Si, their easy fabrication process and their flexibility in material growth process and architecture options[78]. Simple $MAPbI_3$ perovskite is the most common hybrid halide perovskite for photovoltaic applications. However, compositional engineering, like the substitution of the cation/anion, or the use of mixed halide perovskites, was demonstrated to be an effective strategy to further enhance the optoelectronic properties of $MAPbI_3$.

Spin-coating deposition technique is simple and low cost so it has been the most commonly used perovskite deposition method in laboratory researches. However, this method cannot be adopted to fabricate large-scale PSC, hence the need to look up new processes for large scale production of PSCs. As an alternative, the electrodeposition method was recently explored as an efficient technique for perovskite fabrication. This technique is low cost, forms smooth and uniform layers, could be elaborated for large scale devices and most importantly could be performed in ambient atmosphere.

In the upcoming study, electrodeposition will be adopted to develop perovskite solar devices, whether with simple $MAPbI_3$ or mixed perovskites such as $MAPbI_{3-x}Cl_x$ or $MA_xFA_{1-x}Pb(I_yBr_{1-y})_3$. The architecture of the solar cell being one of the main performance deciding factors, it will also be optimized by using a carbon electrode that has proved to be as efficient as metal electrodes, with much less cost.

Chapter II: Impact of the substrate nature and the conversion route on electrodeposited perovskite layers

This chapter presents our first article which concerns the optimization of the electrodeposition of simple $MAPbI_3$. In particular, two different conversion routes were compared. The effects on the morphology, the chemical and the optical properties of the perovskite film of both the substrate nature and the conversion route were also investigated. Finally, the photovoltaic performances of the elaborated perovskite layers were compared in a carbon-based PSC. This first study allowed us to define the most suitable way for the electrodeposition of perovskite. In the following chapters, a similar procedure will be adopted.

Electrochemical deposition of perovskite layers developed for photovoltaic application: Impact of the substrate nature and the conversion route

Mirella Al Katrib [1], Lara Perrin [1, *], and Emilie Planes [1, *]

[1] Univ. Grenoble Alpes, Univ. Savoie Mont Blanc, CNRS, Grenoble INP, LEPMI, 38000 Grenoble, France

Abstract

The electrodeposition method was explored as an efficient method for perovskite fabrication. It possesses the ability to elaborate high-quality perovskite layers on large size substrates, with a minimum manufacturing cost. In this work, the electrodeposition of PbO_2 was conducted as a first step to elaborate perovskite layers. Two conversion routes have been studied to reach the perovskite film. The first one consist in an immediate conversion of PbO_2 into PK1 by immersion in MAI (CH_3NH_3I) solution. The second route is a two-step conversion: first conversion into PbI_2 by immersion of PbO_2 in HI, then immersion of PbI_2 in MAI to convert into PK2. For further evaluation of the impact of the conversion route and the substrate nature, many characterizations such as UV-Visible absorption, photoluminescence, X-ray diffraction and scanning electron microscopy were carried on. A perovskite solar cell has also been developed using the electrodeposited active layers, which opens the way to promising performances using electrodeposition.

Introduction

Recently, halide perovskites have drawn substantial interest in the fields of photovoltaic[154]. They absorb like a direct-gap semiconductor with the slow radiative recombination of an indirect-gap semiconductor[247]. In fact, perovskite solar cell technology was selected as one of the biggest scientific breakthroughs of 2013 by the editors of Science and Nature[248,249]. This is due to the high efficiency of solid-state solar cells based on halide perovskites, which reached 9.7% in 2012, up to 17.9% in 2014, and exceeded 25% in 2020[92,250]. Several techniques were developed to elaborate high-quality perovskite films for photovoltaic application, and improve crystallization of the active layer[251]. Currently, spin coating is the most used technique for perovskite solar cells deposition, either by a one-step or a two-step method[252]. However, it presents many constraints such as limited surface coverage, high production price, relatively low homogeneity, undefined perovskite crystallinity, poor stability. They also must be elaborated under inert atmosphere. Alternative methods must be explored, and the biggest challenge nowadays is to find a better deposition technique that gives high-quality perovskite layers on controllable size substrates, with a minimum manufacturing cost. For instance, vapor deposition is appropriate to elaborate large-scale thin films, but requires high vacuum and thus higher cost[145]. Atomic layer deposition was also studied to elaborate perovskite thin films, but it remains a complex technique and requires precise control of sensitive deposition parameters[253]. Herein, the electrodeposition

method was explored as an efficient alternative for perovskite fabrication, satisfying the as-mentioned advantages[28]. This technique is low cost, forms smooth and uniform layers, could be elaborated for large scale devices and most importantly could be realized in ambient atmosphere[28]. There have been several attempts over the past years to optimize the electrodeposited perovskite layer and adjust its crystallization on dissimilar layers. All sub-techniques started by electrodepositing an initial layer (PbO, PbO_2 or PbI_2) followed by one or several conversions of the as-deposited layer[16–31]. Cui *et al.* and Huang *et al.* both deposited PbO as a first step, before conversion into perovskite[16,20]. Cui chose a two-step conversion, first by exposing the as-prepared PbO films to iodine vapor then converting into perovskite by immersion in MAI[20]. He was able to develop a gold electrode-based solar device with a 9% PCE. However, its technique required vacuum deposition that retains this method as a complex deposition. Huang spin coated MAI directly on PbO_2, under N_2 and obtained a 14% PCE for a gold electrode-based solar cell[16]. This method does not solve neither the spin-coating problem, nor the inert atmosphere. Kosta *et al.* and Li *et al.* chose to deposit PbI_2 as a first step[19]. They both were able to elaborate gold electrode-based solar devices with PCEs reaching 9% and 6.6%. The problem there was that the electrodeposition of PbI_2 is slow, and needs complex optimization of parameters. Pouncing from electrodeposited PbO_2 to perovskite was the most efficient and simple route. Chen *et al.* were able to elaborate a carbon-based solar device with a simple $CH_3NH_3PbI_3$ ($MAPbI_3$) perovskite. They used a two-step conversion method by film-immersion in conversion baths, and were able to develop a carbon-based solar device with a 10% PCE[22].

Hence, to this moment, the effect of the different parameters used in the electrodeposition on the perovskite layer, the impact of the substrate nature, and the conversion route has not been fully understood. In nearly all designs, a three-electrode system is used for electrodeposition composed of a counter electrode, a working electrode and a reference electrode, placed in the electrolyte that can be reused several times and thus reduce production price. In this work, we developed a perovskite solar cell (PCS) using electrodeposition, under ambient atmosphere. An indium tin oxide (ITO) substrate was used as transparent cathode, a spin coated SnO_2 or mesoporous TiO_2 (TiO_{2m}) as an electron transport layer (ETL), the electrodeposited perovskite layer (PK) as the active layer, a spin coated P3HT as a hole transport layer (HTL) and a carbon paste top-layer as conducting anode. Two paths have been chosen to elaborate the perovskite, the first one by immediate conversion of PbO_2 into PK by immersion in CH_3NH_3I (MAI) solution (called PK1) and the second path is a two-step conversion, first by immersion of PbO_2 in HI to convert it into PbI_2 then by immersion of PbI_2 in MAI to convert into perovskite (called PK2). The aim of the work is to understand the different steps for elaborating the electrodeposited perovskite, by studying the impact of the substrate nature and the conversion route on the composition, the morphology and the efficiency of the electrodeposited active layer.

Results and discussion

The first step to obtain $MAPbI_3$ films in the current study is the electrodeposition of PbO_2. As schematized in Figure 14-a, a three-electrode system was used, composed of a counter electrode, a working electrode and a reference electrode, placed in the electrolyte. This deposition was carried out on four different substrates placed as working electrode: ITO, SnO_2, TiO_{2c} and TiO_{2m}.

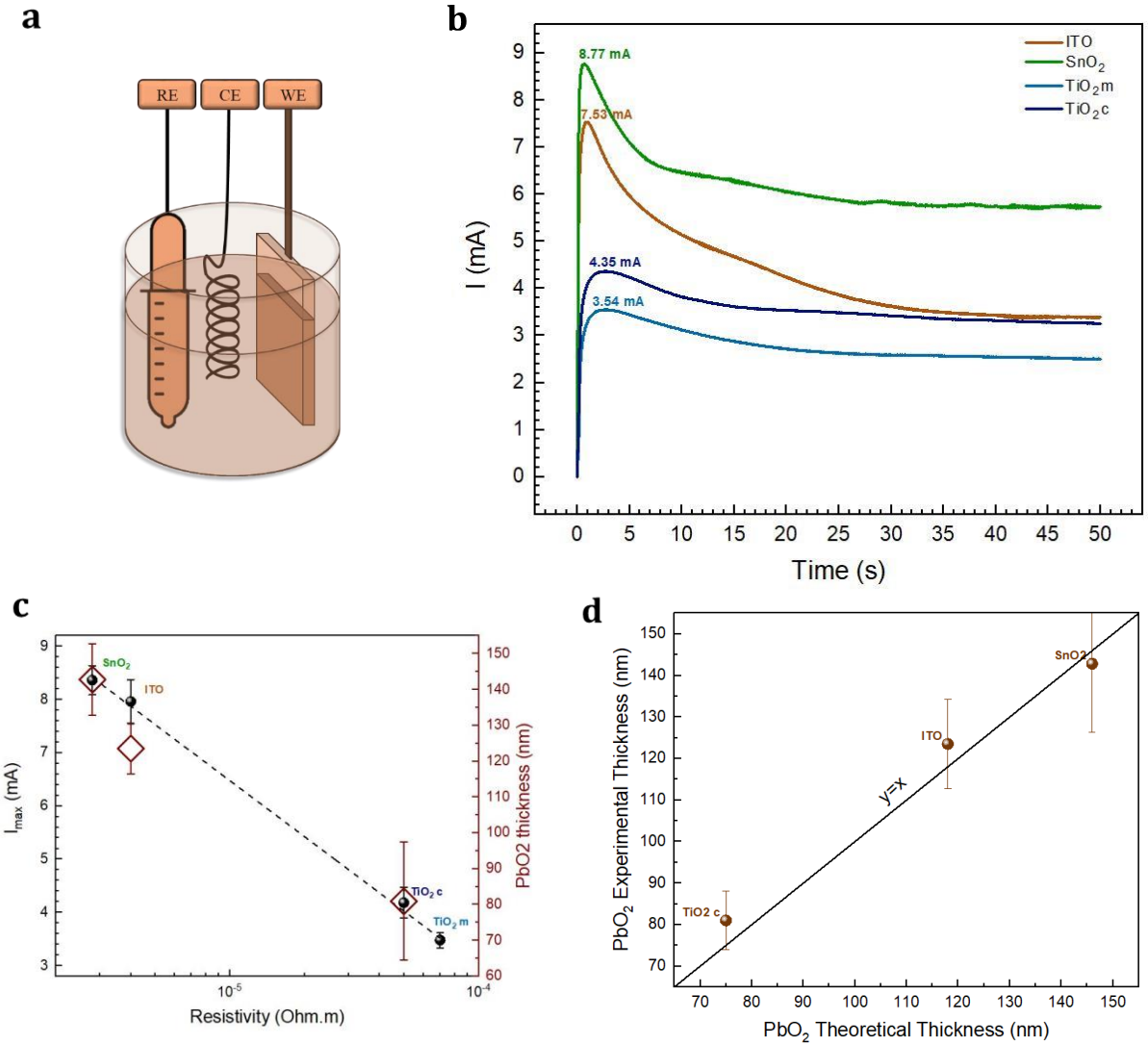

Figure 14: a) Scheme of the electrodeposition setup used in this work, b) Chronoamperometry curves showing the variation of the current versus time during electrodeposition of PbO_2 on four different substrates, c) Maximum current measured determined from the chronoamperometry curves as a function of the substrate resistivity, and d) PbO_2 experimental thickness measured by profilometry versus the theoretical thickness calculated from Faraday Law

Figure 14-b shows the chronoamperometry curves carried out on four substrates of different nature, which play here the role of working electrode. They provide information on the PbO_2 electrodeposition process. We notice a drastic increase in current in a few milliseconds at initial reaction time, representing the formation of the PbO_2 monolayer. As demonstrated in literature[254], this correlates with the full coverage of the substrate with PbO_2. The following decrease in current results from the need of diffusion of electroactive species towards the electrode surface[254,255,256].

The four substrates exhibited the same mechanisms as revealed by qualitatively similar current curves. On the quantitative standpoint, the maximum current I_{max} and the stabilized current at the end of the deposition strongly varied. Figure 14-c shows the correlation between the substrate resistivity and the maximal current measured during the electrodeposition I_{max}. For example, SnO_2, which presents the lowest resistivity, reaches the highest current during electrodeposition. More conductive substrate seems to allow higher maximum current. This shows that the conductivity of the electrodes alter the ability to deposit the PbO_2, and thus that the geometry of the cells should be kept constant for valid comparison. These differences according to the substrate also indicate a probable impact on the deposited thicknesses, the morphology and the microstructure of the layers obtained. As shown in Figure 14-c, the same relation could be deduced between the PbO_2 thickness (measured using profilometry) and the substrate resistivity. This will be further described in the present article.

Concerning the PbO_2 deposited thicknesses, the experimental values determined by profilometry were compared to theoretical values obtained from the Faraday Law[254]:

$$m = \frac{M \int I \, dt}{nF} = \frac{MQ}{nF} = \rho S e \qquad \text{Equation 1}$$

with m the mass of deposited layer, M the molar mass of deposited material, I the current, t the time, n the exchange number, F the Faraday constant (96485 $C.mol^{-1}$), Q the faradic charge, ρ the density of deposited material ($g.cm^{-3}$), S the electrode surface (cm^2) and e the deposited thickness (cm).
This law states that the amount of mass released by the electrodeposition process is proportional to the total charge defined as the integrated curve over time during the deposition process. As seen in Figure 14-d, the experimental measurements are in good agreement with the calculations made with the current usage. This is good indication of a well-controlled electrodeposition of this PbO_2 layer on planar substrates. The thicknesses strongly vary depending on the nature of the substrate. A ratio of about two between the extreme values was measured. These differences depend on the intrinsic resistivity of the underlaying electrode. Better electrodes with higher conductivity favoring thicker deposition.

In the case of the mesoporous TiO_2 substrate, the PbO_2 growth mechanism is expected to be a bottom-up growth on the porous scaffold. The goal here was to try and fill the mesoporous structure with PbO_2 up to the surface. It is therefore impossible to determine the real thickness deposited. As presented in Figure S1, different deposition durations have been tested and the morphology of the resulting layers studied by optical and scanning electron microscopies. By this approach, it is possible to guarantee a good coverage for converted PbI_2 and $MAPbI_3$, which is an essential condition for solar cell elaboration. The authors working with spin-coating on mesoporous scaffolds, commonly increase the temperature up to 100°C to improve infiltration and fill the pores[143,225]. This additional step of annealing seems not to be necessary in the case of the electrodeposition.

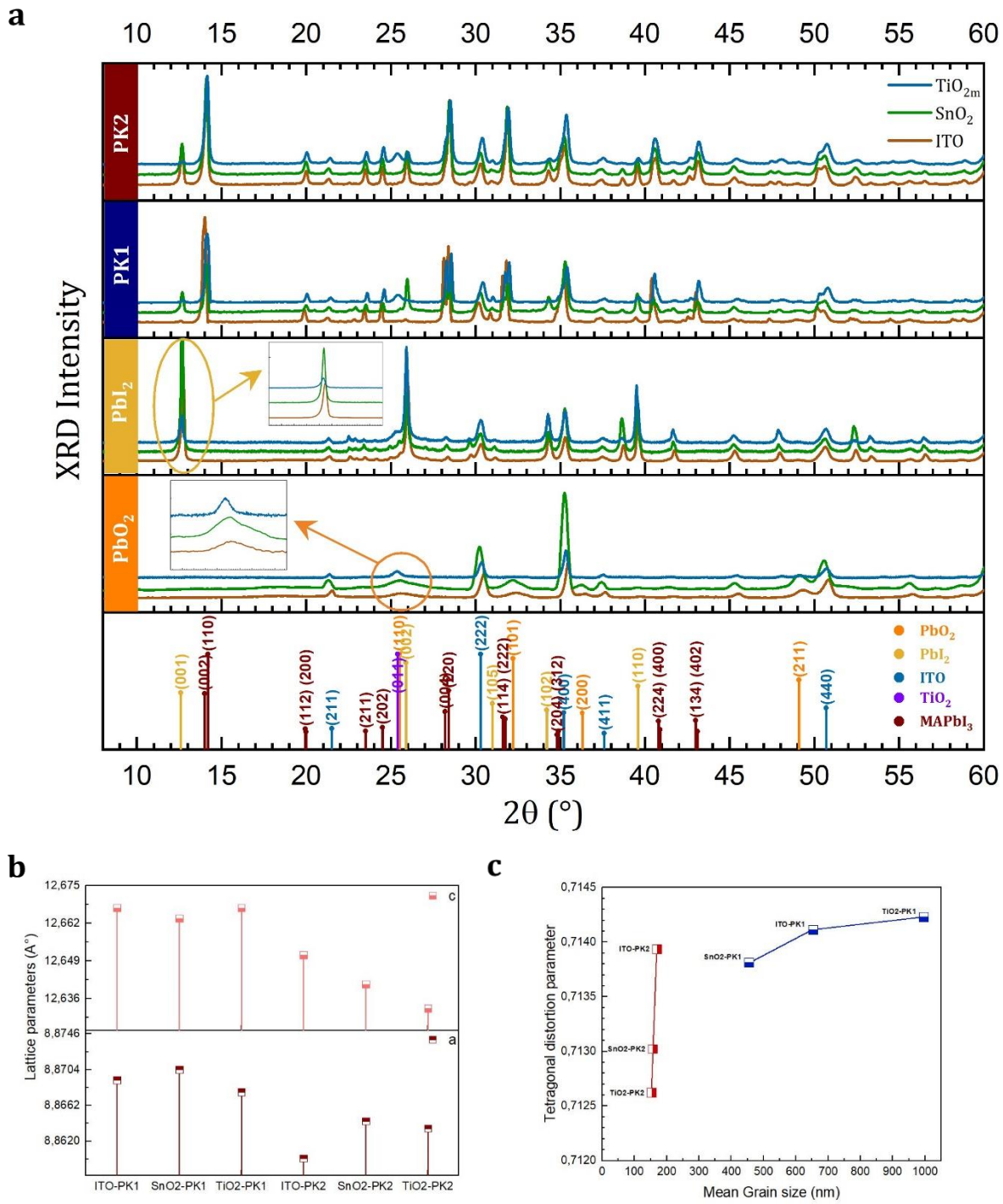

Figure 15: a) X-Ray diffraction patterns of PbO_2, PbI_2, PK1 and PK2 deposited for 50s on ITO, SnO_2 and TiO_{2m}, b) Lattice parameters a and c for tetragonal PK1 and PK2 deposited on ITO,SnO_2 and TiO_{2m} ,c) Tetragonal distortion parameter c/2a and mean grain size of PK1 and PK2 deposited on the three substrates

	Relative Crystallinity (%)			
	PbO_2	**PbI_2**	**PK1**	**PK2**
ITO	70.7	85.2	27.4	30.4
SnO_2	52.2	95.7	22.4	28.7
TiO_{2m}	57.1	79.0	33.0	31.6

Table 1: Relative crystallinity of PbO_2, PbI_2, PK1 and PK2 deposited for 50s on ITO, SnO_2 and TiO_{2m}, calculated from the XRD patterns

As mentioned, the electrodeposited PbO_2 films were either directly converted into PK1 or converted into PbI_2 before final conversion to PK2. It is therefore essential to identify the obtained materials, and understand their phase composition using X-Ray diffraction analyses. Figure 15-a shows the XRD patterns of PbO_2, PbI_2, PK1 and PK2 deposited on three different substrates. We chose to continue the study on mesoporous TiO_2 rather than compact TiO_2, as TiO_{2c} is only used as a blocking layer prior to TiO_{2m} deposition[257,258]. Whatever the substrate nature, PbO_2 layers present four different peaks at 25.5°, 32.2°, 36.4° and 49.3° corresponding to the (110), (101), (200) and (211) lattice planes of tetragonal β-PbO_2. These diffraction peaks have rather low intensities and a large full width at half maximum (FWHM), which indicates a small grain size, according to Scherrer equation. For instance, (110) peak for PbO_2 deposited on ITO has a FWHM of 1.67°, corresponding to a grain size of 5 nm. Similar results have already been reported after electrodepositing PbO_2 before conversion into perovskite[22]. We also note differences with the nature of the substrate. This was verified when calculating the relative crystallinity of PbO_2 on the three different substrates (Table 1).
When immersed in HI, PbO_2 peaks disappear and a main peak shows up at around 13° corresponding to the plane (001) of PbI_2. A peak at 39.5° is also detected corresponding to the (110) plane perpendicular to the (001) plane. Using spin coating, the PbI_2 platelets tend to lie flat on the substrate, the (001) plane is then perpendicular to it and is the one detected in XRD patterns[22]. In contrast, with the electrodeposition, the presence of (110) plane indicates that PbI_2 platelets stand on the substrate in a vertical slanting direction. This should also be investigated with the SEM (Figure 16). The relative crystallinity of PbI_2 was also calculated for the three different substrates. Unlike the PbO_2, the PbI_2 deposited on SnO_2 was formed most crystalline.

Whether directly converted from PbO_2, or by intermediate conversion from PbI_2, PK1 and PK2 spectra both represent a typical XRD pattern of tetragonal $MAPbI_3$. (002), (112) and (114) phases of tetragonal $MAPbI_3$ appear at 14°, 20° and 31.6°, along with other phases[259]. For both perovskites, the lattice parameters have been determined and presented in Figure 2-b. As expected[260], the lattice constant **c** is larger than **a**, for both perovskites deposited on the three different substrates, and when **a** increases, **c** decreases. We can notice that PK1 possesses larger lattice parameters, which explains the more pronounced double peaks at 28° and 32° (see Figure S2).

Changing these parameters modifies the grain size, as revealed by SEM images (Figure 16). The tetragonal distortion parameter TDP (**c**/2**a**) is a very interesting parameter to follow the size of PbI_6 octahedra. It is plotted in function of the grain size, (Figure 15-c). An increase in the TDP indicates an elongation of the PbI_6 octahedra along the c axis[260]. PK2 presents a remarkable variation of the TDP between the substrates with very small changes in grain size. In contrast, PK1 presents a rather constant TDP and large variations in the grain size. The two series of samples also trend to indicate that the grain size and TDP are positively correlated, rather linearly. Although difficult to give definitive conclusion, this is a good indication for process-structure correlation.

The studies related to spin coating often consider the residual reaction products like PbI_2 as an indicator of the complete conversion. PbI_2 is also a degradation product of perovskite. Many authors show that its presence in the initial state fastens the

degradation of perovskite[261], despite being favorable for the initial photovoltaic performance by passivating trap states at the perovskite grain boundaries[262]. A report described the residual PbI_2 as a double-edged sword, since it enhances the photocurrent but reduces the photovoltage[263]. In our study, PbI_2 (001) phase is present in few perovskite layers, as shown on diffraction patterns in Figure 15 and in Table S1. For PK1, this phase is essentially in the film deposited on SnO_2. Since the perovskite conversion was directly made from PbO_2, the presence of PbI_2 indicates a degradation of the perovskite layer. It seems that PK1 is less stable on SnO_2 than on ITO, or TiO_2. PbI_2 is nevertheless more pronounced on the patterns of PK2 for the three substrates, as we notice in Figure 15 and Table S1. It is possible in this case, that it corresponds to residual PbI_2 in the layer after conversion. The amount of PbI_2 in PK2 deposited on ITO and SnO_2 is the most important (~30%), and hence the one deposited on mesoporous TiO_2 has the smallest percentage of PbI_2 (2.4%). It is important to control the quantity of PbI_2 in the perovskite, but as mentioned, a small amount remaining in the layer can enhance the activity of the perovskite inside the solar cell[264].

The relative crystallinity of the elaborated perovskites was also calculated for each sample, and the best crystallinity was detected in layers deposited on TiO_2, exceeding 30% for both types of perovskites (Table 1). A similar percentage was detected by Park *et al.* when depositing perovskite on mesoporous TiO_2[265]. Enhanced crystallinity is important for improving the device performance. It increases the stability of the device and affects the charge conductivity, which reduces the hysteresis and prevents recombination[265–267].

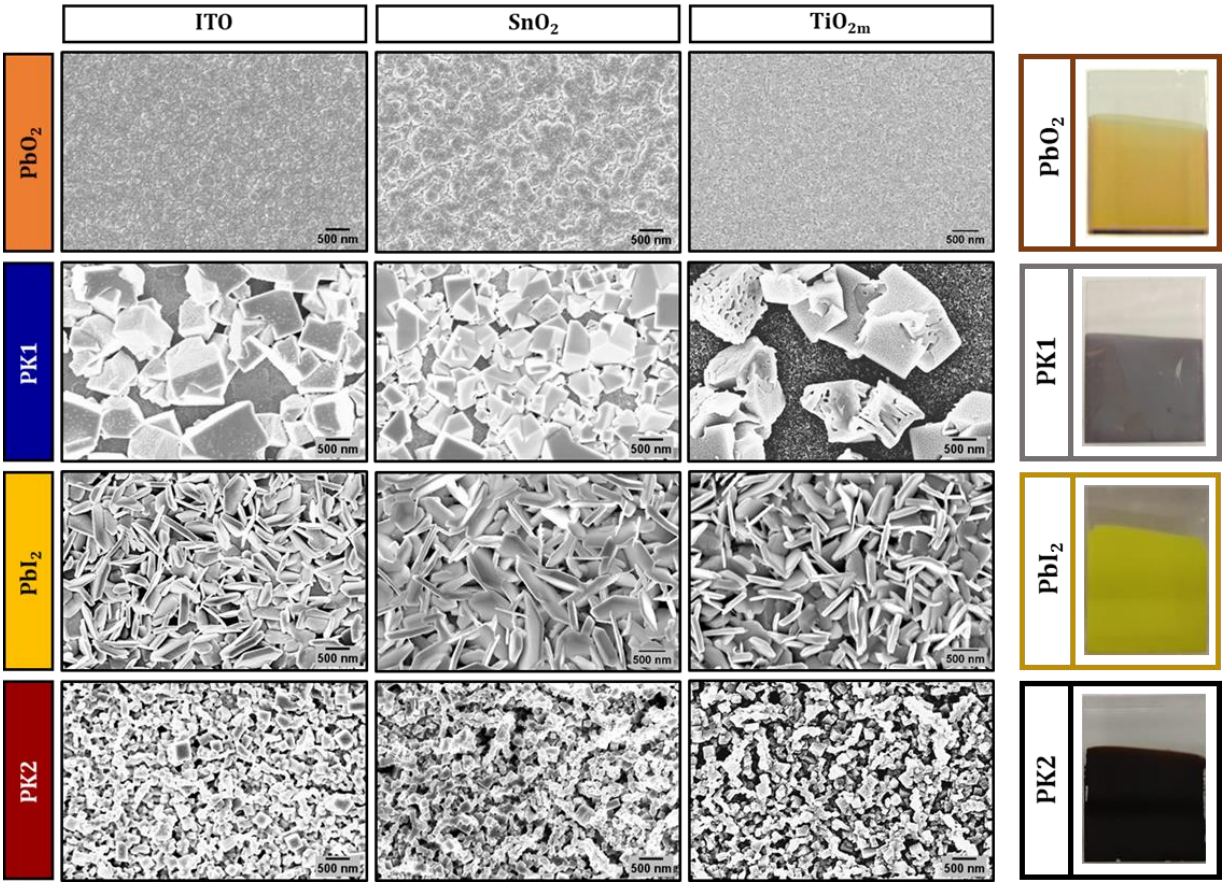

Figure 16: Top-view SEM images of PbO_2, PbI_2, PK1 and PK2 deposited for 50s on ITO, SnO_2 and TiO_{2m}, along with their photographs (1.7cm x 2.5cm)

The in-plane morphology of the different films was analyzed by scanning electron microscopy (SEM), presented in Figure 16. Electrodeposited PbO_2 has a smooth surface morphology with full surface coverage on all three substrates, similar to that observed in the literature[27,28,30,268]. This film is mainly constituted of amorphous material, which is in agreement with the results of XRD analyses. We notice that PbO_2 deposited on SnO_2 has bigger grains than that deposited on ITO, and the film deposited on TiO_2 has the smallest grain size. As mentioned previously, this can be directly related to the electric properties of the substrate, as presented in Figure 14-c. Hence, the greater is the resistivity of the substrate, the smaller are the grains of PbO_2.

When converting into PbI_2, disks with hexagonal platelet structure appear, mostly standing vertically to the substrate. This morphology is typical for PbI_2 converted from PbO_2 [22,29,30]. In the case of planar substrate (ITO and SnO_2), a direct relation between the PbI_2 platelet size and the PbO_2 grain size is evident. SnO_2 prevent larger PbO_2 grains and greater PbI_2 platelets. Nevertheless, for mesoporous TiO_2, we can observe that the PbI_2 platelets are slightly larger than those of ITO. This observation is rather unexpected considering the grain size of PbO_2 obtained on these two substrates. This can probably be explained by the mesoporous structure of TiO_2, which favors the growth of PbI_2 nanoplatelets.

The converted $MAPbI_3$ films consist of rectangular-shaped grains with a non-uniform orientation for PK1[18,22,26,29]. Much smaller grains randomly oriented appear for PK2, with

cubic shapes. The morphologies (size and shape of the grains) are very different from the ones obtained with spin-coated perovskites. These results could be correlated with those from XRD analyses, where the variation in the lattice parameters indicated a variation in the morphology. For PK1, the average grain size close to 0.5-1µm is much larger than those observed in PK2 and those of the PK obtained by spin coating. We can also observe that the perovskite layer is not continuous for this type of perovskite. When comparing the three distinct substrates, the surface coverage is clearly greater on SnO_2 than on ITO or TiO_2, reaching 91% for a deposition duration of 50 s (Figure S3-a). This difference is directly related to the larger grains observed on ITO and TiO_2 substrates. PK2 has much smaller grain sizes close to 150-200nm and complete surface coverage (Figure S3-b). The obtained morphology is very different from that of perovskites deposited by spin coating. There is little variation in morphology depending on the substrate nature. It has been shown in literature in the case of spin-coated perovskite that a larger grain size is favorable for high yield, as it results in lower grain boundary density, improved charge transfer properties, and delayed hydration and decomposition[23]. In our study, the morphology of perovskite obtained by electrodeposition is very different that the one of perovskite deposited by spin-coating. This tendency seems not be essential and the first objective is to achieve complete coverage of the entire surface by the perovskite to prevent the creation of shorts circuits within the device.

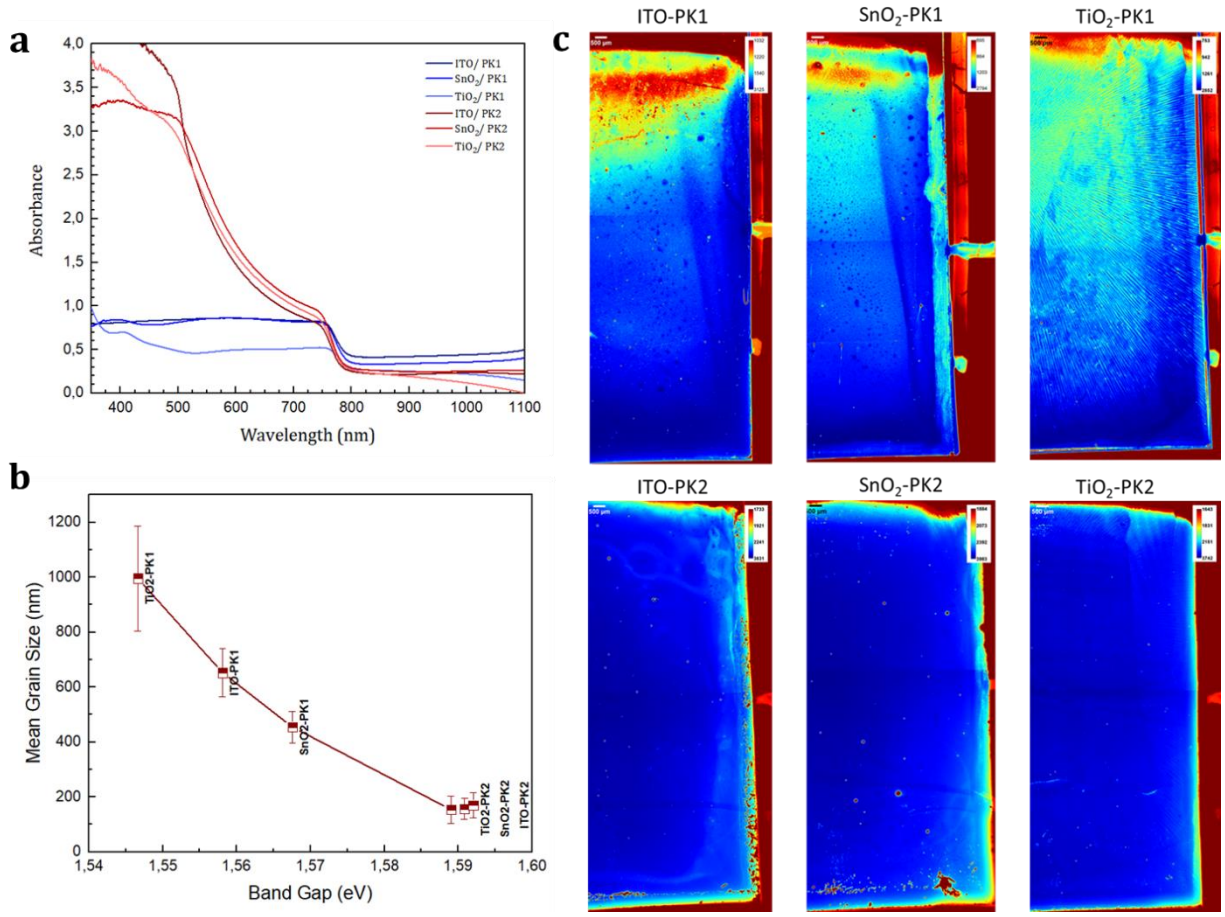

Figure 17: a) UV-visible absorption spectra, b) Mean grain size variation function of the band gap variation, and c) Local thicknesses of PK1 and PK2 deposited on ITO, SnO_2 and TiO_{2m} (scale bar is 500 µm)

UV-vis absorption spectroscopy was used to compare the composition of the perovskite layers PK1 and PK2 formed after conversion on the three substrates ITO, SnO_2 and TiO_{2m} (Figure 17-a). All films freshly converted on the substrates show a typical absorption spectrum of the perovskite with the onset at around 780 nm[269]. Only the first transition of $MAPbI_3$ is detected[181], and there is no sign of the PbI_2 onset at 500 nm (Figure S4). PK2 shows however a higher absorbance at low wavelengths, due to its superior coverage ratio[270]. Scheblykin *et al.* demonstrated that a correct absorption spectrum could be detected when the substrate is totally covered, and it flattens down and forms a plateau when the coverage ratio decreases[270]. This correlates with the results obtained for our samples.

We used the absorption spectra to draw the Tauc plot of the perovskite films (Figure S5), and calculate their energy band gap. Both types of films present a band gap corresponding to that of $MAPbI_3$ [271,272], which was identified by Sarritzu *et al.* as a direct band gap for this material[273]. PK2 has an energy gap of around 1.59 eV, which is higher than that of PK1, and more stable when changing the substrate. However, a band gap ranging between 1.55 eV and 1.57 eV is calculated for PK1, depending on the nature of the substrate. This variation of the band gap for the same material is directly related to the size of the nanocrystallites[274], which was demonstrated in Figure 17-b. The energy band structure is affected by the boundaries of the material, and as the grain size decreases, the electrons tend to become more confined in the material. This quantum confinement results in the increase of the energy gap, which validates the correlation between the results.

We also used these analyses to determine local thicknesses of electrodeposited perovskite layers. According to the work of Combessis *et al.*[275], it is possible to correlate optical density measurements (determined by UV-visible spectroscopy) with gray level measurements (evaluated by optical microscopy) to find a local thickness, thanks to the following relation.

$$e = -\frac{1}{OD} \times \log\left(\frac{GL}{100 \times K \times M^{\beta} \times t^{\upsilon} \times V^{\kappa}}\right) \qquad \text{Equation 2}$$

With OD the optical density determined by UV-Vis spectroscopy between 400 and 800 nm, e the perovskite thickness (µm), GL the gray level, K the microscope constant, M the magnification, t the time (s), and V the voltage of the lamp (V). β, υ, κ are the magnification, the time and the voltage powers and were previously evaluated by a calibration method explained in the article of Combessis *et al.*[275]. Here we assumed that the only material that can absorb in the visible range is perovskite.

To validate this method, a first study was conducted on ITO/PK1 substrates deposited for different durations. The experimental thickness of these films measured using profilometry was compared to the one calculated using Equation 2. Figure S6 shows that the results are similar enough to validate this approach. Hence, the calculations were conducted for PK1 and PK2 deposited on the three different substrates. The results are presented in Figure 17-c, showing the distribution of the thickness of perovskite over all the surface of the substrate. We note that the PK1 layer is very inhomogeneous, and detect large differences between the top and bottom of the sample, indicating a probable effect of the electrodeposition process. The PK2 layers are however much more homogeneous. Since the PbO_2 electrodeposition step is common to both routes, it seems that the conversion step is the determining factor. We also note an impact of the substrate, for PK2 for example, we observe a greater homogeneity in the case of TiO_2. For further

confirmation of these observations, the violin plots describing the distribution of the thickness for the six different samples were drawn in Figure S7.

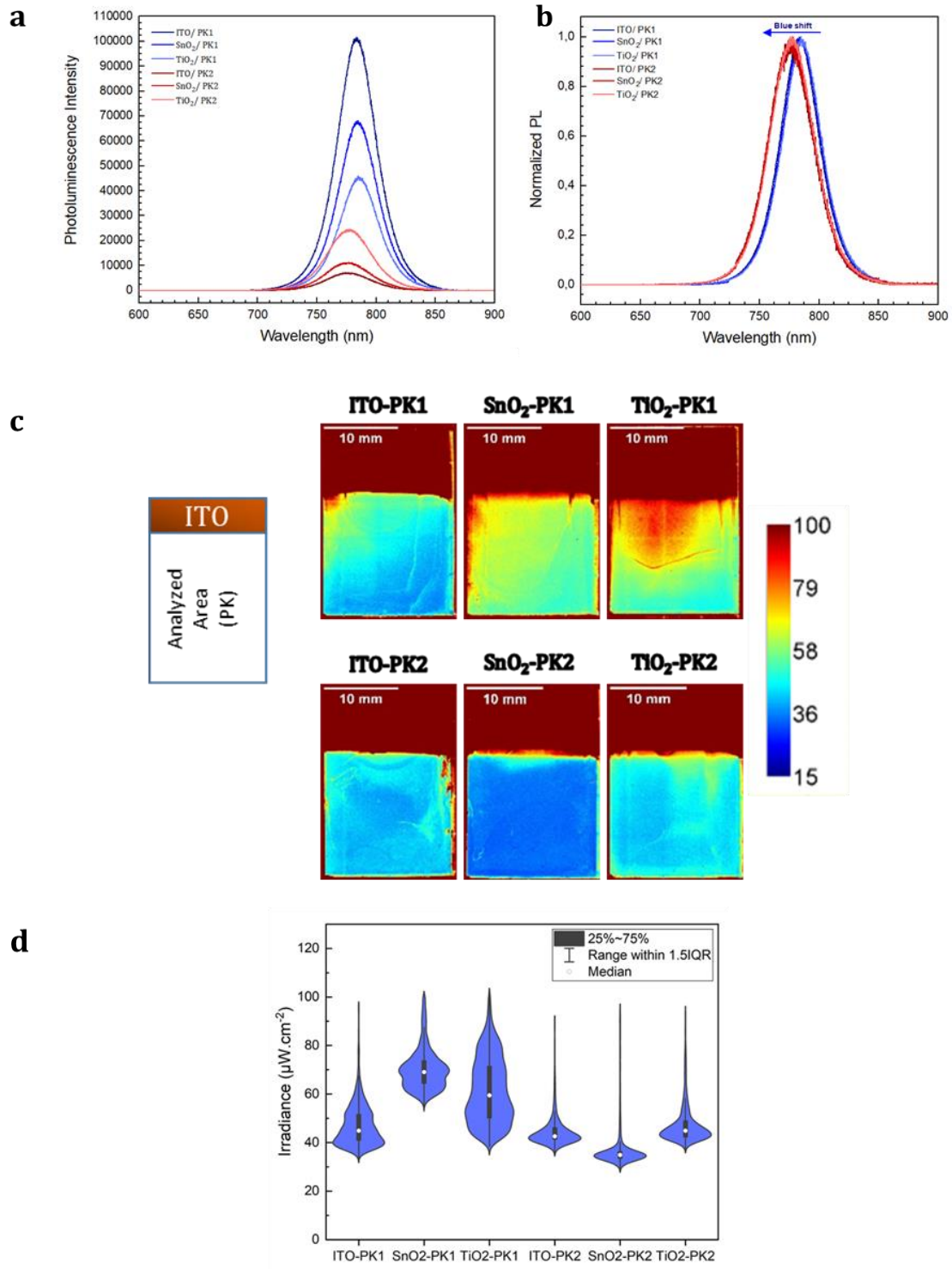

Figure 18: a) Photoluminescence spectra, b) Normalized PL spectra showing the blue shift between PK1 and PK2, c) PL imaging mapping of PK1 and PK2 on the three different substrates, and d) Violin plot distribution of the irradiance for the presented PL images (calculated on indicated analyzed area)

Photoluminescence (PL) spectroscopy was used to characterize the emission properties of the as-prepared perovskites. The effect of the conversion route and the substrate nature on the PL spectra of the layers is presented in Figure 18. The maximum PL intensity is related to the radiative recombination inside the material. To avoid undesired carrier recombination, the radiative recombination coefficient should be low[276]. We notice in Figure 18-a evidences that PK2 samples exhibit lower PL emissions than PK1 ones (slightly changing between substrates), which makes this route a better candidate for photovoltaic application. Normalizing the PL spectra in Figure 18-b illustrates the PL blue shift from PK1 to PK2. Since PK2 is consisted of smaller grains, it presents photoluminescence at lower wavelengths, corresponding to smaller grain size. In fact, as the crystallite size decreases, not only the absorption band gap can increase, but also the luminescence one[274].

PL imaging was used to extract irradiance levels overall the surface and compare the homogeneity of the different films[277]. Figure 18-c displays the PL images of PK1 and PK2 electrodeposited on the three different substrates. Overall, we note lower irradiance values for PK2, in agreement with the photoluminescence spectroscopy results. Although irradiance levels slightly change between substrates, PK2 presents more homogeneous films with less defects and a narrow violin plot distribution (Figure 18-d). It is certainly due to the bigger grains of PK1 and the pinholes present in its scaffold. These results are verified quantitatively when plotting the variation of the irradiance along a vertical line in the center of the film, going from the top to the bottom (Figure S8). This value is relatively constant with PK2 for all substrates, while it decreases for PK1 when approaching the bottom.

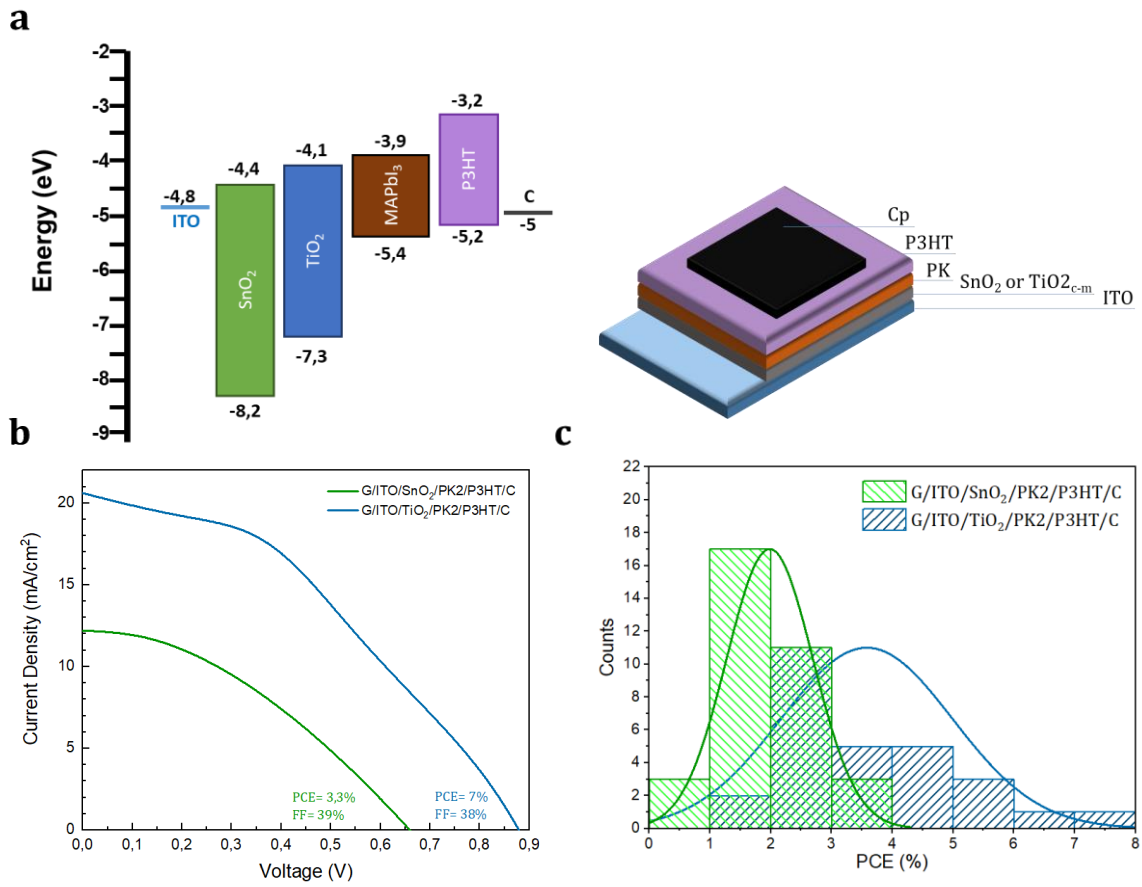

Figure 19: a) Energy diagram and representative stack of layers for the two studied architectures, b) J-V curves of the best performant PSCs elaborated using PK2 as the active layer, with the two different architectures: Glass/ITO/SnO_2/$MAPbI_3$/P3HT/C and Glass/ITO/TiO_2c/TiO_2m/$MAPbI_3$/P3HT/C and c) PCE distribution for these two architectures

	Voc (V)	Jsc (mA/cm²)	FF (%)	Rs (ohm.cm²)	Rsh (ohm.cm²)	Active Surface (cm²)	PCE (%)
Glass/ITO/SnO_2/ PK2/P3HT/C	0.61 ± 0.07	11.24 ± 1.58	33.42 ± 3.14	37.46 ± 8.86	163.99 ± 47.82	0.26 ± 0.05	2.34 ± 0.6
Glass/ITO/TiO_2/ PK2/P3HT/C	0.91 ± 0.07	12.69 ± 3.07	36.79 ± 3.87	44.11 ± 14.37	185.47 ± 53.48	0.15 ± 0.04	4.27 ± 1.21

Table 2: The variation of the parameters resulting from the J(V) curves for the PSCs developed using TiO_2 or SnO_2 as ETL

To evaluate the photovoltaic performance of the two elaborated $MAPbI_3$ layers (PK1 and PK2), two different solar cell architectures were tested: Glass/ITO/SnO_2/$MAPbI_3$/P3HT/C and Glass/ITO/TiO_2c/TiO_2m/$MAPbI_3$/P3HT/C (Figure 19-a). This second structure was proved to have an improved efficiency and an outstanding stability in this present work.

In order to obtain functional devices, many optimizations have been performed. For example, in the first step, the time of PbO_2 electrodeposition has been optimized: 50 s on SnO_2 and 100 s on mesoporous TiO_2. This duration was variated between substrates to optimize the perovskite layer thickness and to ensure a maximum area coverage on the compact substrate or the porous one. Photovoltaic performance of the four solar cells - developed using PK1 and PK2 deposited separately on SnO_2 and TiO_2 - was evaluated by

recording current density-voltage J(V) curves (Figure 19-b). When using PK1 as the active layer, the solar cell shows a small response to illumination, with PCEs lower than 0.1% (not represented here). Although PK1 deposited on TiO_2 shows a higher Voc than on SnO_2, the low photocurrent also resulted in a poor efficiency. The main reason for a similar behavior is the formation of pinholes in the active layer (see SEM images). This can cause a partial short circuit across the junction and decrease the shunt resistance Rsh, which provides an alternate current path for the light-generated current[278].

With fully covered surface, PK2 presents better outcomes, with a PCE reaching 3.3% when deposited on SnO_2 and 7% on mesoporous TiO_2. These results are of the same range or even a little higher as the ones already published when developing a perovskite active layer using electrodeposition[20,22,25,30]. The effect of the active surface on the device's performance was also studied and is presented in Figure S9. As expected, a solar cell with a smaller active surface has less defects, in all its layers, and hence offers a better efficiency. Figure 19-c represents the PCE distribution of the devices elaborated using PK2 for the two previously mentioned architectures. The statistics were deduced from the performance of 20 identically manufactured PSCs. We notice that using mesoporous TiO_2 as an ETL clearly enhances the photovoltaic activity for the solar cell. As noticed in Table 2, the Voc is greater with TiO_2, which could be related to a more suitable energy match between the materials in this second architecture (see Figure 19-a reporting typical literature data[279]). In addition, the solar device elaborated on TiO_2 offers a higher Jsc, since the active layer was deposited on mesoporous material. This enhances the interface between the ETL and the active layer and thus limits the recombination of the excitons if they were to travel more than their diffusion length before dissociation[120]. These results are of the same range as Chen *et al.*'s, the only study elaborating electrodeposited $MAPbI_3$ perovskite carbon-based solar cells[22].

Conclusion

In this work, the electrodeposition method was used to deposit the perovskite layer. It is an innovative technique allowing the deposition in large surface and inexpensive. For this method, a PbO_2 layer is first electrodeposited and then in this study, two routes were conducted: direct conversion to perovskite (PK1 form) and conversion to PbI_2, then to perovskite (PK2 form). At each step of the elaboration, the nature of the deposited layer is determined by UV-Visible absorption, photoluminescence, X-ray diffraction and scanning electron microscopy. For the first step, the thickness of the deposited PbO_2 depends on the nature of the substrate and mainly on its resistivity. The lower its resistivity, the easier the deposition and the higher the thickness. In the following work, the microstructure, morphology, optoelectronic properties and thickness of the perovskite layer were studied according to the route explored and the nature of the substrate. Important differences in terms of composition, crystallinity, thickness and morphology are to be noted. For the PK1 form, we note a rather weak rate of covering as well as an important size of grains, which is not very adapted for an application in solar cells. For the PK2 form, the deposits are much more homogeneous in terms of thickness. The coverage rate is optimal and the grain size is much smaller than that observed for

PK1. We note very important differences according to the nature of the substrates: a better homogeneity, with a lower presence of PbI_2 and a higher rate of crystallinity for the mesoporous TiO_2. In terms of optoelectronic properties, the photoluminescence intensities of the PK2 perovskite layers are much lower and the PL images show much more homogeneous responses for this form. It seems that this shape is the most suitable for solar cell application. Tests have been performed with the following architectures: G/ITO/SnO_2/PK2/P3HT/C and G/ITO/TiO_{2c+m}/PK2/P3HT/C. The obtained cells are functional but we note different performances according to the nature of the N layer. In the case of TiO_2, maximum performances of 7% are obtained which is in accordance with the literature taking into account the nature of the perovskite and the tested architecture.

Experimental section

Materials and chemicals

ITOGLASS 07P ITO-coated glass slides (2.5 × 1.7 cm^2) were purchased from Visiontek Systems. The reagent chemicals used are as follow: lead(II) acetate trihydrate $Pb(CH_3COO)_2.3H_2O$ (Sigma-Aldrich, 99%), sodium nitrate $NaNO_3$ (Sigma-Aldrich, ≥ 99%), methylammonium iodide CH_3NH_3I (MAI) (Greatcell Solar), and hydrogen iodide HI (57 wt% in H_2O, stabilized 99.95%, Sigma-Aldrich). pH adjustments were done using nitric acid (65%, AnalaR NORMAPUR, VWR Chemicals). N-30 SnO_2 nanoparticle formulation was purchased from Avantama, Ti-Nanoxide BL/SC for the compact TiO_2 and Ti-Nanoxide T600/SC for the mesoporous TiO_2 from Solaronix. The carbon paste applied was the DN-CP01 from Dyenamo. Regioregular poly(3-hexylthiophene-2,5-diyl) P3HT (#4002-E, Rieke Metals) was used for the HTL precursor solution, with chlorobenzene (Sigma-Aldrich, anhydrous, 99.8%) as the solvent. The isopropanol and ethanol used in the conversion bath were anhydrous (Sigma-Aldrich, 99.5%). All aqueous solutions were prepared using 18 MΩ cm resistivity water from a Millipore Milli-Q system.

Substrates preparation and ETL deposition

The ITO substrates were first ultrasonically cleaned with acetone, isopropanol, and deionized water in sequence. They were then subjected to UV-O_3 treatment for 30 min before each deposition.

SnO_2 ETL was spin coated on the as-cleaned ITO substrates. The N30 Avantama SnO_2 was filtered using a 0.45 µm GMF pp filter before use. After UV-O_3 treatment of the substrates, the filtered SnO_2 solution was quickly dropped and spread on the spinning substrates. The spinning conditions were set at 40 rps for 3 s, then 67 rps for 40s. The SnO_2 coated substrate was then calcinated at 220 °C for 20 min. The thicknesses of SnO_2 layer was around 55 nm.

TiO_2 compact-mesoporous ETL (TiO_{2m}) was also deposited on ITO using spin coating. First, 50µL of the Ti-Nanoxide BL/SC solution was dropped on the substrate while starting the spinning. Conditions were set at 33 rps for 1 s, then 83 rps for 30s. The compact TiO_2 coated substrate was then sintered at 550 °C for 1h. The resulting compact layer, also called blocking layer has a thickness of around 65 nm. The Ti-Nanoxide T600/SC is a

solution for the formation of 600 nm thick mesoporous titania layers. However, the optimized thickness of TiO_2 scaffold is around 450 nm [22], so the as-mentioned precursor solution was diluted with 0.4 mL of ethanol for each 1 mL. The obtained solution was spin coated using the same conditions as for the blocking layer, and then sintered at 475°C for 30 min. The mesoscopic structure obtained by the sintering of nano-particles in the process makes a perfect host for perovskite crystals.

ITO, SnO_2 and TiO_{2m} substrates were then separately used as working electrodes, to deposit PbO_2 using the same process mentioned below, after being UV-O_3 treated.

Electrodeposition of PbO_2 films

An aqueous solution containing 0.025 M lead(II) acetate trihydrate and 0.05 M sodium nitrate served as an electrodeposition (ED) bath for PbO_2 films. The pH adjustments until having a pH of 5.5 were done with nitric acid. ED was performed without stirring at ambient temperature with a Biologic SP-150 potentiostat and a three-electrode arrangement. ITO substrates, ITO/SnO_2 or ITO/TiO_{2m} substrates acted as working electrodes, with the active deposition area being 2.55 cm^2 (1.5 × 1.7 cm^2). A spring-shaped platinum electrode was used as the counter electrode and an Ag/AgCl/KCl_{sat} electrode as the reference electrode. The electrodeposition was carried out at a potential of 1.5 V versus the reference electrode for a deposition duration of 50s (Reaction 0). A brownish color appears indicating the formation of PbO_2. The obtained substrates were then rinsed with pure isopropanol for the one-step conversion, and pure ethanol for the two-step conversion, to eliminate any hydration.

$Pb^{2+} + 2\ H_2O \rightarrow PbO_2 + 4\ H^+ + 2\ e^-$ Reaction 0

Conversion of PbO_2 into PbI_2

Conversion of PbO_2 to PbI_2 was carried out at ambient temperature in a petri dish. The substrate was immersed in a 0.05M HI - ethanol solution for 3 min. A change of color from brown to yellow indicates the conversion of PbO_2 into PbI_2 films (Reaction 1). The samples were rinsed with ethanol and then dried with N_2 before keeping them in a vacuum desiccator to avoid any hydration.

$PbO_2 + 4\ HI \rightarrow PbI_2 + 2\ H_2O + I_2$ Reaction 1

Conversion of PbO_2 or PbI_2 into $CH_3NH_3PbI_3$

Conversion of PbO_2 or PbI_2 to $MAPbI_3$ was carried out in a petri dish containing a 0.1M MAI - isopropanol solution, preheated at 40°C. The substrate was immersed in the solution for 3 min, before rinsing it with isopropanol and then drying it with N_2. For direct conversion of PbO_2, a change of color from brown to grayish black appears after one minute, indicating the formation of $MAPbI_3$ films, called PK1 (Reaction 2-a). When converting PbI_2, the color changes from yellow to brownish black in a few seconds, which indicates the formation of a different $MAPbI_3$ perovskite, called PK2 (Reaction 2-b). The samples were kept in a vacuum desiccator to avoid any hydration. (Check SI for more information about optimization of the conversion parameters)

$PbO_2 + 5\ MAI \rightarrow 4\ CH_3NH_2\ (g) + 2\ H_2O + I_2 + CH_3NH_3PbI_3$ Reaction 2-a

$PbI_2 + CH_3NH_3I \rightarrow CH_3NH_3PbI_3$ Reaction 2-b

HTL deposition

For the deposition of the HTL layer, a 15 mg/mL P3HT in chlorobenzene solution was spin coated on the perovskite at 25 rps for 40s then 33rps for 30s. These conditions lead to a 30nm thick P3HT layer.

Carbon paste deposition

Finally, a low temperature Dyenamo commercial carbon paste was deposited on the stack using doctor-blading technique. Each substrate formed six different cells with an active surface of around 0.2 cm^2. The final sample was then annealed at 120°C under vacuum, for 2h. This will not only dry the carbon paste and evaporate its solvents, but also help the connection at the interfaces inside the solar cell.

Characterizations

All electrochemical characterizations were carried out using the as-prepared electrolytes, and the three-electrode system described above, via the SP-150 potentiostat/galvanostat of BioLogic. The thickness and roughness of all layers were measured using the Alpha-Step D-500 stylus profiler, and calculating the mean value of five measurements from distinct positions across the film. The structure and texture of the films were determined with a *PANalytical X'Pert PRO MPD X-Ray diffractometer* using Cu-Ka source. Match! and DIFFRAC.EVA softwares were used to identify the phases and determine the lattice parameters. The morphology of the films was studied by scanning electron microscopy (SEM) using FEG ZEISS Ultra 55. The surface coverage was calculated using ImageJ while the grain size was determined by selecting a double dozen of grains from the SEM images, measuring their size using ImageJ and calculating the average value. Absorption measurements in the UV−visible range were performed with a Shimadzu UV-2600 spectrophotometer coupled with an integrating sphere, in the 300-1100 nm range, with a Glass/ITO substrate as a reference. Optical band gaps were calculated from Tauc plots drawn using the absorbance data. Leica DMLS Optical Microscope was used to examine the surface of the samples and deduce the gray scale used for Combessis *et al.* calculations[275]. PL spectra were acquired over the 600− 900 nm range on a Shimadzu RF-6000 spectro fluorophotometer with a 520 nm excitation wavelength. Two filters were used: a 575 nm low-pass in front of the excitation source and a 600 nm high-pass in front of the source of emission in order to suppress any artifact coming from the spectrophotometer. Chosen measurement conditions were a scan rate of 6000 nm/min, an excitation slit of 5 nm, and an emission slit of 5 nm. Luminescence imaging experiments were performed with an home made device composed of an opaque chamber with a camera placed 30 cm above the samples and two monochromatic 520 nm light-emitting diode (LED) arrays. A 650 nm high-pass filter from Edmund Optics (York, UK) was added in order to allow for spectral resolution in the setup and to minimize reflection from the excitation LEDs. Full PSC devices were observed in the open-circuit condition. The acquisition time was set close to 1000 ms with an aperture equal to 16. As the resulting signal varied depending on acquisition conditions (time, opening, filter type), not allowing for a direct quantitative comparison of the evolutions observed, a calibration reported in a previous publication allowing for image correction was employed[277]. Any additional

image treatment (cropping, colorization, or thresholding) was performed with the ImageJ freeware. A standard simulated AM1.5G irradiation system with a 100W ozone free xenon-lamp solar simulator (Oriel LSC-100) was used for solar cell tests. The photocurrent density–voltage (J–V characteristics) measurements of the devices were recorded using a BioLogic-SP300 source with a scan going from +1 to −0.2 V and a scan rate of 40 mV/s. The fill factor FF, short-circuit current J_{sc}, open-circuit voltage V_{oc}, power conversion efficiency PCE, shunt resistance R_{sh} and series resistance R_s parameters were then deduced from J(V) measurements, using a home-made program on Spyder software.

Acknowledgments

Authors thank I-MEP2 doctoral school for the MESR PhD grant (M.A.K.) attribution, and the platform of Consortium des Moyens Technologiques Communs (CMTC) of Grenoble INP for laboratory assistance and laboratory equipment. This work has been partially funded by the EU Framework Program for Research and Innovation HORIZON 2020 (Cofund ERA-NET Action, N° 691664). This work has also been partially funded by the "PROPER" project supported by "EIG Concert Japan" and financed from the French National Centre for Scientific Research under the funding number "IRUEC 222437".

Supplementary Information

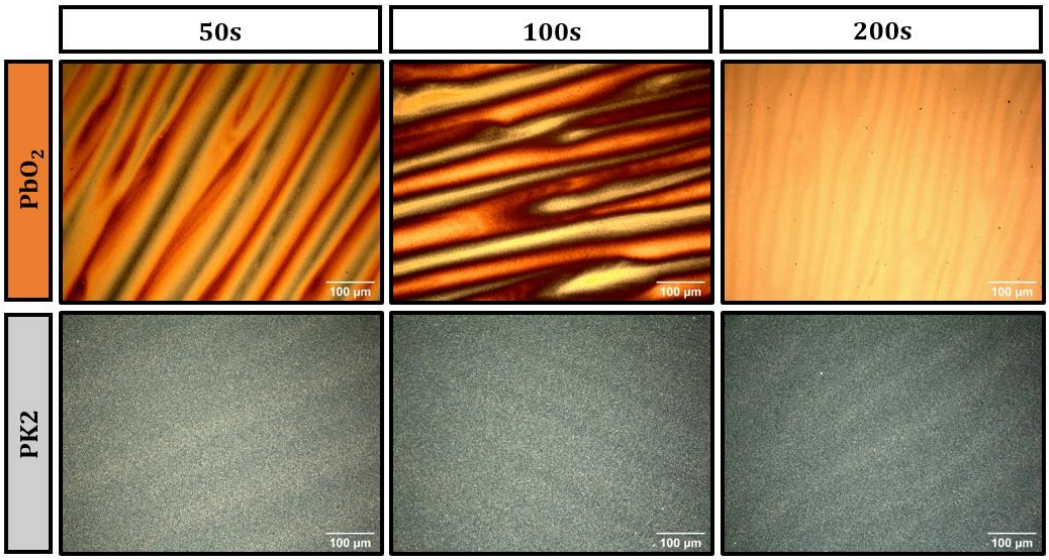

Figure S1: Optical Microscopy images of PbO_2 electrodeposited on mesoporous TiO_2 for 50s, 100s and 200s, and when converted to PK2

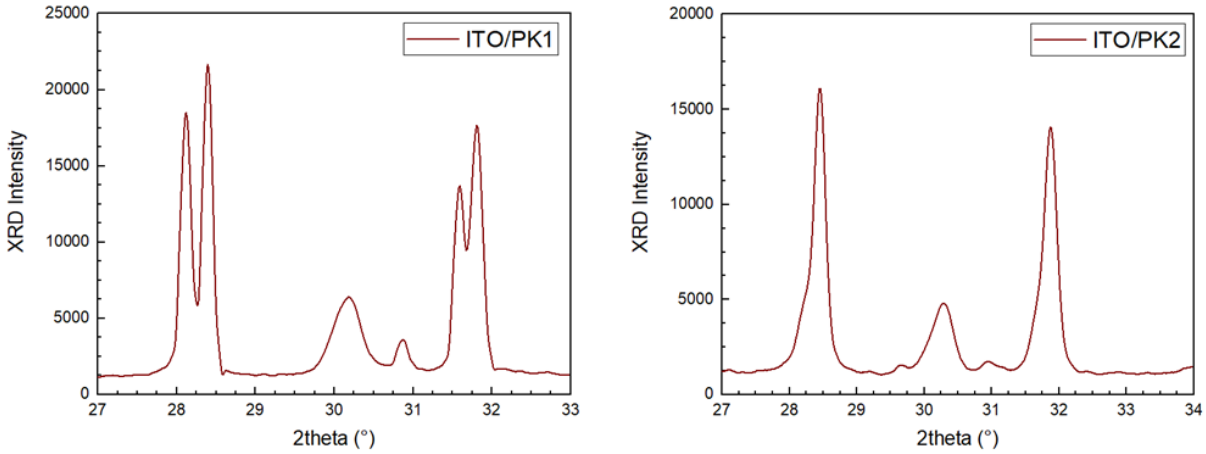

Figure S2: Enlarged XRD patterns of PK1 and PK2 deposited on ITO, showing the (004)-(220) and (114)-(222) double peaks

	PbI_2 (001) / $MAPbI_3$ (002) %	**$MAPbI_3$ (004)/(002) %**
ITO-PK1	1.84	87.35
ITO-PK2	32.78	84.57
SnO_2-PK1	45.24	105.98
SnO_2-PK2	30.75	77.82
TiO_2-PK1	4.30	78.73
TiO_2-PK2	4.24	81.95

Table S1: Ratio of (001) PbI_2 phase and (004) $MAPbI_3$ phase with respect to (002) $MAPbI_3$ phase, calculated using XRD patterns of PK1 and PK2 on three different substrates

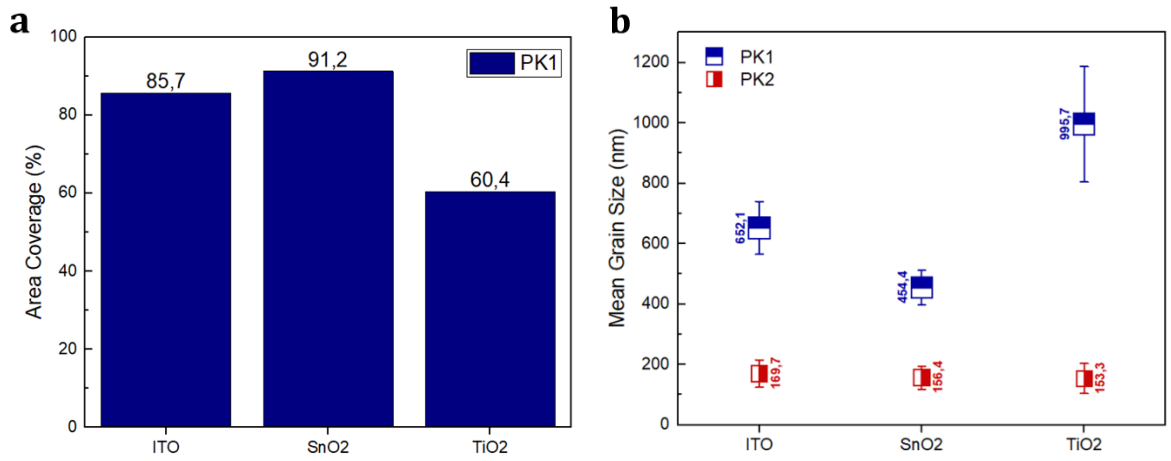

Figure S3: Variation of a) the area coverage of PK1 on ITO, SnO_2 and TiO_2m and b) the grain size of PK1 and PK2 on the three substrates

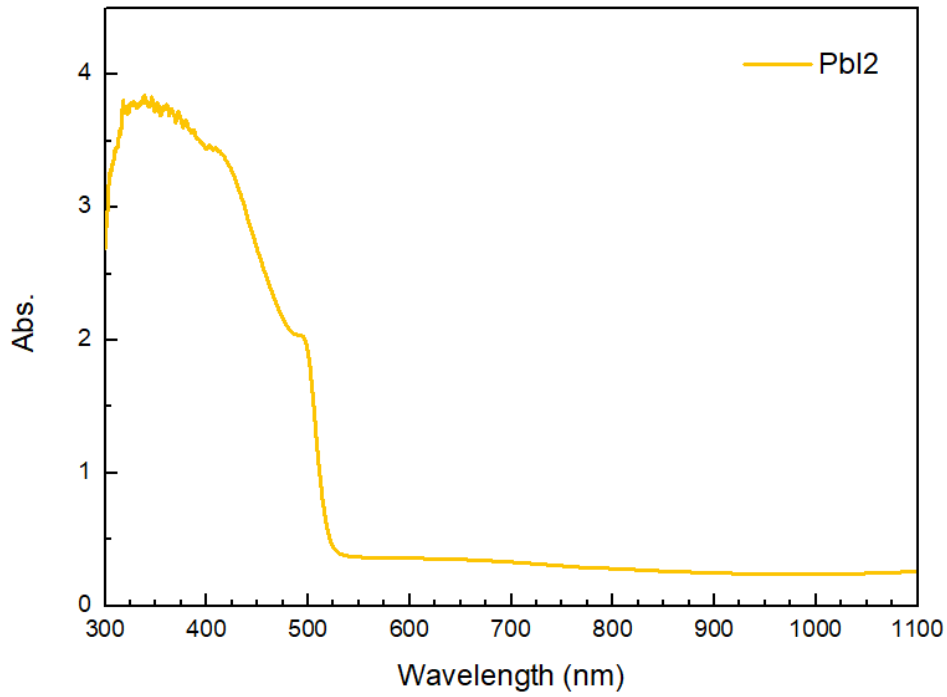

Figure S4: UV-visible absorption spectrum of PbI_2 converted from PbO_2 on ITO

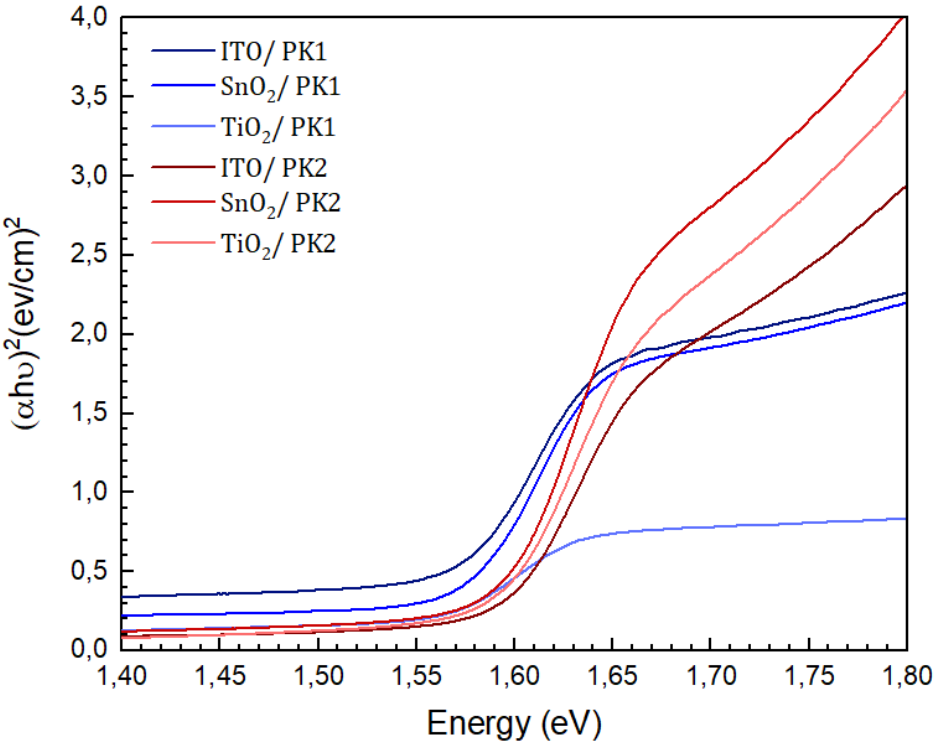

Figure S5: Tauc Plot of PK1 and PK2 on ITO, SnO_2 and TiO_{2m} drawn using UV-absorption data

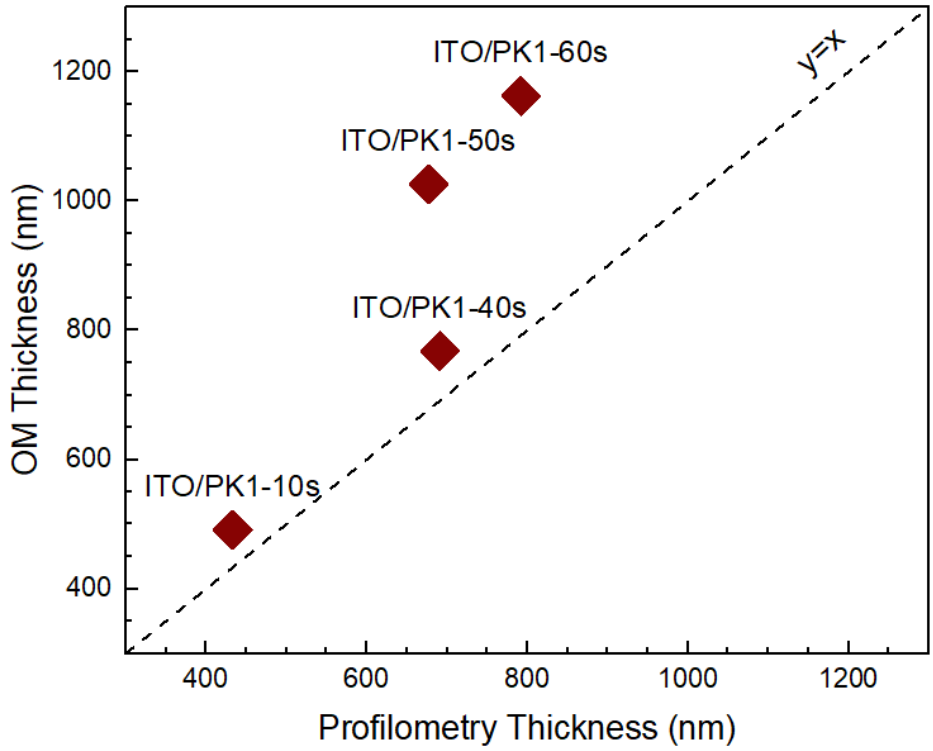

Figure S6: Thickness calculated using optical microscopy for PK1 deposited on ITO for 3 different durations, with respect to their thickness measured using profilometry

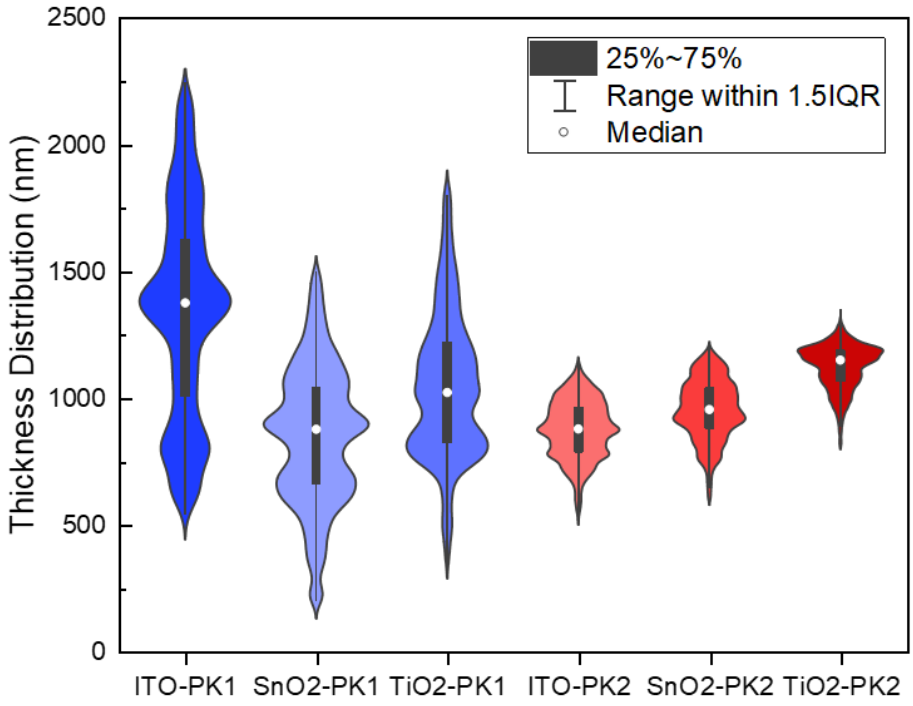

Figure S7: Violin Plot representing the thickness distribution of PK1 and PK2 on ITO, SnO_2 and TiO_2 substrates

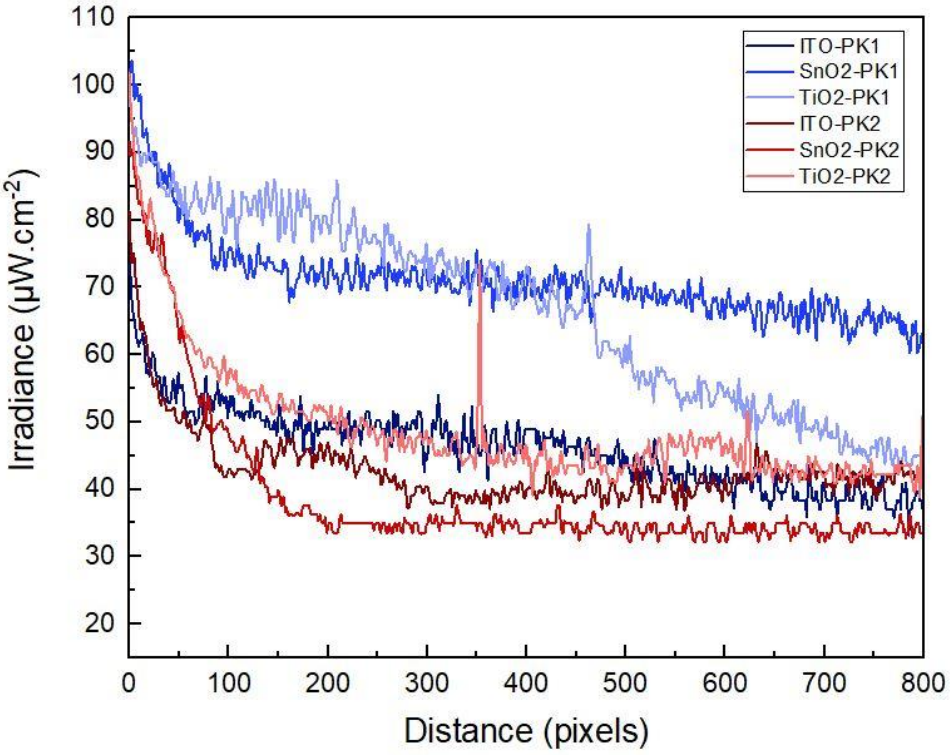

Figure S8: Profile plot showing the variation of the Gray Scale along a vertical line in the center of the PK1 and PK2 films, going from the top to the bottom

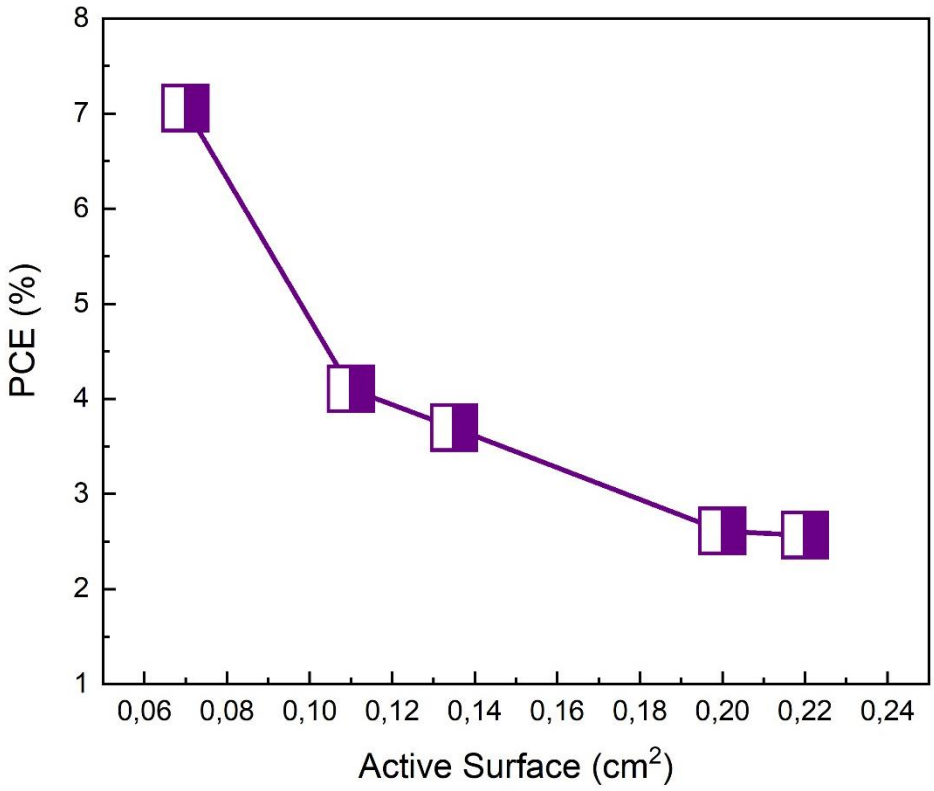

Figure S9: Scatter showing the variation of the PCE with respect to the active surface of the solar cells Glass/ITO/TiO_2C/TiO_2m/$MAPbI_3$/P3HT/C

Experimental: Optimization of conversion parameters for PK1

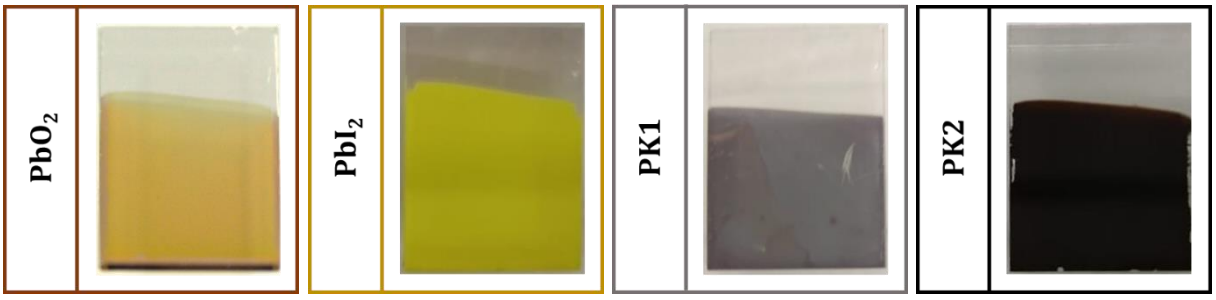

Figure S10: Photographs of PbO_2, PbI_2, PK1 and PK2 samples (1.7cm x 2.5cm)

Conversion for PK1

To optimize the conversion parameters of PbO_2 into PK1, PbO_2 samples electrodeposited on ITO for 15s were immersed in a 16 mg/mL MAI solution, and the conversion was observed at 40°C while changing the duration, or while fixing the duration for 3 min and variating the conversion temperature. The observation are noted in Table S2 and Table S3.

T °C	Duration	Results
40 °C	3 min	Color change observed
40 °C	10 min	Color change observed
40 °C	30 min	Partial degradation
40 °C	60 min	Nearly total degradation

Table S2: Observed results of PK1 conversion for a fixed temperature of 40°C and different conversion durations.

T °C	Duration	Results
30 °C	3 min	Color change observed
40 °C	3 min	Color change observed
50 °C	3 min	Fast but partial degradation

Table S3: Observed results of PK1 conversion for a 3 min duration and different temperatures.

Figure S11 shows the variation PK1 thickness when changing the PK conversion parameters (for PbO_2 samples electrodeposited for 15s). The XRD patterns in Figure S12 indicates that the PbI_2 ratio in the sample increases when increasing the temperature and the conversion duration. The best relative crystallinity for perovskite was for a conversion at 40°C for 3 min (Table S4).

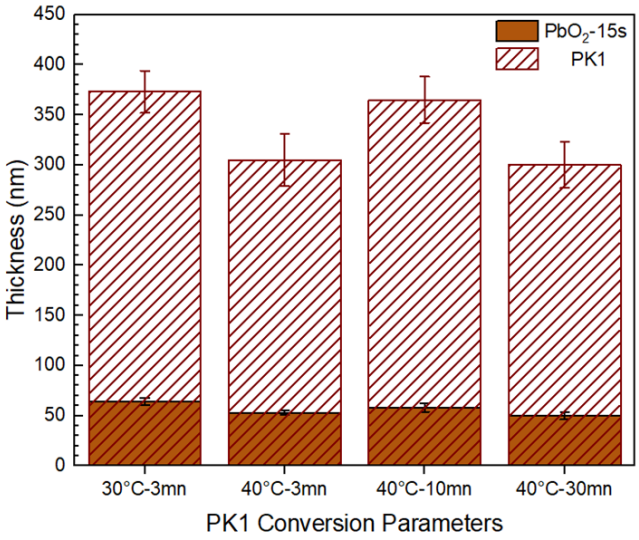

Figure S11: PK1 thickness variation for different PK conversion parameters (thickness of used initial PbO_2 samples is indicated for exact comparison).

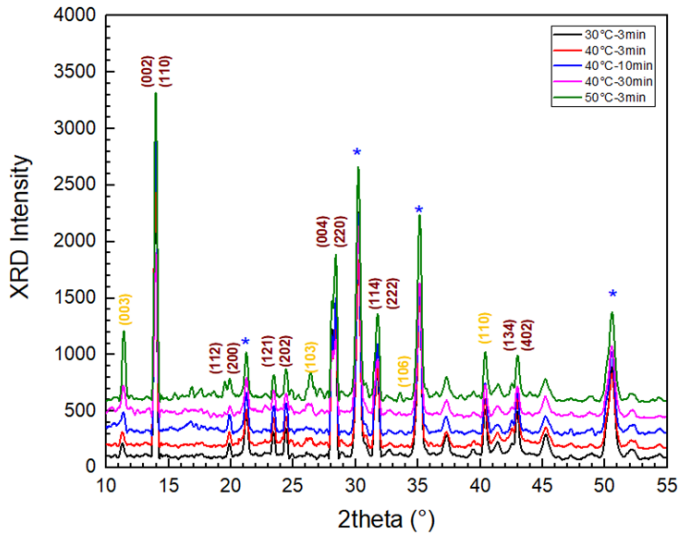

Figure S12: XRD patterns of PK1 converted at different temperatures and durations

	χ %
3 min- 40°C	9.8
10 min- 40°C	6.2
30 min- 40°C	4.85
3 min- 50°C	9.5
3 min- 30°C	9.7

Table S4: Relative crystallinity (χ) of PK1 for different conversion parameters

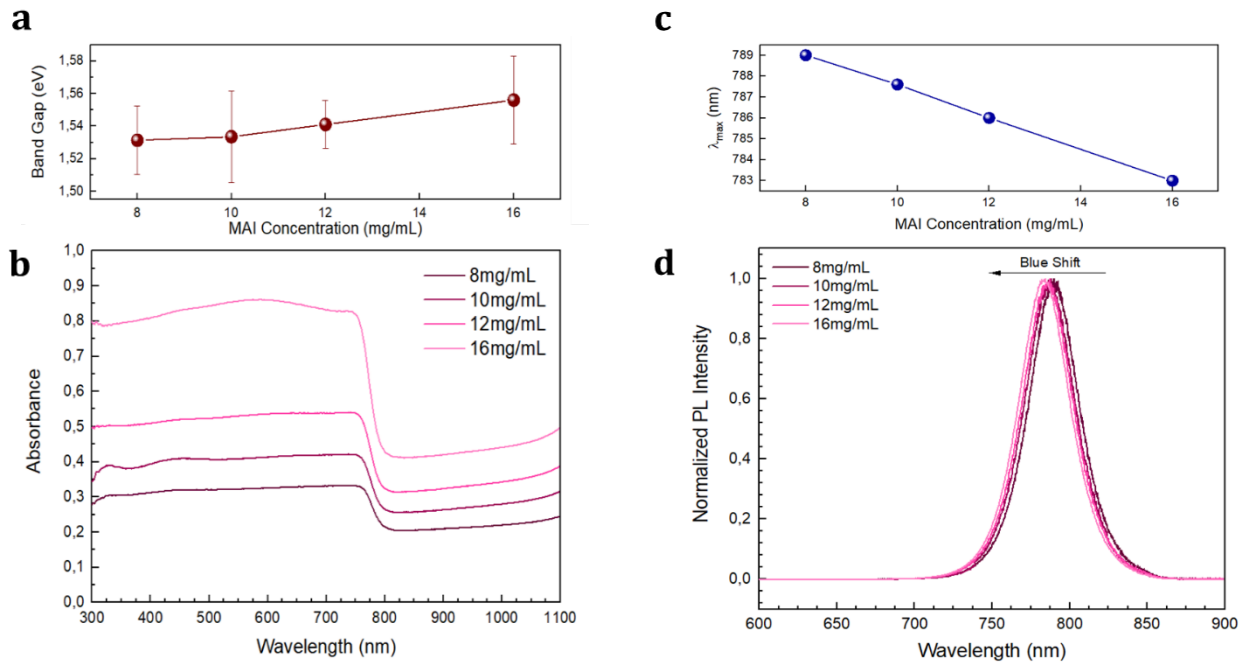

Figure S13: a) Band Gap, b) UV-vis absorption spectra, c) λmax and d) Photoluminescence spectra of PK1 when variating the MAI concentration between 8 mg/mL and 16 mg/mL

The effect of the MAI concentration was also studied. Figure S12 illustrates the case of a conversion fixed at 40°C for 3 min. Increasing the concentration will increase the band gap and the absorbance of the perovskite (Figure S13_a,b,c). A blue shift in the PL spectra of PK1 is also observed when increasing the MAI concentration (Figure S13_d), which may indicate a change in the morphology or the grain size.

Chapter III: Performance and stability of electrodeposited mixed halide perovskite $MAPbI_{3-x}Cl_x$

This chapter presents our second article, where chlorine was infiltrated in $MAPbI_3$ scaffold, prepared using the electrodeposition method developed in chapter II, to enhance its performance and stability. This article will be the first to ever investigate the electrodeposition of $MAPbI_{3-x}Cl_x$. The effect of the Cl ratio used in the conversion bath on the perovskite properties was studied. Then, the prepared $MAPbI_{3-x}Cl_x$ perovskite films were tested in solar devices, and their performance and stability were compared to that of $MAPbI_3$.

Development of electrodeposited mixed perovskite for solar cell application: impact of Chlorine addition on performance and stability

Mirella Al Katrib [1], Emilie Planes [1, *], and Lara Perrin [1, *]

[1] Univ. Grenoble Alpes, Univ. Savoie Mont Blanc, CNRS, Grenoble INP, LEPMI, 38000 Grenoble, France

Abstract

In this work, electrodeposition was explored as an alternative technique for elaborating large-scale and homogeneous perovskite layers for photovoltaic application. This method was here not only used to elaborate simple $MAPbI_3$ but also for the development of mixed halides perovskites $MAPbI_{3-x}Cl_x$. The conversion from electrodeposited PbO_2 into perovskite was conducted while variating the ratio of Chlorine in the conversion bath. According to the Chlorine ratio introduced in the bath, different compositions of perovskites have been obtained, which have hard consequences on their microstructure and functional properties. Theses perovskites were then tested in solar cell devices. The performance obtained with these innovative electrodeposited mixed perovskites are better than that obtained with the most common form $MAPbI_3$, whatever the surface area tested. Finally, the stability of these electrodeposited perovskites has been evaluated under mild aging conditions (40°C, under vacuum or ambient atmosphere) during 500h. For all tested perovskites, a maturation process was evidenced, more efficient under vacuum conditions. The infiltration of Cl in the lattice, highlighted by a deepened study of the perovskite microstructure, not only enhances the efficiency of the prepared solar cells, but also offers a remarkable stability.

Introduction

Hybrid organic / inorganic perovskites (PK) have considerably arisen as efficient active materials in the solar community[154], because of their low cost and performance's fascinating enhancement in the last decade[92,250]. Nowadays, the current techniques for depositing the perovskite are essentially based on spin coating in glove box. This method showed good results[252], but operates with small active areas, limiting the industrialization of perovskite solar cells (PSC). In our previous works (under review), electrodeposition was explored as an efficient alternative for $CH_3NH_3PbI_3$ ($MAPbI_3$) perovskite fabrication. This innovative process could plausibly be the best for low cost industrial development, especially for large active surfaces with an homogeneous performance[18,23]. Chen *et al.* were able to elaborate a carbon-based solar device with a simple electrodeposited $MAPbI_3$ perovskite. They used a two-step conversion method by film-immersion in conversion baths, and were able to develop a carbon-based solar device with a 10% power conversion efficiency (PCE)[22]. Due to electrodeposition process simplicity, not only simple perovskites could now be developed but also mixed cations and mixed halides perovskites, such as chlorine doped perovskites. In the case of perovskite elaborated by spin-coating, incorporating Cl in the $MAPbI_3$ lattice have somehow a profound and beneficial effect on the film morphology, carrier diffusion length, and stability[280]. Studies

conducted on spin-coated perovskites showed that only very low chlorine content should be present in $MAPbI_{3-x}Cl_x$. In a small amount, it could significantly affect the crystallinity and grain size of the perovskite crystal[184]. Excessive Cl would then form a wider-band-gap $MAPbCl_3$ perovskite in $MAPbI_{3-x}Cl_x$ and the lattice distortion induced by Cl atoms will cause shift and broadening of the XRD peaks[281]. The collective effect of Cl doping and $MAPbCl_3$ formation could affect the performance of the perovskite in a solar cell[184]. The study of Cl incorporation effects is even still a very up to date center of interest for the PSC community[282,283]. Therefore, a fundamental question remains regarding the function of Cl atoms during the formation process of the perovskite. Several studies suggested that the chloride ions slow down the nucleation and growth of perovskite crystals, resulting in more continuous and better quality films[280]. However, the film growth parameters such as the Cl ratio in the precursor solution or the deposition temperature should be carefully designed[281]. Furthermore, a deposition process using electrodeposition step could lead to different results than those obtained using spin-coated perovskite layers.

In this study, it is proposed to adapt the previous process developed for $MAPbI_3$ perovskite to elaborate chlorine doped electrodeposited perovskites. To the best of our knowledge, this latter part has never been explored in literature. The direct conversion of PbO_2 into $MAPbI_3$ was already evaluated in our previous work (under review), producing a large-grain perovskite film with many pinholes, preventing its application in a solar device. The electrodeposition of PbI_2 was also tested as reported in the works of Hill *et al.*[31], Li *et al.*[21] and Kosta *et al.*[19]. The bad adhesion of the PbI_2 film on our substrate eliminates the possibility of the application of this method for perovskite elaboration, hence the choice of the as-presented three-step process. The first step is the electrodeposition of PbO_2, followed by its conversion into PbI_2, with a third and final step being the PbI_2 conversion into perovskite. In addition to $MAPbI_3$, a range of $MAPbI_{3-x}Cl_x$ perovskites were here obtained using a conversion solution composed of a CH_3NH_3I (MAI) and CH_3NH_3Cl (MACl) mixture. This step was conducted while variating the ratio of each component to understand the effect of these parameters on the Cl doping of the perovskite, especially its microstructure and optical properties. Then, the photovoltaic performances of the most promising $MAPbI_{3-x}Cl_x$ electrodeposited perovskite are presented and compared to the more standard $MAPbI_3$ form (also electrodeposited). To better understand the role of process on the active layer properties, a study dedicated to the surface area impact has been performed. The stability of these electrodeposited perovskites has been determined at 40°C, either under ambient atmosphere or under vacuum, for 500h. Half and full cells have been studied, to correlate the variations of microstructure, compositions, optoelectronic properties and possible physicochemical degradations of the studied perovskites with those of the PV parameters.

Results and discussion

After conversion of electrodeposited PbO_2 into PbI_2, the conversion of PbI_2 into PK was carried out in four different solutions to elaborate different types of perovskite layers, following Reaction 1 and Reaction 2:

$PbI_2 + CH_3NH_3I \rightarrow CH_3NH_3PbI_3$ Reaction 1

$PbI_2 + (1\text{-}x)\ CH_3NH_3I + x\ CH_3NH_3Cl \rightarrow CH_3NH_3PbI_{3-x}Cl_x$ Reaction 2

To obtain $MAPbI_3$ films, the PbI_2 layer was immersed in a MAI isopropanol (IPA) solution. MCl30, MCl40, and MCl50 are the IPA-based solutions used to convert PbI_2 into the mixed perovskite $MAPbI_{3-x}Cl_x$. Their composition is described in Table 3, the indicated percentage of Cl/I+Cl being the one in the conversion solution and not the actual percentage of Cl inside the perovskite layers, since the reaction is happening with PbI_2 layer already containing iodine. Consequently, three different $MAPbI_{3-x}Cl_x$ films with different compositions were obtained and their photographs are presented in Figure 20-a.

	MAI	MACl	Cl/I+Cl %
MCl30	**0.1 M**	**0.05 M**	**30%**
MCl40	**0.1 M**	**0.075 M**	**40%**
MCl50	**0.1 M**	**0.1 M**	**50%**

Table 3: The composition of the used conversion solutions for $MAPbI_{3-x}Cl_x$ (MAI+MACl mixture in IPA)

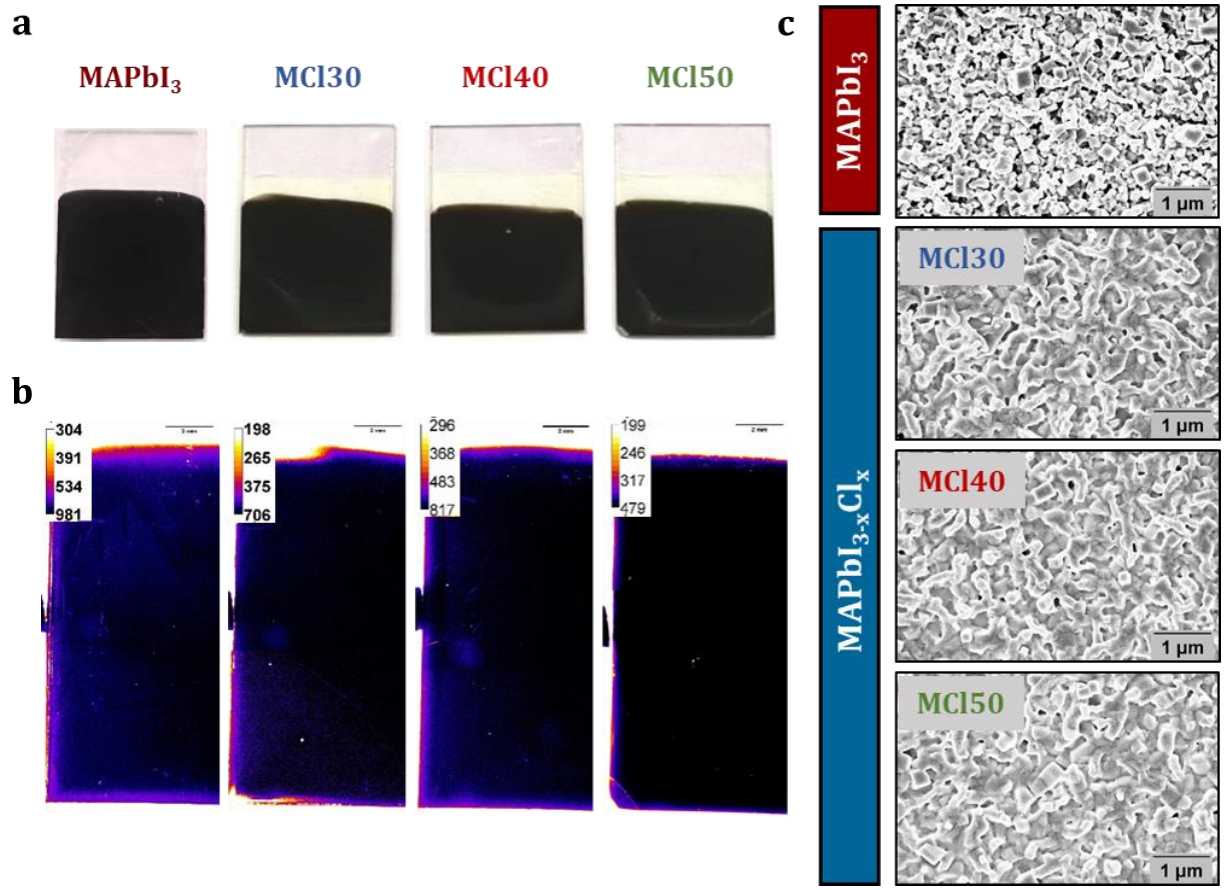

Figure 20: a) Photographs showing the appearance of the four obtained $MAPbI_3$ and $MAPbI_{3-x}Cl_x$ films (2.5 x 1.7 cm^2), b) Local thicknesses of the four corresponding perovskite layers deposited on TiO_{2m} (the colored scale bar for thickness is in nm, and photo scale bar is 2 mm), and c) Top-view SEM images of $MAPbI_3$ and $MAPbI_{3-x}Cl_x$ elaborated using four different conversion baths

Before testing these active layers in solar devices, their morphology, microstructure, chemical composition and properties were investigated using a set of characterization methods (scanning electron microscopy (SEM), X-Ray diffraction (XRD), UV-visible

absorption spectroscopy, photoluminescence (PL) spectroscopy and imaging). To start, as shown by the photographs in the Figure 20-a, the perovskite deposition at the macroscopic scale seems similar and relatively homogeneous, whatever the formulation. To check this, optical microscopy was used to determine local thicknesses of electrodeposited perovskite layers. According to the work of Combessis *et al.*[275], it is possible to correlate optical density measurements (determined by UV-visible spectroscopy) with gray level measurements (evaluated by optical microscopy) to find a local thickness, thanks to the following relation.

$$e = -\frac{1}{OD} \times \log\left(\frac{GL}{100 \times K \times M^{\beta} \times t^{\upsilon} \times V^{\kappa}}\right) \qquad \text{Equation 1}$$

With e the perovskite thickness (µm), OD the optical density determined by UV-visible spectroscopy between 400 and 800 nm, GL the gray level, K the microscope constant, M the magnification, t the time (s), and V the voltage of the lamp (V). β, υ, κ are the magnification, the time and the voltage powers and were previously evaluated by a calibration method explained in the article of Combessis *et al*.[275]. Here, we assumed that the only material that can absorb in the visible range is perovskite. These image treatments were applied on several photographs of the four elaborated perovskite layers deposited on TiO_2. Some results are presented in Figure 20-b, showing the distribution of the thickness of perovskite over all the surface of the substrate. We note that the perovskite layers are rather homogeneous, with an average of 1µm of thickness for $MAPbI_3$, 800 nm for the first two $MAPbI_{3-x}Cl_x$ samples, and a thinner layer of 500 nm for the $MAPbI_{3-x}Cl_x$ layer elaborated using MCl50.

At the microscopic scale, the in-plane morphology of the different converted perovskites was studied by SEM and presented in Figure 20-c. After conversion of PbI_2 in MAI, $MAPbI_3$ surface is completely covered by small cubic-shaped grains with a non-uniform orientation, and a grain size ranging between 150-200 nm[18,22,26,29]. When converting PbI_2 into $MAPbI_{3-x}Cl_x$, we notice similar surface morphologies for the three films. It consists of cubic grains, a little bigger than $MAPbI_3$, more entangled and less spaced. This agrees with literature for spin-coated perovskites, and confirms the chlorine addition induces larger

grain. This can prevent a partial short-circuit across the junction, by limiting the presence of pinholes.

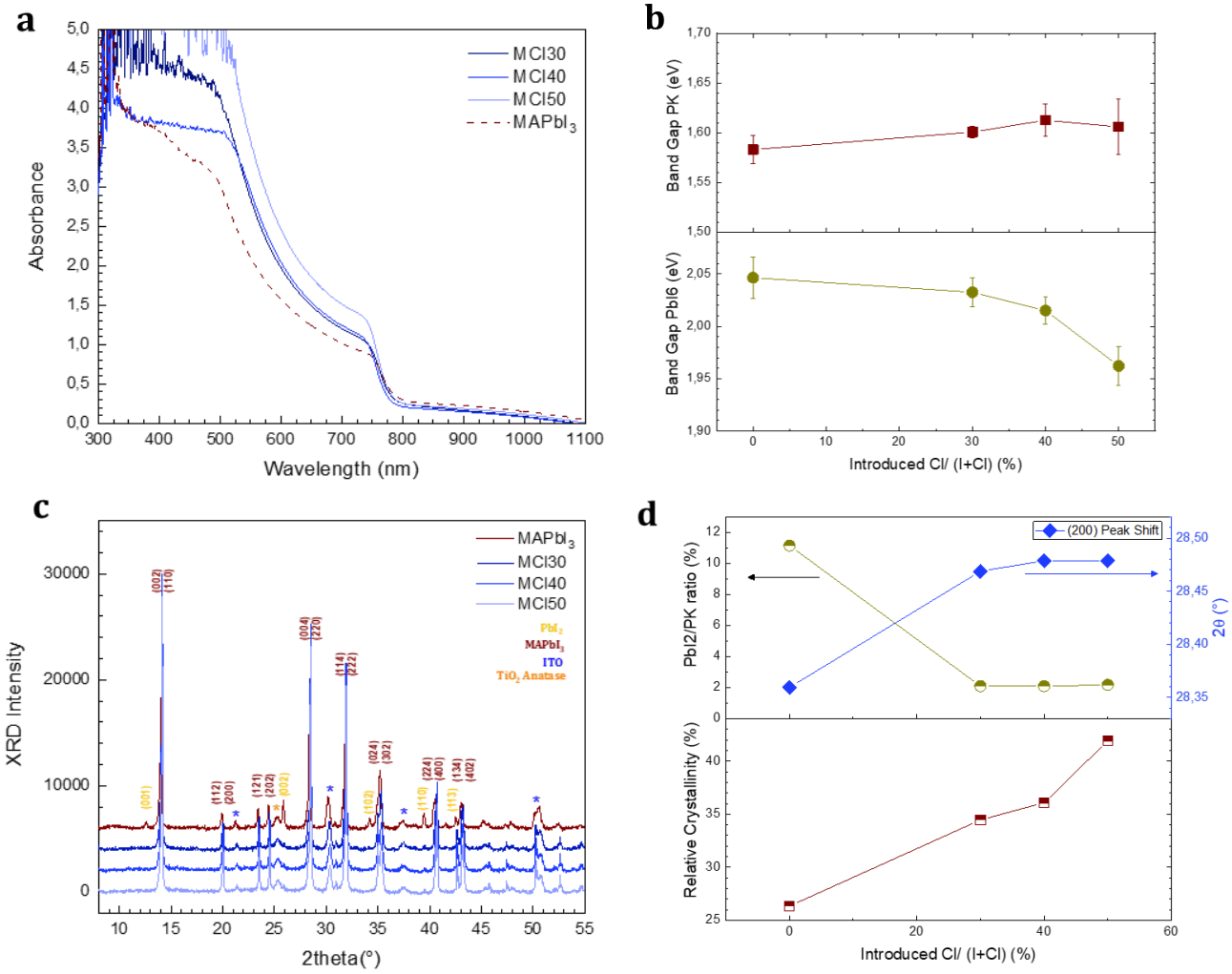

Figure 21: a) UV-visible absorption spectra of the four elaborated perovskite films, b) the band gap of the first and second transition as a function of the Cl percentage in the conversion solutions, c) XRD patterns of the electrodeposited perovskite films, d) the PbI_2/ PK ratio determined from XRD analyses, the XRD peak shift at 28° and the relative crystallinity as a function of the Cl percentage present in the conversion solutions ($MAPbI_3$ being the one with 0% Cl)

The composition of all perovskite layers has been determined by UV-visible spectroscopy and by XRD. Hence, UV-visible absorption spectroscopy was applied on the different elaborated perovskites to further investigate their chemical composition and determine their band gaps (Figure 21-a). For the four different samples, two optical transitions can be identified. The first transition at around 770 nm corresponds to the one of $MAPbI_3$ used to determine the band gap of the perovskite[181]. The second transition at 500 nm is attributed to the lead iodide octahedral present in the $MAPbI_3$ perovskite lattice[265]. The chlorinated perovskite phase $MAPbCl_3$ which transition is at 400 nm was not detected[284]. However, this will have to be confirmed by XRD as the absorbance signal at 400 nm is close the spectrometer detectors saturation. The band gaps of the elaborated perovskites were calculated for the two transitions from the Tauc plots drawn using the UV-visible

absorption spectra (Figure S14). Figure 21-b describes the variation of these band gaps as a function of the percentage of Cl in the conversion solution (0% representing the results for the $MAPbI_3$ sample). Electrodeposited $MAPbI_3$ possesses a band gap of 1.58 eV, equal to literature data for its spin-coated counterpart[181]. According to the literature[184,285], the band gap increase of the electrodeposited $MAPbI_{3-x}Cl_x$ confirms here the infiltration of Cl in the $MAPbI_3$ lattice. This is due to the presence of the Cl ions that modify the perovskite lattice, thereby widening the band gap[280]. However, even for a high content of Cl in the perovskite, the band gap cannot be tuned widely[280]. This was observed for our $MAPbI_{3-x}Cl_x$ films that exhibit a rather constant band gap of 1.6 eV, with slight variations. Concerning the second transition, the band gaps of PbI_6 is relatively constant whatever the Cl content, moving from 2.04 to 1.96 eV, Figure 21-d. This transition can be largely impacted by the presence of amorphous PbI_2, inducing an increase of this bandgap, since the one of this product is close to 2.4 eV. This is often observed in the case of spin-coated perovskite, where PbI_2 is a residual product of the perovskite conversion. This latter is photo-inactive and can induce a potential degradation of perovskite performance. Here it seems that this electrodeposition process induces a less important formation PbI_2. This will be confirmed by XRD analyses.

XRD analyses of the four different elaborated films are presented in Figure 21-c. The attribution of identified crystallographic structures is also reported. $MAPbI_3$ pattern shows a perovskite crystallization under the tetragonal phase, with no preferred orientation[259]. A main peak appears at 14° presenting the (002) plane, and at 28.5° for the parallel plane (004). Another peak appears at 32° corresponding to the (114) plane of $MAPbI_3$. When converting PK in the MACl+MAI mixed solutions, the three different films present a similar $MAPbI_3$ pattern. This does not discredit the possibility of the infiltration of Cl in the lattice, since Cl atoms tend to occupy the apical positions of the crystal structure[184,286]. In fact, it has been widely reported that $MAPbI_{3-x}Cl_x$ films show the main XRD characteristics as $MAPbI_3$, since the two compounds possess identical crystal lattices[281]. The crystalline PbI_2 ratio in the different films was calculated to understand the effect of the Cl percentage in the conversion bath on the completion of the conversion reaction and to confirm the UV-visible spectroscopy results. As shown in Figure 21-d, the presence of PbI_2 in the pattern decreases when inserting Cl in the perovskite lattice, it remains however constant when increasing the Cl ratio in the bath. Consequently, $MAPbI_3$ possesses the highest PbI_2 percentage. These results also validate the incorporation of Cl in the lattice[185], which favors the conversion reaction and thus reduces the presence of PbI_2 in the mixed perovskites. Conforming to the UV-visible spectroscopy results, $MAPbCl_3$ planes[284] do not appear for the $MAPbI_{3-x}Cl_x$ samples. This is very interesting for the application, since this phase is completely photo inactive. According to literature, for high content of Cl exceeding 30%[181,184], the insertion of Cl atoms in the lattice is no longer possible which engenders the appearance of crystalline $MAPbCl_3$ on the pattern[191]. This is not the case here, which validates that the percentage of Cl inside the perovskite is evidently lower than that inside the conversion bath. In addition, the double peak of the tetragonal phase at 28° is known to tend to split when the ratio of Cl increases in the $MAPbI_{3-x}Cl_x$ layer[171], which is also not detected in our case. However, a peak shift is detected on the same peak when inserting Cl in the lattice, slightly changing when increasing the Cl content, as presented in Figure 21-d (zoom in Figure S15). This peak

shift validates the infiltration of Cl in the crystal lattice of $MAPbI_3$, since the shifts are larger than the XRD measurement steps (0.013°)[183]. According to literature, when the Cl percentage in the lattice is less than 10%, the $MAPbI_3$ peaks shift toward greater angles[183,287], which is observed in our case. Furthermore, increasing the Cl percentage in the conversion bath increases the relative crystallinity of the films. The relative crystallinities of the elaborated films were compared in Figure 21-d, showing that electrodeposited $MAPbI_{3-x}Cl_x$ samples has a higher crystallinity than electrodeposited $MAPbI_3$. This confirms the gradual infiltration of Cl in the lattice[185], meaning the actual Cl content in the lattice increases when increasing the Cl ratio in the conversion solution.

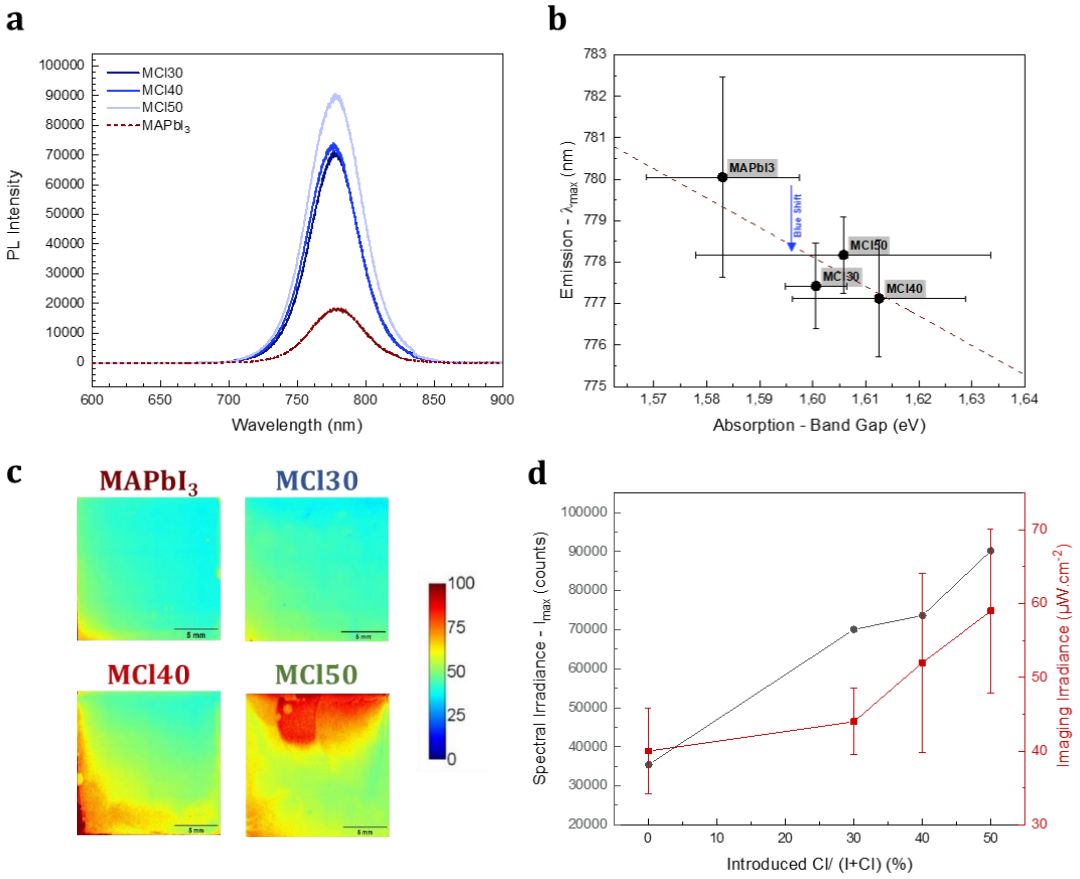

Figure 22: a) PL spectra of the four elaborated films excited with a 520 nm wavelength, b) λ_{max} detected in the PL spectra in function of the corresponding optical band gaps , c) the quantified PL images (the unit of calibration bar is $\mu W \cdot cm^{-2}$) of perovskite layers and d) the variation of the irradiance (I_{max}) of the PL spectra and the average irradiance calculated from the PL images, as a function of the percentage of Cl in the conversion solutions

Photoluminescence spectroscopy was then used to characterize the emission properties of the electrodeposited elaborated films. Figure 22-a presents the PL spectra of the MAPbI3-xClx films compared to MAPbI3. For the mixed perovskites, only the emission of the $MAPbI_3$ phase could be detected. The wavelength at maximum emission intensity λ_{max} was then drawn for the different $MAPbI_{3-x}Cl_x$ samples in Figure 22-b, to evaluate the spectrum shift in function of the Cl ratio and the absorption band gap. As expected, $MAPbI_{3-x}Cl_x$ emission peaks present a blue shift with respect to $MAPbI_3$[288]. This is related to the Cl incorporation within the perovskite as it usually implies a blue shift[181]. For the three $MAPbI_{3-x}Cl_x$ samples, the emission shows a slight variation around 778 nm, related

to the band gap variation detected in the UV-visible spectra. Usually, as the absorption band gap increases, the wavelength at maximum emission intensity λ_{max} decreases[181,274]. This correlation is emphasized in Figure 22-b, presenting the linear relation between λ_{max} and the band gap.

PL images in Figure 22-c are presented using an absolute quantification method developed in our lab[277,289]. This method allows a better comparison even when changing the acquisition parameters. The irradiance on the overall substrate was found less homogenous for the mixed perovskite films than for $MAPbI_3$ film, especially for MCl40 and MCl50. The maximum PL spectral intensity I_{max}, affected by the radiative recombination, is also traced, in Figure 22-d, along with the average irradiance extracted from the PL images. Both curves have the same tendency, validating the correlation between PL spectroscopy and PL imaging. It must be mentioned that since the characterizations are applied on half-cells (Glass/ITO/TiO_2/PK), a quenching with ITO/TiO_2 is expected. The electrodeposited $MAPbI_{3-x}Cl_x$ samples present higher photoluminescence than electrodeposited $MAPbI_3$, which increases when increasing the Cl percentage. In PL, recombination can be radiative (electron-hole) and non radiative (Auger)[290], especially for the half-cells. Hence, this increase in PL intensity is not necessarily negative for the targeted application. According to the literature, it could be due to the decrease in the defects in the layer, so charge carriers reach less non-radiative recombination centers (defects) and instead recombine radiatively, which gives rise to an increase in photoluminescence quantum yield[291]. It could also be attributed to an increase of the grain size and of the crystal quality of the perovskite, which is in agreement with the XRD results [185,292].

In the upcoming studies, we chose the sample converted in MCl40 as the best candidate for photovoltaic application. Although $MAPbI_{3-x}Cl_x$ sample converted in MCl50 presents good relative crystallinity, it presents a less homogeneous surface. On the other hand, the sample converted with MCl40 offers higher relative crystallinity than that with MCl30, which makes it a better candidate for solar application.

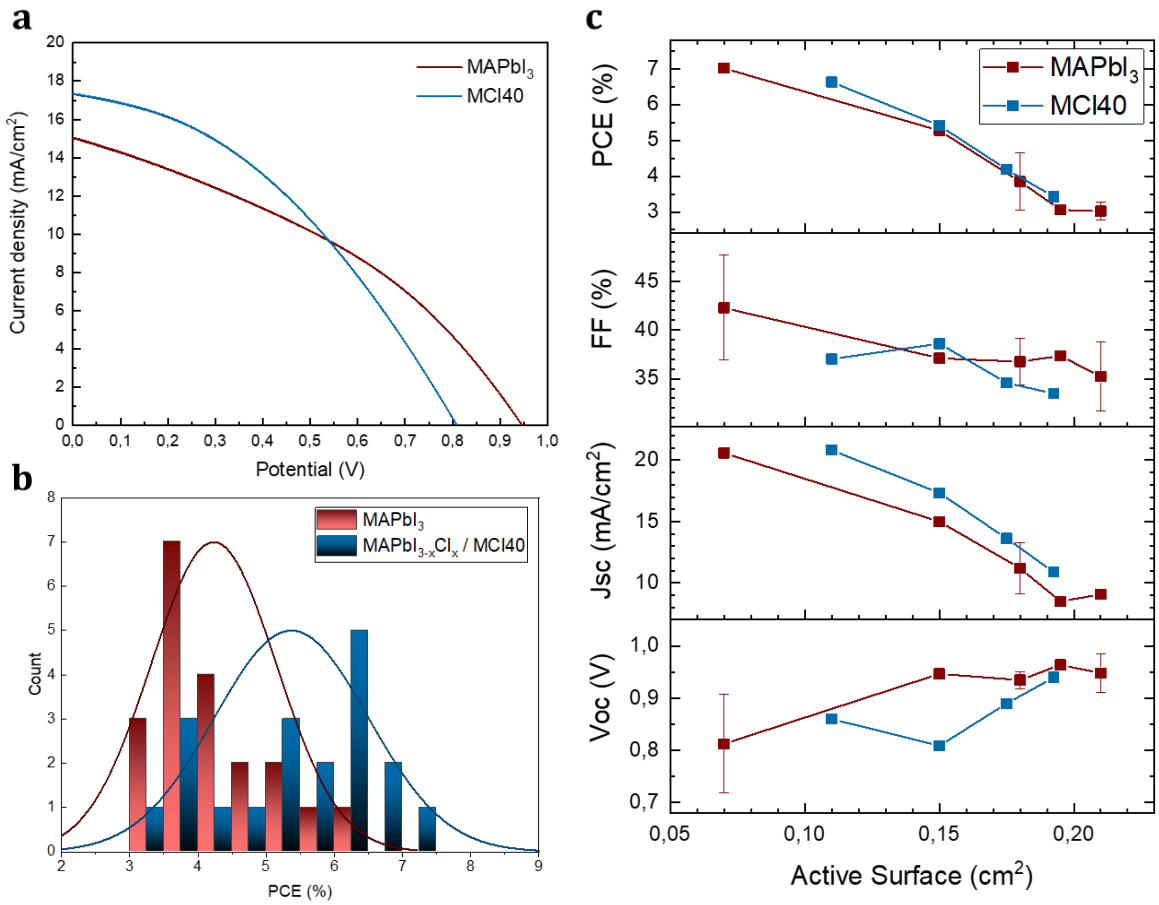

Figure 23: a) J(V) curves, b) PCE values distribution (histogram) and mean PCE distribution (curve) of the two developed solar devices, with the following architecture: Glass/ITO/TiO_2c/TiO_2m/Perovskite/P3HT/Cp (20 devices of each), the measurements were applied on PSCs with a 0.15 cm² active surface, using a scan rate of 40 mV/s, and c) their PCE, FF, J_{sc} and V_{oc} variation as a function of the active surface

The photovoltaic performance of the elaborated electrodeposited perovskite active layers was evaluated by measuring the J(V) curves of the solar cells with the following architectures: Glass/ITO/TiO_2c/TiO_2m/Perovskite/P3HT/C. The perovskite layer was consisted either of pure $MAPbI_3$ or $MAPbI_{3-x}Cl_x$. According to the above full comprehensive study, the most promising $MAPbI_{3-x}Cl_x$ layer was selected for solar cell elaboration (PK converted at 40°C using MCl40 as conversion bath). Figure 23-a presents the J(V) curves of the two developed solar devices, with an active surface of 0.15 cm². We notice a greater V_{oc} but a smaller J_{sc} for $MAPbI_3$ than for $MAPbI_{3-x}Cl_x$. The PCE distribution of 20 identical PSCs for these two different architectures in Figure 23-b shows that the solar device elaborated using $MAPbI_{3-x}Cl_x$ as an active layer possesses a better performance than the one using $MAPbI_3$, the mean PCE value being 5.5% for $MAPbI_{3-x}Cl_x$/MCl40 and 4.5% for $MAPbI_3$. This is due to an increase of the J_{sc} for $MAPbI_{3-x}Cl_x$ although its V_{oc} is lower, as already detected in Figure 23-a. The chlorine doping of the perovskite does not always enhance the performance of the solar cell[184], as observed for spin-coated perovskites. It only works when it is implemented in a small dose, which is the case here. It reduces charge recombination and increases the excited lifetime[285], since $MAPbI_{3-x}Cl_x$ has a charge diffusion length greater than 1 µm , whereas it is only 100 nm for $MAPbI_3$[293,294].

To deepen these results, the effect of the active surface on the performances of these two types of cells have been studied, as presented in Figure 23-c. We noticed a drastic decrease of the PCE, the FF and the J_{sc} when increasing the active surface for both $MAPbI_3$ and $MAPbI_{3-x}Cl_x$ PSCs. The PCE is also strongly impacted and divided by about a factor 2 for both $MAPbI_3$ and $MAPbI_{3-x}Cl_x$ when increasing the active surface between 0.07 and 0.21 cm^2. This also divides by about 2.5 the J_{sc} value, since a large active surface encourages the presence of defects. However, we notice a V_{oc} increase when increasing the active surface, for both solar devices, going from 0.8 V to 0.95 V for $MAPbI_3$. In fact, it was proven in the literature that weakening the Coulomb interaction at the interface and suppressing photoinduced charge transfer and recombination usually increase V_{oc} and decrease J_{sc}[295]. At the end, even when variating the active surface, PSCs with $MAPbI_{3-x}Cl_x$/MCl40 have a small advantage in PCE comparing to those with $MAPbI_3$.

Admitting the fact that electrodeposited $MAPbI_{3-x}Cl_x$ offers a small enhancement in the PCE comparing to electrodeposited $MAPbI_3$, the stability of these devices has also to be studied. For that, the ageing behavior of these solar cells has been studied at 40°C, either under ambient atmosphere (R.H. = 20%, noted **"a"**) or under vacuum (noted **"v"**), for 500h. To correlate the performance variation of solar cells during the physico-chemical and microstructural modifications of perovskite, some half-cells have been aged under the same conditions.

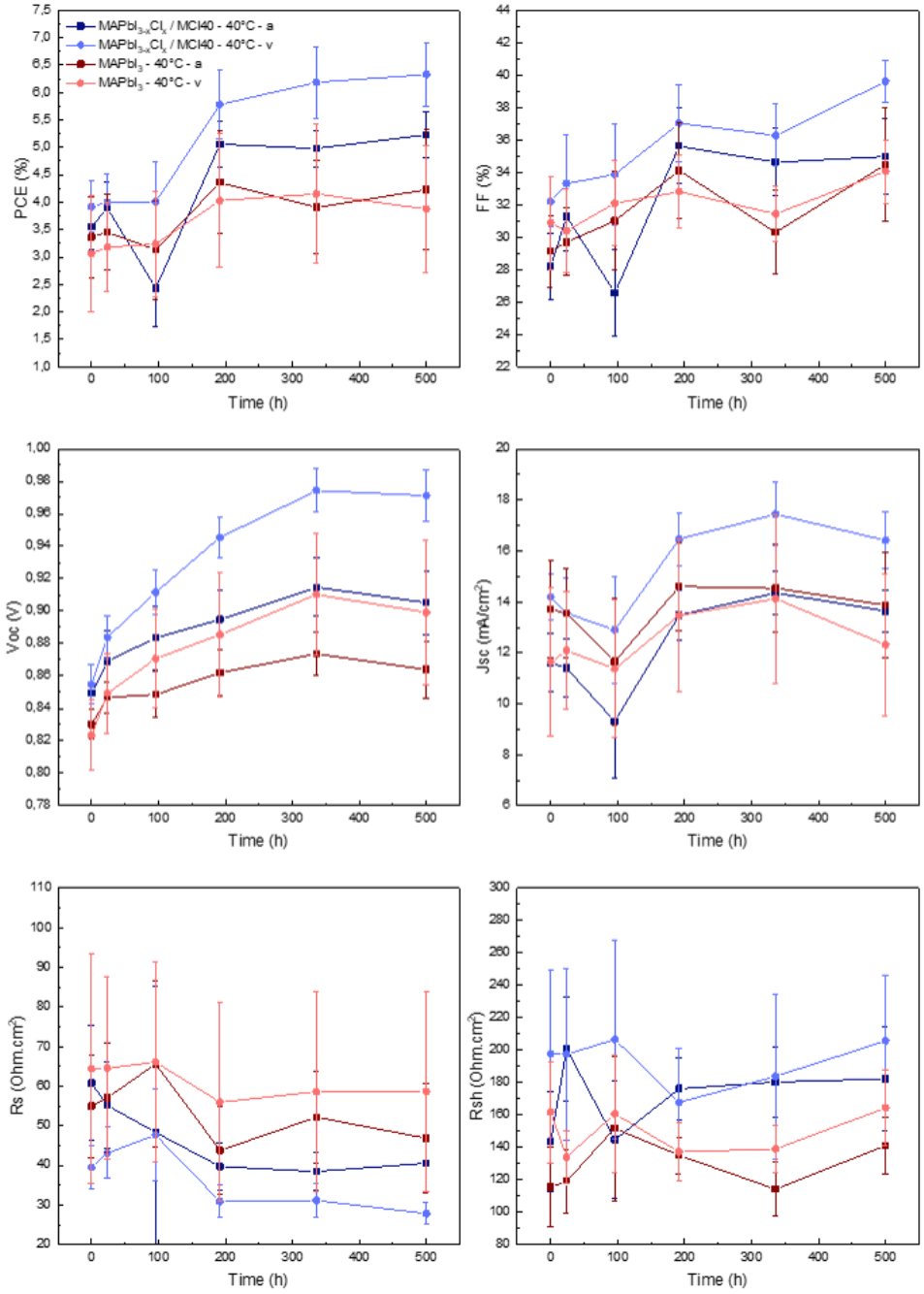

Figure 24: PCE, FF, V_{oc}, J_{sc}, R_s and R_{sh} evolution with time for the two types of solar cells aged at 40°C, either at ambient atmosphere or under vacuum

The photovoltaic performance of the aged solar cells was monitored during aging by performing photocurrent density-voltage measurements. Figure 24 presents the variation of all photovoltaic parameters (PCE, FF, V_{oc}, J_{sc}, R_s and R_{sh}) during aging for the two conditions tested. We notice an increase of the PCE with time, for $MAPbI_3$ or MCl40, whatever the ageing conditions, which validates a maturation process. The solar devices based on MCl40 encounter a better enhancement than the ones with $MAPbI_3$, allowing an increase of PCE value of 40% between electrodeposited $MAPbI_3$ and $MAPbI_{3-x}Cl_x$ based devices. This maturation process seems to be more pronounced for the treatment under vacuum than in ambient atmosphere, since the devices do not probably endure the same

concurrent degradation mechanisms. We also notice that the PCE variates at the same pace as the short-circuit current density J_{sc} and the fill factor FF. This must be due to a reduction in the defects inside the active layer or at the interfaces between the layers. On the other hand, when examining the variation of the V_{oc} with time, we notice a continuous increase of the V_{oc} over the time, independent of the variation of the J_{sc} or the FF. A variation of the V_{oc} could possibly originate from a variation in the energy levels of the materials constructing the solar cell. It could also derive from an enhancement in the quality of the layers to minimize the recombination. We deduce that the elaborated perovskites are rather stable, and even after 500 h of ageing, the maturation had still a greater impact than the degradation.

To better understand this maturation mechanism, half-cells have been aged under same aging conditions. It must be noted however that the degradation for the half-cells is faster than for the cells, since these latter contain both a P3HT layer and a carbon layer that work as protective layers and slow down the degradation. The following figure presents the optical properties or studied perovskites during aging.

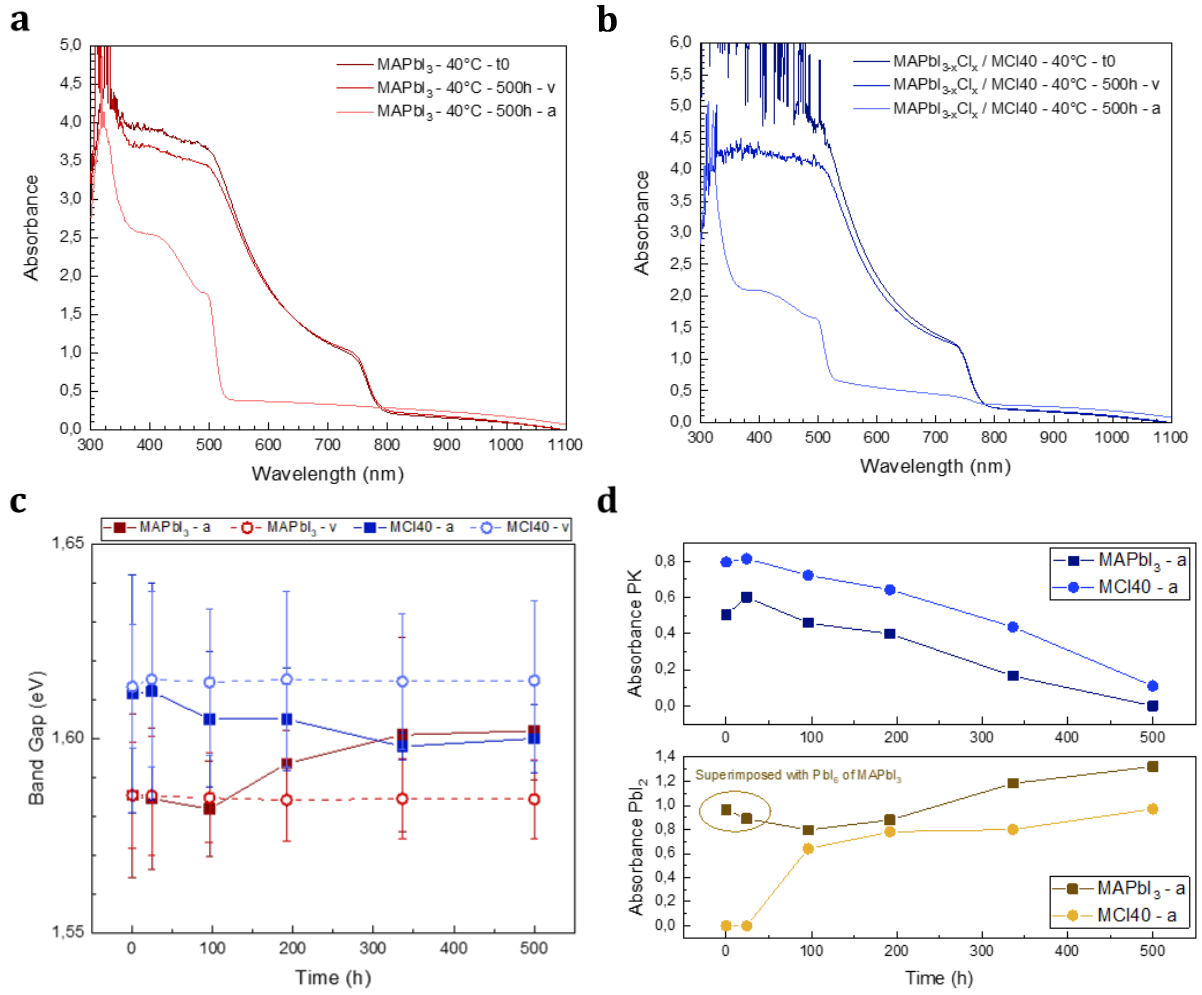

Figure 25: The evolution with time of the UV-visible absorption spectra of the a) $MAPbI_3$ and b) $MAPbI_{3-x}Cl_x$ half-cells aged at 40°C in ambient atmosphere or under vacuum, at t0 and after 500h, c) Band Gap variation with time of the perovskite for the two different half-cells, and d) The variation with time of the absorbance difference for the perovskite onset (between 730 and 800 nm) and the PbI_2 onset (between 480 and 530 nm) for the two half-cells aged at ambient atmosphere

First, the UV-visible absorption spectra of the two types of half-cells are presented in Figure 25-a and Figure 25-b. Figure S16 presents a more detailed variation of the UV-visible spectra of four different half-cells elaborated using $MAPbI_3$ and $MAPbI_{3-x}Cl_x$. When the samples are aged under vacuum, no strong change in the UV-visible spectra was noticed. Hence, no variation was observed in $MAPbI_3$ and $MAPbI_{3-x}Cl_x$ band gaps (Figure 6-c, dotted lines). For the samples aged in ambient atmosphere, the onset of both perovskites slightly shift with time (Figure 6-c, solid line), while another transition emerges from the background at around 500 nm, indicating the formation of PbI_2 (Figures 6 a-b). This confirms the progressive degradation of the perovskites[296]. However, if $MAPbI_3$ band gap slightly increases with time (related with the perovskite degradation[297]), that of $MAPbI_{3-x}Cl_x$/MCl40 presents a soft continuous decrease until reaching at 500h a value identical to that of $MAPbI_3$. Such behavior could be attributed to a reduction of the Cl content inside the mixed perovskite, also indicating a chemical degradation of the $MAPbI_{3-x}Cl_x$ material.

We can thus deduce that the additional effect of oxygen and/or humidity is more remarkable than the effect of sole temperature. To better quantify the transformation of perovskite into PbI_2, we calculated an estimated absorption for perovskite and PbI_2 peaks, presented in Figure 25-d, and drew their variation with time. $MAPbI_3$ shows greater degradation with time than $MAPbI_{3-x}Cl_x$, with the most important decrease of PK and increase in PbI_2, confirming the stability enhancement of the perovskite with Cl incorporation.

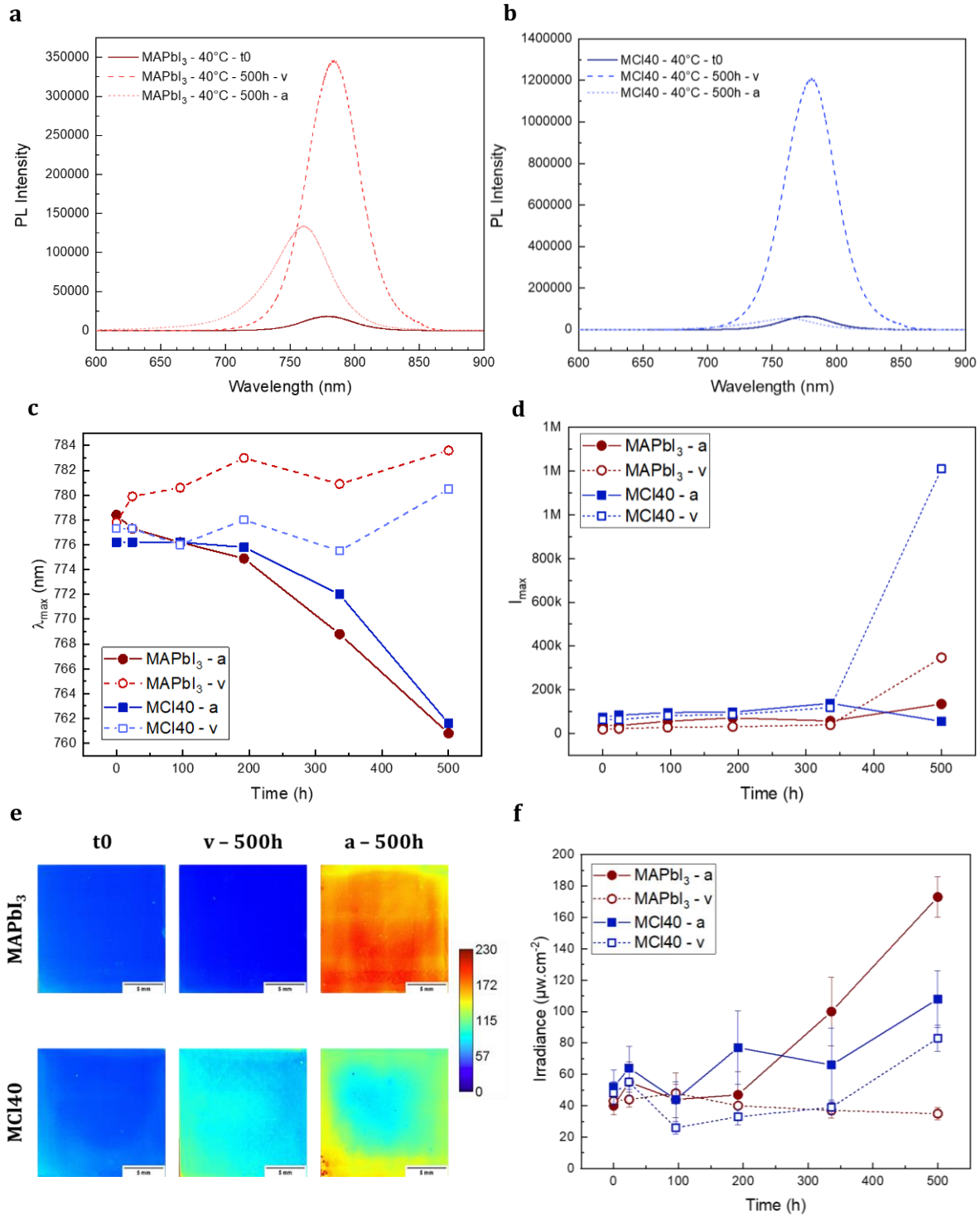

Figure 26: The variation with time of the photoluminescence spectra for the a) $MAPbI_3$ and b) $MAPbI_{3-x}Cl_x$ based half-cell aged in ambient atmosphere or under vacuum, The variation with time of c) λ_{max} and d) I_{max} extracted from the PL spectra of the aged perovskite half-cells, e) Photoluminescence images showing the variation of the irradiance (the unit of calibration bar is $\mu W \cdot cm^{-2}$) for the two half-cells after 500h of ageing at ambient atmosphere or under vacuum (scale bar: 5 mm), and f) the variation with time of the average irradiance calculated from the PL images of the aged perovskite half-cells

Photoluminescence spectroscopy was also used to explore mechanisms occurring during half-cells ageing and/or maturation. From externally detecting the emitted photons, the

luminescence intensity gives information about the quantity of radiative recombination, and the emission wavelength about the energy of the recombined electron–hole pairs[298]. PL spectra of the $MAPbI_3$ and $MAPbI_{3-x}Cl_x$ based half-cells at t0 and after 500h for ageing campaigns conducted under vacuum or under ambient atmosphere are shown in Figure 26-a and Figure 26-b. The λ_{max} values were extracted from PL spectra and plotted as a function of time in Figure 26-c. First, all the samples aged under vacuum (dotted lines) exhibit a PL redshift. As any band gap shift or significant degradation was detected on absorption spectra, this PL redshift can be associated to a positive mechanism occurring during the observed maturation process leading to PCE increase. As shown by Tabuchi *et al.* [299], a redshift can originate from a decrease in the quantum confinement effect because of the expansion of the exciton Bohr radius, which causes a decrease in exciton binding energy. The conduction and the valence bands become wider, because the transfer energy among $[PbI_6]$ octahedra becomes larger. Liu *et al.* also attributed the redshift to atomic distortion[300]. Hong *et al.* mentioned that among the reasons of redshift for perovskite[301], there may be an inclusion of a different crystal phase[302–304], an atmosphere effect[297,305,306], reabsorption effects[307], or radiative recombination involving shallow trapping levels[308]. Contrarily, for the samples aged under ambient atmosphere (Figure 26-c, solid line), a blueshift of λ_{max} value is observed, quite equivalent for $MAPbI_3$ and $MAPbI_{3-x}Cl_x$ / MCl40, which is correlated to a more classical degradation behavior of perovskites[297,305,306].

Additionally, the quantity of radiative recombination is detected from the luminescence intensity, and traced in function of time in Figure 26-d. The maximum intensity of the PL spectra I_{max} increases more upon ageing under vacuum than under air. Nevertheless, its relatively stable value for the samples aged in ambient atmosphere does not eliminate the degradation probability, since an important shift in λ_{max} is detected. Regarding the drastic increase in the PL intensity under vacuum, it should be correlated to the maturation process. According to the literature, an increase in the maximum PL intensity could also be attributed to an increase of the grain size and the crystal quality of the perovskite[185,292]. These results indicate that both $MAPbI_3$ and $MAPbI_{3-x}Cl_x$/MCl40 samples aged under vacuum exhibit a maturation while same samples aged in ambient atmosphere predominantly degrade. In addition, $MAPbI_{3-x}Cl_x$ simultaneously undergoes a higher PL (intensity and redshift) enhancement than $MAPbI_3$, together with a higher PCE gain (PCE increase of 60% vs. 20%, respectively).

On the other hand, PL imaging was used to extract irradiance levels overall the surface and compare the homogeneity of the different perovskite films[277]. Figure 26-e displays the PL images of the aged half-cells at time t0 and after 500h, along with the corresponding irradiance variation in Figure 26-f. When aged under vacuum, the maturation phenomena could be barely noticed using PL imaging, so the detected variation is negligible, although always higher for the mixed halide (I/Cl) perovskite. Otherwise, the half-cells aged in ambient atmosphere undergo an important degradation, already confirmed in the previous characterizations, so they enclose a big amount of PbI_2. The irradiance detected in this case is mainly a response of the LED beam on the PbI_2 that does not absorb the exitation wavelength (Check Figure S17). Coupled with Figure S18, we can confirm in ambient atmosphere a degradation that starts from the borders and gradually propagates to the center.

Conclusion

In this work, electrodeposition was conducted as an alternative deposition method for perovskites. After studying the electrodeposition of $MAPbI_3$ perovskite layers, the same process was applied on double halides perovskites $MAPbI_{3-x}Cl_x$, while variating the ratio of Cl. The impact of chlorine proportion on the microstructural, morphological and functional properties of these perovskite layers were studied by SEM imaging, UV-visible absorption, X-Ray diffraction, photoluminescence spectroscopy and imaging. The results showed that the ratio variation of each mixture induces a composition modification of the obtained perovskite material. Increasing the Cl ratio in the conversion solution increases its infiltration in the perovskite lattice and enhances the relative crystallinity of the perovskite films. The photovoltaic performances of the elaborated $MAPbI_3$ and the $MAPbI_{3-x}Cl_x$ perovskite were then compared in a solar device. Chlorine-doped electrodeposited perovskites offer a PCE enhancement, with an average PCE of 5.5% instead of 4.5% for a 0.15 cm^2 PSC. Their stability was also tested in complete solar cells or half-cells when aged at 40°C under vacuum or in ambient atmosphere, and compared to that of electrodeposited $MAPbI_3$. The PSCs are subject to maturation when aged in the as-mentioned conditions, with a PCE improvement of 60% for $MAPbI_{3-x}Cl_x$ and 20% for $MAPbI_3$. From the collected results, we note that the incorporation of Cl in the perovskite lattice not only enhances its photovoltaic performance but also improve its stability.

Experimental section

Materials and chemicals

ITOGLASS 07P ITO-coated glass slides (2.5 × 1.7 cm^2) were purchased from Visiontek Systems. The reagent chemicals used are as follow: lead(II) acetate trihydrate $Pb(CH_3COO)_2.3H_2O$ (Sigma-Aldrich, 99%), sodium nitrate $NaNO_3$ (Sigma-Aldrich, ≥ 99%), methylammonium iodide CH_3NH_3I (MAI) and chloride CH_3NH_3Cl (MACl) (Greatcell Solar), and hydrogen iodide HI (57 wt% in H_2O, stabilized 99.95%, Sigma-Aldrich). pH adjustments were done using nitric acid (65%, AnalaR NORMAPUR, VWR Chemicals). Ti-Nanoxide BL/SC for the compact TiO_2 and Ti-Nanoxide T600/SC for the mesoporous TiO_2 were purchased from Solaronix. The carbon paste applied was the DN-CP01 from Dyenamo. Regioregular poly(3-hexylthiophene-2,5-diyl) P3HT (#4002-E, Rieke Metals) was used for the HTL precursor solution, with chlorobenzene (Sigma-Aldrich, anhydrous, 99.8%) as the solvent. The isopropanol and ethanol used in the conversion bath were anhydrous (Sigma-Aldrich, 99.5%). All aqueous solutions were prepared using 18 MΩ. cm resistivity water from a Millipore Milli-Q system.

Substrates preparation and ETL deposition

The ITO substrates were first ultrasonically cleaned with acetone, isopropanol, and deionized water in sequence. They were then subjected to UV-O_3 treatment for 30 min before each deposition.

TiO_2 compact-mesoporous ETL (TiO_{2m}) was deposited on ITO using spin coating. First, 50µL of the Ti-Nanoxide BL/SC solution was dropped on the substrate while starting the spinning. Conditions were set at 33 rps for 1 s, then 83 rps for 30s. The compact TiO_2 coated substrate was then sintered at 550 °C for 1h. The resulting compact layer, also

called blocking layer has a thickness of around 65 nm. The Ti-Nanoxide T600/SC is a solution for the formation of 600 nm thick mesoporous titania layers. However, the optimized thickness of TiO_2 scaffold is around 450 nm [22], so the as-mentioned precursor solution was diluted with 0.4 mL of ethanol for each 1 mL. The obtained solution was spin coated using the same conditions as for the blocking layer, and then sintered at 475°C for 30 min. The mesoscopic structure obtained by the sintering of nano-particles in the process makes a perfect host for perovskite crystals.

Electrodeposition of PbO_2 films

An aqueous solution containing 0.025 M lead(II) acetate trihydrate and 0.05 M sodium nitrate served as an electrodeposition (ED) bath for PbO_2 films. The pH adjustments until having a pH of 5.5 were done with nitric acid. ED was performed without stirring at ambient temperature with a Biologic SP-150 potentiostat and a three-electrode arrangement. ITO substrates or ITO/TiO_{2m} substrates acted as working electrodes (after being UV-O_3 treated), with an active deposition area of 2.55 cm^2 (1.5 × 1.7 cm^2). A spring-shaped platinum electrode was used as the counter electrode and an Ag/AgCl/KCl_{sat} electrode as the reference electrode. The electrodeposition was carried out at a potential of 1.5 V versus the reference electrode for a deposition duration of 50s (Reaction 0). A brownish color appears indicating the formation of PbO_2. The obtained substrates were then rinsed with pure ethanol before conversion into PbI_2, to eliminate any hydration.

$Pb^{2+} + 2\ H_2O \rightarrow PbO_2 + 4\ H^+ + 2\ e^-$ Reaction 0

Conversion of PbO_2 into PbI_2

Conversion of PbO_2 to PbI_2 was carried out at ambient temperature in a petri dish. The substrate was immersed in a 0.05M HI - ethanol solution for 3 min. A change of color from brown to yellow indicates the conversion of PbO_2 into PbI_2 films (Reaction 1). The samples were rinsed with ethanol and then dried with N_2 before keeping them in a vacuum desiccator to avoid any hydration.

$PbO_2 + 4\ HI \rightarrow PbI_2 + 2\ H_2O + I_2$ Reaction 1

Conversion of PbI_2 into $CH_3NH_3PbI_3$ or $CH_3NH_3PbI_{3-x}Cl_x$

Conversion of PbI_2 into $MAPbI_3$ was carried out in a petri dish containing a 0.1M MAI - isopropanol solution, preheated at 40°C. To convert into $MAPbI_{3-x}Cl_x$, the conversion solution consisted of a mixture of MAI and MACl in isopropanol. This conversion was carried out 40°C and for three different Cl/(I+Cl) ratio (30%, 40% and 50%). The substrate was immersed in the solution for 3 min, before rinsing it with isopropanol and then drying it with N_2. When converting PbI_2, the color changes from yellow to brownish black in a few seconds, which indicates the formation of $MAPbI_3$ perovskite (Reaction 2-a) and of $MAPbI_{3-x}Cl_x$ (Reaction 2-b). It is important to mention that the stoichiometric coefficients presented in the reaction are not equal to the quantity of MAI and MACl in the conversion solution, but to the quantity that reacts. The samples were kept in a vacuum desiccator to avoid any hydration.

$PbI_2 + CH_3NH_3I \rightarrow CH_3NH_3PbI_3$ Reaction 2-a

$PbI_2 + (1-x)\ CH_3NH_3I + x\ CH_3NH_3Cl \rightarrow CH_3NH_3PbI_{3-x}Cl_x$ Reaction 2-b

HTL deposition

For the deposition of the HTL layer, a 15 mg/mL P3HT in chlorobenzene solution was spin coated on the perovskite at 10 rps for 5s then 15rps for 60s. These conditions lead to a 50nm thick P3HT layer.

Carbon paste deposition

Finally, a low temperature Dyenamo commercial carbon paste was deposited on the stack using doctor-blading technique. Each substrate formed six different cells with an active surface of around 0.2 cm^2. The final sample was then annealed at 120°C under vacuum, for 2h. This will not only dry the carbon paste and evaporate its solvents, but also help the connection at the interfaces inside the solar cell.

Ageing

We studied first the ageing of two different types of solar cells with the following architecture: Glass/ITO/TiO_2c/TiO_2m/Perovskite/P3HT/Cp, then of the corresponding half-cells: Glass/ITO/TiO_2c/TiO_2m/Perovskite, the perovskite being either $MAPbI_3$ or $MAPbI_{3-x}Cl_x$ converted in MCl40. The stability of the following devices was tested at 40°C, either under ambient atmosphere (R.H. = 20%, noted **"a"**) or under vacuum (noted **"v"**), for 500h. Nondestructive characterizations were applied at different sampling times in order to elucidate occurring mechanisms. For each type of solar device, the test was elaborated on two substrates containing 6 solar cells each (12 solar cells in total for each type).

Characterizations and methods

All electrochemical characterizations were carried out using the as-prepared electrolytes, and the three-electrode system described above, via the SP-150 potentiostat/galvanostat of BioLogic. Depositions and characterizations were realized on Glass/ITO/TiO_2c/TiO_2m substrates. The thickness and roughness of all layers were measured using the Alpha-Step D-500 stylus profiler, and calculating the mean value of five measurements from distinct positions across the film. The structure and texture of the films were determined with a *PANalytical X'Pert PRO MPD X-Ray diffractometer* using Cu-Ka source. Match! and DIFFRAC.EVA softwares were used to identify the phases and determine the lattice parameters. The morphology of the films was studied by scanning electron microscopy (SEM) using FEG ZEISS Ultra 55. Absorption measurements in the UV−visible range were performed with a Shimadzu UV-2600 spectrophotometer coupled with an integrating sphere, in the 300-1100 nm range, with a Glass/ITO substrate as a reference. Optical band gaps were calculated from Tauc plots drawn using the absorbance data. The estimated absorption variation for PK and PbI_2 was calculated by measuring the absorption difference between the maximum and minimum point of each onset. Leica DMLS Optical Microscope was used to examine the surface of the samples and deduce the gray scale used for Combessis *et al.* calculations[275]. PL spectra were acquired over the 600− 900 nm range on a Shimadzu RF-6000 spectro fluorophotometer with a 520 nm excitation wavelength. Two filters were used: a 575 nm low-pass in front of the excitation source

and a 600 nm high-pass in front of the source of emission in order to suppress any artifact coming from the spectrophotometer. Chosen measurement conditions were a scan rate of 6000 nm/min, an excitation slit of 5 nm, and an emission slit of 5 nm. Luminescence imaging experiments were performed with a home made device composed of an opaque chamber with a camera placed 30 cm above the samples and two green light-emitting diode (LED) arrays with emission spectrum between 400 and 550 nm. A 650 nm high-pass filter from Edmund Optics (York, UK) was added in order to allow for spectral resolution in the setup and to minimize reflection from the excitation LEDs. Full PSC devices were observed in the open-circuit condition. The acquisition time was set close to 1000 ms with an aperture equal to 16. As the resulting signal varied depending on acquisition conditions (time, opening, filter type), not allowing for a direct quantitative comparison of the evolutions observed, a calibration reported in a previous publication allowing for image correction was employed[277]. Any additional image treatment (cropping, colorization, or thresholding) was performed with the ImageJ freeware. A standard simulated AM1.5G irradiation system with a 100W ozone free xenon-lamp solar simulator (Oriel LSC-100) was used for solar cell tests. The photocurrent density–voltage (J–V characteristics) measurements of the devices were recorded using a BioLogic-SP300 source with a scan going from +1 to −0.2 V and a scan rate of 40 mV/s. The fill factor FF, short-circuit current J_{sc}, open-circuit voltage V_{oc}, power conversion efficiency PCE, shunt resistance R_{sh} and series resistance R_s parameters were then deduced from J(V) measurements, using a home-made program on Spyder software.

Acknowledgments

Authors thank I-MEP2 doctoral school for the MESR PhD grant (M.A.K.) attribution, and the platform of Consortium des Moyens Technologiques Communs (CMTC) of Grenoble INP for laboratory assistance and laboratory equipment. This work has been partially funded by the EU Framework Program for Research and Innovation HORIZON 2020 (Cofund ERA-NET Action, N° 691664). This work has also been partially funded by the "PROPER" project supported by "EIG Concert Japan" and financed from the French National Centre for Scientific Research under the funding number "IRUEC 222437".

Supplementary Information

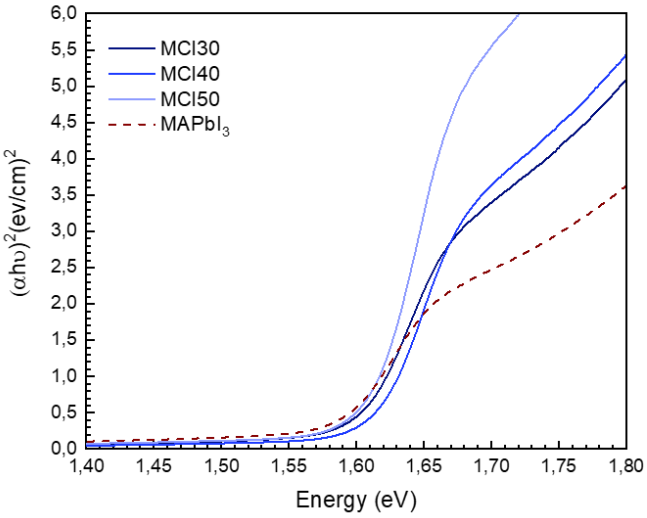

Figure S14: Tauc plot of elaborated PK films (deduced from their UV-visible absorption spectra)

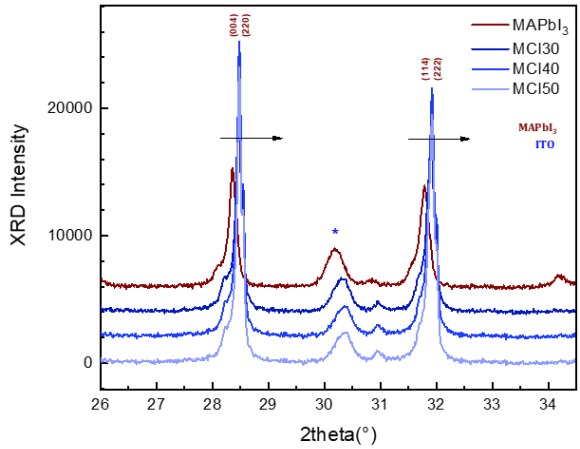

Figure S15: Zoomed XRD pattern of the elaborated $MAPbI_3$ and $MAPbI_{3-x}Cl_x$ films showing the shift of the PK peaks

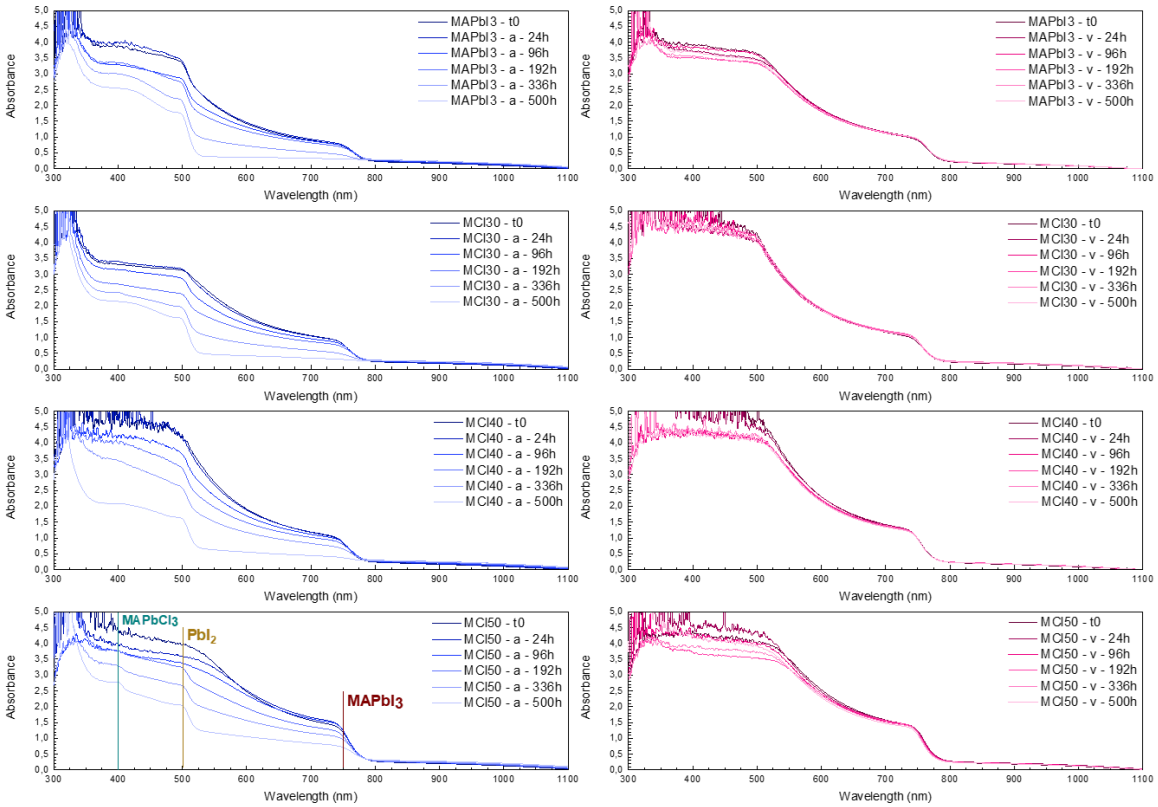

Figure S16: The evolution with time of the UV-visible absorption spectra for the four different half-cells aged at ambient atmosphere or under vacuum

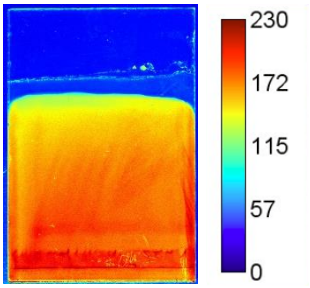

Figure S17: PL image of a 2.5x1.7 cm² PbI_2 sample (the unit of calibration bar is µW·cm⁻²)

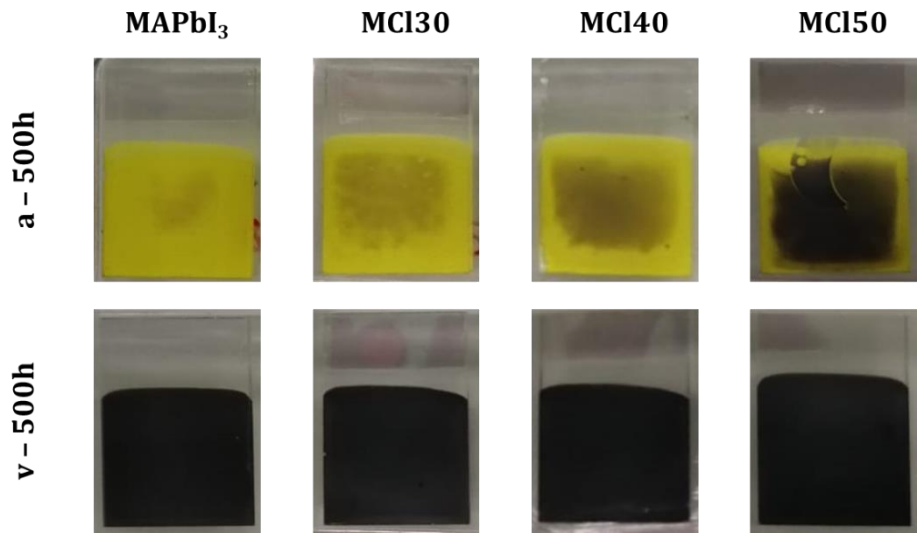

Figure S18: Photos showing the allure of the four aged samples after 500h at ambient atmosphere (a) or under vacuum (v)

Chapter IV: Performance and stability of electrodeposited $MA_{1-y}FA_yPbI_{3-x}Br_x$ mixed-cation mixed-halide perovskite solar cells

This chapter presents our third article, where another mixed perovskite is prepared using electrodeposition, being $MA_{1-y}FA_yPbI_{3-x}Br_x$. This study is the first of its kind, since this double mixed perovskite was never developed using electrodeposition before. Similarly to chapter III, the effect of the FA and Br ratios infiltrated in the perovskite lattice on the properties of the perovskite was investigated. Solar devices using these materials were developed and their performances and stabilities were compared to those elaborated using electrodeposited $MAPbI_3$.

Environment-friendly multi-stage treatment using electrodeposition for the development of $MA_{1-y}FA_yPbI_{3-x}Br_x$ mixed-cation mixed-halide perovskite solar cells

Mirella Al Katrib [1], Lara Perrin [1, *], and Emilie Planes [1, *]

[1] Univ. Grenoble Alpes, Univ. Savoie Mont Blanc, CNRS, Grenoble INP, LEPMI, 38000 Grenoble, France

Abstract

Electrodeposition was investigated in this work as a substitute method to develop large area perovskite active layer for solar device application. Along with the simple $MAPbI_3$ perovskite, the deposition of a mixed $MA_{1-y}FA_yPbI_{3-x}Br_x$ perovskite was studied, while variating the FABr proportion in the elaborated active material. This present study is one of its kind, since this double mixed perovskite was never developed using electrodeposition before. It was noticed that according to the FA and Br ratios infiltrated in the perovskite lattice, different microstructures, optical and chemical properties are obtained. This difference impacts the photovoltaic activity of the perovskite layer when applied is a photovoltaic cell. In fact, increasing the FA and Br percentages in the mixed perovskite enhances its photovoltaic activity. It also enhances its stability when evaluated in mild ageing conditions (40°C, under vacuum or ambient atmosphere) during 500h. The different perovskites elaborated using electrodeposition experience a maturation phenomenon for the first 360 h. To sum up, this work illustrates the importance of electrodeposition and its flexibility to develop different types of perovskites. It was shown how using a mixed electrodeposited $MA_{1-y}FA_yPbI_{3-x}Br_x$ perovskite enhances the efficiency of the solar devices, rather increasing when increasing the FABr ratio, and improves their stability comparing to simple $MAPbI_3$.

Introduction

Halide perovskites have recently emerged as promising materials for low-cost, high-efficiency solar cells[154]. They have drawn substantial interest in the field of material research due to the rapidly efficiency increase of perovskite solar cells (PSCs) based on halide perovskites, which reached 9.7% in 2012, up to 17.9% in 2014, and exceeded 25.5% in 2021[8,92,250]. The evolution of these solar cells revolutionized the field not only because of their high efficiency, but also because of flexibility in material growth and architecture[154], and of their tunable band gap[309]. Many techniques were investigated to improve the quality of the perovskite films and its crystallization for photovoltaic application[251]. Nowadays, the most common technique used for perovskite solar cell deposition is spin coating[252]. Although it delivers good results, this method is not ideal since it must be applied under inert atmosphere, which makes it more complex and raises its cost. Spin coating presents many more disadvantages such as non-homogeneity, undefined crystallinity, poor stability, limited surface application and could not be used for an industrial development. Electrodeposition could potentially be the best alternative

method for perovskite deposition since it is low cost, forms smooth and uniform layers, could be elaborated for large scale devices and most importantly is applied in ambient atmosphere[28]. Over the last years, many researchers attempted to optimize and understand the electrodeposition of perovskite materials. All sub-techniques started by electrodepositing a former layer, being either PbO, PbO_2 or PbI_2, followed by one or several conversions of the as-deposited layer[16–31]. The converted perovskite was mainly the simple cation-anion methyl ammonium lead iodide $MAPbI_3$, although in 2020, Lv *et al.* were the first group to have developed a mixed perovskite via electrodeposition[30]. They studied the preparation of all-inorganic mixed anion $CsPbI_{2-x}Br_{1+x}$ perovskite solar cells based on electrodeposited PbO_2 film. In the case of spin-coated $MAPbI_3$ perovskite, its main disadvantage is stability. To improve this, the methyl ammonium (MA) cation has been replaced by formamidinium (FA) in many studies which showed good durability improvements[13,310,311]. To enhance its performance, the iodine in the perovskite could also be replaced by other halides such as bromide, whether for the methylammonium or formamidinium analogues[13,209,312–315]. The bromide incorporation in the $MAPbI_3$ perovskite lattice has led to an increase in the optical band gap, tunable according to the ratio of added Br, which raises the open circuit voltage V_{oc} of the corresponding PSCs[312]. High PCEs were achieved when using composition engineering of $MA_{1-y}FA_yPbI_{3-x}Br_x$ perovskite[314]. Given the opposing effects of FA and Br substitutions on the perovskite in terms of band gap change and photoluminescence shift, the role of their incorporation together is not fully understood yet. In one of our previous works (under review), the electrodeposition of $MAPbI_3$ was optimized on different substrates and corresponding devices offered a PCE of 4%. In this study, for the first time, the electrodeposition of $MA_{1-y}FA_yPbI_{3-x}Br_x$ perovskite with different FA and Br contents is presented and compared to the more standard $MAPbI_3$ form (also obtained by electrodeposition). To validate the prospect of a PCE and durability enhancement, the photovoltaic performance and stability of the electrodeposited solar cells based on $MA_{1-y}FA_yPbI_{3-x}Br_x$ perovskites have been then tested under mild aging conditions (40°C under vacuum and air) and compared to $MAPbI_3$ electrodeposited solar cells.

Results and discussion

To elaborate the perovskite layer, electrodeposited PbO_2 was first converted into PbI_2 by immersion in HI-EtOH solution (Reaction 1). PbI_2 films were then converted into $MAPbI_3$ by immersion in MAI-IPA solution (Reaction 2-a). To obtain $MA_{1-y}FA_yPbI_{3-x}Br_x$ double anion-cation perovskites, PbI_2 films were immersed in three different MAI-FABr-IPA solutions, called FB30, FB40 and FB50. The chemical reaction associated with this conversion is presented below (Reaction 2-b).

$PbO_2 + 4\ HI \rightarrow PbI_2 + 2\ H_2O + I_2$ Reaction 1

$PbI_2(s) + z\ CH_3NH_3I \rightarrow CH_3NH_3PbI_3(s)$ + "residual CH_3NH_3I" Reaction 2-a

$PbI_2(s) + (1\text{-}z)\ CH_3NH_3I + z\ CH(NH_2)_2Br \rightarrow (CH_3NH_3)_{1-y}(CH(NH_2)_2)_yPbI_{3-x}Br_x\ (s)$ + "residual ammonium and amidinium halides" Reaction 2-b

The composition of the different MAI-FABr-IPA conversion solutions is described in Table 4. It is important to mention here that the indicated percentage of Br/(I+Br) is inside the

solution. Since the conversion is held from PbI_2 already containing iodine atoms, the percentage of Br/(I+Br) in the whole set is less than that presented in the table. Consequently, three different $MA_{1-y}FA_yPbI_{3-x}Br_x$ films with different compositions were obtained and their photographs are presented in Figure 27-a.

	MAI	FABr	Br/I+Br %
FB30	**1**	**0,5**	**30**
FB40	**1**	**0,75**	**43**
FB50	**1**	**1**	**50**

Table 4: The composition of the used conversion mixtures (MAI+FABr in IPA)

Before testing these active layers in solar devices, their morphology, microstructure, chemical composition and properties were investigated using a set of characterization methods (scanning electron microscopy (SEM), X-Ray diffraction (XRD), UV-visible absorption spectroscopy, photoluminescence (PL) spectroscopy and imaging). To start, the photographs in the Figure 27-a shows that the perovskite deposition at the macroscopic scale seem similar and relatively homogeneous, whatever the formulation. To further investigate the difference between these layers, we used optical microscopy to determine local thicknesses of electrodeposited perovskite layers. According to the work of Combessis *et al.*[275], it is possible to correlate optical density measurements (determined by UV-visible spectroscopy) with gray level measurements (evaluated by optical microscopy) to find a local thickness, thanks to the following relation.

$$e = -\frac{1}{OD} \times \log\left(\frac{GL}{100 \times K \times M^{\beta} \times t^{\upsilon} \times V^{\kappa}}\right) \qquad \text{Equation 1}$$

With e the perovskite thickness (µm), OD the optical density determined by UV-Visible spectroscopy between 400 and 800 nm, GL the gray level, K the microscope constant, M the magnification, t the time (s), and V the voltage of the lamp (V). β, υ, κ are the magnification, the time and the voltage powers and were previously evaluated by a calibration method explained in the article of Combessis *et al.*[275]. Here we assumed that the only material that can absorb in the visible range is perovskite. These image analyses were applied on several photographs of the four elaborated perovskite layers deposited on TiO_2. Some results are presented in Figure 27-b, showing the distribution of the thickness of perovskite over all the surface of the substrate. We note that the perovskite layers are rather homogeneous, with an average of 1µm of thickness for $MAPbI_3$ and for the three $MA_{1-y}FA_yPbI_{3-x}Br_x$ samples.

At the microscopic scale, the in-plane morphology of the different converted perovskites (PK) was examined by SEM and presented in Figure 27-c. The $MAPbI_3$ film converted from PbI_2 has a fully covered surface of small cubic-shaped grains with a non-uniform orientation, and a grain size ranging between 150-200 nm. When converting PbI_2 into $MA_{1-y}FA_yPbI_{3-x}Br_x$, we notice similar surface morphologies for the three films converted via FB30, FB40 and FB50. It consists of cubic grains, slightly larger than $MAPbI_3$ cubes, more entangled and less spaced. This can limit the presence of gap areas and counter a partial short-circuit across the junction when we use the perovskite in a solar device.

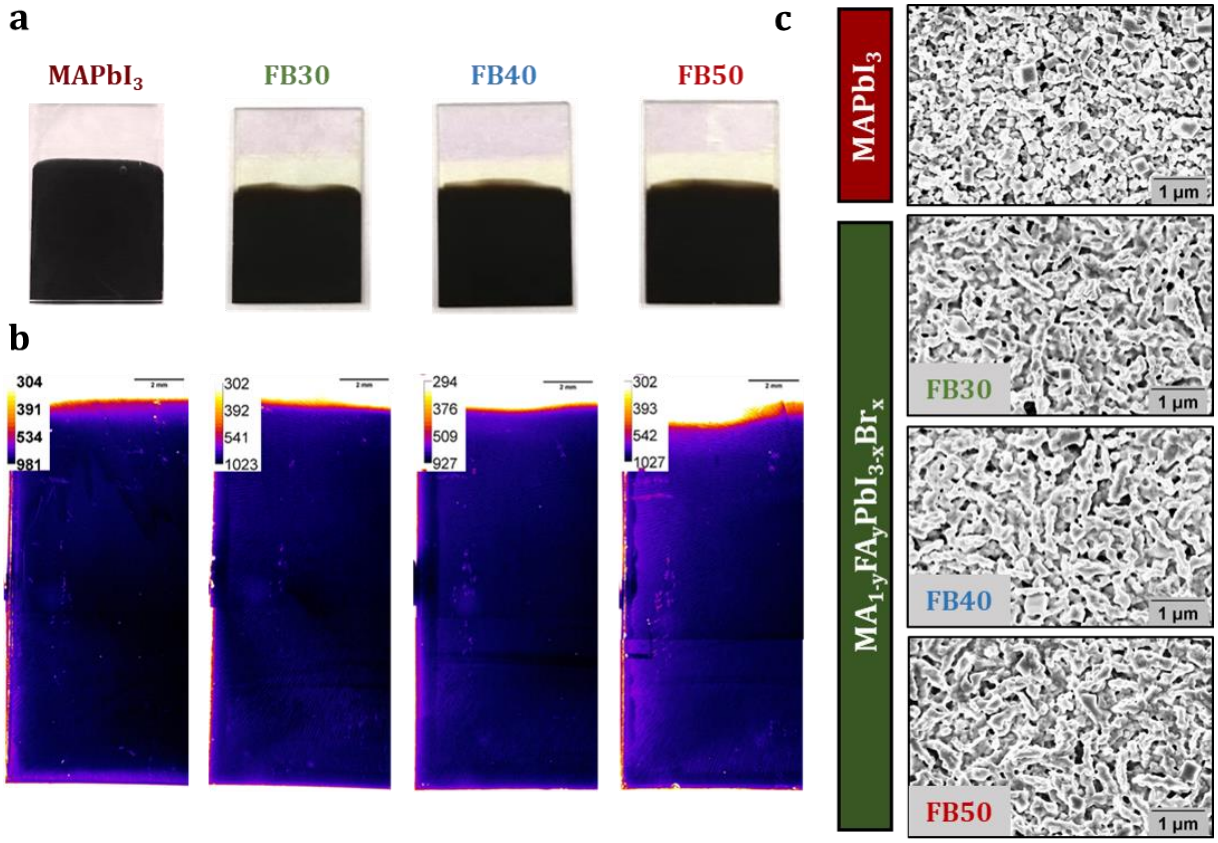

Figure 27: a) Photographs showing the appearance of the four obtained $MAPbI_3$ and $MA_{1-y}FA_yPbI_{3-x}Br_x$ films (2.5 x 1.7 cm^2), b) Local thicknesses of the four corresponding perovskite layers deposited on TiO_{2m} (the colored scale bar for thickness is in nm, and photo scale bar is 2 mm), and c) Top-view SEM images of $MAPbI_3$ and $MA_{1-y}FA_yPbI_{3-x}Br_x$ elaborated using four different conversion baths

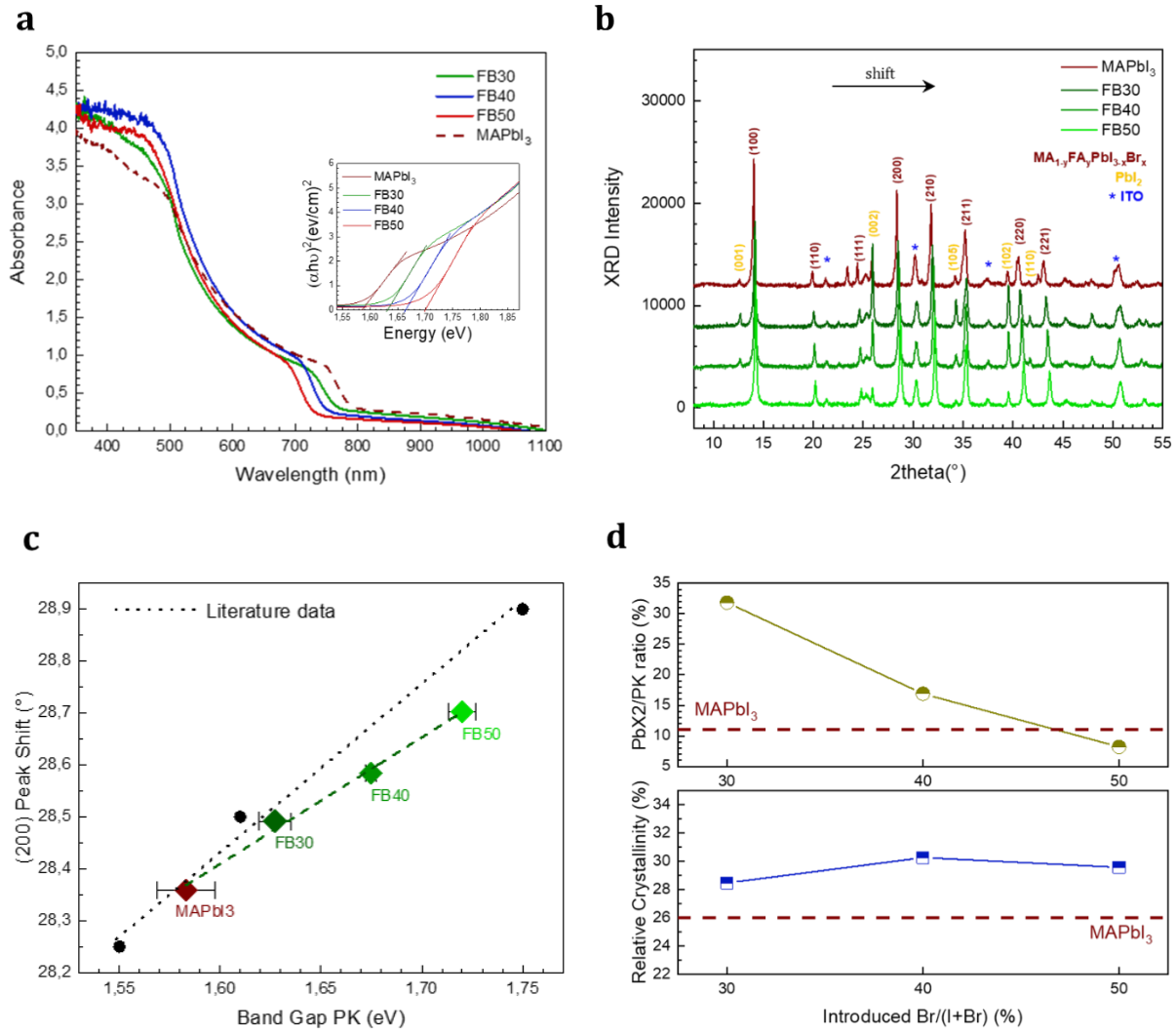

Figure 28: a) UV-visible absorption spectra of the four elaborated perovskite films along their Tauc plot in the inset, b) their XRD patterns, c) the XRD peak shift at 28° as a function of the Band Gap of the four elaborated perovskite films, d) the PbX_2/ PK ratio determined from XRD analyses, and the relative crystallinity as a function of the Br percentage present in the conversion solutions

UV-visible absorption spectroscopy and XRD analysis were conducted on the elaborated films to identify the obtained materials, and better understand their optical properties and their phase composition. UV-visible spectra presented in Figure 28-a show a band edge shifting from 780 to 750 nm when increasing the Br ratio, corresponding to the perovskite transition[316]. We also identify an onset at around 600 nm corresponding to the transition of PbI_6 octahedra (possibly PbX_6 in case of Br insertion, X= I or Br), which remains quite identical for all the samples. In fact, a systematic shift of the absorption band edge toward a shorter wavelength is usually detected when the Br content is increased in the perovskite composition[209,215,309,312]. However, increasing the FA ratio leads to a decrease is the band gap[13]. The absorption band edges were used to construct the Tauc plots and calculate the band gaps for the first transition. $MAPbI_3$ presents a band gap of 1.58 eV, while $MA_{1-y}FA_yPbI_{3-x}Br_x$ converted via FB30, FB40 and FB50 have band gaps of 1.63 eV, 1.68 eV, and 1.72 eV successively. Apparently, we notice a band gap increase when the Br content of the conversion solution is increased from 0% to 50% (from $MAPbI_3$ to FB30 to FB40 to FB50), Figure 28-c. As bromine is introduced by the way

of FABr, this indicates that the Br incorporation has a greater effect than FA on the optical properties of the perovskite film. By comparing the calculated band gaps on perovskites with variable FA and Br contents obtained by Jacobsson *et al.* [13], a band gap between 1.63 eV and 1.72 eV corresponds to a Br content between 15% and 30% and a FA content between 15% and 50% (reported in Figure 28-c as literature data).

$MAPbI_3$ spectrum in Figure 28-b represent a typical XRD pattern of tetragonal $MAPbI_3$[259], with double peaks and no preferred orientation. (002)(110), (112)(200), (211), (202) and (114)(222) phases appear at 14°, 20°, 23.5°, 24.5° and 31.6° relatively, along with others. We detect, however, a cubic $MAPbI_3$ pattern[259] for the $MA_{1-y}FA_yPbI_{3-x}Br_x$ perovskites converted via FB30, FB40 and FB50 (Zoomed pattern in Figure S19). Bi *et al.* already proved that the Br incorporation transferred the perovskite crystal from tetragonal to cubic structure[315]. Therefore, the observed results validate again the incorporation of Br inside the $MAPbI_3$ lattice, since no specific peaks for $FAPbI_3$, $FAPbBr_3$ or $MAPbBr_3$ are detected[309,313].

Furthermore, the XRD pattern encounters a shift toward higher theta for mixed perovskites, Figure S19. It also continue to shift in the same direction when we increase the Br ratio in the conversion solution (see data drawn for the (200) plane in function of the Band Gap in Figure 28-c, along with some literature data calculated by Jacobsson *et al.* [13]). A linear relation could be then detected between the band gap increase and the peak shift. This behavior also confirms the increase in Br content inside the perovskite lattice when increasing the Br percentage inside the conversion bath[13,309,313]. It was proven that the incorporation of FA^+ cations shifts the XRD pattern toward lower theta[13,317], which was not detected here since the shift due to Br was clearly predominant. This does not exclude the possibility of the presence of FA^+ in the elaborated mixed perovskites.

To confirm the FA presence inside elaborated perovskites, infrared spectroscopy was thus applied to the perovskites: in the 400 to 4000 cm^{-1} range to study the organic cation environment located at the center of the lattice (CH, NH, and CN bonds)[181], and therefore verify the presence of FA^+ ($CH(NH_2)_2$). We can clearly detect in the IR spectra presented in Figure S20 the C=N symmetric stretch at 1714 cm^{-1} and the NH_2 symmetric stretch at 3270 cm^{-1}, confirming the presence of FA^+ in the mixed perovskite[318,319].

To better understand the effect of the FA and Br presence in the perovskite lattice, the relative crystallinity and the PbX_2/PK percentages were finally calculated for the prepared films, as presented in Figure 28-d. The relative crystallinity of the $MA_{1-y}FA_yPbI_{3-x}Br_x$ perovskites is higher than that of $MAPbI_3$ and slightly increases when increasing the Br content in the conversion solution, while the PbX_2 ratio decreases. This also verifies the gradual infiltration of Br inside the perovskite lattice.

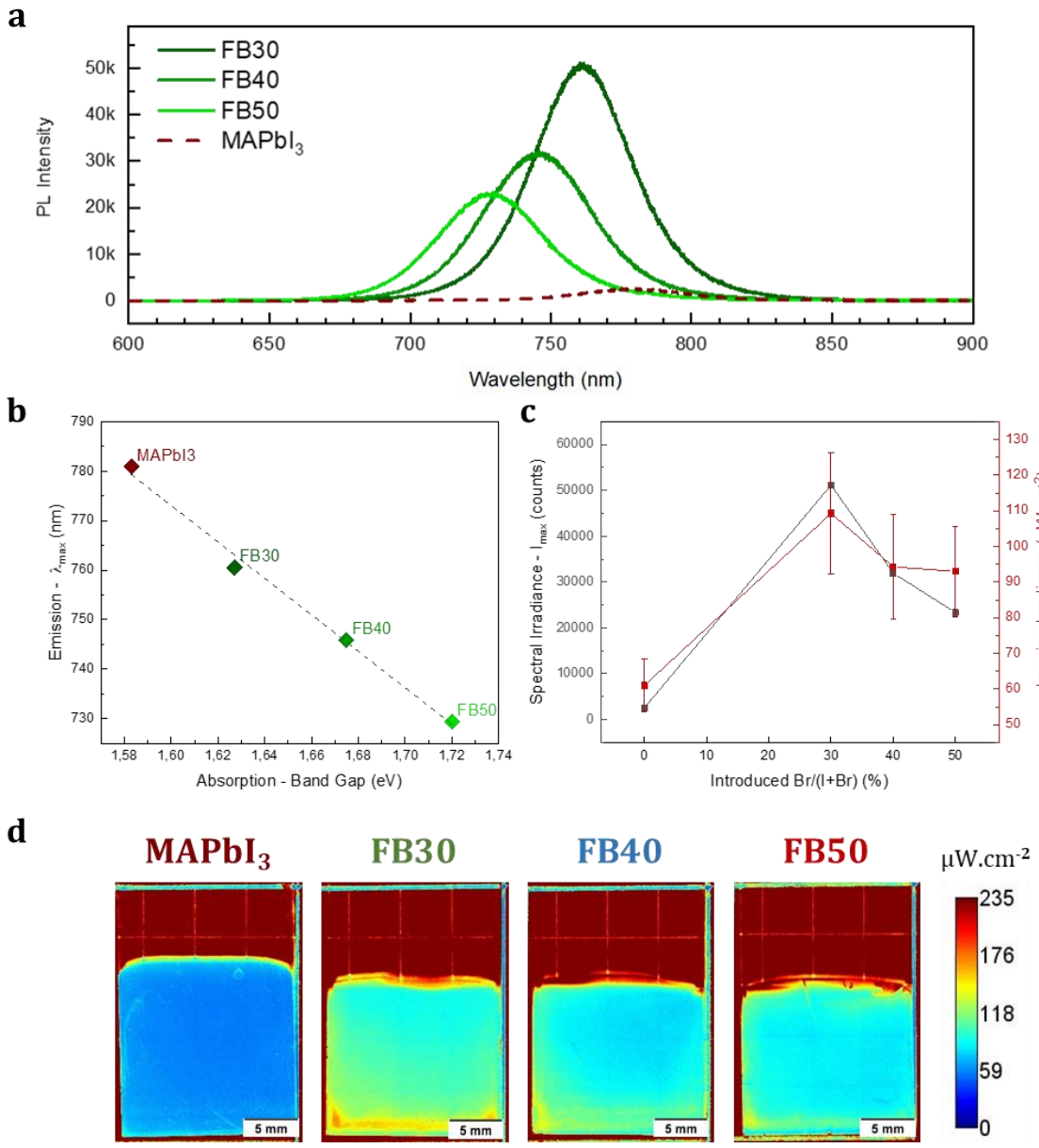

Figure 29: a) Photoluminescence spectra of the four elaborated films excited at 520 nm, b) the variation of λ_{max} as a function of the Band Gap when increasing the Br content in the conversion solution, c) the variation of I_{max} of the PL spectra and the average irradiance calculated from the PL images as a function of the Br percentage in the conversion solution, and d) the quantified PL images of the perovskite layers (the unit of calibration bar is µW·cm⁻²)

Photoluminescence spectroscopy was also conducted to investigate the emission properties of the developed perovskite films. Figure 29-a presents the PL spectra of the four different perovskites. As already detected in the UV-visible spectra, the perovskites undergo in PL spectroscopy a blue shift when incorporating and increasing the Br ratio. According to the literature, this relationship between absorption and emission is quite coherent [181,274]. The λ_{max} of emission is presented in function of the absorption band gap in Figure 29-b, and a linear relation could be thus detected when increasing the Br ratio in the conversion solution. Due to the blue shift, the wavelength at maximum emission intensity λ_{max} decreases from 760 to 755 nm when increasing the Br content in the perovskite crystal lattice. Such a behavior was expected since prior studies already

proved that the photoluminescence peak exhibits a blue shift when using Br anions in the perovskite and a less intense red shift when using FA cations[13].

The maximum PL spectral intensity I_{max}, affected by the radiative recombination, is then drawn in Figure 29-c as a function of the Br ratio in the conversion solution. We notice an increase in I_{max} when incorporating FA and Br in the perovskite lattice. It could be attributed to an increase of the grain size and of the crystal quality of the perovskite, which is in agreement with the SEM and XRD results [185,292].

PL imaging was then applied on the four samples to extract irradiance levels overall the surface of the electrodeposited perovskite layers and compare the homogeneity of the three different $MA_{1-y}FA_yPbI_{3-x}Br_x$ films with respect to the $MAPbI_3$ film. PL images are presented in Figure 29-d using an absolute quantification method developed in our lab[277,289], which allows a better comparison even when changing the acquisition parameters. The average radiant flux intensity is less homogenous overall the substrate for the mixed perovskite films, comparing to the $MAPbI_3$ film. The irradiance extracted from the PL images was traced in Figure 29-c, along with the spectral I_{max}, as a function of the Br percentage present in the conversion solution. A decrease in the average irradiance can be noticed when comparing the three mixed perovskites converted using FB30, FB40 and FB50. These results match the PL spectroscopy maximum intensities detected for the four evaluated samples.

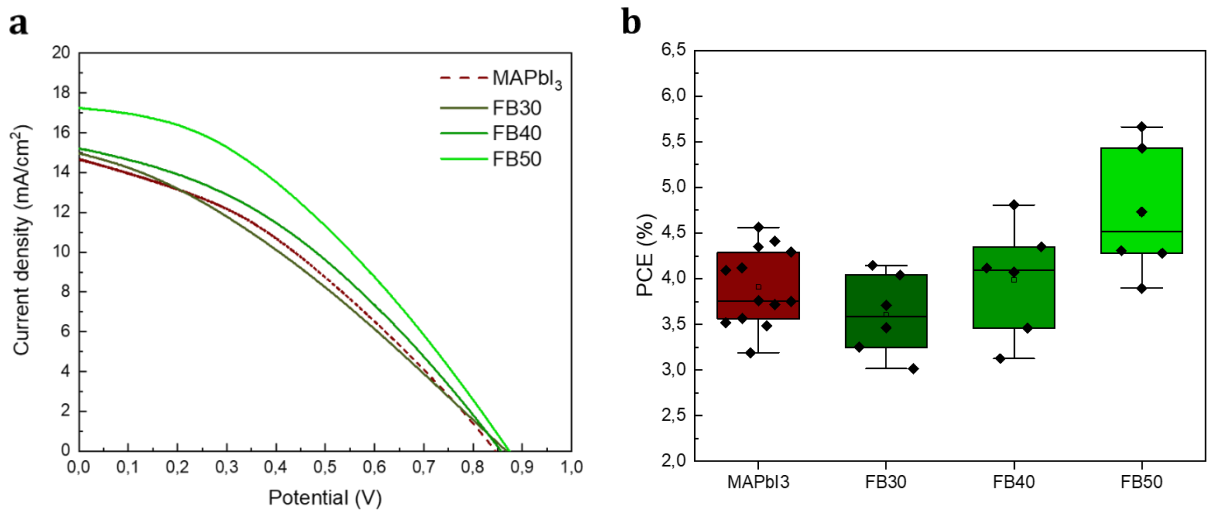

Figure 30: a) J(V) curves of the 3 electrodeposited solar devices elaborated using FB30, FB40 and FB50 comparing to that with electrodeposited $MAPbI_3$, and b) box plots showing their average PCE variation

To evaluate the photovoltaic performance of the developed electrodeposited perovskite active layers, we measured the J(V) curves of Glass/ITO/TiO_2c/TiO_2m/Perovskite/P3HT/C solar cells. The perovskite layer was either $MAPbI_3$ or $MA_{1-y}FA_yPbI_{3-x}Br_x$ converted with respectively MAI, FB30, FB40 and FB50 at 40°C, and the active surface of the presented solar devices is 0.14 cm^2. In literature, spin-coating based formamidinium based perovskites were proven to provide better photovoltaic activity than methylammonium ones because of their broader absorption of the solar spectrum[210]. Nevertheless, doping with Br usually lowers the efficiency of the PSCs, because of the consequent increase in the band gap, which results in a decrease of

the J_{sc}[210,215,285,309]. It has been proven however, that increasing Br content in an iodine-based perovskite achieves high V_{oc} under low-intensity ambient light sources[312,320]. Therefore, the improvement in the PCE cannot be considered as definite for the here electrodeposited elaborated mixed perovskites, and it is important to verify whether using $MA_{1-y}FA_yPbI_{3-x}Br_x$ enhances or not the efficiency of the solar device. Figure 30-a presents the J(V) curves of the 3 electrodeposited solar devices elaborated using FB30, FB40 and FB50 comparing to that with electrodeposited $MAPbI_3$. The average corresponding parameters are drawn in Figure S21. When comparing FB30 to $MAPbI_3$, we notice that both solar devices present the same J_{sc}, with a slightly better FF for $MAPbI_3$, and a slightly better V_{oc} for FB30. This explains the enhancement in the average PCE of $MAPbI_3$ comparing to FB30 in Figure 30-b. For FB40, it offers a slightly better average PCE than $MAPbI_3$ due to a small increase in its J_{sc} and V_{oc}, and the best PCE is that of FB50 having the highest J_{sc}. We deduce that increasing the FABr percentage in the conversion bath engenders an increase in the V_{oc}, the J_{sc} and the FF, leading to a PCE enhancement. This is probably due to an increase of the FA content in the perovskite, as previously explained.

We also studied the effect of the variation of the active surface on the performances of the cells elaborated using electrodeposited $MA_{1-y}FA_yPbI_{3-x}Br_x$, as presented in Figure S22. We notice a decrease of the FF, J_{sc} and V_{oc} when increasing the active surface. This results in a decrease of the PCE for the three solar devices. This decrease seems to be more important when increasing the Br ratio in the active layer.

In addition to the PCE enhancement that electrodeposited $MA_{1-y}FA_yPbI_{3-x}Br_x$(FB50) delivers comparing to electrodeposited $MAPbI_3$, it seems also relevant to verify the impact on stability. Indeed, Lim et al. proved that a substitution by Br increases the stability of the conventional perovskite by forming a pseudo-cubic phase[320]. For that, we studied the aging of our four different perovskites types with the help of both full cells and half-cells. Their architecture of the latter was as follows: Glass/ITO/TiO_{2c}/TiO_{2m}/Perovskite. Applied conditions were: 40°C, either under ambient atmosphere (R.H. = 20%, noted **"a"**) or under vacuum (noted **"v"**) for 500h. The following figures present the photovoltaic parameters evolution during conducted ageing campaigns.

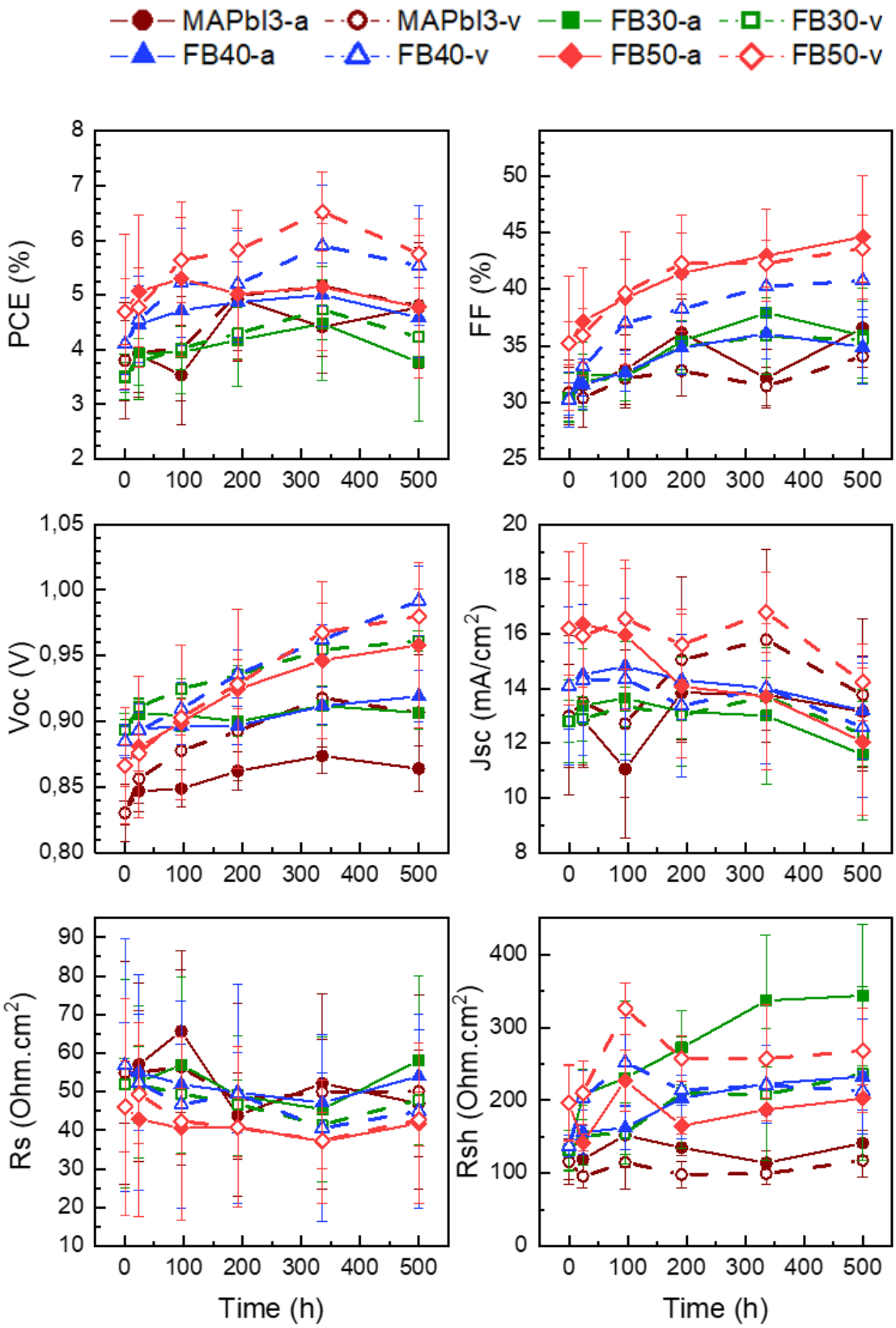

Figure 31: a) PCE, FF, V_{oc}, J_{sc}, R_s and R_{sh} variation with time for the four electrodeposited solar cells aged at 40°C either at ambient atmosphere or under vacuum

The photocurrent density-voltage measurements J(V) of the electrodeposited solar cells was recorded during aging to detect the variation of their photovoltaic performance. Figure 31 shows the variation with time of the power conversion efficiency PCE, the fill factor FF, the short circuit current density J_{sc}, the open circuit voltage V_{oc}, the series resistance R_s, and the shunt resistance R_{sh}, for the aged solar devices. Whether aged under vacuum or in ambient atmosphere, all types of solar devices first display an increase of their PCE with time, until reaching 350 h. This highlights a first step of maturation phenomenon. However, the maturation is more important for the devices aged under vacuum than in ambient atmosphere, since they do not endure the same competitive degradation phenomenon. The solar device elaborated using FB50 and aged under vacuum reached the highest PCE after 350h, consequently upgraded from 4.7% to 6.5%. The FB40-based PSCs come next with a PCE reaching 5.5%, then the ones with $MAPbI_3$ as an active layer with a PCE of 5%, followed finally by the FB30-based PSCs reaching a PCE of 4.5%. Nevertheless, after 350 h of ageing, all the elaborated PSCs start to endure a decrease in their efficiency. We notice that the PCE decrease is due to the decrease of the J_{sc}, since the V_{oc} and FF still manifest an increase in their values. This mainly indicates an increase in the defects in the active layer or at the interfaces between the layers, probably due to the important presence of PbX_2 after degradation. In parallel, when exploring the variation of the V_{oc} with time, we notice a continuous increase of the V_{oc} over the time, independent from the variation of the J_{sc} or the FF. It reaches a mean value going from 0.88V to 0.99 V for FB40-based solar devices aged under vacuum. A variation of the V_{oc} could plausibly originate from a variation in the energy levels of the materials constructing the solar cell. However, in our case, it derives from an enhancement in the quality of the layers that minimizes the recombination, since it is assisted by a FF increase. The fill factor went from 35% to 50% for the FB50-based PSCs after 500 h. These results help us deduce that the elaborated perovskites are rather robust. For the samples aged under vacuum, during the 350 h of maturation, PCE enhancement reached 40% for FB50 and FB40, 30% for FB30, and 35% for $MAPbI_3$, comparing to their initial PCE value.

To better understand the observed maturation mechanism, half-cells were also aged under the same aging conditions and nondestructive characterizations were then applied at different sampling times. It must be noted however that the degradation for the half-cells is faster than for the cells, since these latter contain P3HT and carbon upper layers acting as protective layers and slowing down the potential degradation. The following figures present the evolution of their optical characteristics during the ageing campaigns.

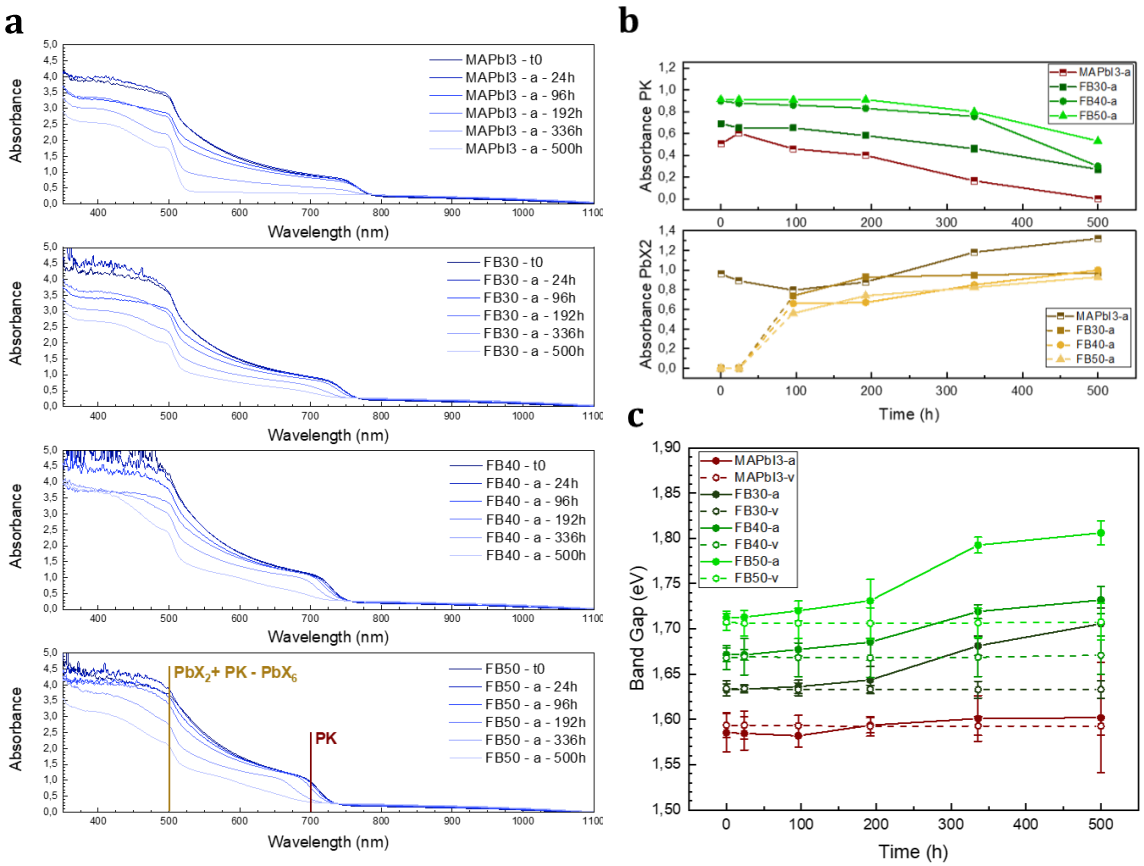

Figure 32: The variation with time of a) the UV-visible absorption spectra for the four different half-cells aged at ambient atmosphere, b) the absorbance difference for the perovskite and the PbX_2 band-edges for the four samples aged at ambient atmosphere (PbX_2 band-edges being superimposed with PbX_6 octahedra of perovskite), and c) the Band Gap of the perovskite for the four different half-cells aged under ambient atmosphere or vacuum,

First, we studied the variation of the UV-visible absorption spectra for the four half-cells aged in ambient atmosphere and under vacuum. We can first deduce that the effect on the electrodeposited perovskites of temperature with oxygen and/or humidity is more remarkable than the effect of sole temperature, since the ageing under vacuum at 40°C did not degrade the perovskite (presented in Figure S23). However, when aged in ambient atmosphere, as presented in Figure 32-a, we notice a decrease in the absorbance of the four band edges situated around 700-780 nm. The formation of PbX_2 (potential mix/intermediate between PbI_2 and $PbBr_2$) is then indicated by the increase of the band edge at about 500nm, which confirms the progressive degradation of the perovskite samples[296]. We thus quantified the transformation of perovskite into PbX_2 for the samples aged in ambient atmosphere, by calculating an estimated absorption for both perovskite and PbX_2 equal to the absorption differences between the maximum and minimum points of each band edge. The results are presented in Figure 32-b. $MAPbI_3$ shows the most important degradation with time, with the most important decrease of PK and increase in PbX_2. The degradation rate of $MA_{1-y}FA_yPbI_{3-x}Br_x$ perovskites decreases when increasing the Br and/or FA content in the lattice. Although the absorption intensity for PbX_2 is not detected for the first two points due to the saturation of the spectrometer detectors (notified using dotted lines on corresponding curves), it increases with time and reaches close level at 500 h for the three $MA_{1-y}FA_yPbI_{3-x}Br_x$ samples.

Using the Tauc plots drawn from the UV-visible spectra's data, the band gap of the different perovskites were calculated and Figure 32-c presents their variation with ageing time under both vacuum and air conditions. No notable change in the band gaps was detected for all the samples aged under vacuum. When aged in ambient atmosphere, $MAPbI_3$ and the three $MA_{1-y}FA_yPbI_{3-x}Br_x$ samples encounter a progressive increase in their optical band gaps. This indicates the degradation of the perovskites. The observed blue shift should mainly indicate a grain size decrease for $MAPbI_3$ perovskite[274], but can also indicate a chemical composition change for $MA_{1-y}FA_yPbI_{3-x}Br_x$ perovskites (richer in Br and/or MA)[13,312].

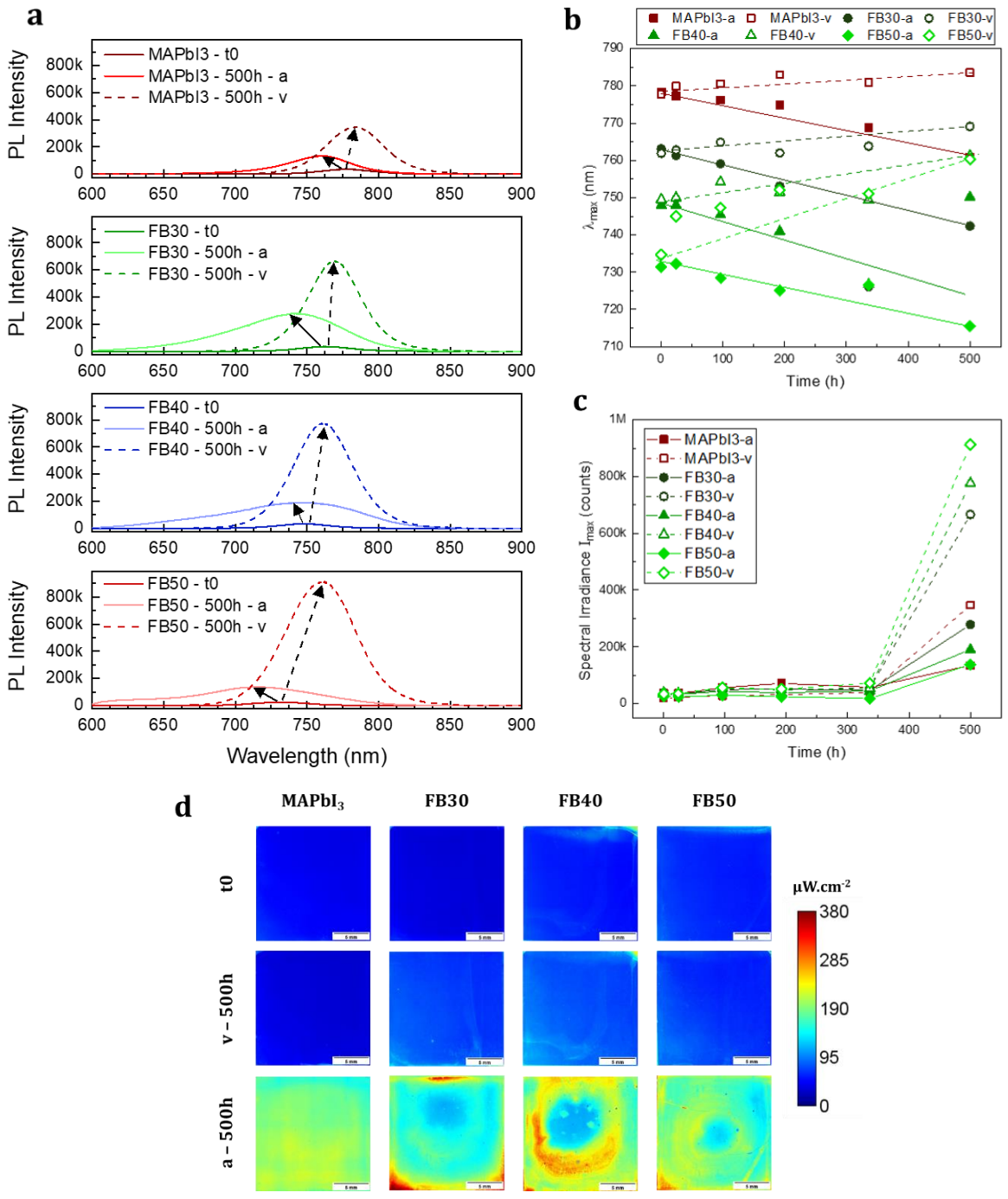

Figure 33: The variation with time of a) the photoluminescence spectra for the four half-cells aged in ambient atmosphere and under vacuum b) λ_{max} and c) I_{max} extracted from the PL spectra for the four half-cells aged in ambient atmosphere or

under vacuum, d) Photoluminescence images showing the variation of the irradiance (the unit of calibration bar is μW·cm⁻²) for the four half-cells after 500h of ageing under vacuum or at ambient atmosphere (scale bar: 5 mm)

Detecting the emitted photons with photoluminescence spectroscopy also helped us tracking the ageing of perovskite with time. The emission wavelength gives information about the energy of the recombined electron–hole pairs, and the luminescence intensity about the quantity of radiative recombination[298]. The variations of the PL spectra of all sampling points are presented in Figure S24. The corresponding PL spectra at t0 and 500h for samples aged either under ambient atmosphere or vacuum are drawn in Figure 33-a. To better interpret these results, the λ_{max} and I_{max} emission values were extracted from and their variation is drawn as a function of ageing time in Figure 33-b and Figure 33-c. Despite the fact that they did not show strong degradation in their UV-visible spectra, all the samples aged under vacuum exhibit a red shift in the PL spectroscopy (more pronounced when increasing the Br ratio). This shift cannot be attributed to a variation in their optical band gap since it was proven to remain intact in this case. From literature, an emission red shift is not necessary associated with an absorption red shift. Tabuchi *et al.* mentioned that it can also come from a decrease in the quantum confinement effect because of the expansion of the exciton Bohr radius, which causes a decrease in exciton binding energy[299]. While Liu *et al.* attributed the red shift to atomic distortion[300], Hong *et al.* mentioned that among the reasons of red shift for perovskite[301], we can have inclusion of a different crystal phase[302–304], atmosphere effect[297,305,306], reabsorption effects[307], or radiative recombination involving shallow trapping levels[308]. All the mentioned reasons could be a sign of the beneficial maturation of the perovskite samples. To the contrary, an emission blue shift is deduced from the decrease of λ_{max} for all the samples aged under ambient atmosphere. This emission blue shift is compatible with the absorption blue shift already detected with UV-visible spectroscopy under air ageing conditions.

In parallel, the luminescence intensity gives an idea about the quantity of the radiative recombination in the aged perovskites. The maximum intensity of the PL spectra I_{max} was found to increase more under vacuum than under air, and become more and more important when the Br ratio is increased. According to previous results (PCE increase, quite stable absorption), this increase in PL could be due to a decrease in the defects inside the perovskite layers, so charge carriers reach less non-radiative recombination centers and instead recombine radiatively[291]. In addition, according to the literature, an increase in the maximum PL intensity could also be attributed to an increase of the grain size and the crystal quality of the perovskite[185,292]. These PL results confirm that both $MAPbI_3$ and $MA_{1-y}FA_yPbI_{3-x}Br_x$ materials aged under vacuum exhibit a maturation process.

Regarding perovskite half-cells aged in ambient atmosphere, the expansion of spectral PL intensity reaches values 2 to 6 times less important. This, combined with the blue shift observed both in absorption and emission, confirms here the large participation of a competitive degradation mechanism due to additional oxygen/humidity stress.

In addition to the previously applied characterizations, PL imaging was performed to visualize irradiance levels overall the surface and compare the homogeneity of the different electrodeposited generated films[277]. Figure 33-d presents the PL images of the four perovskite samples at time t0 and after 500h ageing, whether aged under ambient atmosphere or vacuum. We can see a slight increase in the irradiance for the samples aged

under vacuum. These results are correlated to the PL spectroscopy maximum intensities that undergo the same increase, associated with a maturation of the perovskites. On the other hand, the drastic increase in irradiance observed on imaging for samples aged in ambient atmosphere, and not observed in a such huge intensity from spectral PL data, indicates the degradation of the perovskite. Indeed, we can clearly detect the presence of PbI_2 in the photographs in Figure S25 ($PbBr_2$ being uncoloured). The imaging irradiance level detected in this case is not only a response of the perovskite, but also a residual part of diffuse reflection of the 520 nm beam on the PbI_2 that does not absorb this wavelength (see PbI_2 PL imaging in Figure S26). This degradation starts from the borders and gradually propagates to the center (check Figure S26). The PL images also confirm that electrodeposited $MA_{1-y}FA_yPbI_{3-x}Br_x$ perovskites are more stable than electrodeposited $MAPbI_3$ and the stability is enhanced when we increase the Br ratio. This was also noticed in the UV-visible spectroscopy where the absorption difference for PbI_2 reaches the same level after 500h for the three $MA_{1-y}FA_yPbI_{3-x}Br_x$ samples, but that of PK remains more important for a higher FABr proportion, leading to a PK/PbX_2 ratio increasing when increasing the Br percentage .

Conclusion

In this work, an alternative deposition method for perovskites was explored, by electrodepositing PbO_2 and converting it into perovskite. The electrodeposition of $MAPbI_3$ perovskite as well as $MA_{1-y}FA_yPbI_{3-x}Br_x$ mixed perovskites was studied, while variating the ratio of Br and FA infiltrated in the perovskite lattice. The advantages of such mixed perovskites lie in their tunable bandgap and their enhanced stability[311,315,321]. The impact of bromine percentage on the microstructural, morphological and functional properties of these perovskite layers was studied by SEM imaging, UV-visible absorption, X-Ray diffraction, photoluminescence spectroscopy and imaging. A composition modification of the obtained perovskite material is noticed when variating the ratio variation of each mixture. Increasing the Br ratio in the conversion solution increases its infiltration in the perovskite lattice and decreases the PbI_2 presence. The photovoltaic performances of the elaborated $MAPbI_3$ and $MA_{1-y}FA_yPbI_{3-x}Br_x$ perovskites were then compared in a solar device. The electrodeposited mixed perovskites offer a PCE enhancement, with an average PCE going from of 3.7% to 5% instead of 4% with electrodeposited $MAPbI_3$ for a 0.14 cm^2 PSC. Furthermore, their stability was investigated in complete solar cells or half-cells when aged at 40°C under vacuum or in ambient atmosphere, and compared to that of $MAPbI_3$. The electrodeposited PSCs are subject to maturation when aged in the as-mentioned conditions, with a PCE improvement of 40% for $MA_{1-y}FA_yPbI_{3-x}Br_x$ and 35% for $MAPbI_3$ after 350 h of ageing under vacuum. From the collected results, we note that the incorporation of Br and FA in the perovskite lattice not only enhances its photovoltaic performance but also offers a remarkable stability.

Experimental section

Materials and chemicals

ITOGLASS 07P ITO-coated glass slides (2.5 × 1.7 cm^2) were purchased from Visiontek Systems. The reagent chemicals used are as follow: lead(II) acetate trihydrate

$Pb(CH_3COO)_2.3H_2O$ (Sigma-Aldrich, 99%), sodium nitrate $NaNO_3$ (Sigma-Aldrich, ≥ 99%), methylammonium iodide CH_3NH_3I (MAI) and formamidinium bromide $CH(NH_2)_2Br$ (FABr) (Greatcell Solar), and hydrogen iodide HI (57 wt% in H_2O, stabilized 99.95%, Sigma-Aldrich). pH adjustments were done using nitric acid (65%, AnalaR NORMAPUR, VWR Chemicals). Ti-Nanoxide BL/SC for the compact TiO_2 and Ti-Nanoxide T600/SC for the mesoporous TiO_2 were purchased from Solaronix. The carbon paste applied was the DN-CP01 from Dyenamo. Regioregular poly(3-hexylthiophene-2,5-diyl) P3HT (#4002-E, Rieke Metals) was used for the HTL precursor solution, with chlorobenzene (Sigma-Aldrich, anhydrous, 99.8%) as the solvent. The isopropanol and ethanol used in the conversion bath were anhydrous (Sigma-Aldrich, 99.5%). All aqueous solutions were prepared using 18 MΩ. cm resistivity water from a Millipore Milli-Q system.

Substrates preparation and ETL deposition

The ITO substrates were first ultrasonically cleaned with acetone, isopropanol, and deionized water in sequence. They were then subjected to UV-O_3 treatment for 30 min before each deposition.

TiO_2 compact-mesoporous ETL (TiO_{2m}) was deposited on ITO using spin coating. First, 50µL of the Ti-Nanoxide BL/SC solution was dropped on the substrate while starting the spinning. Conditions were set at 33 rps for 1 s, then 83 rps for 30s. The compact TiO_2 coated substrate was then sintered at 550 °C for 1h. The resulting compact layer, also called blocking layer has a thickness of around 65 nm. The Ti-Nanoxide T600/SC is a solution for the formation of 600 nm thick mesoporous titania layers. However, the optimized thickness of TiO_2 scaffold is around 450 nm [22], so the as-mentioned precursor solution was diluted with 0.4 mL of ethanol for each 1 mL. The obtained solution was spin coated using the same conditions as for the blocking layer, and then sintered at 475°C for 30 min. The mesoscopic structure obtained by the sintering of nano-particles in the process makes a perfect host for perovskite crystals.

Electrodeposition of PbO_2 films

An aqueous solution containing 0.025 M lead(II) acetate trihydrate and 0.05 M sodium nitrate served as an electrodeposition (ED) bath for PbO_2 films. The pH adjustments until having a pH of 5.5 were done with nitric acid. ED was performed without stirring at ambient temperature with a Biologic SP-150 potentiostat and a three-electrode arrangement. ITO substrates or ITO/TiO_{2m} substrates acted as working electrodes (after being UV-O_3 treated), with an active deposition area of 2.55 cm^2 (1.5 × 1.7 cm^2). A spring-shaped platinum electrode was used as the counter electrode and an Ag/AgCl/KCl_{sat} electrode as the reference electrode. The electrodeposition was carried out at a potential of 1.5 V versus the reference electrode for a deposition duration of 50s (Reaction 0). A brownish color appears indicating the formation of PbO_2. The obtained substrates were then rinsed with pure ethanol before conversion into PbI_2, to eliminate any hydration.

$Pb^{2+} + 2\ H_2O \rightarrow PbO_2 + 4\ H^+ + 2\ e^-$ Reaction 0

Conversion of PbO_2 into PbI_2

Conversion of PbO_2 to PbI_2 was carried out at ambient temperature in a petri dish. The substrate was immersed in a 0.05M HI - ethanol solution for 3 min. A change of color from brown to yellow indicates the conversion of PbO_2 into PbI_2 films (Reaction 1). The samples were rinsed with ethanol and then dried with N_2 before keeping them in a vacuum desiccator to avoid any hydration.

$PbO_2 + 4\ HI \rightarrow PbI_2 + 2\ H_2O + I_2$ Reaction 1

Conversion of PbI_2 into $CH_3NH_3PbI_3$ or $(CH_3NH_3)_{1-y}(CH(NH_2)_2)_yPbI_{3-x}Br_x$

Conversion of PbI_2 into $MAPbI_3$ was carried out in a petri dish containing a 0.1M MAI - isopropanol solution, preheated at 40°C. To convert into $MA_{1-y}FA_yPbI_{3-x}Br_x$, the conversion solution consisted of a mixture of MAI and FABr in isopropanol. This conversion was also carried out at 40°C for three different Br/(I+Br) solution ratios (30%-FB30, 40%-FB40 and 50%-FB50). The substrate was immersed in the solution for 3 min, before rinsing it with isopropanol and then drying it with N_2. When converting PbI_2, the color changes from yellow to brownish black in a few seconds, which indicates the formation of $MAPbI_3$ perovskite (Reaction 2-a), and to a slightly lighter brownish black for $MA_{1-y}FA_yPbI_{3-x}Br_x$ (Reaction 2-b). The samples were kept in a vacuum desiccator to avoid any hydration.

$PbI_2(s) + z\ CH_3NH_3I \rightarrow CH_3NH_3PbI_3(s)$ + "residual CH_3NH_3I" Reaction 2-a

$PbI_2(s) + (1\text{-}z)\ CH_3NH_3I + z\ CH(NH_2)_2Br \rightarrow (CH_3NH_3)_{1-y}(CH(NH_2)_2)_yPbI_{3-x}Br_x(s)$ + "residual ammonium and amidinium halides" Reaction 2-b

HTL deposition

For the deposition of the HTL layer, a 15 mg/mL P3HT in chlorobenzene solution was spin coated on the perovskite at 10 rps for 5s, then 15rps for 60s. These conditions led to a 50 nm thick P3HT layer.

Carbon paste deposition

Finally, a low temperature Dyenamo commercial carbon paste was deposited on the stack using doctor-blading technique. Each substrate formed six different cells with an active surface of around 0.2 cm^2. The final sample was then annealed at 120°C under vacuum, for 2h. This will not only dry the carbon paste and evaporate its solvents, but also help the connection at the interfaces inside the solar cell.

Ageing

We studied first the ageing of two different types of solar cells with the following architecture: Glass/ITO/TiO_2c/TiO_2m/Perovskite/P3HT/Cp, then of the corresponding half-cells: Glass/ITO/TiO_2c/TiO_2m/Perovskite, the perovskite being either $MAPbI_3$ or $MA_{1-y}FA_yPbI_{3-x}Br_x$ converted either in FB30, FB40 or FB50. The stability of the following devices was tested at 40°C, either under ambient atmosphere (R.H. = 20%, noted **"a"**) or under vacuum (noted **"v"**), for 500h. Nondestructive characterizations were applied at different sampling times in order to elucidate occurring mechanisms. For each type of solar device, the test was elaborated on two substrates containing 6 solar cells each (12 solar cells in total for each type).

Characterizations

Photovoltaic performances and ageing study, depositions and characterizations were realized on Glass/ITO/TiO_{2c}/TiO_{2m} substrates. The thickness and roughness of all layers (except perovskite) were measured using the Alpha-Step D-500 stylus profiler, and calculating the mean value of five measurements from distinct positions across the film. Leica DMLS Optical Microscope was used to examine the surface of perovskite samples and deduce the gray scale used for Combessis *et al.* calculations[275], allowing an estimation of perovskite thickness. The morphology of the perovskite films was studied by scanning electron microscopy (SEM) using FEG ZEISS Ultra 55. The structure and texture of the films were determined with a *PANalytical X'Pert PRO MPD X-Ray diffractometer* using Cu-Ka source. Match! and DIFFRAC.EVA softwares were used to identify the phases and determine the lattice parameters. Absorption measurements in the UV−visible range were performed with a Shimadzu UV-2600 spectrophotometer coupled with an integrating sphere, in the 300-1100 nm range, with a Glass/ITO substrate as a reference. Optical band gaps were calculated from Tauc plots drawn using the absorbance data. PL spectra were acquired over the 600− 900 nm range on a Shimadzu RF-6000 spectro fluorophotometer with a 520 nm excitation wavelength. Two filters were used: a 575 nm low-pass in front of the excitation source and a 600 nm high-pass in front of the source of emission in order to suppress any artifact coming from the spectrophotometer. Chosen measurement conditions were a scan rate of 6000 nm/min, an excitation slit of 5 nm, and an emission slit of 5 nm. Luminescence imaging experiments were performed with a homemade device composed of an opaque chamber with a camera placed 30 cm above the samples and two green light-emitting diode (LED) arrays with emission spectrum between 400 and 550 nm. A 650 nm high-pass filter from Edmund Optics (York, UK) was added in order to allow for spectral resolution in the setup and to minimize reflection from the excitation LEDs. Full PSC devices were observed in the open-circuit condition. The acquisition time was set close to 1000 ms with an aperture equal to 16. As the resulting signal varied depending on acquisition conditions (time, opening, filter type), not allowing for a direct quantitative comparison of the evolutions observed, a calibration reported in a previous publication allowing for image correction was employed[277]. Any additional image treatment (cropping, colorization, or thresholding) was performed with the ImageJ freeware. A standard simulated AM1.5G irradiation system with a 100W ozone free xenon-lamp solar simulator (Oriel LSC-100) was used for solar cell tests. The photocurrent density−voltage (J−V characteristics) measurements of the devices were recorded using a BioLogic-SP300 source with a scan going from +1 to −0.2 V and a scan rate of 40 mV/s. The fill factor FF, short-circuit current J_{sc}, open-circuit voltage V_{oc}, power conversion efficiency PCE, shunt resistance R_{sh} and series resistance R_s parameters were then deduced from J(V) measurements, using a home-made program on Spyder software.

Acknowledgments

Authors thank I-MEP2 doctoral school for the MESR PhD grant (M.A.K.) attribution, and the platform of Consortium des Moyens Technologiques Communs (CMTC) of Grenoble INP for laboratory assistance and laboratory equipment. This work has been partially funded by the EU Framework Program for Research and Innovation HORIZON 2020 (Cofund ERA-NET Action, N° 691664). This work has also been partially funded by the

“PROPER” project supported by “EIG Concert Japan” and financed from the French National Centre for Scientific Research under the funding number “IRUEC 222437”.

Supplementary Information

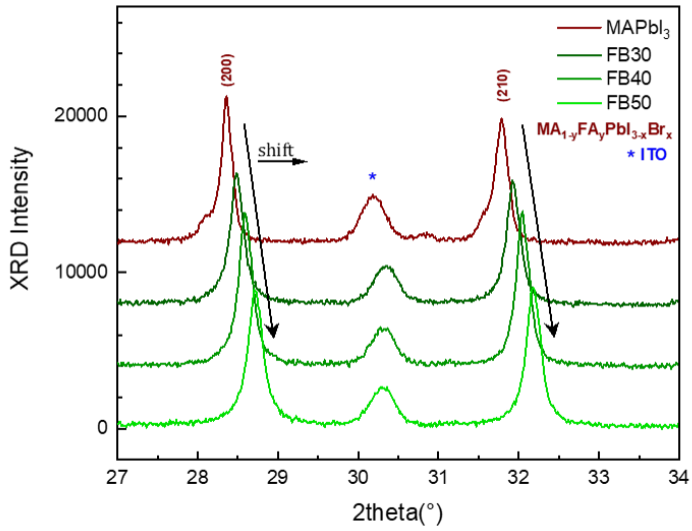

Figure S19: Zoomed XRD pattern of the three elaborated $MA_{1-y}FA_yPbI_{3-x}Br_x$ films showing the shift of the perovskite peaks versus pure $MAPbI_3$ peaks

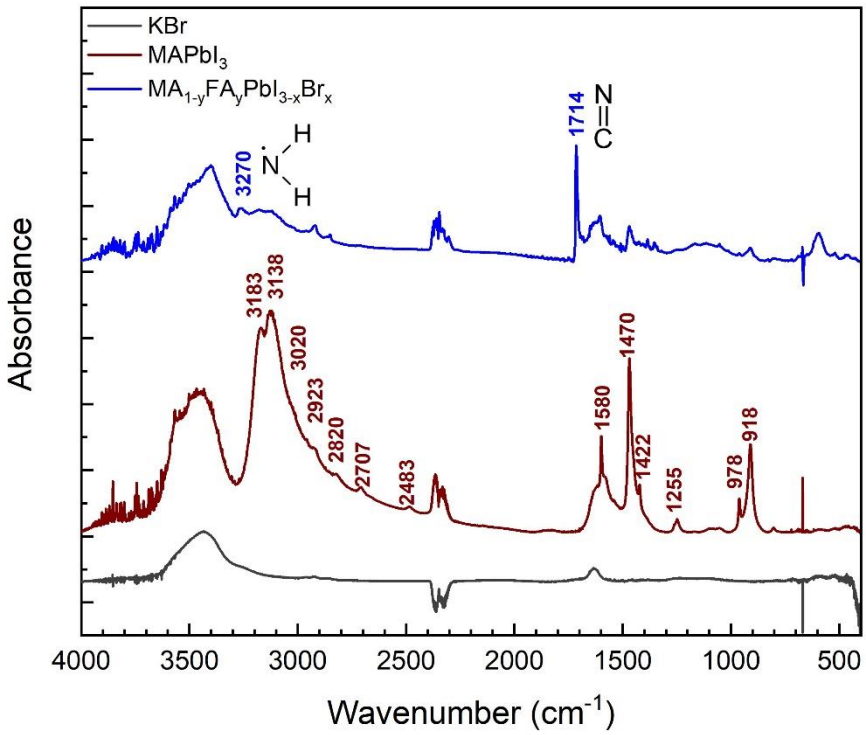

Figure S20: The FTIR spectra of the $MA_{1-y}FA_yPbI_{3-x}Br_x$ film (FB40 as example) compared to the $MAPbI_3$ film, confirming the presence of FA in the lattice

	Peak (cm^{-1})	Assignment
$MAPbI_3$	918	CH_3-NH_3^+ rock
	978	C-N stretch
	1255	CH_3-NH_3^+ rock
	1422	CH_3 asym. bend
	1470	NH_3^+ sym. bend
	1580	NH_3^+ asym. bend
	2483	2 x CH_3-NH_3^+ rock
	2707	NH_3^+ sym. bend + CH3-NH_3^+ rock
	2820	NH_3^+ asym. bend + CH_3-NH_3^+ rock
	2923	CH_3 sym. stretch
	3020	CH_3 asym. stretch
	3138	NH_3^+ sym. stretch
	3183	NH_3^+ asym. stretch
$MA_{1-y}FA_yPbI_{3-x}Br_x$	1714	C=N sym. stretch
	3270	NH_2 sym. stretch

Table S5: Infrared measured Resonance Frequencies of Vibrational Modes with Peak Assignments for the $MAPbI_3$ and additional peaks detected for $MA_{1-y}FA_yPbI_{3-x}Br_x$ film

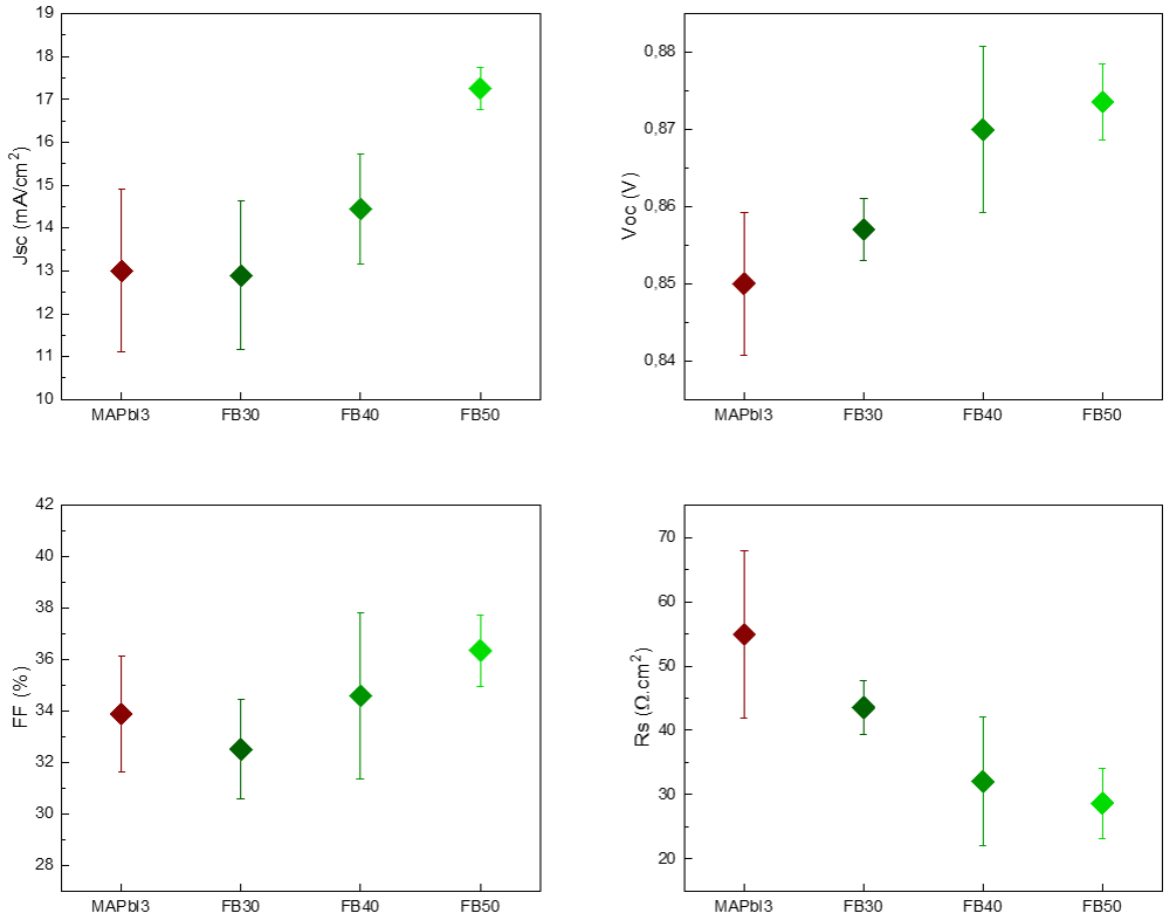

Figure S21: J_{sc}, V_{oc}, FF and R_s variation of the 3 electrodeposited solar devices elaborated using FB30, FB40 and FB50 comparing to that with electrodeposited $MAPbI_3$

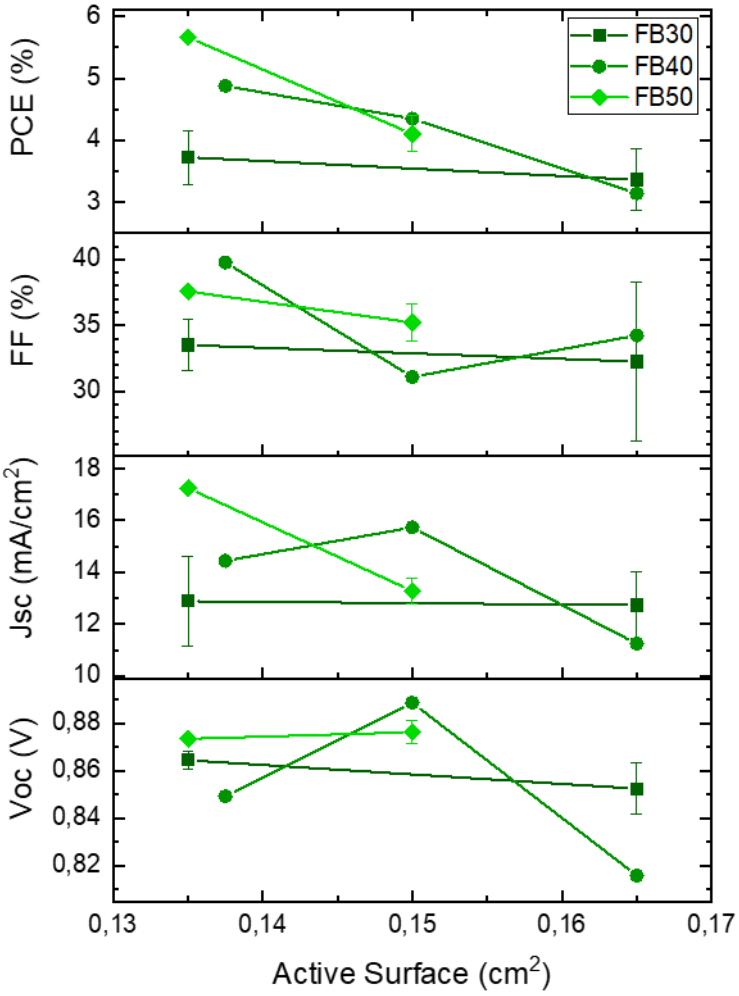

Figure S22: PCE, FF, J_{sc} and V_{oc} variation of the three $MA_{1-y}FA_yPbI_{3-x}Br_x$-based solar devices as a function of the device active surface

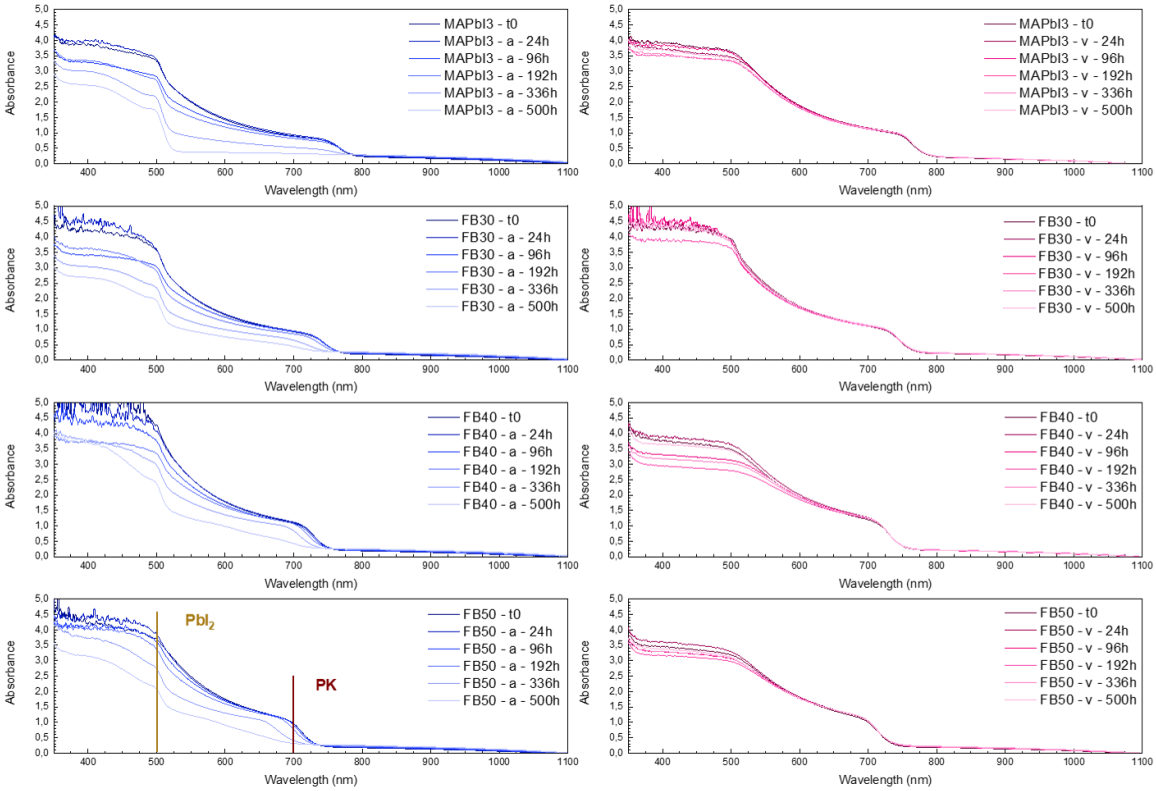

Figure S23: The evolution with time of the UV-visible absorption spectra for the four different half-cells aged at 40°C under ambient atmosphere or vacuum

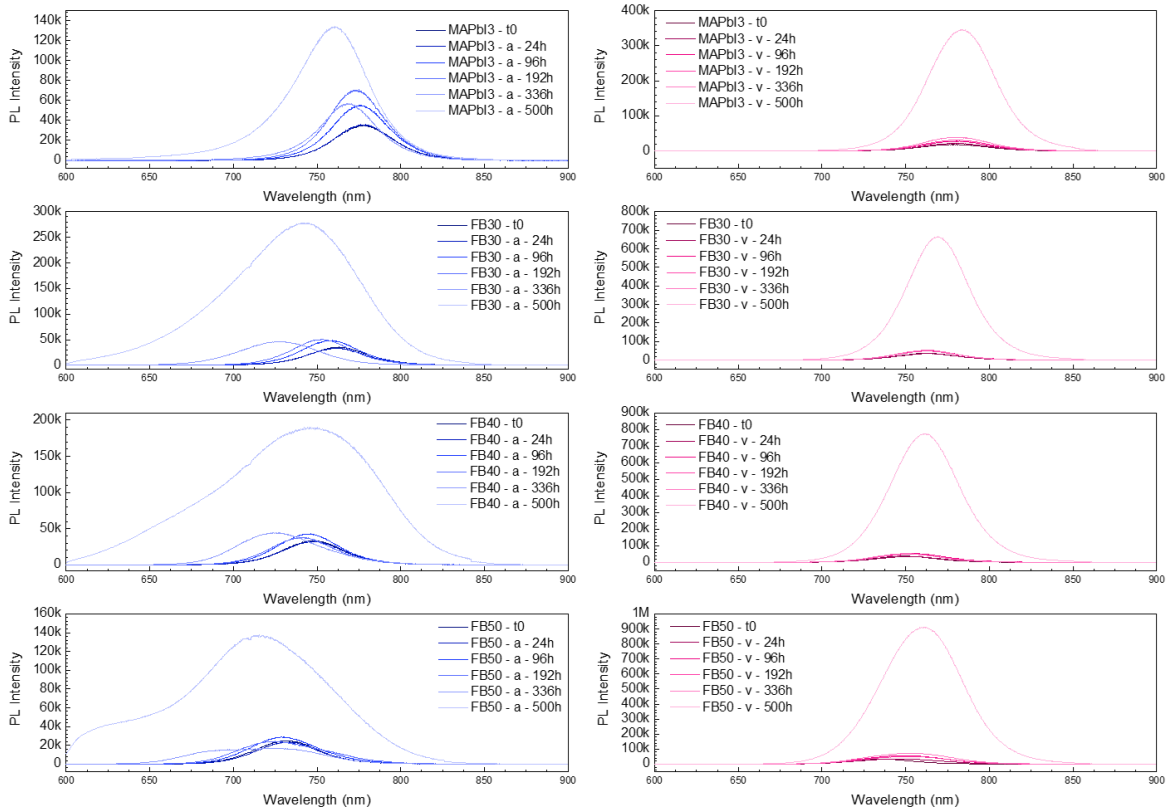

Figure S24: The evolution of the photoluminescence spectra for the four half-cells aged at 40°C under ambient atmosphere or vacuum

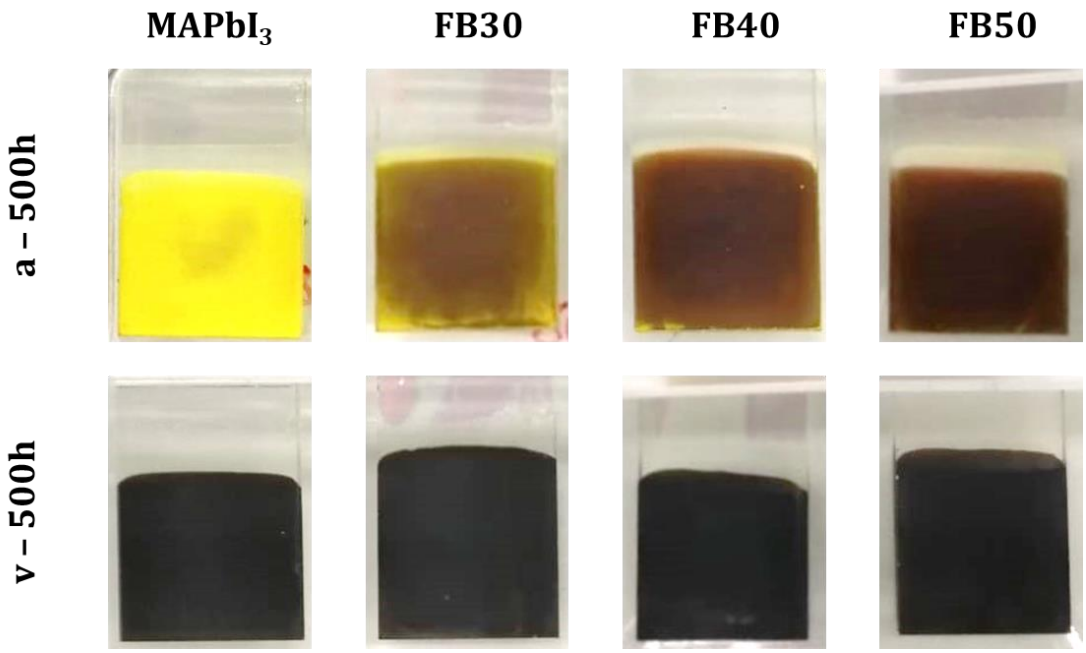

Figure S25: Photos showing the aspect of the four aged samples after 500h at ambient atmosphere or under vacuum (T=40°C)

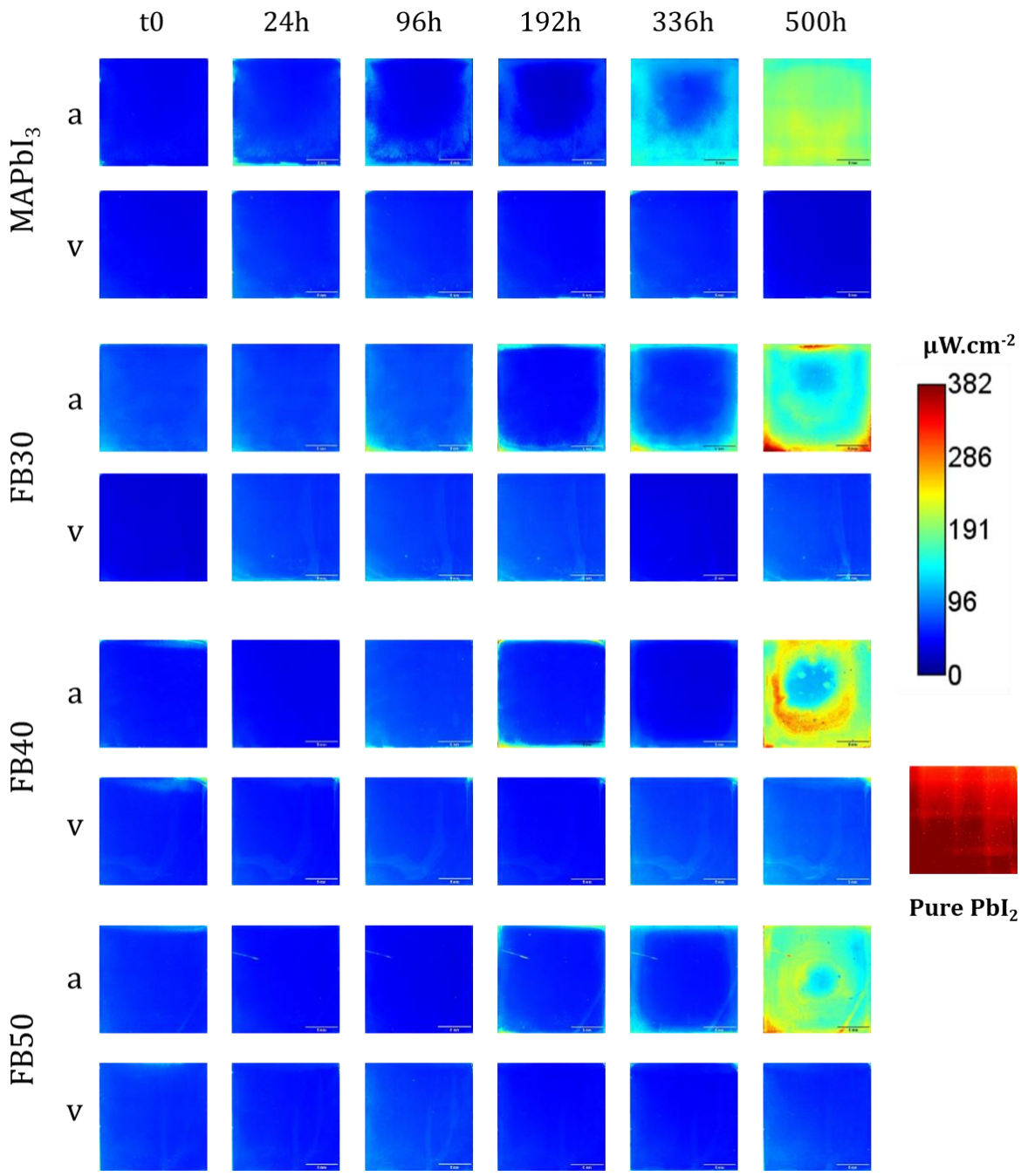

Figure S26: Photoluminescence images showing the variation of the irradiance with time on the whole surface for the four samples aged at 40°C under ambient atmosphere or vacuum (scale bar: 5 mm)

Chapter V: Architecture optimization of perovskite solar cells elaborated by electrodeposition

In this chapter, we investigate the options for the choice of the different transport layers, the contact electrodes and the structure of the solar cell, since the architecture of the solar device has a key role on its photovoltaic performance. The optimization of the active layer was studied, and different solar devices with different architectures were compared.

Introduction

Achieving a high efficiency in the development of a PSC is related to various parameters, such as the architecture and the elaboration processes of all layers of a device. As for all solar cells, the choice of the HTL, ETL and contact cathode plays an important role in the improvement of the efficiency of perovskite-based devices. Thus, in a first step, an optimization related to the electrodeposition process is proposed. For this process, both the nature of the substrate on which the perovskite layer is deposited and the conversion step are the key parameters according to our experience. In particular, the concentration of the solution used for the conversion of the perovskite seems to affect the morphology and the crystallinity of the perovskite. In the final section, a study concerning more specifically the optimization of the full architecture is presented. All the results obtained finally allow to conclude about the influence of the various parameters on the performances of electrodeposited PSC solar cells obtained.

V.1. Choice of interfacial layers for PbO_2 electrodeposition

Generally, whatever the solar cell architecture (n-i-p or p-i-n), the choice of the HTLs and ETLs is crucial for the optimization of a PSC. In addition to the nature of the materials that mainly influences the energy levels, other properties are very important in the case of the electrodeposition process. As presented previously, the first step to obtain $MAPbI_3$ films is the electrodeposition of PbO_2. From our point view, two properties can thus influence the electrodeposition: the underlayer conductivity and its wettability. Therefore, to validate the use of different materials for the electrodeposition process, a specific study was conducted on eight different materials: SnO_2, TiO_2 and PCBM as ETLs; NiO_x, PTAA, P3HT and CuSCN as HTLs; and ITO only. Figure 34-a presents the chronoamperometry curves carried out on the eight substrates of different nature, playing the role of working electrode during the electrodeposition at 1.5 V (vs RE). These curves are very useful to better understand the PbO_2 electrodeposition process.

We can notice a drastic current increase in a few milliseconds at initial reaction stage, representing the formation of the PbO_2 monolayer. As demonstrated in literature[254], this correlates with the full coverage of the substrate with PbO_2. The following decrease in current results from the need of diffusion of electroactive species towards the new electrode surface[254,255,256], until reaching a plateau[322]. Among all the tested layers, PCBM could not reach a maximum current, also matching with the absence of a PbO_2 monolayer formation. This is probably due to the reaction of PCBM that could be responsive to the solution[323].

ITO, SnO_2 and TiO_2 show similar current curves revealing similar mechanisms. Elsewhere, NiO_x, PTAA, P3HT and CuSCN exhibit an second minor increase in the current, before following the same trend as the other materials. This difference is likely due to the solution interaction with the substrate [255]. To validate this hypothesis, the wettability of the tested layers will be below evaluated by water contact angle measurements.

On the quantitative standpoint, the maximum current reached during the electrodeposition (I_{max}) strongly varied, as did the current plateau value observable at the

end of the deposition. Figure 34-b shows the correlation between the substrate resistivity and observed I_{max}. For instance, TiO_2 presents the highest resistivity and reaches the lowest current during electrodeposition, while SnO_2 possesses the lowest resistivity and the highest current. A more conductive substrate seems thus to allow higher maximum current. This shows that the conductivity of the electrodes alters the ability to deposit the PbO_2. Proportional results were noticed for all oxide layers. However, PTAA and P3HT do not precisely follow the deduced correlation, probably due to their organic nature.

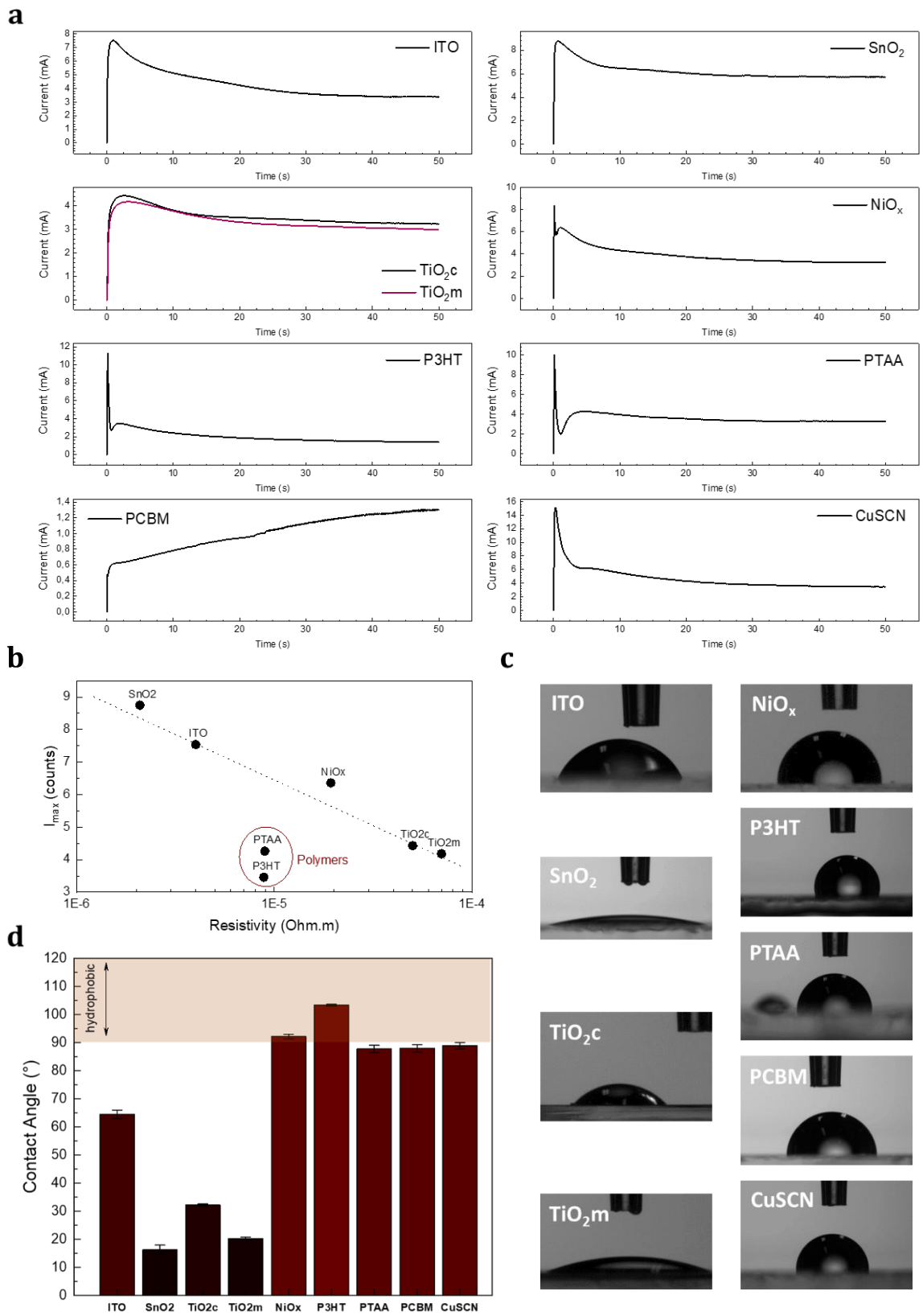

Figure 34: a) Chronoamperometry curves showing the variation of the current versus time during electrodeposition of PbO_2 on eight different substrates, b) Maximum current measured determined from the chronoamperometry curves as a function of the substrate resistivity, c) Optical images of the contact angle measurements by the sessile drop method, and d) Histogram showing the contact angle calculated from the optical images for each substrate

To better understand the effect of the wettability of the working electrode on the electrodeposition process, some water contact angle measurement have been performed since the electrodeposition is conducted in an aqueous medium. The sessile drop method was applied on the different types of substrates using a 3 µL water drop. The average contact angle was deduced from the obtained images, presented in Figure 34-c. The extracted contact angles are then compared in the histogram displayed in Figure 34-d. Results show that the four substrates exhibiting a second increase in chronoamperometry (NiO_x, P3HT, PTAA and CuSCN) are hydrophobic. This validates the suggested hypothesis, assigning this behavior to the higher surface hydration of PbO_2 layer in growth in comparison to these hydrophobic substrates. In fact, the non-wetting surface of the four substrates will enhance grain formation. This is due to the increased nucleation spacing between solution droplet and low surface tension dragging force, which increase grain boundary mobility and allow the film to grow in larger degree of freedom[324]. This explains the faster decrease in chronoamperometry for these four substrates. Afterwards, when the first PbO_2 monolayer is created, PbO_2 will start to deposit on this monolayer, having a smaller contact angle (80°) than the substrate, which explains the second small peak.

In conclusion, after such investigations and in the view of subsequently developing perovskite layer using electrodeposition, SnO_2 and TiO_2 could be considered good candidates as ETLs for the n-i-p structure, and NiO_x is the best candidate to be used as an HTL for the p-i-n structure. As observed in chapter 2, after the electrodeposition of PbO_2 on the chosen substrates, the latter must undergo a two-step conversion to obtain a perovskite layer suitable for photovoltaic application. After a first conversion of PbO_2 into PbI_2, the obtained film encounters a second conversion into either simple $MAPbI_3$ or mixed perovskites. To go further, the optimization of the elaborated perovskite active layer is also an important step to better enhance the photovoltaic activity of the PSC.

V.2.Optimization of $MAPbI_3$ (PK2) conversion

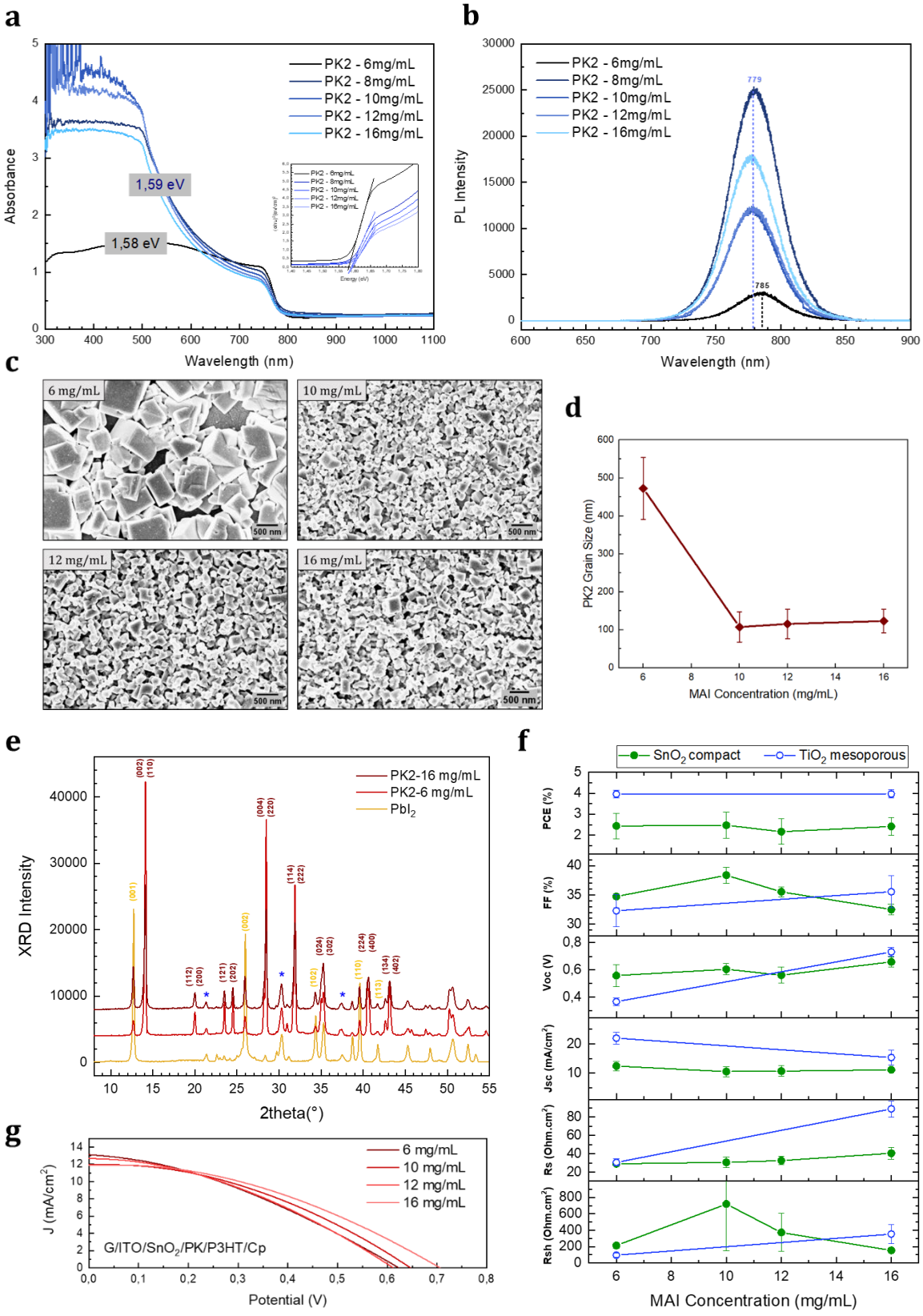

Figure 35: a) UV-visible absorption spectra, b) Photoluminescence spectra, c) Top-view SEM images of PK2 converted at different MAI concentrations, d) PK2 grain size variation with respect to MAI concentration in the conversion bath, e) XRD

patterns of PbI_2 and PK2 converted at two different MAI concentrations, f) PCE, FF, Voc, Jsc, Rs and Rsh variation as a function of MAI concentration for two types of solar cells with the two different architectures: Glass/ITO/SnO_2/$MAPbI_3$/P3HT/C and Glass/ITO/TiO_2c/TiO_2m/$MAPbI_3$/P3HT/C, and g) J(V) curves variation according to MAI concentration in the perovskite conversion bath for a PSC with the architecture Glass/ITO/SnO_2/$MAPbI_3$/P3HT/C

The conversion of PbI_2 into $MAPbI_3$ is a key step for elaborating good perovskite layers using electrodeposition. Many conversion parameters could affect the morphology, crystallography and chemistry of the obtained perovskite film. On one hand, the choice of the conversion technique is important since it affects the kinetics of the conversion (immersion in MAI, exposure to MAI vapor, spin coating of MAI, followed or not by annealing)[16,20,31]. On the other hand, the characteristics of the conversion solution could also affect the obtained film. Indeed, in addition to the choice of the solvent(s) mixture in the conversion bath, the choice of the concentration of the conversion solution is also crucial.

Therefore, in this study, the variation of the composition and morphology of electrodeposited $MAPbI_3$ layer (using PK2 process) was studied when changing the MAI conversion solution concentration between 6 mg/mL and 16 mg/mL (PK2-6, PK2-8, PK2-10, PK2-12 and PK2-16), all the samples being converted for 3 min. First, UV-visible absorption spectroscopy was applied on the different films converted using different MAI concentrations to investigate the impact on optical band gap and absorption pattern. Figure 35-a shows that all samples present a typical absorption spectrum of perovskite with a onset at around 780 nm[269], and only this first transition[181] of $MAPbI_3$ was detectable. However, a remarkable change was noticed for PK2-6. It shows a smaller absorbance at low wavelengths, probably due to a weaker coverage ratio (to be detected in SEM), since the absorption spectrum usually flattens down and forms a plateau when the coverage ratio decreases[270]. In parallel, the band gaps for the different perovskites were compared, and only PK2-6 presents a slightly smaller band gap, going from 1.59 eV (for PK2-16, PK2-12, PK2-10, PK2-8) to 1.58 eV for PK2-6, which can be due to a bigger grain size[325].

Photoluminescence spectroscopy was then used to characterize the emission properties of the elaborated films. Figure 35-b presents the PL spectra of the PK2 samples converted at different MAI concentrations. When comparing the wavelength at maximum intensity λ_{max} of the elaborated films, a red shift is detected between all the samples (779 nm) and PK2-6 (785 nm). If the absorption shift was quite marginal, the luminescence one really highlight the plausible contribution of a bigger crystallite size[274] for PK2-6. Furthermore, the maximum PL spectral intensity I_{max} of PK2-6 is rather low comparing to the other samples. If we compare the values of $A_{peak}/OD(\lambda_{max})$ to I_{max}, we also obtain the same tendency. An increase in the PL intensity could also be attributed to an increase of the crystal quality of the perovskite[185,292], and to a decrease in the defects in the layer[291].

In order to validate previous made assumption, the different films were analyzed by scanning electron microscopy (SEM), and their in-plane morphology is presented in Figure 35-c. As expected, PK2-6 shows a different morphology than other samples. Its surface is not fully covered, which explains the low absorbance level at small wavelengths. It also presents a bigger grains size with larger defects, inducing the slight band gap decrease and the significant PL red shift. The average grains size was calculated and drawn in function of the MAI concentration in Figure 35-d. It evidenced that the shift in the grains size only occurs between 6 mg/mL and 10 mg/mL, and then the grains size

remains relatively stable. The all above results confirm the fact that there is a threshold concentration between 6 mg/mL and 8 mg/mL. To elaborate an intermediate state between PK2-6 and the others, it can be suggested to immerse the precursor PbI_2 film in two different MAI concentrations successively. However, it was here not applicable since the speed of conversion is remarkably quick. Indeed, different conversion durations were applied to verify the real conversion time needed, and results presented in Figure S27 indicate that obtained films are already quite similar for conversion duration of either 30 s or 3 min. Hence, an intermediate state could hardly be elaborated, corroborating 8 mg/mL as the minimal threshold value for MAI conversion bath concentration.

Furthermore, X-Ray diffraction analyses were applied on two representative elaborated perovskite films, to control their relative composition. Their XRD patterns are presented in Figure 35-e, along the PbI_2 XRD pattern. The attribution of identified crystallographic structures is also reported. For both samples, PK2 pattern shows a perovskite crystallization under the tetragonal phase, with no preferred orientation[259], with main peaks at 14° representing the (002) plane, and at 28.5° for the parallel plane (004). PbI_2 (001) phase is also present in the perovskite layers, as shown on the diffraction patterns. It should mainly corresponds to residual PbI_2 in the layer after conversion. However, a smaller PbI_2/(PK2+PbI_2) percentage was detected for PK2-6 (6% PbI_2 for PK2-6 versus 35% PbI_2 for PK2-16). This can be attributed to a slower conversion rate for PK2-6, hence the MAI solution was able to infiltrate more easily in the scaffold during conversion, leading to a quasi-total conversion. Although it is important to control the quantity of PbI_2 in the perovskite, a small amount remaining in the layer can enhance the activity of the perovskite inside the solar cell[264]. Therefore, it seems interested to test the photovoltaic performance of both type of perovskite in order to compare the impact of larger crystal size with associated voids against smaller crystals but with larger PbI_2 amount.

V.3.Performance comparison of PSCs with different architectures

V.3.a. Focus on the performances of $MAPbI_3$ reference material using different devices architectures

Accordingly, the efficiency of PK2 converted at different MAI concentrations were compared. It was tested with two different solar cell architectures: Glass/ITO/c-SnO_2/$MAPbI_3$/P3HT/C and Glass/ITO/c-TiO_2/m-TiO_2/$MAPbI_3$/P3HT/C. The corresponding PCE, FF, V_{oc}, J_{sc}, R_s and R_{sh} are drawn as a function of the MAI concentration in Figure 35-f. Surprisingly, a relatively stable PCE was detected when changing the MAI concentration of the conversion bath. However, this steadiness is accompanied by an inverted variation of other parameters. Increasing the conversion bath concentration induces an important V_{oc} increase and J_{sc} decrease. This can also be noticed on typical J(V) curves presented in Figure 35-g. PK2-16 shows a higher V_{oc}, which could be related to a more suitable energy match between the materials. It could also derive from the observed enhancement in the quality of the layers that minimize the recombination. According to the literature, weakening the electrostatic interaction at the interface and suppressing

photoinduced recombination usually increase the V_{oc} and decrease the J_{sc}[295], which is what is observed in our case.

Although both morphologies offer a similar PCE, the surface with PK2-6 is not fully covered, so it is better to further optimize the solar cell architecture with PK2-16 to avoid the presence of large pinholes. This developed electrodeposited perovskite was then used as an active layer in a PSC, whether in regular n-i-p structure or in inverted p-i-n structure. The choice of the used ETL and HTL, together with associated electrodes, is crucial to develop the best architecture.

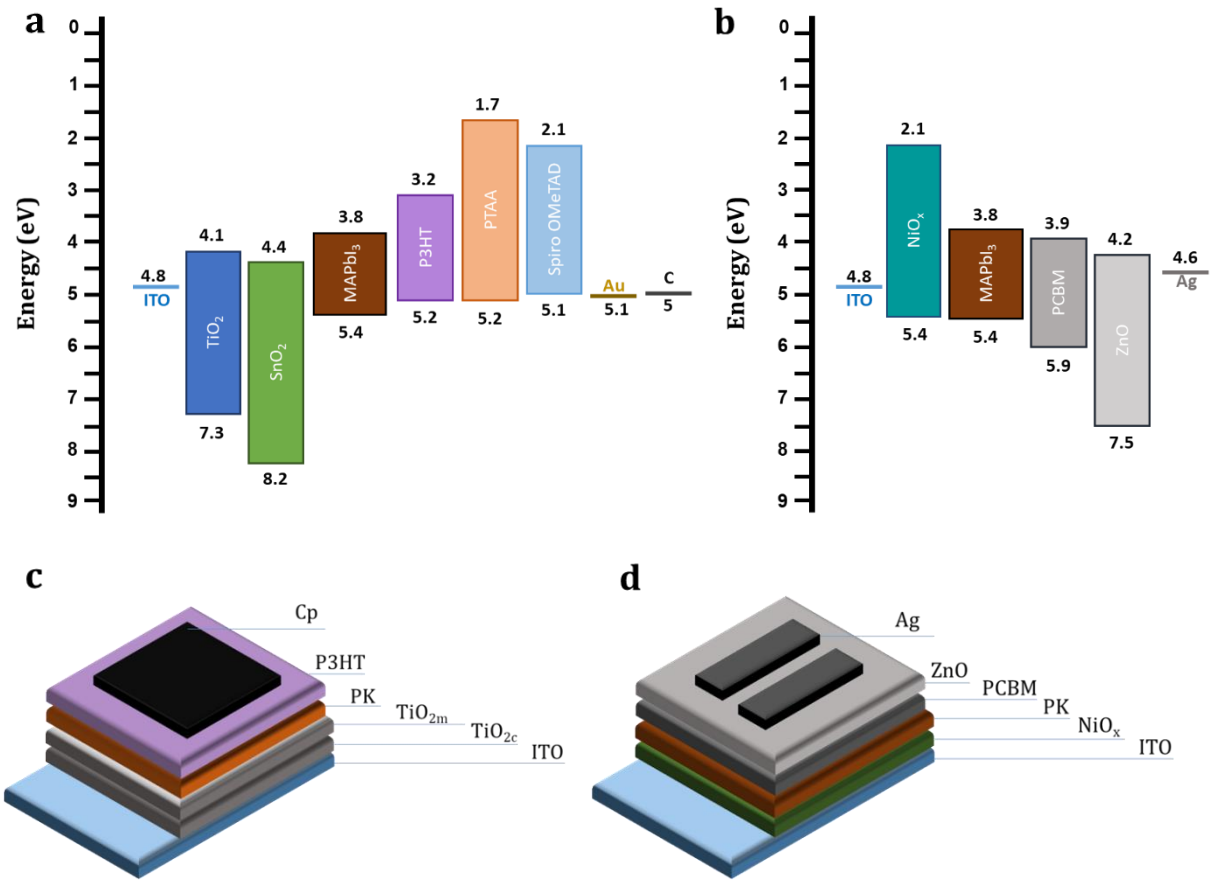

Figure 36: Energy diagrams of suggested a) regular n-i-p structure and b) inverted p-i-n structure, and representative stack of layers for reference samples for c) n-i-p structure and d) p-i-n structure

In n-i-p structure, SnO_2 and TiO_2 were selected as best ETM candidates. SnO_2 has been well considered in many state-of-the-art PSCs due to its high mobility and wide bandgap. It suffers however from degradation in high temperature, and the main concern with its application as an ETL is that it presents a much lower conduction band compared to perovskite (Figure 36-a), which may result in a voltage loss of PSCs[118]. TiO_2 is typically used as ETL in planar heterojunction solar cells due to its suitable band alignment with perovskite absorber layer (Figure 36-a) and good transparency for visible light[119]. The main concern in its application as ETL is that it suffers from low electron mobility, limiting the overall device performance. Consequently, using mesoporous TiO_2 can efficiently enhance the electron transport properties since the porous network of TiO_2 scaffold can be totally filled in this case[22]. This feature of good pore filling and full coverage enhances the interface between the ETL and the active layer and thus limits the recombination of

the excitons (occurring when they have to travel more than their diffusion length before dissociation[120]).

Moving to the choice of the HTM, a wide range of potential HTLs has been explored over the past decade, from organic small molecules and polymers to inorganic compounds with the inclusion of various additives. There is however a tendency to develop a dopant-free HTM in consideration of the stability of devices. P3HT is a commonly used HTM in organic solar cells with a relatively high hole mobility and great stability. This polymer is also a dopant-free HTM and thus could be a suitable choice for stable PSCs[127,326]. However, the most widely used solid-state materials as HTL in high efficiency PSCs are spiro-OMeTAD and PTAA[128,129]. In fact, the pristine spiro-OMeTAD possesses an inherent low hole mobility and poor conductivity due to its triangular pyramid configuration and large intermolecular distance. Therefore, appropriate doping can be applied to resolve this problem. The common p-type dopants of the spiro-OMeTAD are bis(trifluoromethane) sulfonamide lithium salt (Li-TFSI) and 4-*tert*-butylpyridine (TBP). It is observed that lithium salt helps in oxidation process of spiro-OMeTAD whereas tBP improves conductivity of active layer by dissolving in perovskite layer[130]. However, the added dopants are usually hygroscopic and thus would decompose the perovskite film that is sensitive to moisture. Both spiro-OMeTAD and PTAA have properties that inhibit their optimal functioning as HTLs, which include sub-optimal conductivity, significant recombination at the perovskite/HTL interface and stability issues linked to dopant hydrophilicity and reactivity[129]. Accordingly, we chose P3HT as the HTM is our control sample.

For the choice of the contact cathode, carbon-based electrodes have been widely applied in PSCs because they resolve the issues faced by record-breaking “metal/HTM”-based PSCs[134]. Their importance reigns in their chemical inertness and compatibility with up-scalable techniques, signifying their solid potential for mass-production[135]. We chose then to elaborate carbon-based PSCs for the n-i-p structure. Our control sample for further comparison will thus be Glass/ITO/TiO_{2c}/TiO_{2m}/$MAPbI_3$/P3HT/C, presented in Figure 36-c.

The p-i-n structure of PSCs has offered efficiencies as high as 18%, lower temperature processing, flexibility, and negligible J(V) hysteresis effects[327]. Hence, inverted p-i-n planar structures have also been proposed and developed. In this case, the perovskite layer is electrodeposited on the HTL. Many organic materials such as PEDOT:PSS and PTAA has proven to be reliable for high efficiency p-i-n perovskite solar cells[328–330]. However, their insertion in the electrolyte before electrodeposition might engender some surface modification or degradation. As an alternative, nickel oxide (NiO_x) is an inorganic stable material with a suitable HOMO level for hole extraction (Figure 36-b) and electron blocking properties in perovskite related applications[131]. The NiO_x is also a suitable candidate due to its high optical transmittance, sufficient conductivity and chemical stability. In addition, the NiO_x HTMs can be elaborated easily via solution from corresponding precursors at low temperatures[132]. Moving to the opposite side of the perovskite active layer, the typical ETM in such inverted PSCs is a fullerene derivative (PCBM) that has the tendency to passivate perovskite surface with a significant suppression of hysteresis and recombination losses[121]. However, PCBM/metal contact is

not optimized for electron extraction due to the energy level mismatch[122,123]. Therefore, interface engineering has been carried out between the PCBM and metal contact by inserting additional layers, such as ZnO. The additional ZnO layer not only improves the energy level alignment at the cathode, but also blocks the possible reactions (leading to AgI production) between the Ag electrode and the perovskite iodine-containing components (either present at initial state or produced during aging)[124–126].

Consequently, ITO/NiO_x/$MAPbI_3$/PCBM/ZnO/Ag was selected as the architecture to elaborate, for the first time, a PSC with a p-i-n structure using electrodeposited perovskite (Figure 36-d).

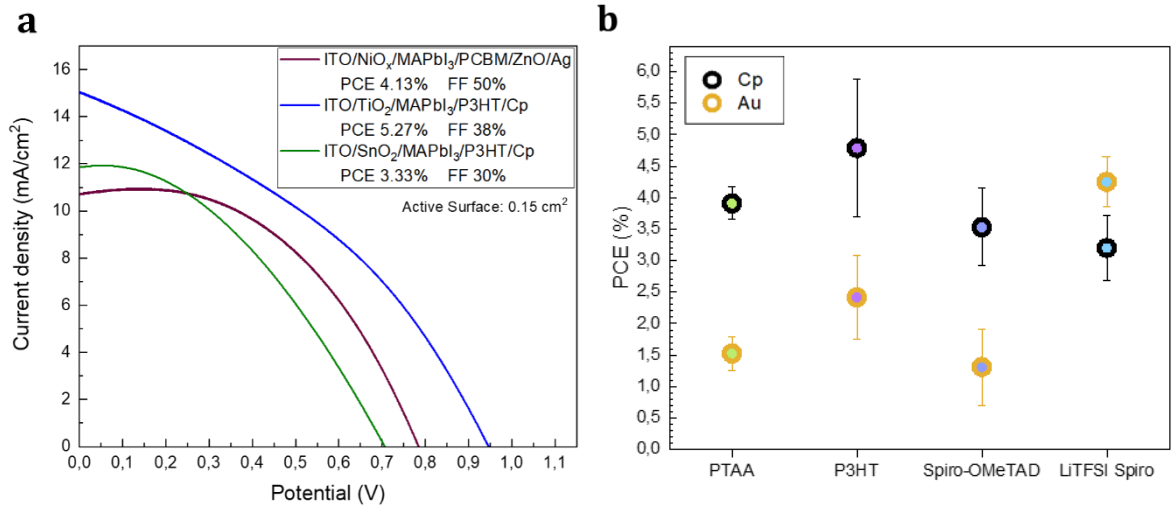

Figure 37: a) J(V) curves of PSCs with the following architectures: Glass/ITO/NiO_x/$MAPbI_3$/PCBM/ZnO/Ag, Glass/ITO/TiO_{2c}/TiO_{2m}/$MAPbI_3$/P3HT/C and Glass/ITO/SnO_2/$MAPbI_3$/P3HT/C, having an active surface of 0.15 cm^2, and b) average PCE variation of the PSCS with the following architecture: Glass/ITO/TiO_{2c}/TiO_{2m}/$MAPbI_3$/HTL/Contact , when changing the HTL and the contact cathode

For further investigation, the photovoltaic performances of the PSCs with the different architectures were compared. First, we compared the performances of two PSCs elaborated either using the n-i-p structure (Glass/ITO/TiO_{2c}/TiO_{2m}/$MAPbI_3$/P3HT/C) or the inverted p-i-n structure (ITO/NiO_x/$MAPbI_3$/PCBM/ZnO/Ag). Then, the impact of the ETL nature on the photovoltaic performance was studied by comparing the performances of two PSCs with the following architecture: Glass/ITO/ETL/$MAPbI_3$/P3HT/C, the ETL being either TiO_{2c}/TiO_{2m} or compact SnO_2. The corresponding J(V) curves are presented in Figure 37-a.

Even though an electrodeposited perovskite was never previously used in a p-i-n structure, it presents interesting results, with a PCE of 4.13% and an FF of 50%. Although it presents a much more important fill factor than the n-i-p structure with TiO_2 as an ETL, its smaller V_{oc} of 0.8 V and J_{sc} of 11 mA/cm^2 engenders a lower PCE. Hence, an enhancement of this architecture must be followed, by optimizing the choice of the materials to better provide matching energy levels and enhance the V_{oc}, or by optimizing the thickness of the layers to avoid any interface recombination and increase the J_{sc}.

When comparing the performance of the two PSCs elaborated with the two different ETLs TiO_{2m} and SnO_2, as previously observed, mesoporous TiO_2 offers a better efficiency

reaching 5.3% versus 3.3% with compact SnO_2. This increase in the efficiency is first due to a V_{oc} enhancement since TiO_2 presents better band alignment with perovskite absorber layer (Figure 36-a). It is also because of a J_{sc} enhancement, since electrodeposition on mesoporous scaffold enhances the interface between the ETL and the active layer.

The impact of the HTL and the contact cathode was also studied. The average PCEs of the PSCs with the control architecture Glass/ITO/TiO_2c/TiO_2m/$MAPbI_3$/HTL/Contact are presented in 4-b when variating the HTL (PTAA, P3HT, spiro-OMeTAD or Li-TFSI doped spiro-OMeTAD) and variating the contact cathode (Carbon paste Cp or gold Au). It must be mentioned that the PSCs elaborated with a Cp contact cathode have an active surface ranging between 0.15 and 0.2 cm^2, whereas the ones elaborated using Au have an active surface of 0.28 cm^2. This prevents the direct comparison between carbon and gold electrodes. We can however still compare the impact of the HTL for each contact electrode. For instance, among all the tested HTLs, P3HT offers the best PCE with carbon because of its great stability. The carbon paste deposited on the HTL contains different solvents and must be annealed at 120°C, which can cause some degradation of PTAA and spiro-OMeTAD. More precisely, the Li-TFSI doped spiro-OMeTAD shows the lowest performance with carbon, since the ionic salts added are hygroscopic which enhances the degradation of the perovskite. On the other hand, when comparing the PCEs of these solar devices elaborated using gold electrode, Li-TFSI doped spiro-OMeTAD provides the best PCE since it enhances the charge transport inside the solar device, but does not cause degradation when used with gold electrode deposited using Joule effect evaporation in vacuum chamber.

V.3.b. Full comparison of electrodeposited PSC performances using either various device architectures and various perovskite formulations

The previously developed electrodeposited $MAPbI_3$ perovskite presents a high amount of PbI_2. Working with mixed electrodeposited perovskites may therefore be a solution to reduce undesired PbI_2 in the layer. In fact, $MAPbI_{3-x}Cl_x$ and $MA_{1-y}FA_yPbI_{3-x}Br_x$ mixed perovskites were successfully investigated using electrodeposition in our previous work, offering better photovoltaic performances and an enhanced stability.

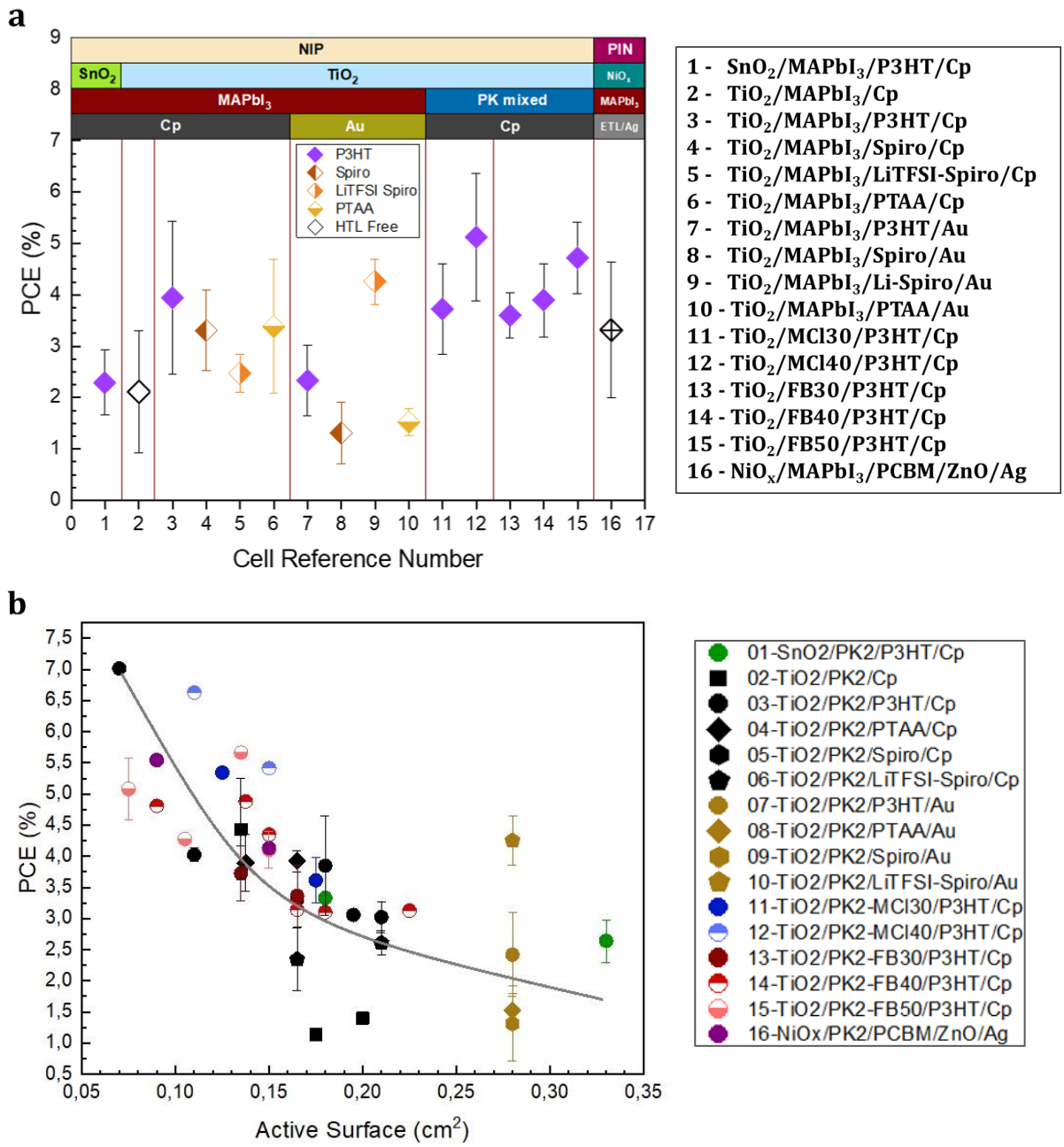

Figure 38: Average PCE variation for all the tested devices architectures and perovskite formulation a) as a function of the PSC architecture, and b) as a function of the devices active surface

Many architecture were developed using the electrodeposition process, whether with n-i-p or p-i-n structure, and for n-i-p whether for comparing the impact of ETL nature, the impact of HTL nature with Cp or Au, or even comparing simple $MAPbI_3$ with mixed perovskites ($MAPbI_{3-x}Cl_x$ for 30% and 40% Cl, or $MA_{1-y}FA_yPbI_{3-x}Br_x$ for 30%, 40% and 50% Br). The average PCE of the developed architectures and formulations are presented in Figure 38-a.

For n-i-p structure, when comparing the impact of the ETL for the cells numbered 1 and 3: as previously explained, TiO_2 shows a better performance than SnO_2 because of its mesoporous nature and its more suitable energy match. HTL-free PSC was also elaborated, and when comparing architecture 2 to 3/4/5/6, we confirm that our

electrodeposited PSC can function without an HTL, however it is less performant. For the carbon based PSCs, when comparing the impact of the HTL in architectures 3, 4, 5 and 6, we detect that P3HT is the best performant for the previously mentioned reasons. Spiro-OMeTAD and PTAA show close efficiencies whereas doped spiro-OMeTAD is the least performant, probably due to a degradation created when applying the carbon paste on the HTL. However, with a gold based PSC in architectures 7, 8, 9 and 10, Li-TFSI doped spiro-OMeTAD has the best performance among other HTLs, since no annealing of a carbon paste is performed on the material but a less stressful evaporation of a gold electrode. In addition, whether using carbon or gold as a cathode, we notice the same efficiency decrease order for the three other non-doped HTLS: P3HT, PTAA and then spiro-OMeTAD.

We also compared the performance of the simple $MAPbI_3$ in the cell numbered 3 with that of mixed perovskites in cells numbered 11, 12, 13, 14 and 15 (purple symbols). We notice an increase in the PCE when using $MAPbI_{3-x}Cl_x$, which also increases when increasing the Cl ratio. Likewise, better PCEs are detected for $MA_{1-y}FA_yPbI_{3-x}Br_x$, also increasing with the Br ratio. However, $MAPbI_{3-x}Cl_x$ with 40% Cl in the conversion mixture shows the best performance with the highest average PCE of 5.1%, exceeding 6% for some of the samples. It is also important to mention that these values are detected before maturation, directly after preparation of the solar cells. In previous chapters, we noticed that those perovskites undergo a beneficial maturation phenomenon after an exposure of several hundred hours at 40°C.

Finally, if we compare the $MAPbI_3$-based PSC developed with p-i-n structure in cell architecture 16 with the best performant $MAPbI_3$-based n-i-p cell in architecture 3, we note that it offers relatively good results, but a lower performance as previously explained.

The photovoltaic parameters such as the power conversion efficiency PCE, fill factor FF, short-circuit current J_{sc}, open-circuit voltage V_{oc}, series resistance R_s and shunt resistance R_{sh} were extracted for all the elaborated cells and presented in Table 5.

On the other hand, the variation of the PCE for all the developed architectures was compared while variating the active surface, as presented in Figure 38-b. Whatever the architecture, a PCE decrease is detected when increasing the active surface. This tendency is however the most important for the carbon-based PSCs elaborated using $MAPbI_3$ (in black symbols). A less significant variation is observed for the mixed perovskites. We can also note that Au-based PSC with Li-TFSI doped spiro-OMeTAD as an HTL (architecture 9) offers a very high PCE, considering its bigger active surface comparing to other PSCs.

Cell architecture	PCE (%)	FF (%)	J_{sc} (mA/cm²)	V_{oc} (V)	R_s (ohm.cm²)	R_{sh} (ohm.cm²)
ITO/SnO_2/$MAPbI_3$/P3HT/Cp	2.98	36.45	11.73	0.69	34.41	860.81
ITO/TiO_2/$MAPbI_3$/Cp	2.24	34.09	7.33	0.85	76.31	263.13
ITO/TiO_2/$MAPbI_3$/P3HT/Cp	3.86	37.44	11.67	0.88	85.49	212.5
ITO/TiO_2/$MAPbI_3$/Spiro/Cp	3.30	33.32	11.42	0.86	53.5	185.95
ITO/TiO_2/$MAPbI_3$/LiTFSI-Spiro/Cp	2.47	35.24	7.93	0.88	65.3	248.67
ITO/TiO_2/$MAPbI_3$/PTAA/Cp	3.90	31.21	13.14	0.92	39.1	98.78
ITO/TiO_2/$MAPbI_3$/P3HT/Au	2.41	36.22	10.61	0.62	32.42	135.22
ITO/TiO_2/$MAPbI_3$/Spiro/Au	1.31	35.29	5.24	0.69	89.84	306.32
ITO/TiO_2/$MAPbI_3$/LiTFSI-Spiro/Au	4.25	41.79	12.79	0.79	28.73	304.63
ITO/TiO_2/$MAPbI_3$/PTAA/Au	1.52	37.86	5.74	0.69	60.08	335.79
ITO/TiO_2/MCl30/P3HT/Cp	4.01	34.7	13.21	0.86	44.88	272.63
ITO/TiO_2/MCl40/P3HT/Cp	5.42	36.4	18.15	0.81	25.05	135.77
ITO/TiO_2/FB30/P3HT/Cp	3.54	32.88	12.81	0.85	48.38	149.15
ITO/TiO_2/FB40/P3HT/Cp	3.90	35.11	13.02	0.85	42.28	202.29
ITO/TiO_2/FB50/P3HT/Cp	4.78	39.19	13.74	0.89	32.91	310.51
ITO/NiO_x/$MAPbI_3$/PCBM/ZnO/Ag	4.83	57.84	10.29	0.81	21.34	1563.3

Table 5: Average PCE, FF, Jsc, Voc, Rs and Rsh for all the developed cells with various device architectures and perovskite formulations

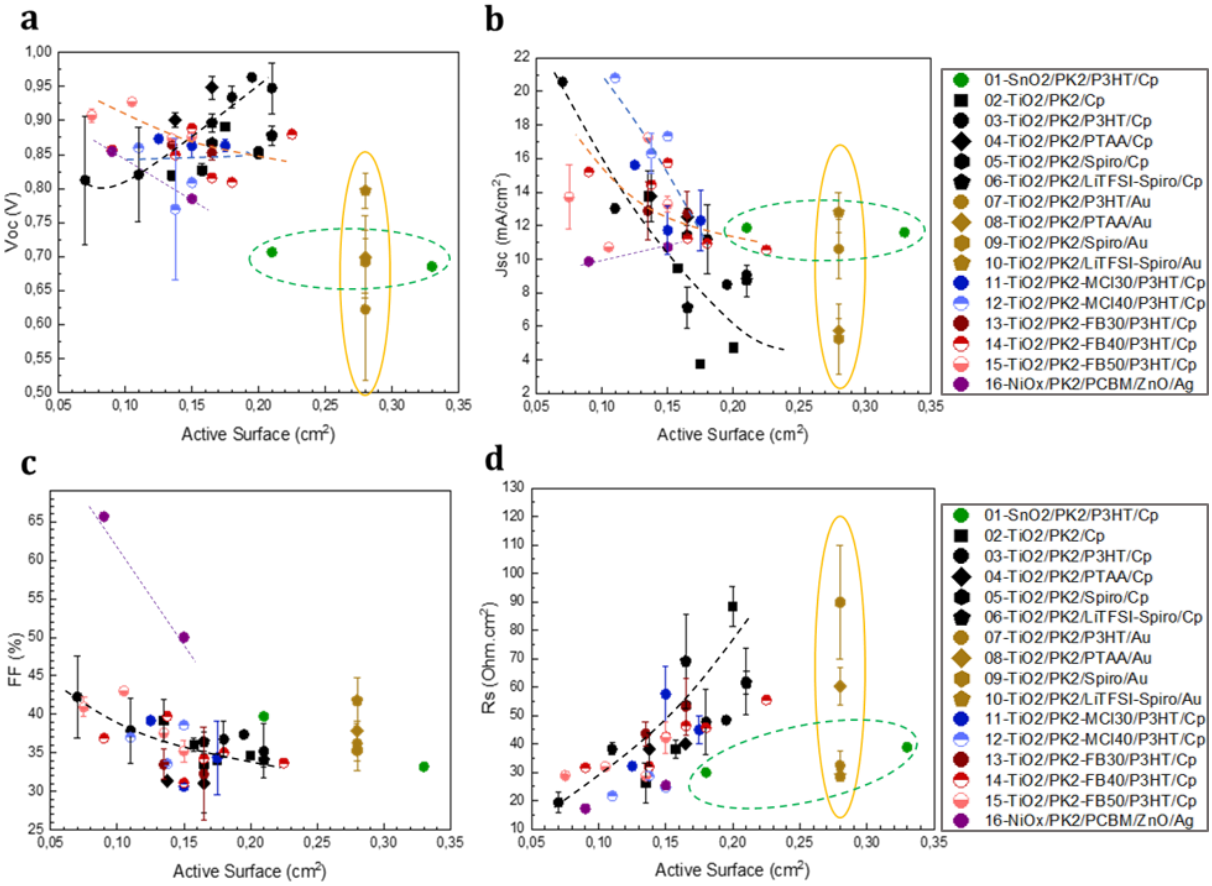

Figure 39: a) Average Voc variation, b) average Jsc variation, c) average FF variation and d) average Rs variation, for all the tested device architectures and perovskite formulations as a function of the active surface

In addition to the PCE variation for all the developed architectures according to the active surface, the active surface dependence of the photovoltaic parameters such as the open-circuit voltage V_{oc}, the short-circuit current J_{sc}, the fill factor FF, and the series resistance R_s were also investigated for the different architectures.

First, the variation of the V_{oc} is presented in Figure 39-a as a function of the active surface. Different thoughts can be extracted from the presented results. When using SnO_2 instead of TiO_2 as ETL, a smaller V_{oc} is detected. Also, using Au as the contact electrode instead of Cp decreases the V_{oc}. In both cases, the reason for such behavior is the decline of the energy levels alignment matching when changing the chosen layers. On the other hand, for the carbon based PSCs, an increase in the V_{oc} is noticed when increasing the active surface. According to the literature, weakening the surface photoinduced recombination at the interface can increase the V_{oc}, much more than the decrease of bulk recombination[331]. Such act is valid in our case since increasing the active surface gives the excitons more diffusion space within the active surface, so more freedom of motion towards the electrodes. However, as shown in Figure 39-b, the J_{sc} of corresponding cells decreases. This time, this can be related to an increase of defect probability within the bulk perovskite, probably increasing the bulk recombination rate and the local carrier transport losses[332]. This statement is supported by the observed R_s increase.

Although J_{sc} undergoes an important decrease when increasing the active surface for the carbon based PSCs, a better J_{sc} is detected for the PSCs elaborated using $MAPbI_{3-x}Cl_x$. On the other hand, it remains relatively important for higher active surfaces when SnO_2 is used as an ETL. When Au is used as the contact electrode, for solar cells elaborated with P3HT and doped spiro-OMeTAD as the HTL, the extracted J_{sc} is relatively high taking into consideration the bigger active surface.

Moreover, the FFs of the elaborated devices are presented as a function of the active surface in Figure 39-c. PSCs with a p-i-n structure offer a highly enhanced FF comparing to the other devices, reaching 65% for a 0.1 cm^2 active surface. This could be due to better interfaces between the elaborated layers for this structure. Au-based PSCs also provide a slightly better FF comparing to the carbon-based PSCs, since Au is directly evaporated on the HTL. Such deposition method grants a better interface comparing to a carbon paste layer deposited by doctor-blading. Furthermore, increasing the active surface leads to a slight decrease in the FF for the carbon-based PSCs. A bigger surface implies more defects which will not only decrease the FF but also increase the R_s, as detected in Figure 39-d. The Rs detected for the SnO_2-based PSCs remains however relatively low at greater active surface. The Au-based PSCs, with P3HT and doped spiro-OMeTAD as the HTL, offer a low R_s, a result matching the one detected for the J_{sc} of these architectures.

Conclusion

In this chapter, the choice of the electrodeposition substrate, the interfacial layers and electrode materials, together with the optimization of both conversion and formulation of the active layer have been studied and compared. Many architecture were thus developed using the electrodeposition process, whether with n-i-p or p-i-n structure, and for n-i-p whether for comparing the impact of ETL nature, the impact of HTL nature with Cp or Au, or even comparing simple $MAPbI_3$ with mixed perovskites. SnO_2 and TiO_2 were chosen to be good candidates as ETLs for the n-i-p structure, and P3HT as the HTL for it is dopant-free relatively high hole mobility and great stability. NiO_x was chosen as the best candidate to be used as an HTL for the p-i-n structure, with a ZnO/PCBM as ETL. The control sample for comparison was chosen to be: Glass/ITO/TiO_2c/TiO_2m/$MAPbI_3$/P3HT/C. The photovoltaic parameters such as the PCE, the V_{oc}, the J_{sc}, the FF, and the R_s were investigated for the different architectures as a function of the active surface. Generally, increasing the active surface engenders a regression in the photovoltaic parameters. Such result is expected since it is also confronted when using spin-coated PSCs.

Experimental section

The deposition of the PK, SnO_2, TiO_2, P3HT, and Cp layers are explained in the previous chapters. In addition to that, NiO_x, PTAA, Spiro-OMeTAD, ZnO and PCBM layers are deposited using spin-coating and the metallic cathodes Au and Ag are evaporated on the samples.

For the deposition of the PTAA layer, a 10 mg/mL PTAA in chlorobenzene solution was spin coated on the perovskite at 25 rps for 40s then 33rps for 30s. These conditions lead to a 60 nm thick PTAA layer.

For the deposition of Spiro-OMeTAD, 100 µL of a Spiro-OMeTAD precursor solution (containing 72.3 mg Spiro and 28.8 µL TBP in 1 mL CBZ) was spin coated at 67 rps for 30s. The obtained film had a thickness of 135 nm. For the doped Spiro-OMeTAD, we used the same solution and added to it 17.5 µL of a solution containing 520 mg/mL LiTFSI in acetonitrile. 100 µL of this solution was spin coated at 25 rps for 30s. The obtained film had a thickness of 250 nm.

For the deposition of the NiO_x layer, 0.1 M NiAc (Nickel acetate) was dissolved in EtOH and mixed for 45 min (3x15min) by sonification. 50 µL of this solution was spin coated at 67 rps for 45s, then annealed for 1h at 300°C. The obtained films had a thickness smaller than 10 nm.

PCBM was deposited using a 20 mg/mL PCBM in chlorobenzene solution. 50 µL of this solution was spin coated at 17 rps for 60 s. The obtained layer had a thickness of 50 nm.

Avantama N-10 ZnO precursor solution was used to spin coat the ZnO layer at 67 rps for 60s. The thickness of the obtained layer was 30 nm.

Gold electrodes were deposited using Joule effect evaporation in vacuum chamber at 1.10-6 bar to complete the device fabrication. Two cells of about 0.28 cm^2 active area were obtained on each substrate.

Silver electrodes were also evaporated using the same process, but the obtained cells have an active surface between 0.10 and 0.15 cm^2.

The control PSC sample used for the comparison in this chapter was Glass/ITO/TiO_2c/TiO_2m/$MAPbI_3$/P3HT/C.

The characterizations used for this chapter are explained in the previous chapters. In addition, the thickness and roughness of all layers were measured using the Alpha-Step D-500 stylus profiler. The resistivity of the layers was measured using the four-point method on a homemade device. Sessile drop technique was used for the water contact angle (WCA) measurements on a GBX Goniometer coupled with drop shape analysis software. The WCA values reported in this work are the average of at least three measurements. A standard simulated AM1.5G irradiation system with a 100W ozone free xenon-lamp solar simulator (Oriel LSC-100) was used for solar cell tests. The photocurrent density–voltage (J–V characteristics) measurements of the devices were recorded using a BioLogic-SP300 source with a scan going from +1 to −0.2 V and a scan rate of 40 mV/s. The fill factor FF, short-circuit current J_{sc}, open-circuit voltage V_{oc}, power conversion efficiency PCE, shunt resistance R_{sh} and series resistance R_s parameters were then deduced from J(V) measurements, using a home-made program on Spyder software.

Supporting Information

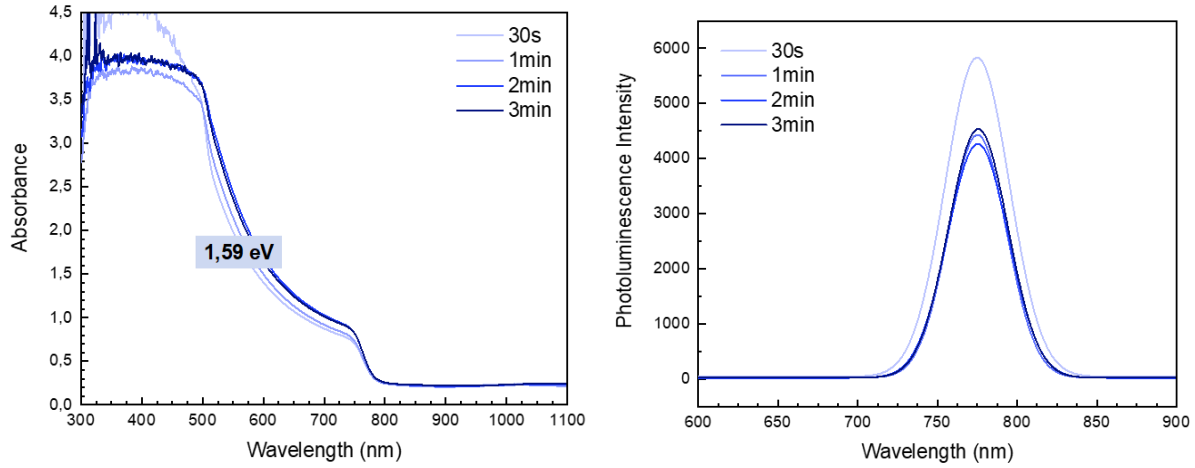

Figure S27: UV-visible absorption spectra and Photoluminescence spectra variation of PK2 converted in MAI-16mg/mL bath variation with respect to the conversion time

General Conclusion and Perspectives

General Conclusion

In this study, the electrodeposition method was investigated to deposit the perovskite layer. The elaborated work started from scratch since the team had minimal knowledge concerning this process. It was however chosen as the main topic of this thesis because it presents many advantages. This method is easy to manipulate, and the electrodeposited films could grow on surfaces as large as desired, inside an electrolyte, allowing its application in ambient atmosphere, with no need of a glove box. It is also solvent engineering eco-friendly, since no toxic solvents are needed to stabilize or enhance the morphology of the obtained films. The main solvents used are deionized water, ethanol and isopropanol.

In the first presented article, a PbO_2 layer is electrodeposited as a starting material and then perovskite is obtained using two different routes: direct conversion to perovskite (PK1 form) and conversion to PbI_2, then to perovskite (PK2 form). At each step of the elaboration, the nature of the deposited layer is determined by UV-Visible absorption, photoluminescence, X-ray diffraction and scanning electron microscopy. After conversion, the microstructure, morphology, optoelectronic properties and thickness of the perovskite layer were studied according to the route explored and the nature of the substrate. Important differences in terms of composition, crystallinity, thickness and morphology were noticed. For the PK1 form, we note a rather weak rate of covering as well as an important size of grains, which is not very adapted for an application in solar cells. For the PK2 form, the deposits are much more homogeneous in terms of thickness, with an optimal coverage rate and smaller grains. Important differences also appears according to the nature of the substrates: a better homogeneity, with a lower presence of PbI_2 and a higher rate of crystallinity for the mesoporous TiO_2. This chosen route allowed the deposition of large surface films, with a uniform morphology containing negligible defects. Photovoltaic performances of the as-prepared films were also tested using two different architectures: G/ITO/SnO_2/PK2/P3HT/C and G/ITO/TiO_{2c+m}/PK2/P3HT/C. The obtained cells are functional but we note different performances according to the nature of the ETL. In the case of TiO_2, maximum performances of 7% are obtained for a 0.1 cm^2 PSC, which is in accordance with the literature taking into account the deposition method, the nature of the perovskite and the tested architecture. It is important to mention that electrodeposition of perovskites is not so far optimized as much as the spin-coating. Also, the films are not elaborated in the same conditions, since electrodeposition offers much more simple procedures. The performance of the $MAPbI_3$ perovskite fabricated in this work might seem low, but it was much better than that of the spin coated $MAPbI_3$, showing negligible PCEs when using similar device architecture for this simple perovskite[181].

The second article investigates the possibility of developing a mixed perovskite using the technique investigated in the first article. After studying the electrodeposition of $MAPbI_3$ perovskite layers, the same process was applied on double halides perovskites $MAPbI_{3-x}Cl_x$, while variating the ratio of Cl. The infiltration of chlorine inside the $MAPbI_3$ lattice usually enhances its stability. This successful attempt is one of its kind, since $MAPbI_{3-x}Cl_x$ was never developed using electrodeposition before. We studied the impact of chlorine proportion on the microstructural, morphological and functional properties of these perovskite layers. The results showed that the ratio variation of each mixture induces a

composition modification of the obtained perovskite material. Increasing the Cl ratio in the conversion solution increases its limited infiltration in the perovskite lattice and enhances the relative crystallinity of the perovskite films. The photovoltaic performances of the elaborated $MAPbI_3$ and the $MAPbI_{3-x}Cl_x$ perovskites were then compared in a solar device. Chlorine-doped electrodeposited perovskites offer a PCE enhancement, with an average PCE of 5.5% instead of 4.5% for a 0.15 cm^2 PSC. Their stability was also tested in complete solar cells or half-cells, when aged at 40°C under vacuum or in ambient atmosphere and compared to that of electrodeposited $MAPbI_3$. The PSCs are subject to maturation when aged in the as-mentioned conditions, with a PCE improvement of 60% for $MAPbI_{3-x}Cl_x$ and 20% for $MAPbI_3$ after 500h. From the collected results, we note that the incorporation of Cl in the perovskite lattice not only enhances the stability of the layer but also its efficiency in PSCs. The obtained stability is impressive, since the elaborated solar devices are not encapsulated, and such ageing usually leads toa direct degradation and decrease in the photovoltaic performance under such conditions[333]. Although the obtained efficiencies are not very high compared to the spin-coated perovskite found in the literature, the results remain promising and even novel considering the tested activated surfaces. Finally, it is also important to note their high stability compared to devices elaborated by spin coating. This elaboration method seems to lead to a better compromise between performance and stability. These results are therefore extremely promising in the objective of a future industrialization of this technology..

After a first successful attempt to elaborate a mixed halide perovskite using electrodeposition, the electrodeposition of the simultaneous mixed cation-anion perovskite $MA_{1-y}FA_yPbI_{3-x}Br_x$ was studied, while variating the ratio of Br and FA infiltrated in the perovskite lattice. The advantages of such mixed perovskites lie in their tunable bandgap and their enhanced stability[311,315,321]. A composition modification of the obtained perovskite material is noticed when variating the ratio variation of each mixture. Increasing the Br ratio in the conversion solution increases its infiltration in the perovskite lattice and decreases the PbI_2 presence. The photovoltaic performances of the elaborated $MAPbI_3$ and $MA_{1-y}FA_yPbI_{3-x}Br_x$ perovskites were then compared in a solar device. The electrodeposited mixed perovskites offer a PCE enhancement, with an average PCE going from of 3.7% to 5% instead of 4% with electrodeposited $MAPbI_3$ for a 0.14 cm^2 PSC. Furthermore, their stability was investigated in complete solar cells or half-cells same as in the second article. The electrodeposited PSCs are subject to maturation when aged in the as-mentioned conditions, with a PCE improvement of 40% for $MA_{1-y}FA_yPbI_{3-x}Br_x$ and 35% for $MAPbI_3$ after 350 h of ageing under vacuum. From the collected results, we note that the incorporation of Br and FA in the perovskite lattice also enhances the photovoltaic performance and the stability of the perovskite. Still, the infiltrated ratio should be further optimized since the obtained band gaps are rather high, considering the optimal band gap for a single-junction solar cell is between 1.1 and 1.4 eV on the basis of the Shockley–Queisser limit[45].

In the last chapter, we studied the influence of the electrodeposition substrate, interfacial layers and electrode materials, as well as the optimization of the conversion and formulation of the active layer. Many architectures have been developed using the electrodeposition process, either with an n-i-p or p-i-n structure, and in the case of the n-i-p architecture the impact of the nature of the ETL, of the HTL, of the electrodes (Cp or

Au) and of the nature of the perovskite ($MAPbI_3$ or mixed). The device chosen for the comparison is: Glass/ITO/TiO_{2c}/TiO_{2m}/$MAPbI_3$/P3HT/C. Photovoltaic parameters such as PCE, V_{oc}, J_{sc}, FF and R_s were studied for the different architectures as a function of active surface area. SnO_2 and TiO_2 were chosen as good candidates as ETLs for the n-i-p structure, and P3HT as HTL because it is dopant-free, with relatively high hole mobility and high stability. NiOx was chosen as the best candidate to be used as HTL for the p-i-n structure, with a ZnO/PCBM bilayer as ETL. This work was innovative because no inverted PSCs had been developed by electrodeposition before. It was noticed that the increase of the active surface area leads to a regression of the photovoltaic parameters. Such a result is expected since it is also encountered when using spin-coated PSCs.

Perspectives

Major concerns for the commercialization of perovskite photovoltaic technology include lead toxicity. Since they possess a suitable band gap, lead-free perovskites have emerged as alternatives in PSCs to ensure clean and green photovoltaic technology. The substitution of lead by Sn, Ge, Bi, Sb, Cu and other potential candidates could be one of the perspectives of this work. Another concern is the stability of the perovskite material, especially when in contact with water. Although the electrodeposited perovskites elaborated in this work offered a remarkable stability comparing to spin-coated ones, their stability could be further enhanced. It was proven that the use of additives has a significant effect on the efficiency of PSCs and their stability, such as with 5-AVAI[334].

One of the main performance deciding factors in PSCs is also the architecture of the solar cell. This topic needs to be investigated more, by optimizing the transport layer's deposition, their thickness and their nature. Enhancing the interfaces between the different layers is a way to guarantee a good charge transfer and no short circuits in the device. In addition, using electrodeposited perovskites in a p-i-n structure was applied for the first time in this work. It was anyhow a first successful attempt that needs to be developed more.

Another major perspective of this work is the elaboration of a PSC entirely by electrodeposition. The purpose of this work was mainly to substitute spin coating because it is non-applicable on large surfaces. However, we used it to deposit the other layers of the solar device. Electrodepositing the transport layers, in addition to the active perovskite layer, is a great idea to expand this subject. Several materials used in this work as HTM or ETM could be electrodeposited, such as TiO_2[335,336], SnO_2[337,338], CuSCN[339,340], P3HT[341,342], PTAA[343], ZnO[344,345]. The main issue here is regarding the fact that perovskites are sensitive to water. It is important to find an applicable architecture were the layer following the perovskite could be electrodeposited in a non-aqueous solution.

Finally, in addition to the ageing campaigns applied in this work, the stability of the as-prepared solar devices needs to be investigated when they are encapsulated. This will offer a more clear vision of the potential of these PSCs in term of their stability.

Résumé Français

L'énergie photovoltaïque est considérée de nos jours comme la source d'énergie naturelle la plus utile. En ce moment, différents types de technologies solaires sont disponibles industriellement, et les tentatives de recherche et développement pour améliorer leur potentiel se poursuivent. Alors qu'un certain nombre de matériaux différents avec des rendements différents peuvent réaliser la conversion de l'énergie solaire photovoltaïque, jusqu'à présent, aucun matériau ou combinaison en particulier n'est suffisamment bon marché pour concurrencer l'électricité produite à grande échelle par des combustibles fossiles. De nos jours, les cellules à base de silicium sont les plus commercialisées et elles produisent des rendements de conversion solaire élevés. Cependant, des procédés coûteux à haute température et utilisant un vide poussé sont nécessaires afin d'élaborer du Si pur. Un autre matériau actif appelé pérovskite, vient d'émerger dans la communauté solaire. Il a attiré une grande attention dans le monde entier car il se distingue par ses performances photovoltaïques exceptionnelles, son processus de fabrication facile, ses bandes interdites réduites, ses coefficients d'extinction élevés et sa mobilité de porteurs élevée. Leur coût étant inférieur à celui des cellules solaires au silicium, les cellules solaires à pérovskite (PSC) sont considérées comme l'avenir de la technologie photovoltaïque, car elles sont aujourd'hui capables de générer un rendement de conversion d'énergie proche de celui des principales cellules solaires au silicium. L'énorme potentiel des PSCs réside dans l'augmentation de leur efficacité, passant de 3,8% à 25,2% en une décennie, et ne cessant d'augmenter à ce jour. Cette dernière efficacité de conversion record a été atteinte en avril 2021 par des chercheurs de l'Institut national sud-coréen des sciences et technologies d'Ulsan (UNIST) et de l'Ecole polytechnique fédérale de Lausanne (EPFL). En plus de leur efficacité rapidement accrue, les PSC se caractérisent par une grande flexibilité en terme de possibilités à la fois lors du choix de la méthode de déposition ou de l'architecture.

Habituellement dans les PSCs, la couche active de pérovskite est prise en sandwich entre une couche de transport d'électrons (ETL) et une couche de transport de trous (HTL). Les couches de transport doivent présenter de bonnes propriétés, telles qu'une bonne stabilité thermique, une non-toxicité et doivent être résistantes aux facteurs de dégradation externes. Par conséquent, les couches prenant en sandwich la pérovskite jouent un rôle essentiel dans l'amélioration de l'efficacité de la conversion de puissance et la gestion de la stabilité du système final. Le choix de la nature de la pérovskite est également une clé pour de bonnes performances. $MAPbI_3$ est la pérovskite hybride halogénée la plus courante pour les applications photovoltaïques, mais elle est connue pour son manque de stabilité. Le design de nouvelles architectures moléculaires par substitution de cations ou d'anions, ou même en utilisant un combinaison de plusieurs cations ou anions, s'est avéré être une stratégie efficace pour améliorer davantage les propriétés optoélectroniques de la pérovskite. En ce qui concerne les électrodes de contact, les cathodes de contact métalliques sont généralement utilisées en raison de leur bonne conductivité. Elles présentent cependant de nombreux inconvénients tels que le coût élevé, la complexité du dépôt et leur impact sur la stabilité des PSCs. Comme alternative, les électrodes à base de carbone ont été largement appliquées dans les PSCs

car elles résolvent les problèmes rencontrés avec les électrodes métalliques. Elles sont connues pour leur bonne conductivité, leur flexibilité de traitement, leur grande inertie chimique et leur faible coût, ce qui les rend compatibles avec des techniques évolutives, signifiant leur solide potentiel pour la production de PSCs à l'échelle industrielle.

De plus, l'un des facteurs les plus importants pour déterminer les performances des PSCs est la qualité de la couche active élaborée. La plupart des propriétés de ce film comme sa cristallinité, sa morphologie et son uniformité dépendent de la méthode de fabrication utilisée. Le revêtement par enduction centrifuge (spin-coating) est actuellement la méthode de dépôt de pérovskite la plus couramment utilisée. Cependant, elle nécessite un travail en milieu inerte (boîte à gants), ce qui augmente son coût, ne permet le dépôt que sur de petites surfaces, et nécessite quelques additifs toxiques pour maintenir la stabilité de la pérovskite. Il existe un besoin de rechercher d'autres méthodes de dépôt, plus écologiques, à moindre coût, applicables à une production à grande échelle de PSCs. La méthode d'électrodéposition a récemment été explorée très brièvement dans la littérature comme une alternative efficace pour la fabrication de pérovskite. Cette technique est peu coûteuse, forme des couches lisses et uniformes, pourrait être appliquée pour des dispositifs à grande échelle et, surtout, est élaborée en conditions ambiantes. Il y a eu plusieurs tentatives dans la littérature au cours des dernières années pour optimiser la couche de pérovskite électrodéposée et ajuster sa cristallisation sur des couches différentes. Toutes les sous-techniques commencent par l'électrodéposition d'une couche initiale (PbO, PbO_2 ou PbI_2) suivie d'une ou plusieurs conversions de la couche déposée.

Dans ce manuscrit de thèse, la méthode d'électrodéposition a été étudiée en détail afin de déposer la couche de pérovskite (PK). Le travail élaboré est parti de zéro car l'équipe avait une connaissance minimale de ce processus. Il a cependant été choisi comme sujet principal de cette thèse car il présente de nombreux avantages. Cette méthode est simple, et les films électrodéposés pourraient croître sur des surfaces aussi grandes que souhaitées, à l'intérieur d'un électrolyte, permettant son application sans avoir besoin de boîte à gants. Il est également écologique concernant l'ingénierie des solvants, car aucun solvant toxique n'est nécessaire pour stabiliser ou améliorer la morphologie des films obtenus. Les principaux solvants utilisés sont l'eau déminéralisée, l'éthanol et l'isopropanol.

Dans le premier article présenté, une couche de PbO_2 est électrodéposée comme matériau de départ, puis la pérovskite est obtenue par deux voies différentes : une conversion directe en pérovskite (forme PK1) et une conversion en deux étapes : PbI_2, puis pérovskite (forme PK2). A chaque étape de l'élaboration, la nature et les propriétés de la couche déposée sont déterminées par absorption UV-Visible, photoluminescence, diffraction des rayons X et microscopie électronique à balayage. Après conversion, la microstructure, la morphologie, les propriétés optoélectroniques et l'épaisseur de la couche de pérovskite ont été étudiées en fonction de la voie explorée et de la nature du substrat. Des différences importantes en termes de composition, de cristallinité, d'épaisseur et de morphologie ont été remarquées. Pour la forme PK1, il est noté un taux de recouvrement assez faible ainsi qu'une taille de grains importante, ce qui est peu adapté pour une application en cellules solaires. Pour la forme PK2, les dépôts sont beaucoup plus homogènes en épaisseur, avec

un taux de recouvrement optimal et des grains plus petits. Des différences importantes apparaissent également selon la nature des substrats : une meilleure homogénéité, avec une présence mineure de PbI_2 et un taux de cristallinité plus élevé en déposant sur du TiO_2 mésoporeux. Cette voie choisie a permis le dépôt de films de grande surface, avec une morphologie uniforme contenant des défauts négligeables. Les performances photovoltaïques des films préparés ont également été testées en utilisant deux architectures différentes : Verre/ITO/SnO_2/PK_2/P3HT/C et Verre/ITO/TiO_{2c+m}/PK2/P3HT/C (cf. Figure 40 pour la présentation des différentes étapes d'élaboration d'une cellule solaire via électrodéposition). Les cellules obtenues sont fonctionnelles mais on note des performances différentes selon la nature de l'ETL. Dans le cas du TiO_2, des performances maximales de 7 % sont obtenues pour une PSC de 0,1 cm^2, ce qui est conforme à la littérature compte tenu du mode de dépôt, de la nature de la pérovskite et de l'architecture testée. Il est important de mentionner que l'électrodéposition des pérovskites n'est pas autant optimisée dans la littérature que la méthode par enduction centrifuge. De plus, les films ne sont pas élaborés dans les mêmes conditions, car l'électrodéposition offre des procédures beaucoup plus simples. Les performances de la pérovskite $MAPbI_3$ fabriquée dans ce travail peuvent sembler faibles, mais elles sont en réalité bien meilleures que celles d'une même pérovskite simple $MAPbI_3$ réalisée par enduction centrifuge en boite à gants, et menant à des performances négligeables pour une architecture de cellule solaire similaire.

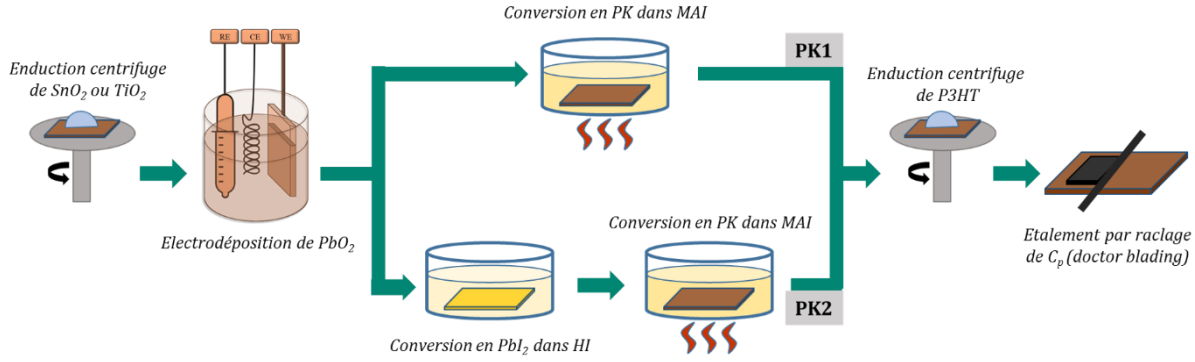

Figure 40: Schéma montrant les étapes consécutives d'élaboration de la cellule solaire proposée dans ces travaux en utilisant deux voies différentes

Le deuxième article étudie la possibilité de développer une pérovskite mixte en utilisant la technique élaborée dans le premier article. Après avoir étudié l'électrodéposition de couches de pérovskites $MAPbI_3$, le même procédé a été appliqué sur des pérovskites doubles halogénures $MAPbI_{3-x}Cl_x$, en faisant varier le ratio de Cl. L'infiltration de chlore à l'intérieur du réseau $MAPbI_3$ améliore généralement sa stabilité. Cette tentative réussie est unique en son genre, puisque $MAPbI_{3-x}Cl_x$ n'a jamais été développé par électrodéposition auparavant. Nous avons étudié l'impact de la proportion de chlore sur les propriétés microstructurales, morphologiques et fonctionnelles de ces couches de pérovskite. Les résultats ont montré que la variation du ratio de chaque mélange de conversion induit une modification de la composition du matériau pérovskite obtenu. L'augmentation du ratio Cl dans la solution de conversion augmente son taux d'infiltration dans le réseau de pérovskite et améliore la cristallinité relative des films de pérovskite. Les performances photovoltaïques des pérovskites $MAPbI_3$ et $MAPbI_{3-x}Cl_x$ réalisées par

électrodéposition ont ensuite été comparées en les intégrant dans l'architecture d'une cellule solaire. Les pérovskites électrodéposées dopées au chlore offrent une amélioration du PCE, avec un PCE moyen de 5,5% au lieu de 4,5% sans chlore pour une PSC de 0,15 cm^2. Leur stabilité a également été testée dans des cellules solaires complètes ou en demi-cellules, vieillies à 40°C sous vide (v) ou en atmosphère ambiante (a), et comparée à celle de $MAPbI_3$ électrodéposée. Les PSCs ont alors démontré un phénomène de maturation bénéfique lorsqu'elles sont vieillies dans les conditions mentionnées, avec une amélioration du PCE de 60% pour $MAPbI_{3-x}Cl_x$ et de 20% pour $MAPbI_3$ après 500h (Figure 41).

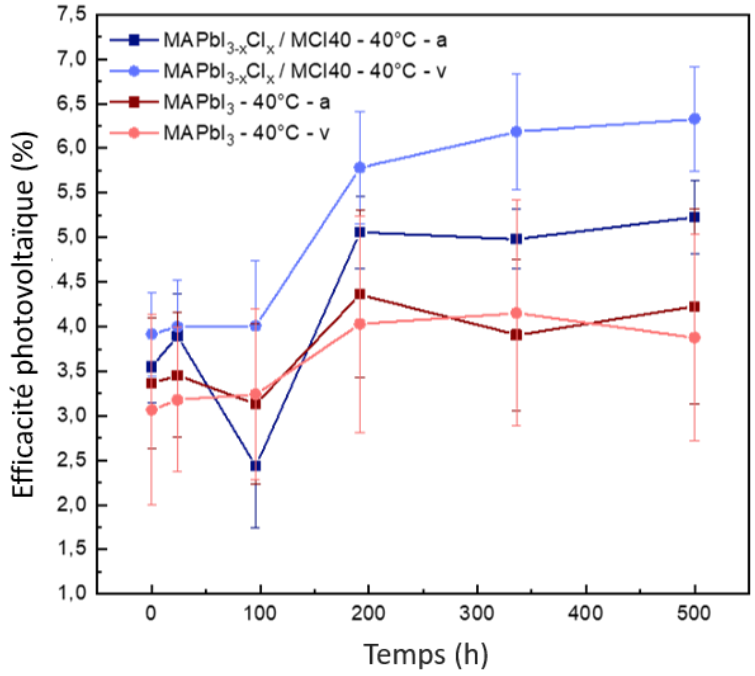

Figure 41: Evolution du PCE en fonction du temps pour deux types de cellules solaires à base de $MAPbI_{3-x}Cl_x$ (conditions : 40°C, atmosphère ambiante (a) ou vide (v))

D'après les résultats collectés, nous notons que l'incorporation de Cl dans le réseau de pérovskite améliore non seulement la stabilité de la couche mais aussi son rendement dans les PSCs. La stabilité obtenue est impressionnante, car les dispositifs solaires élaborés ne sont pas encapsulés, et un tel vieillissement met généralement en œuvre une dégradation directe et une diminution des performances photovoltaïques. Bien que les rendements obtenus ne soient pas si élevés par rapport à la pérovskite trouvée dans la littérature et obtenue par enduction centrifuge, les résultats restent prometteurs. Pour pouvoir être commercialisés, il parait en effet plus apprécié d'avoir un PCE de 7% pour des cellules solaires qui ne commencent pas à se dégrader même après 500h sans encapsulation, que d'avoir des PSCs avec un rendement de 15% qui perdent leurs performances en quelques jours même lorsque encapsulées.

Après une première tentative réussie pour élaborer une pérovskite aux halogénures mixtes par électrodéposition, l'électrodéposition de la pérovskite mixte cation-anion $MA_{1-y}FA_yPbI_{3-x}Br_x$ a été étudiée, tout en faisant varier les rapports de Br et FA infiltrés dans le réseau pérovskite. Ceci fait l'objet du troisième article présenté. Les avantages de ces pérovskites mixtes résident dans leur bande interdite adaptable et leur stabilité

améliorée. Une modification de la composition du matériau pérovskite obtenu via notre procédé d'électrodéposition a pu être remarquée lors de la variation du mélange contenu dans le bain de conversion de la pérovskite. L'augmentation du ratio de Br dans la solution de conversion augmente son infiltration dans le réseau de pérovskite et diminue la présence de PbI_2. Les performances photovoltaïques des pérovskites $MAPbI_3$ et $MA_{1-y}FA_yPbI_{3-x}Br_x$ élaborées ont ensuite été comparées en application cellule solaire. Les pérovskites mixtes électrodéposées offrent un rehaussement de PCE, avec un PCE moyen passant de 3,7% à 5% au lieu de 4% avec $MAPbI_3$ électrodéposée pour une PSC de 0,14 cm^2 (Figure 42).

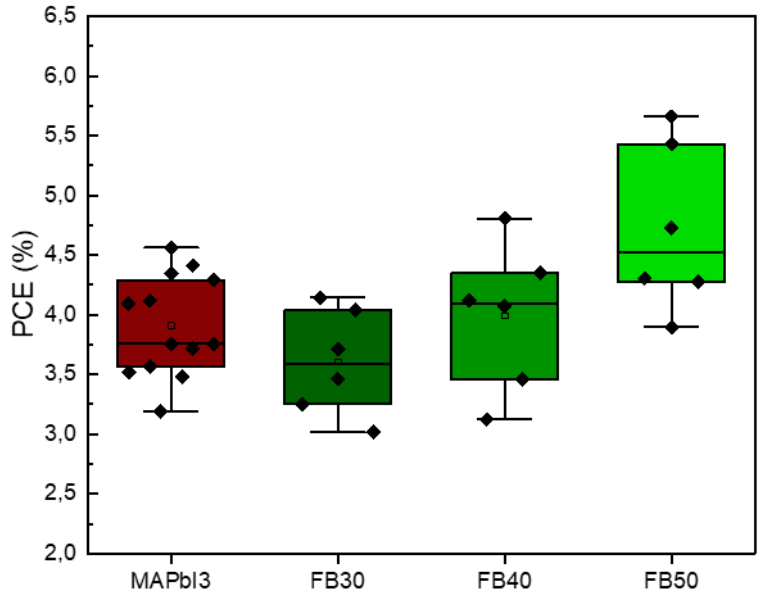

Figure 42: Variation du PCE des cellules solaires des pérovskites $MA_{1-y}FA_yPbI_{3-x}Br_x$ en fonction du taux de FABr/(MAI+FABr) introduit dans la solution de conversion (en vert), comparé au PCE de la simple pérovskite $MAPbI_3$ (en rouge)

De plus, leur stabilité a été étudiée dans des cellules solaires complètes ou des demi-cellules comme dans le second article. Les PSCs électrodéposées ont également démontré une maturation lorsqu'elles sont vieillies dans les mêmes conditions que précédemment, avec une amélioration du PCE de 40 % pour $MA_{1-y}FA_yPbI_{3-x}Br_x$ et de 35 % pour $MAPbI_3$ après 350 h de vieillissement sous vide. D'après les résultats collectés, nous notons que l'incorporation de Br et FA dans le réseau de pérovskite améliore à la fois les performances photovoltaïques et la stabilité de la pérovskite obtenue. Néanmoins, le ratio infiltré devrait être encore optimisé car les bandes interdites obtenues sont plutôt élevées, étant donné que la bande interdite optimale pour une cellule solaire à simple jonction est comprise entre 1,1 et 1,4 eV sur la base de la limite de Shockley-Queisser.

Dans le dernier chapitre, nous avons étudié le choix du substrat d'électrodéposition, des couches interfaciales et des matériaux d'électrode, ainsi que l'optimisation de la conversion et de la formulation de la couche active. De nombreuses architectures ont ainsi été développées en utilisant le procédé d'électrodéposition, que ce soit en structure n-i-p ou p-i-n. Nous avons en particulier pu comparer l'impact de la nature de l'ETL, de l'HTL, de l'électrode supérieure, ainsi que la formulation des pérovskites. SnO_2 et TiO_2 ont été choisis pour être de bons candidats en tant qu'ETL pour la structure n-i-p, et P3HT en tant

que HTL car il est efficace et ce même sans dopant. Il possède une mobilité de trou relativement élevée et une grande stabilité. NiO_x a été choisi comme le meilleur candidat pour être utilisé en temps qu'HTL pour la structure p-i-n, avec une bicouche ZnO/PCBM comme ETL. Ce dernier travail est très innovant car aucune PSC de structure inverse n'avait été développée auparavant par électrodéposition. Les paramètres photovoltaïques tels que le PCE, la Voc, la Jsc, le FF et la Rs ont été étudiés en fonction de différentes architectures de cellule et de formulation de pérovskite (Figure 43), ainsi que en fonction de la dimension de surface active des dispositifs.

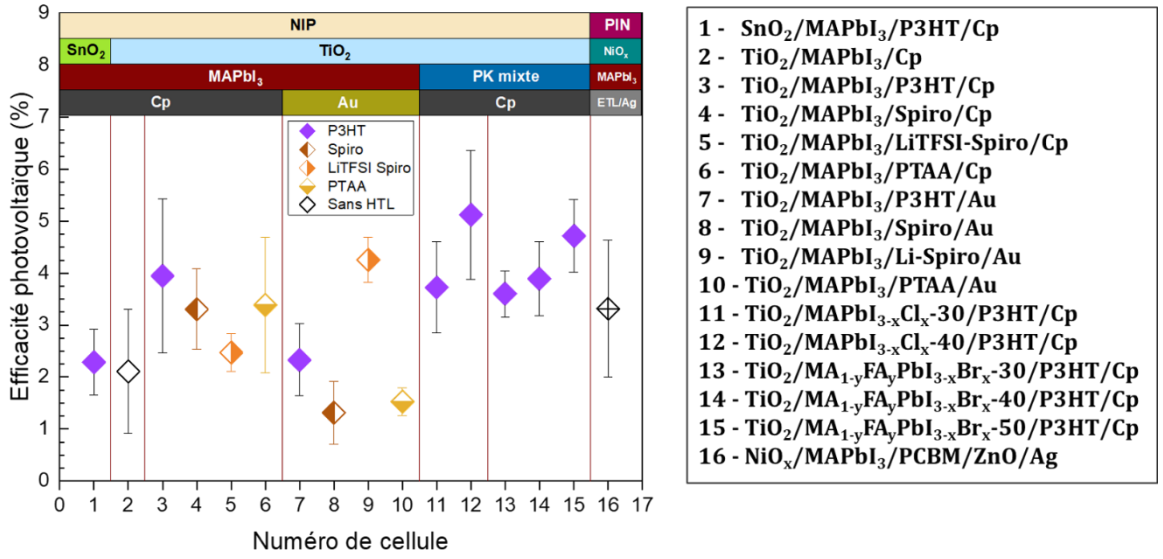

Figure 43: Variation du PCE moyen pour toutes les architectures de cellules solaires et formulations pérovskites testées dans ces travaux de thèse

En terme de perspectives à ces travaux de thèse, nous pouvons tout d'abord imaginer le développement d'une stratégie par électrodéposition permettant de répondre à une préoccupations majeure concernant la toxicité du plomb. Puisqu'elles possèdent une bande interdite appropriée, les pérovskites sans plomb sont apparues comme élément principal dans les PSCs pour garantir une technologie photovoltaïque propre et verte. La substitution du plomb par Sn, Ge, Bi, Sb, Cu et d'autres candidats potentiels pourrait être l'une des perspectives de ce travail de thèse. Une seconde préoccupation concernant la formulation de la pérovskite est la stabilité du matériau pérovskite en lui-même. Bien que les pérovskites électrodéposées élaborées dans ce travail aient offert une stabilité remarquable par rapport à celles développée par enduction centrifuge, leur stabilité pourrait probablement être encore améliorée. En effet, il a été prouvé que l'utilisation d'additifs, comme le 5-AVAI, a un effet significatif sur l'efficacité des PSCs et leur stabilité. Une méthode d'incorporation de ce genre d'additif pourrait donc être imaginé lors de notre processus d'élaboration de la PK.

Par ailleurs, l'architecture des dispositifs solaires est également l'un des principaux facteurs déterminants des performances des PSCs. Ce sujet mérite donc d'être approfondi, en optimisant le dépôt des couches de transport, leur épaisseur et leur nature. Améliorer les interfaces entre les différentes couches est un moyen de garantir un bon transfert de charge. Afin de contribuer de façon innovante à ce segment de recherche et

développement, une perspective ambitieuse et majeure à ce premier travail sur l'électrodéposition pourrait consister à l'élaboration d'une PSC entièrement par électrodéposition. En effet, le but du travail présenté dans ce manuscrit était principalement de substituer la méthode de dépôt par enduction centrifuge car elle est non-applicable sur de grandes surfaces. Cependant, nous l'avons utilisée pour déposer des couches autres que la PK au sein de nos dispositifs photovoltaïques. L'électrodéposition des couches de transport, en plus de la couche de pérovskite active, est donc une excellente idée pour élargir ce sujet. D'après la littérature, plusieurs matériaux traditionnellement utilisés comme couches HTL ou ETL pourraient être réalisés par électrodéposition, tels que TiO_2, SnO_2, CuSCN, P3HT, PTAA, ZnO. La problématique principale réside dans le fait que les pérovskites sont sensibles à l'eau. Il est donc important de trouver une architecture applicable où la couche suivant la pérovskite pourrait être électrodéposée dans une solution non aqueuse et non délétère pour sous-couche pré-déposée de pérovskite.

Enfin, en plus des campagnes de vieillissement appliquées dans le travail présenté, la stabilité des dispositifs solaires tels que préparés se doit être étudiée avec un système adéquat d'encapsulation. Cela offrira une vision plus claire du potentiel de ces PSCs électrodéposées en termes de stabilité.

Annex

In this annex, we will first present the optimization of the electrodeposition of the PbO_2 layer chosen as a starting material for the elaboration of a perovskite layer.

In order to enhance the efficiency of the solar cell, the optimization of the different ETLs and HTLs used is also essential. Hence, we present the optimization of the TiO_2, the P3HT and the Spiro-OMeTAD layers, by changing the precursor solution's concentration or the spin coating parameters, and comparing the different formulations in solar devices.

In addition, a comparison will be presented between the commercial carbon paste used in this work and other carbon pastes elaborated in our laboratory.

1- Optimization of the electrodeposition parameters of PbO_2

Many parameters can affect the film thickness and morphology such as the pH of the electrolyte, its concentration, its temperature, the voltage applied on the electrodes and the time of electrodeposition. The effect of these parameters needs to be investigated.

For the electrodeposition tests, an aqueous solution containing 0.1 M lead(II) acetate trihydrate and 0.2 M sodium nitrate served as an electrodeposition (ED) bath for PbO_2 films. This electrolyte was labeled C and it was diluted for later experiments. The pH adjustments were done with nitric acid until having pH values of 2, 4 and 5.5 respectively for several solutions. ITO substrates, or ITO/$SnO_{2\ spin\text{-}coated}$ substrates acted as working electrodes, with the active deposition area being 2.55 cm^2 (1.5 × 1.7 cm^2). A spring-shaped platinum electrode was used as the counter electrode and an Ag/AgCl/KCl_{sat} electrode as the reference electrode. The electrodeposition was carried out at a potential range between 1.2 V and 2 V versus the reference electrode for a deposition time between 15 s and 60 s, to be able to optimize the parameters. A brownish color appears indicating the formation of PbO_2. The perovskite conversion presented in this section was direct from PbO_2 (PK1 method).

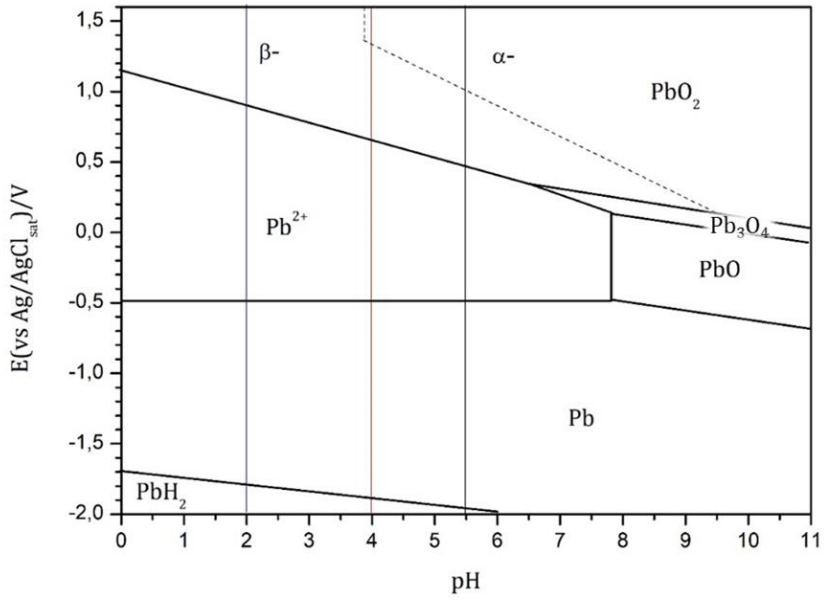

Figure A1: Pourbaix diagram of lead

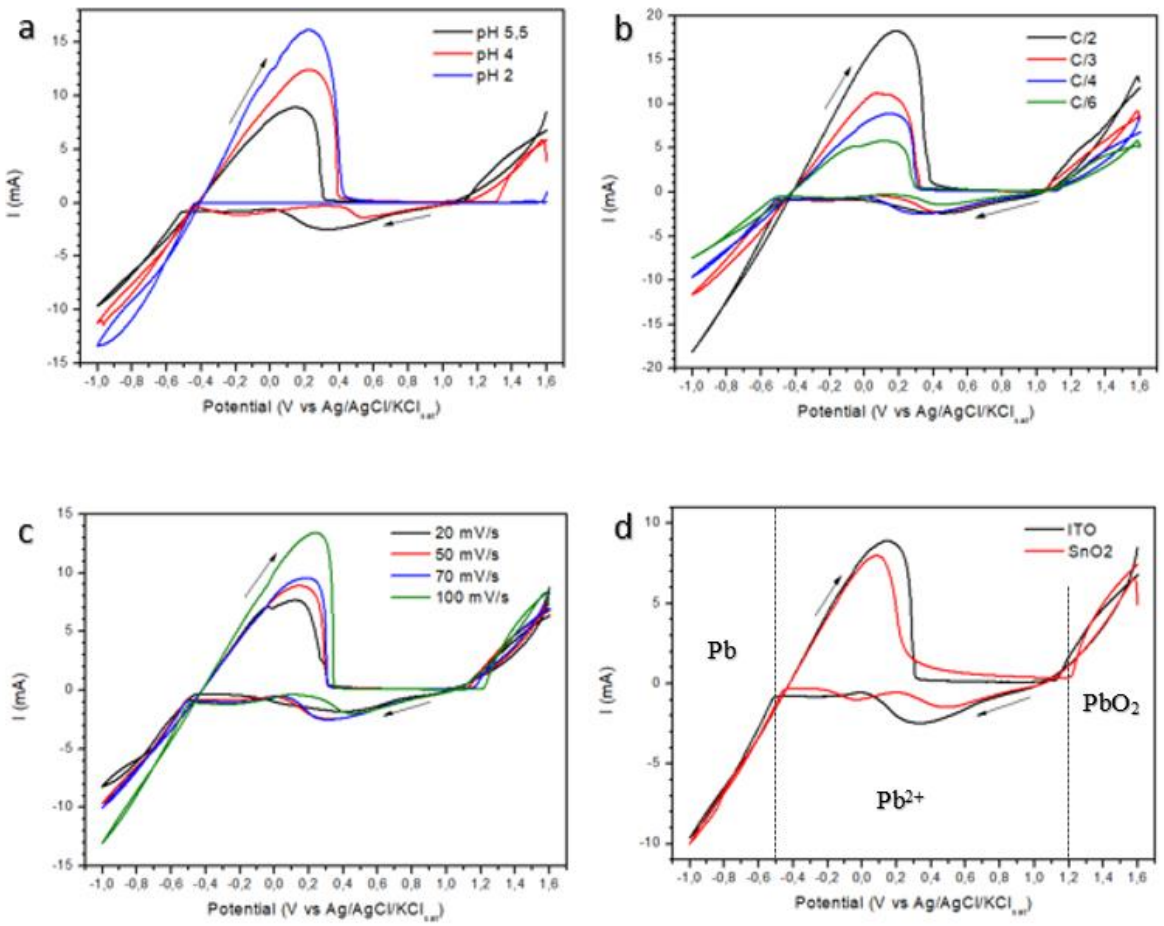

Figure A2: Cyclic voltammograms of the aqueous solution of $Pb(CH_3COO)_2{\cdot}3H_2O$ and $NaNO_3$ (1:2) obtained (a) at different pH values on ITO for the concentration C/4 and a scan rate of 50mV/s, (b) on ITO with different electrolyte concentrations having a pH of 5.5 and with a scan rate of 50 mV/s , (c) at different scan rates on ITO for a concentration of C/4 and a pH of 5.5 and (d) for different substrates at a scan rate of 50mV/s for the concentration C/4 and a pH of 5.5.

First, cyclic voltammetry was conducted in the selected electrolyte to deduce the onset oxidation potential for PbO_2 deposition, on different substrates, for different solutions with varying pH and concentrations, and at different scan rates. As observable in Figure A2 and after comparison with the Pourbaix diagram of lead in Figure A1 (adapted from Hyde *et al.* [346]), the PbO_2 formation is reachable for potentials above 1.1 V. A potential of 1.5 V versus $Ag/AgCl/KCl_{sat}$ was thus chosen for the following experiments.

In fact, the current brutally increases in the forward sweep. This potential corresponds to the oxidation potential for the formation of PbO_2 via Reaction 1:

$$Pb^{2+} + 2H_2O \rightarrow PbO_2 + 4H^+ + 2e^- \qquad \text{Reaction 1}$$

This onset potential changes a little with the change of the substrate because of the variation of the deposition kinetics (Figure A2-d).

As the potential proceed backward in the reverse sweep, a cathodic peak appears at lower potentials (onset starting from about 0.7V), representing the reduction reaction of the PbO_2 previously deposited during the forward sweep, according to Reaction 2:

$$PbO_2 + 4H^+ + 2e^- \rightarrow Pb^{2+} + 2H_2O \qquad \text{Reaction 2}$$

The reduction potential as the oxidation potential varies when changing the pH of the electrolyte (Figure A2-a). Its value well corresponds to that noticed on the Pourbaix diagram where this value increases when decreasing the pH ($E_{Pourbaix}$ = 0.4V and 0.6V vs. $Ag/AgCl_{sat}$ for respectively pH=5.5 and 4). This value is barely visible for a pH=2. In fact, for such low pH, the PbO_2 electrodeposition was difficult to conduct (longer time or shift to higher potentials > 1.6V needed), but not impossible. As shown in Figure A2-b and Figure A2-c, changing the concentration of the electrolyte does not affect the onset oxidation potential, but increasing the scan rate of the voltammetry can slightly delay the start of oxidation.

Otherwise, the second oxidation peaks appearing around 0V in the forward scan represent the ionization of formed lead in negative potentials. Thus, we need to be careful to stay at voltage higher than the end of this peak, i.e above 0.5V.

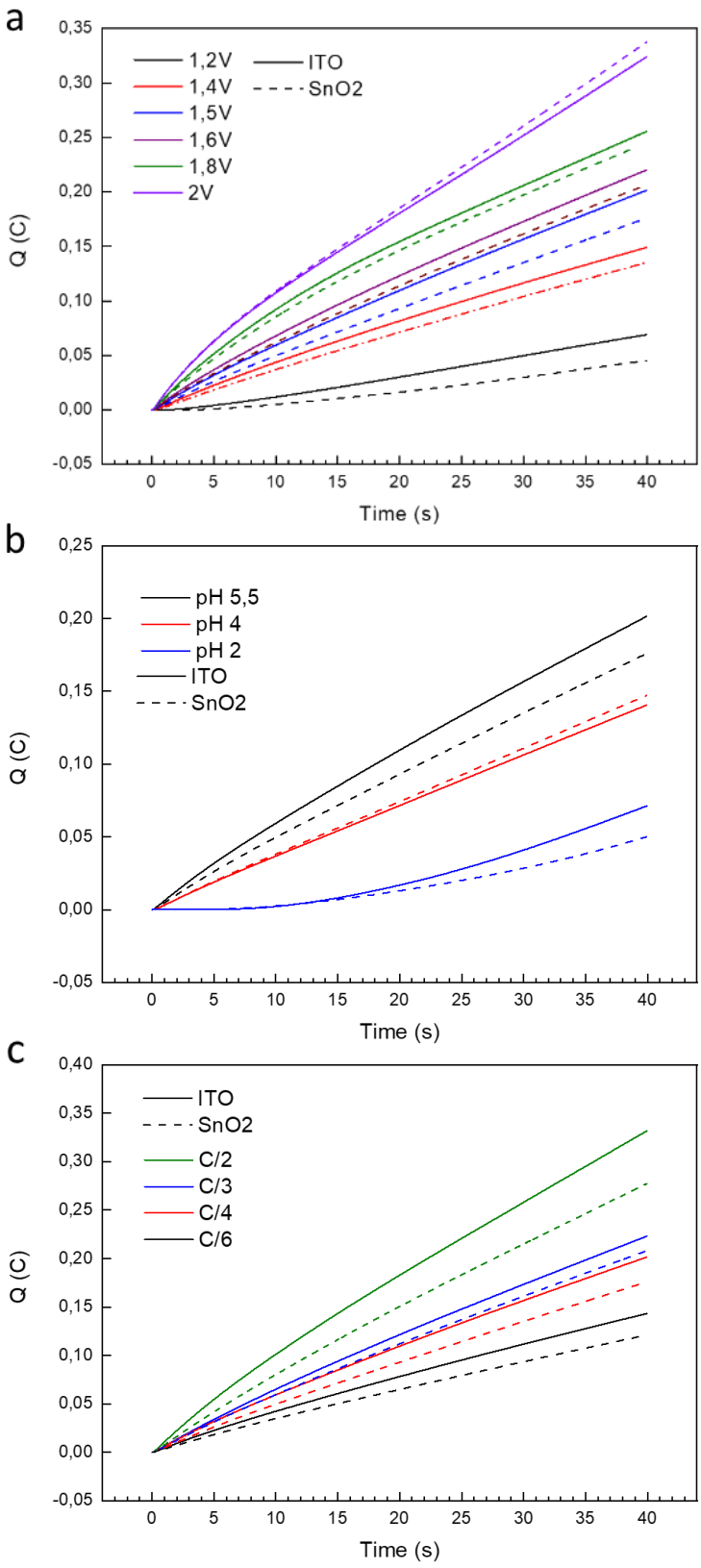

Figure A3: Chronocoulometry curves showing the variation of the charge as a function of time during electrodeposition of PbO_2 for the two substrates ITO and SnO_2, a) at different potential values for the concentration C/4 and a pH of 5.5, b) at different pH values for the concentration C/4 and a potential of 1.5 V, c) at different concentrations for a pH of 5.5 and a potential of 1.5V

First, chronocoulometry curves were registered during PbO_2 electrodeposition showing the variation of the charge as a function of time for different deposition potentials, as shown in Figure A3-a (pH = 5.5 and concentration = C/4). We can see that the selected deposition potential at 1.5V is a good compromise between PbO_2 deposition speed and the occurrence of water oxidation.

Then, chronocoulometry curves were registered at different pH values and for different solution concentrations, as shown in Figure A3-b and c. For each pH, the concentration was fixed at C/4 and the potential at 1.5 V. Also, when variating the electrolyte concentration, we worked with the same voltage and a pH of 5.5. The comparison of these curves by calculating their slopes is important to identify the parameter that most affects the electrodeposition.

The slope in Figure A4 represents the variation of charge with time, hence the velocity of charge transfer. When comparing for same parameters on different substrates, it is noticed that this slope has a lower value for SnO_2 substrates than for ITO. This could be due to the sheet resistance of each substrate that affects directly the charge transfer, and more precisely its velocity. ITO substrates used here have a sheet resistance of 7 Ohm/sq whereas elaborated SnO_2 substrates have a higher one of 139 Ohm/sq.

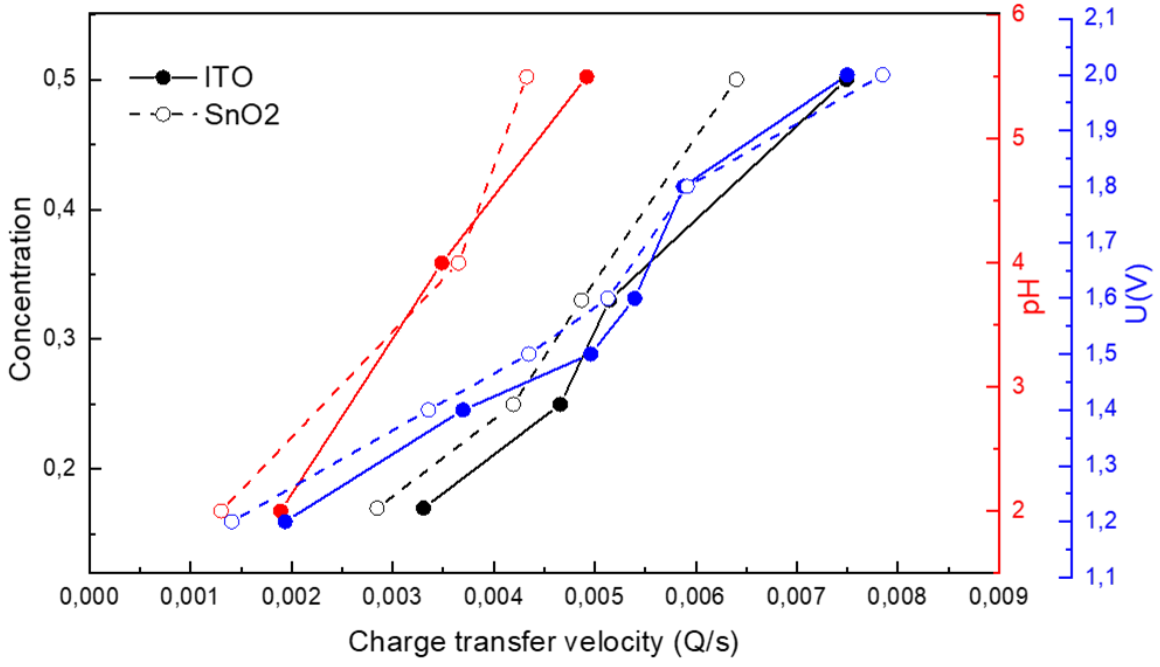

Figure A4: Impact of the concentration of the electrolyte, the pH of the electrolyte and the applied potential on the slope variation of chronocoulometry curves

The variation of the films thickness was studied when variating the parameters. Previous results show good homogeneous films with average thickness for a potential of 1.5 V, so it was chosen as a fixed potential for the upcoming work. Figure A5 shows the distribution of PbO_2 and perovskite thicknesses when changing parameters. It is clear that the thickness of both types of films increases when increasing the deposition time and decreases when decreasing the concentration of the electrolyte. However, there is no clear relation between the thickness of the films and the pH of the solution. On the other

hand, when analyzing the distribution of different films thicknesses with same parameters, the distribution variation between PbO_2 and perovskite thicknesses is opposite.

When it comes to the variation of perovskite thickness for different electrolyte concentrations, the distribution is large for the smallest electrolyte concentration used (i.e. also corresponding to the smallest PbO_2 layer thickness). It is thus advised to work with an average concentration of at least C/4 to avoid having very thick perovskite layers (undoubtedly related to some large crystals growth). When increasing the deposition time, as expected the thickness of the films increases. The deposition time was thus optimized using additional characterizations using SEM images for the final obtained perovskite layers.

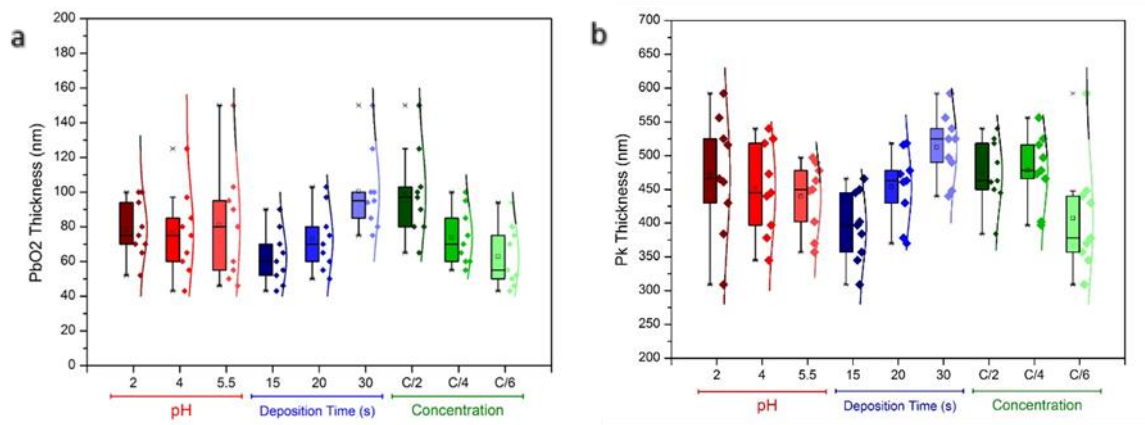

Figure A5: Boxplot showing the variation of (a) PbO_2 and (b) Perovskite thickness deposited on ITO for different pH values, different deposition times and different electrolyte concentrations (only the potential was fixed at 1.5V)

A relation between the roughness and thickness of initial PbO_2 and final perovskite films was also demonstrated in Table A1. Perovskite layers possess an average roughness of 24 nm, whereas PbO_2 layers had an average roughness of 3 nm, which was extracted from profilometry profiles. Although there is a big difference in roughness when converting the PbO_2 films into $MAPbI_3$, the ratio of this roughness compared to the thickness is not that different. This ratio is slightly higher for perovskite films than for PbO_2. Also, no big change of the roughness is noted when changing the parameters if checking the standard deviation of the average value. Hence, the morphology of the films had to be studied to explain this behavior.

Table A1: Table showing the ratio of the roughness versus the thickness for both PbO_2 and perovskite films.

	Average Thickness (nm)	Average Roughness (nm)	Roughness/Thickness
PbO_2	96.8	3.2 ± 1	3.8 %
Perovskite	465.6	24.2 ± 4	5.4 %

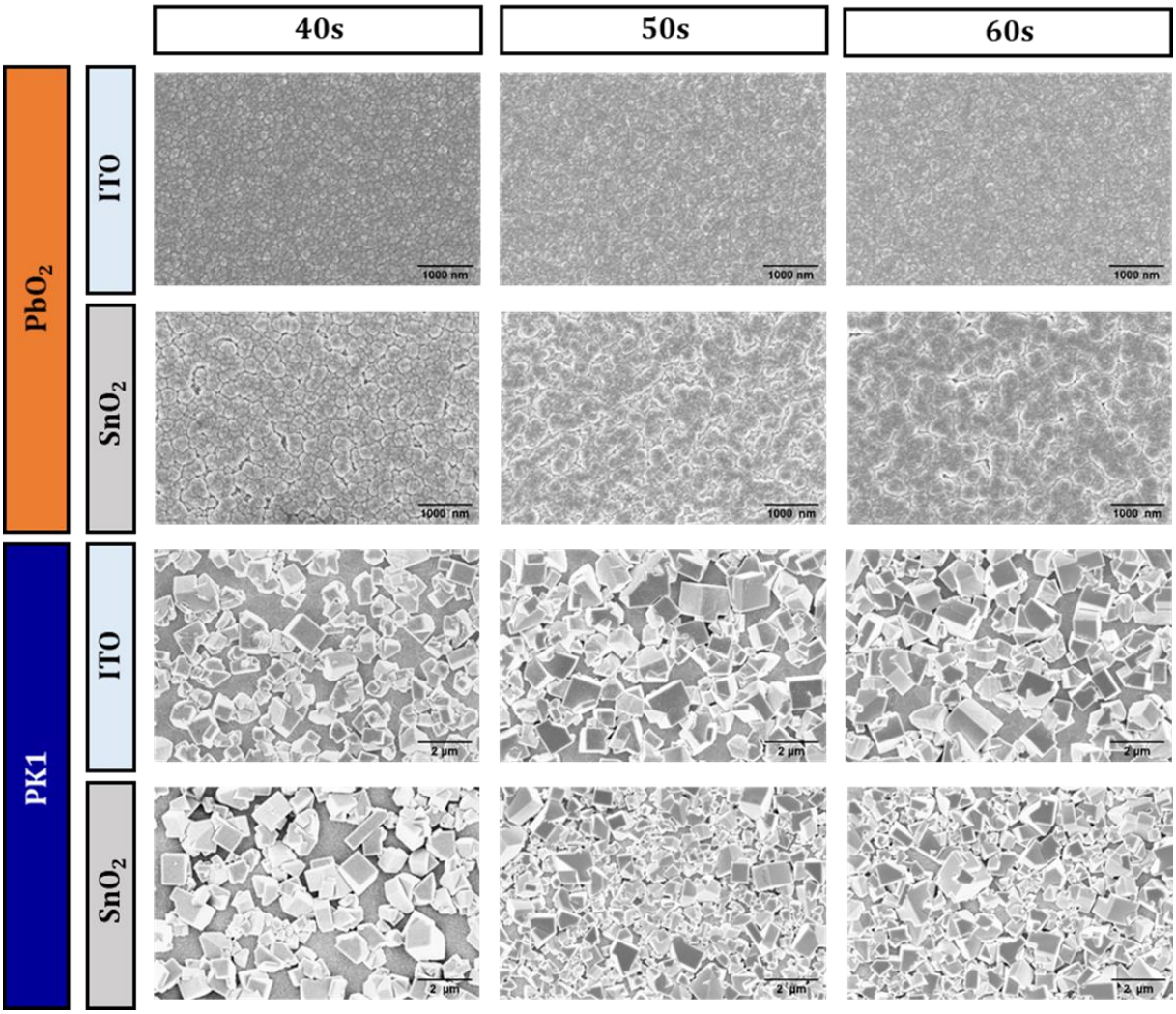

Figure A6: Top-view SEM images of (a) ITO/PbO_2, (b) SnO_2/PbO_2, (c) ITO/$MAPbI_3$ and (d) SnO_2/$MAPbI_3$ electrodeposited for respectively 40, 50 and 60s.

The in-plane morphology of the PbO_2 and $MAPbI_3$ films directly converted was checked using scanning electron microscope (SEM) images. Figure A6 shows the variation of the morphology of PbO_2 and perovskite films when increasing the deposition time on both ITO and SnO_2 substrates. The deposition time was chosen to be more than 30s, since the previously deposited PK layers had a very small thickness and showed minimum coverage. Electrodeposited PbO_2 has a smooth surface morphology with full surface coverage on both ITO and SnO_2 substrates. It can be noticed that PbO_2 deposited on SnO_2 has bigger grains than that deposited on ITO for all different deposition times. However, depositing on SnO_2 may incite the grains to coalesce into global agglomerates which are separated by small gaps. Using higher magnifications allows the detection of small granules that adds up to form these agglomerates.

The converted $MAPbI_3$ films consist of rectangular-shaped grains with a non-uniform orientation. An increase in the grain size is easily noticed for the $MAPbI_3$ films comparing to the initial PbO_2 films. Clearly, increasing the deposition time increases the surface coverage on both substrates, but it is greater for SnO_2 than for ITO, reaching 91% of area coverage on SnO_2 substrate for a deposition time of 50s, and maintaining this percentage for 60s, as shown in Figure A6. Although a larger grain size is favorable for obtaining high

efficiency in perovskite-based devices as it translates to a lower grain boundary density, improving the charge transfer properties, and retard hydration and decomposition, covering all the surface is more important when developing photovoltaic cells to prevent the creation of short circuits inside the device. EDS spectra were coupled with the SEM to check the composition of the films and to verify the nature of the uncovered surface. The change of the substrate does not affect the EDS spectra of PbO_2 or $MAPbI_3$. On the other hand, the uncovered surface shows no sign of Pb which indicates that this surface is mainly the substrate surface. After these analyses, the deposition time was fixed at 50s, leading to a perovskite film with average thickness of 600 nm with a grain size of about 500 nm and a maximization of the coverage area (see Figure A7).

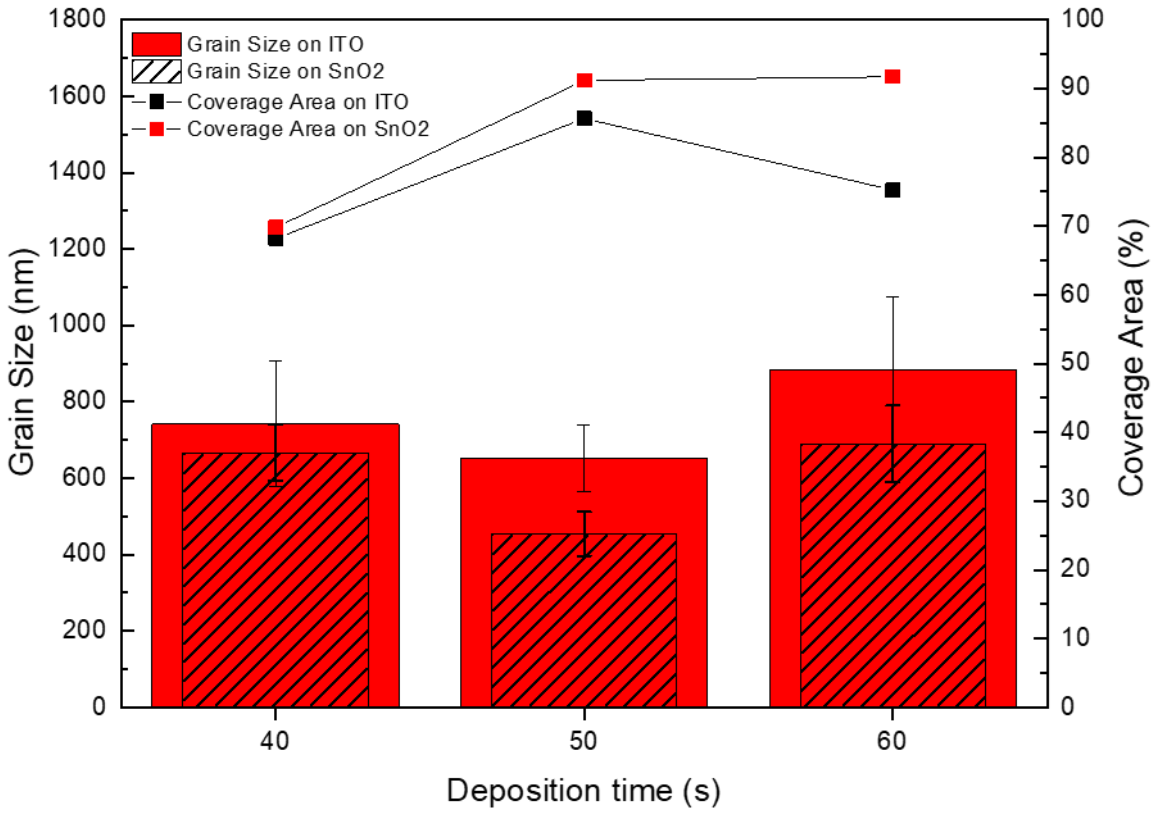

Figure A7: The variation of the grain size of perovskite and the coverage area with respect to the deposition time for both substrates

2- Optimization of the TiO_2 ETL layer

We used spin coating for the deposition of the mesoporous TiO_2 layer on compact TiO_2. The Ti-Nanoxide T600/SC is a solution for the formation of 600 nm thick mesoporous titania layers purchased from Solaronix. However, the optimized thickness of TiO_2 scaffold is around 400 nm [22], so the as-mentioned precursor solution must be diluted with ethanol. The obtained solution was spin coated using the same conditions as for the blocking layer, and then sintered at 475°C for 30 min.

The diluted solutions are as follows:

- T600: 7% TiO_2 – (100% T600 solution)
- T300: 5% TiO_2 – (1000 µL T600 + 400 µL EtOH)
- T225: 4% TiO_2 – (1000 µL T600 + 750 µL EtOH)
- T150: 3% TiO_2 – (1000 µL T600 + 1330 µL EtOH)

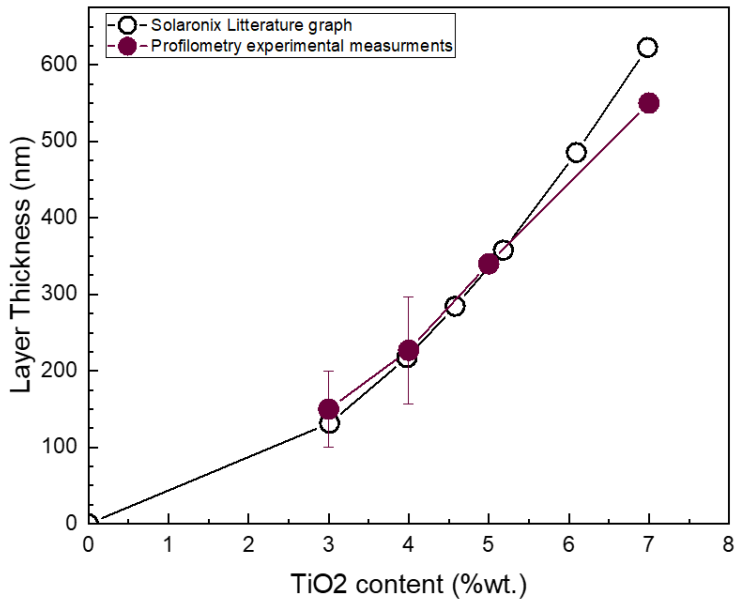

Figure A8: TiO_{2m} thickness function of TiO_2 content in precursor solution

To elaborate different thicknesses of TiO_2, we used Solaronix graph[347] showing variation of TiO_2 layer thickness as a function of its content in the precursor solution, and obtained similar results as presented in Figure A8.

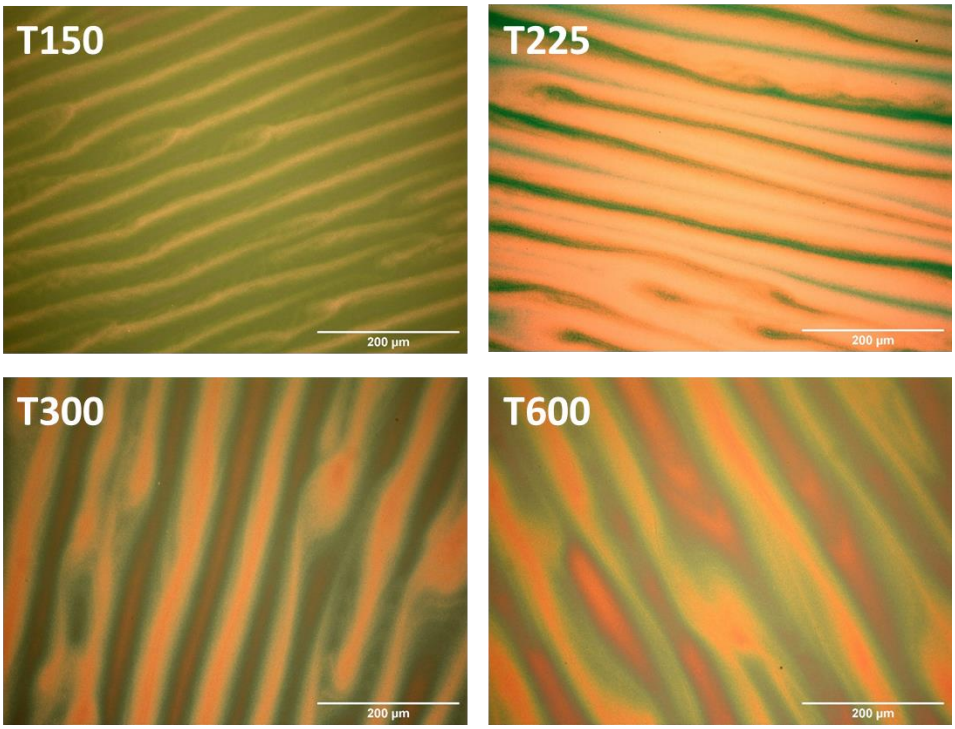

Figure A9: Optical microscopy images of TiO_{2m} with different thicknesses

When checking the elaborated TiO_{2m} films in the optical microscope in Figure A9, the pores can be easily detected and not only the TiO_2 thickness changes, but also the pore sizes.

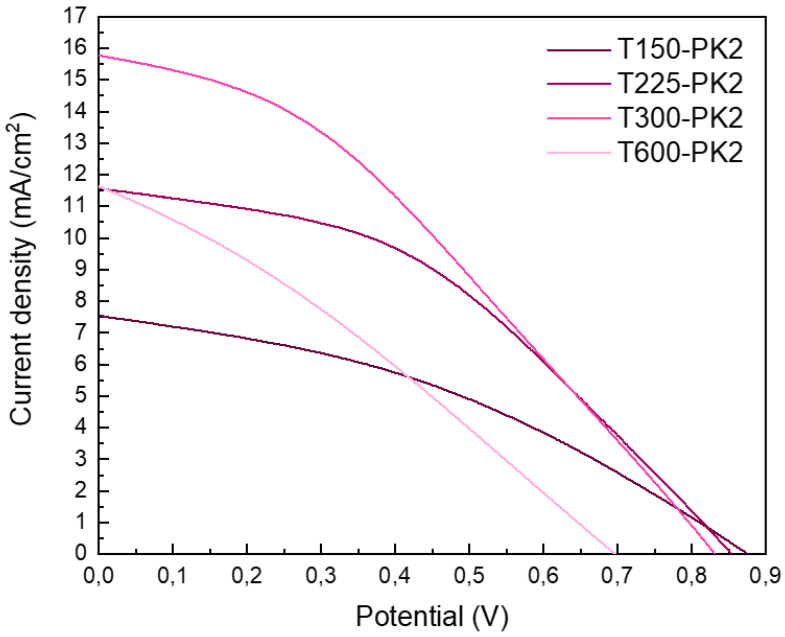

Figure A10: J(V) curves of solar devices elaborated using different TiO_{2m} thicknesses (active surface 0.13 cm^2)

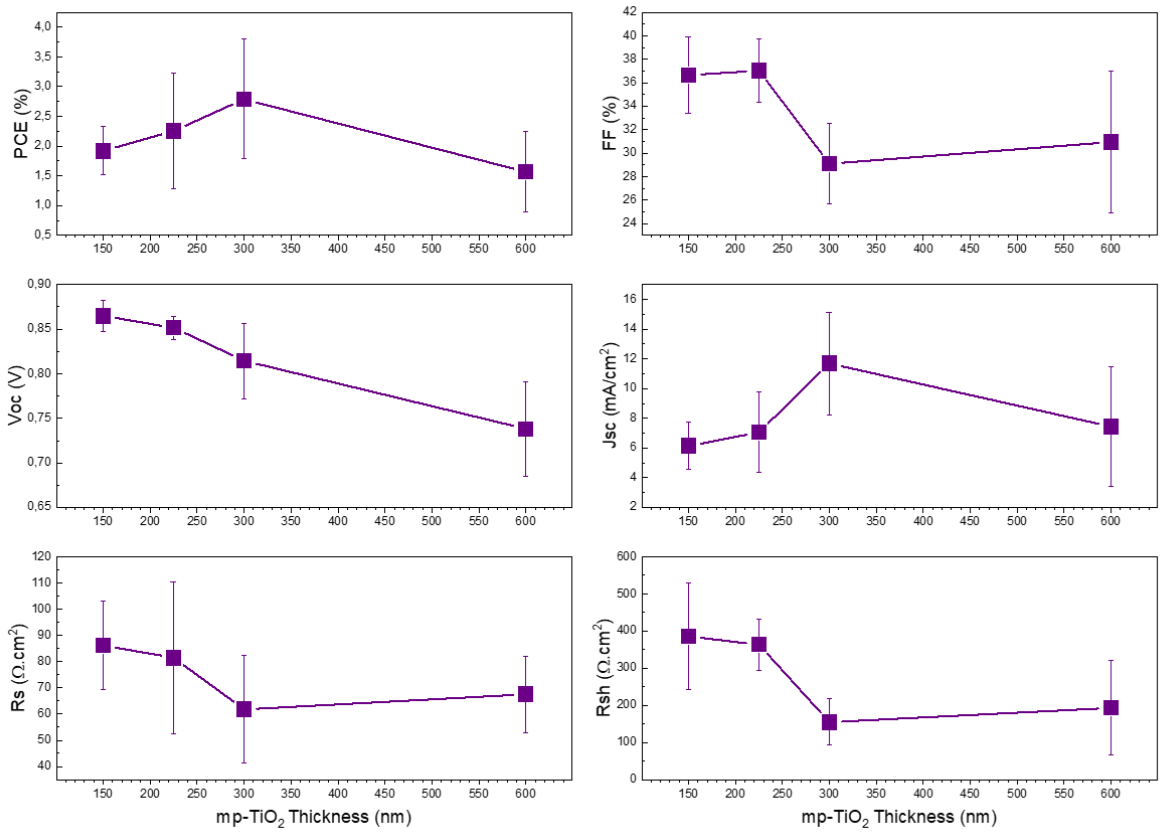

Figure A11: Variation of the photovoltaic parameters as a function of TiO_{2m} thickness (electrodeposition conditions were here fixed at 100s in order to cover all the TiO_2 scaffold by perovskite and thus avoid short-circuit)

When verifying the efficiency of the solar devices in Figure A10 and Figure A11, we notice the best PCE for T300 because its offers the best J_{sc}. However FF tends to decrease when we increase the TiO_{2m} thickness, as for the Rs. V_{oc} gradually decrease when we increase TiO_{2m} thickness, which can be assigned to better quality layer and less recombination for lower TiO_{2m} thicknesses. J_{sc} depends on the thickness of the absorber. It must be thick enough to absorb the highest cut off wavelength of the incident solar radiation. However, for T600 it is too thick, so there will be recombination of the excitons if they left travelling more than their diffusion length before dissociation.

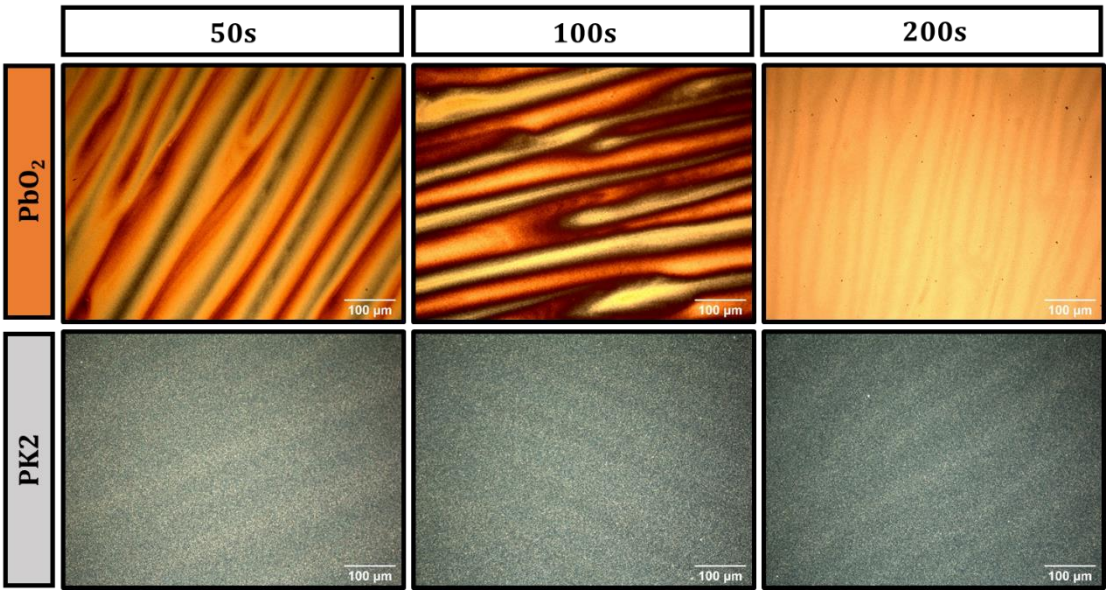

Figure A12: Optical Microscope images showing the growth mechanism of PbO_2 in TiO_2 porous scaffold T300 by electrodeposition when increasing ED duration

The PbO_2 growth mechanism is expected to be a bottom-up growth on the porous scaffold. The goal here is to try and fill the mesoporous structure with PbO_2 up to the surface. Since TiO_2 is mesoporous, we should verify that PK covers all the pores to avoid short circuits in the solar device. We can see in Figure A12 that for a 200s duration of the electrodeposition (ED) process, PbO_2 fully covers the TiO_2 pores; however, when converting to PK, it give very thick layers. In optical microscopy images for converted PK, we see that for 50, 100 and 200s of ED, PK will cover the pores. This analysis was verified with SEM. Figure A13 presents the top-view images of PK2 deposited on T300 for 50 and 100s ED duration and comparing it to PK2 deposited on T600 for 100s ED duration.

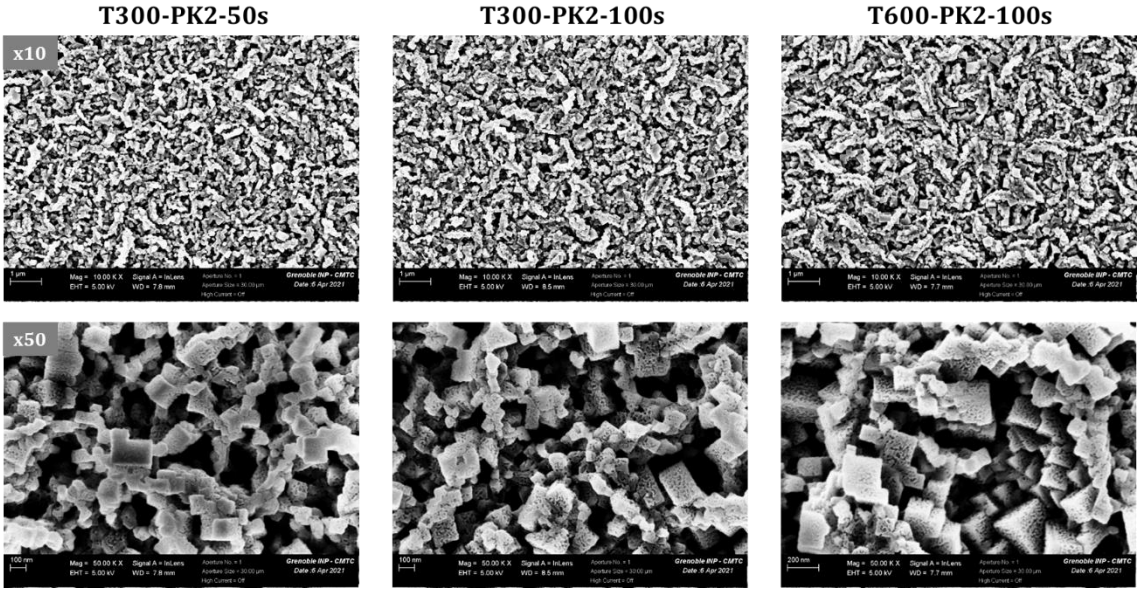

Figure A13: SEM images for PK2 on T300 (50s and 100s ED) and T600 (100 s ED)

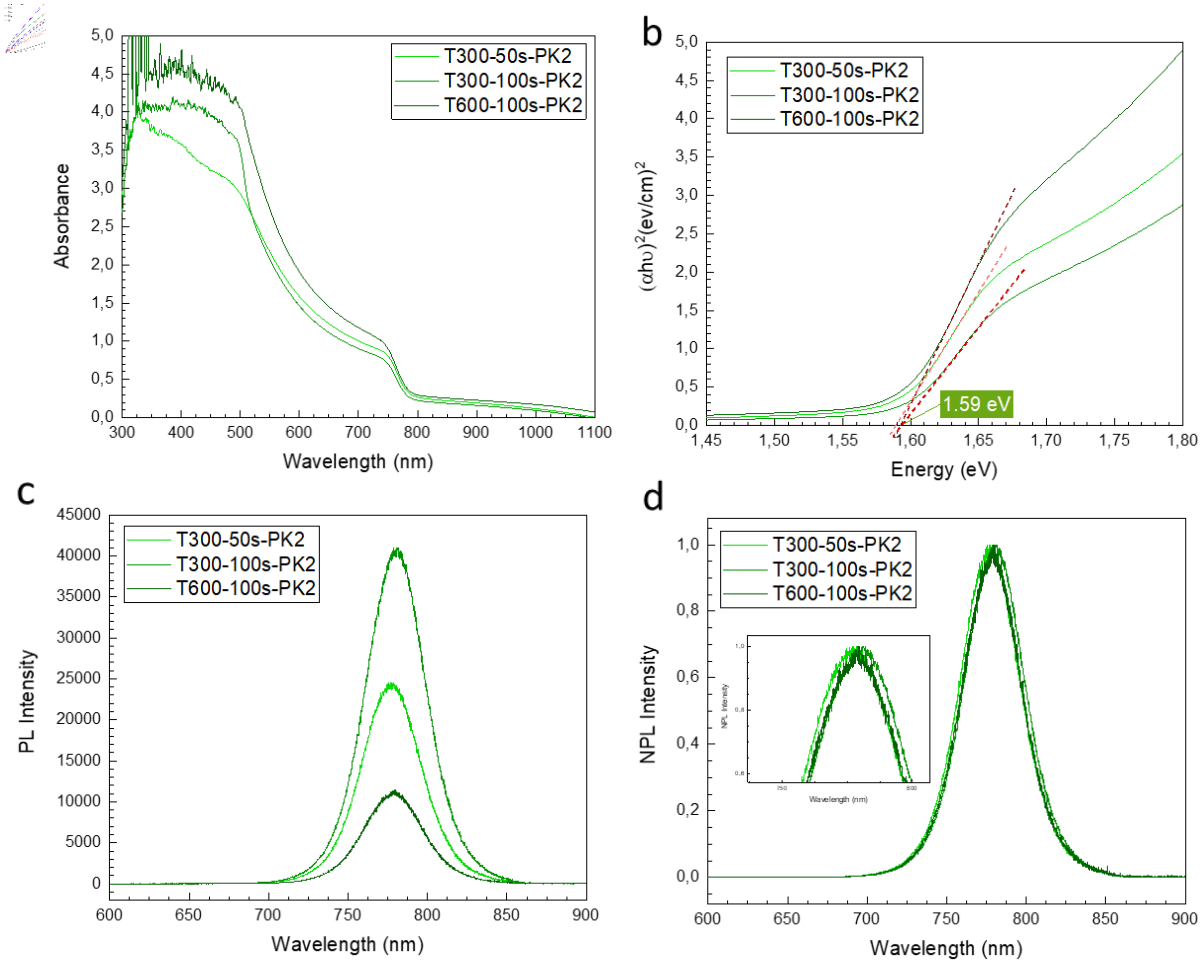

Figure A14: UV-visible absorption spectra, their Tauc plots, PL spectra and Normalized PL spectra for PK2 on T300 (50s and 100s) and on T600 (100s)

The UV-visible absorption spectra, presented in Figure A14 along with their Tauc plots, show that the PK2 deposited on T300 (50s et 100s) and on T600 (100s) have the same band gap, slightly smaller absorbance at lower wavelength for T300-50s, which can be explained in a smaller surface coverage. In the PL spectra in Figure A14, the shift is negligible. We notice that T600-100s presents the smallest I_{max}, and T300-100s the highest I_{max}, although we detected better efficiency for T300-100s.

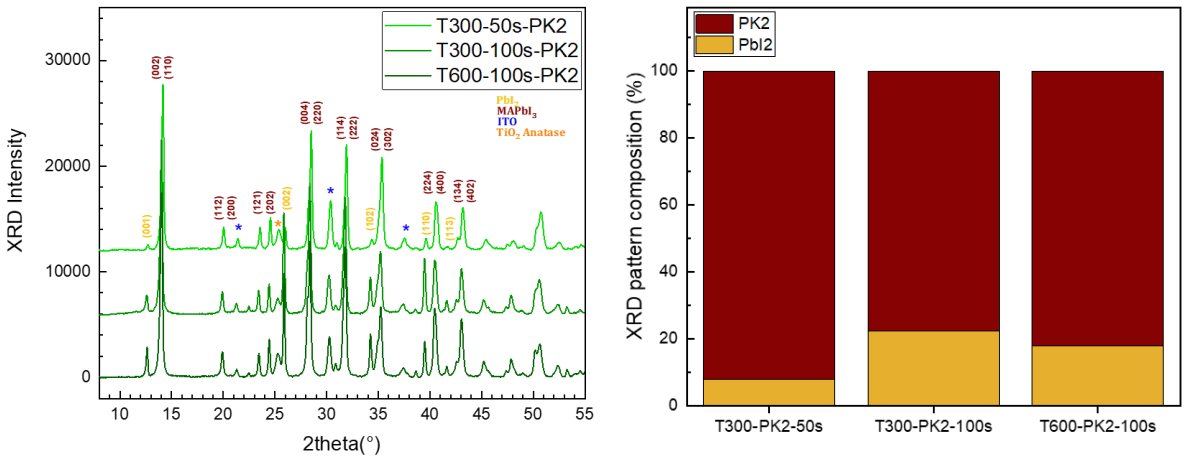

Figure A15: XRD pattern for PK2 on T300 (50s and 100s) and on T600 (100s) and the composition of these films deduced from these patterns

The XRD patterns of the PK2 deposited on T300 (50s and 100s) and on T600 (100s) are presented in Figure A15, along with the composition of these films. They show identical patterns, the only difference being the ratio of crystalline PbI_2 that is lower for T300-50s and higher for T300-100s.

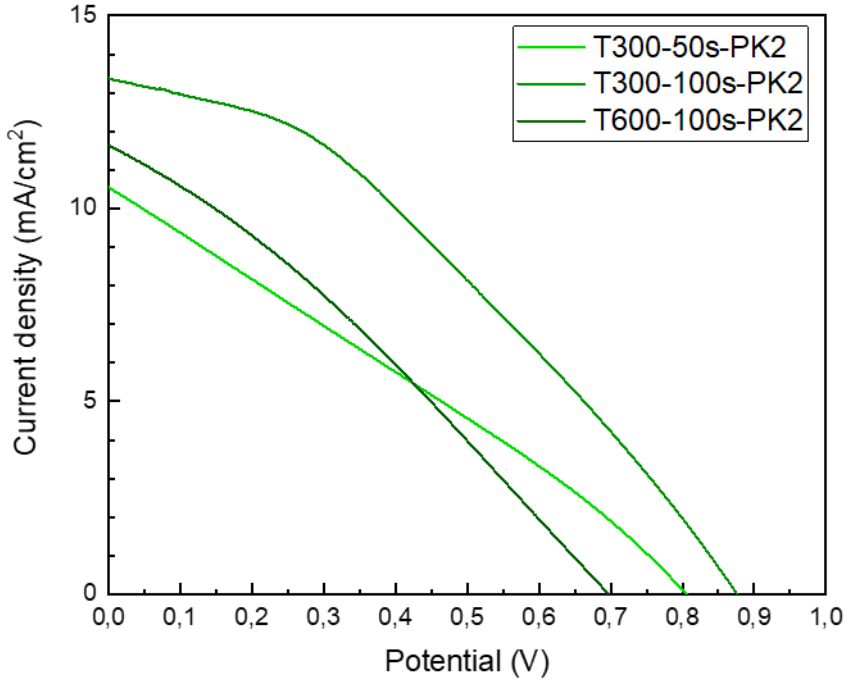

Figure A16: J(V) curves for PK2 on T300 (50s et 100s) and on T600 (100s) (0.1 cm²)

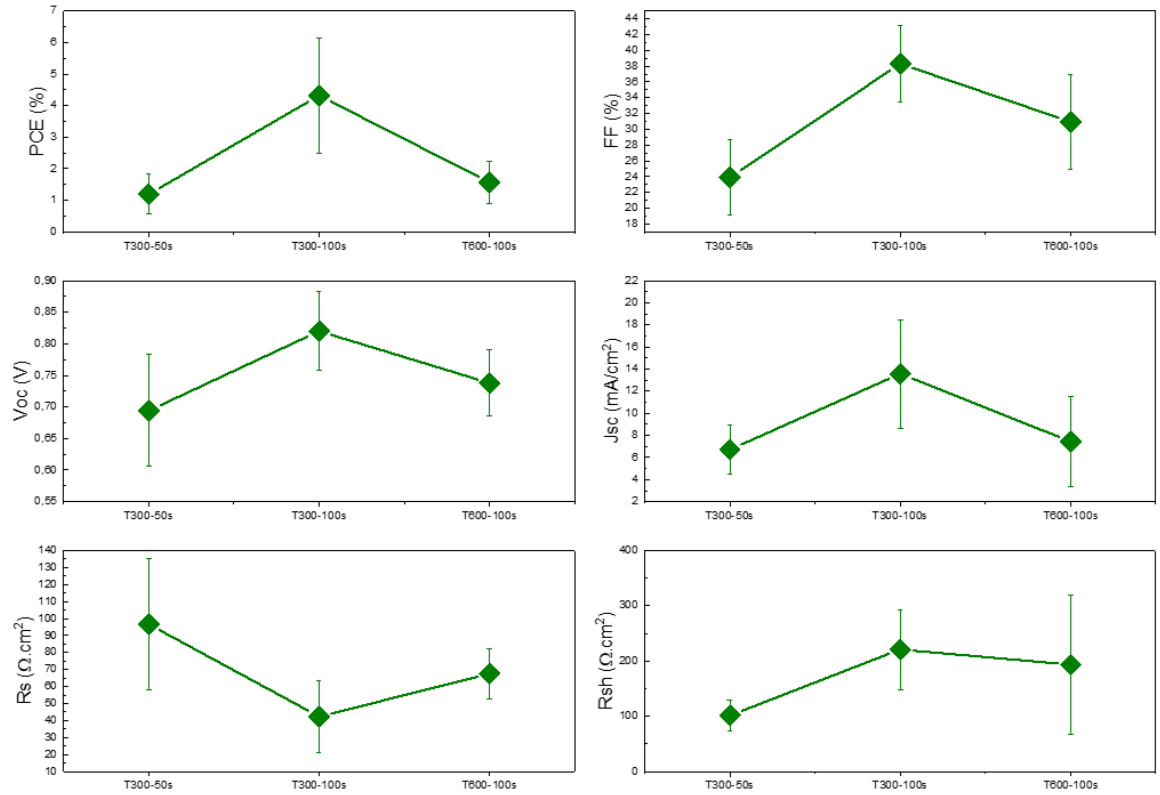

Figure A17: Variation of the photovoltaic parameters for PK2 on T300 (50s et 100s) and on T600 (100s)

Although T300-50s seemed to be a good candidate (same BG, lower I_{max}, lower PbI_2 content), we can see in Figure A16 and Figure A17 that it gave the lowest PCE, FF, Jsc and Voc, which validates the fact that the coverage for 50s is not optimal. The best TiO_2 to work with is T300, with PK2 electrodeposited for 100s.

3- Optimization of P3HT HTL layer

The P3HT was first deposited on PK using a 15 mg/mL P3HT in chlorobenzene solution, spin coated on the perovskite using the velocity V1 (25rps/4s/40s, 33rps/4s/30s).

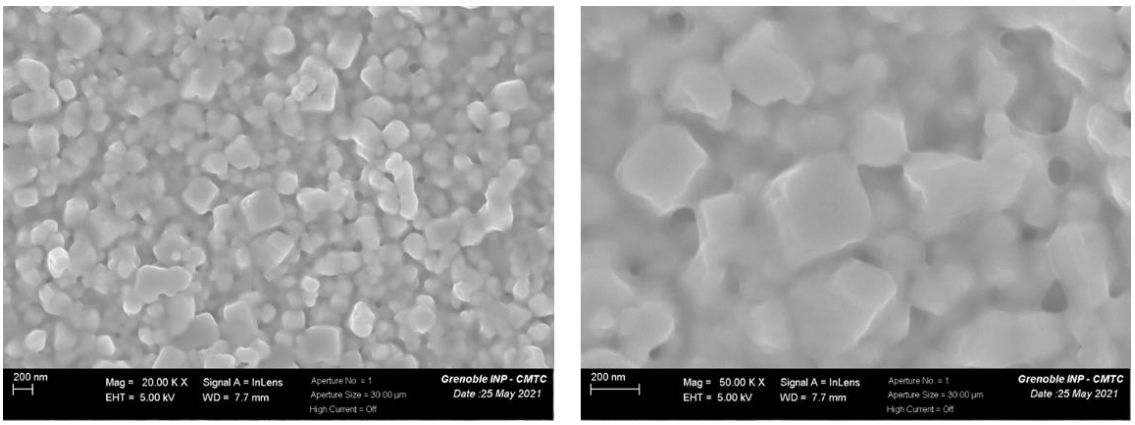

Figure A18: Top-view SEM images of ITO/ TiO_{2c}/T300/PK2/P3HT when P3HT is deposited with the conditions V1 (Mag 20K x and 50K x)

In the SEM images presented in Figure A18, we can see that P3HT does not totally cover the PK, because PK2 has a high roughness. A fully covered surface must be obtained to avoid any direct contact between the perovskite and the carbon electrode. Hence we should optimize the deposition of P3HT to obtain a higher thickness.

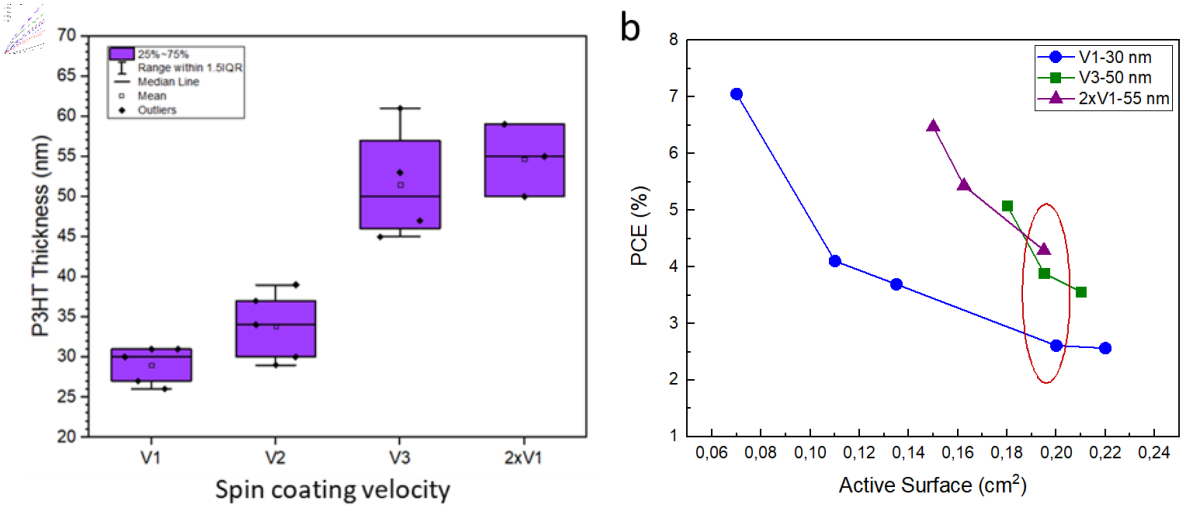

Figure A19: Box plots showing a) the variation of P3HT thickness function of the spin coating velocity, and b) the PCE of ITO/ TiO_{2c}/T300/PK2/P3HT/Cp PSCs function of the active surface when changing the spin coating velocity

The variation of the thickness of P3HT when increasing the spin-coating velocity is presented in Figure A19. The spin-coating parameters for the tested velocities are as follows: V1 (25rps/4s/40s, 33rps/4s/30s), V2 (15rps/1s/1s, 25rps/1s/30s), V3 (10rps/2s/5s, 15rps /2s/60s), and 2xV1 is a P3HT layer deposited twice using V1 on the same substrate. The most homogeneous film having the greater thickness is the one to choose, since the obtained perovskite layers have a rather important roughness. To verify this hypothesis, solar devices with different active surfaces were elaborated using the different P3HT layers (ITO/TiO_{2c}/T300/PK2/P3HT/Cp). We can see that for the same active surface, 2xV1 has the highest PCE, however this layer is more complicated to elaborate. We chose to work with V3 since it is always homogeneous and easier to elaborate than 2xV1.

4- Optimization of Spiro-OMeTAD HTL layer

Our first attempt to use Spiro-OMeTAD (Spiro) as HTL in our PSCs was by spin coating 50 µL of a Spiro solution (containing 72.3 mg Spiro and 28.8 µL TBP in 1 mL CBZ). The spin coating velocity called VS1 was 15rps/1s/1s, then 25rps/1s/30s. PSCs using this formulation with an architecture ITO/TiO_2c/T300/PK2/Spiro/Cp (0,18 cm^2) were tested while verifying a proposition by Li *et al* in the literature noting that the Spiro layer should be exposed to air for 20h after deposition[348]. These Spiro films were also compared to Spiro doped with LiTFSI (72.3 mg Spiro and 28.8 µL TBP in 1 mL CBZ + 17.5 µL of a solution containing 520 mg/mL LiTFSI in acetonitrile). The results are presented in Figure A20.

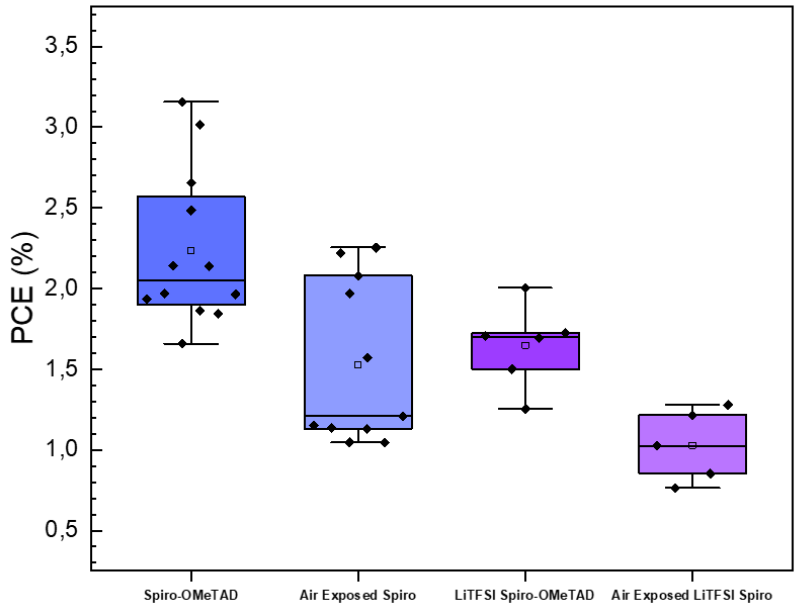

Figure A20: Box plots showing the variation of the PCE when using Spiro and doped Spiro with and without exposing to air before depositing the contact electrode.

We noticed that when using a carbon electrode on top of the Spiro HTL layer, it is better to use a non-doped Spiro film. Also, it is better to not expose the films to air. However, the obtained efficiencies are not as high as expected, so we decide to check if it is a thickness problem. The thickness of the Spiro (non-doped and doped) elaborated using VS1 is between 220 nm and 260 nm which is relatively high. We can also see in the SEM images in Figure A21 that the Spiro layer covers totally the surface of the PK, contrarily to what we saw with P3HT. Hence, the thickness of the Spiro layer must be decreased by increasing the spin coating velocity.

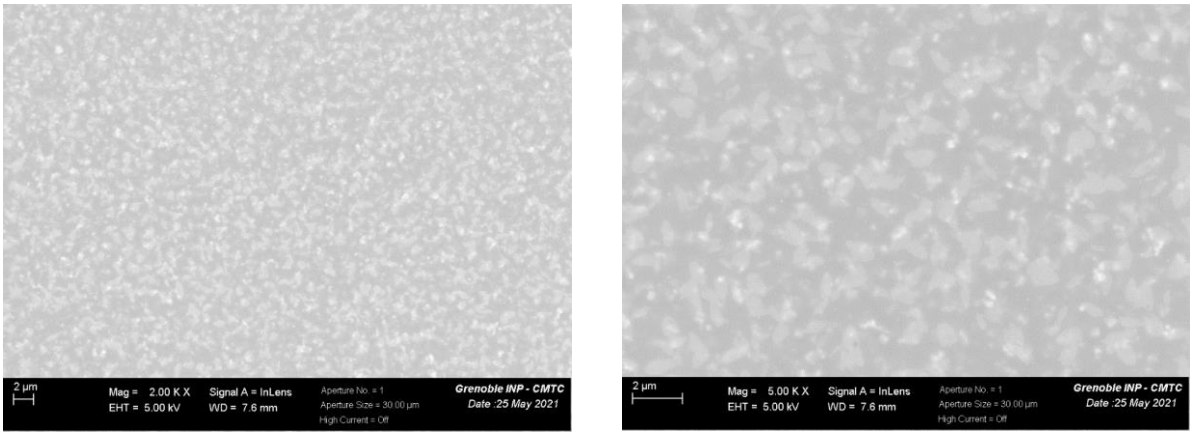

Figure A21: Top-view SEM images of ITO/ TiO_{2c}/T300/PK2/Spiro when Spiro is deposited with the conditions VS1 (Mag 2K x and 5K x)

The thickness of different Spiro films (LiTFSI-doped and non-doped) was measured using profilometry while changing the spin coating velocities as follows: VS1(15rps/1s/1s, 25rps/1s/30s), VS2 (25rps/2s/40s, 33rps/4s/30s), VS3 (40rps/2s/10s, 50rps/2s/25s) and VS4 (25rps/2s/1s, 67rps /2s/30s). This time 100 µL of the former precursor solutions were used for the spin coating. The results are presented in Figure A22. As

expected, increasing the spin coating velocity decreases the film thickness until reaching a thickness of 100 nm for LiTFSI-doped Spiro films spin coated with VS4.

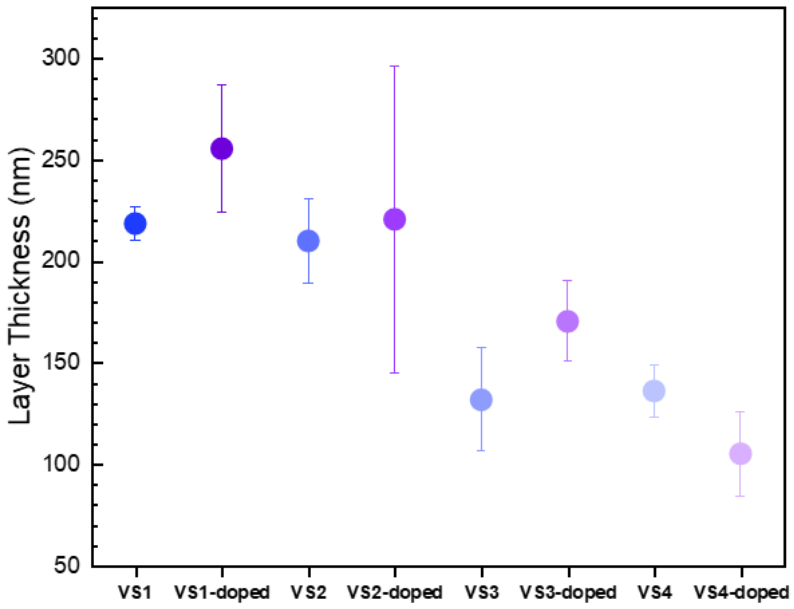

Figure A22: The variation of the Spiro layer thickness when changing the spin coating velocity.

We then compared the efficiencies of the PSCs elaborated using VS1 and VS4 (ITO/TiO_{2c}/T300/PK2/Spiro/Cp) and the results are presented in Figure A23. VS4 gives better efficiencies for non-doped Spiro and VS1 is better for LiTFSI-doped Spiro.

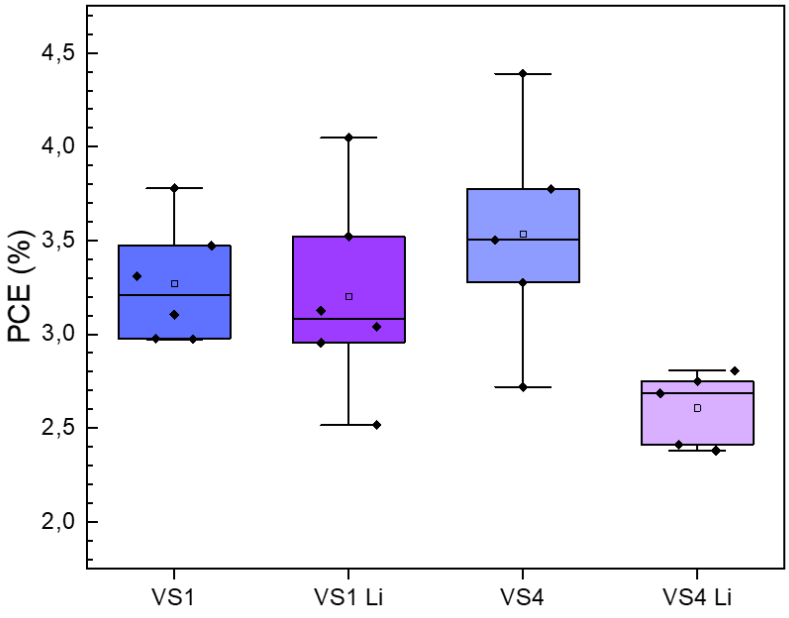

Figure A23: Box plots showing the variation of the PCE when using Spiro and doped Spiro spin coated at the velocities VS1 and VS4.

5- Optimization of the annealing conditions of the commercial Dyenamo carbon paste and attempts to formulate a carbon paste in the laboratory

In this thesis, the carbon electrode used on the PSCs was elaborated by doctor-blading a commercial carbon paste (Cp) by Dyenamo (DN-CP01). This carbon paste is characterized by its low-temperature annealing conditions. However, it is important to choose the best annealing conditions of this carbon paste on top of our perovskite since the perovskite material in general is unstable. First, we measured the thickness (using profilometry) and the sheet resistance (using the four-point method) of Cp layers deposited on glass and annealed for 15 min at different temperatures under vacuum and at 120°C in air. 120°C under vacuum for 15 min are the conditions suggested by the provider. The results are presented in Figure A24.

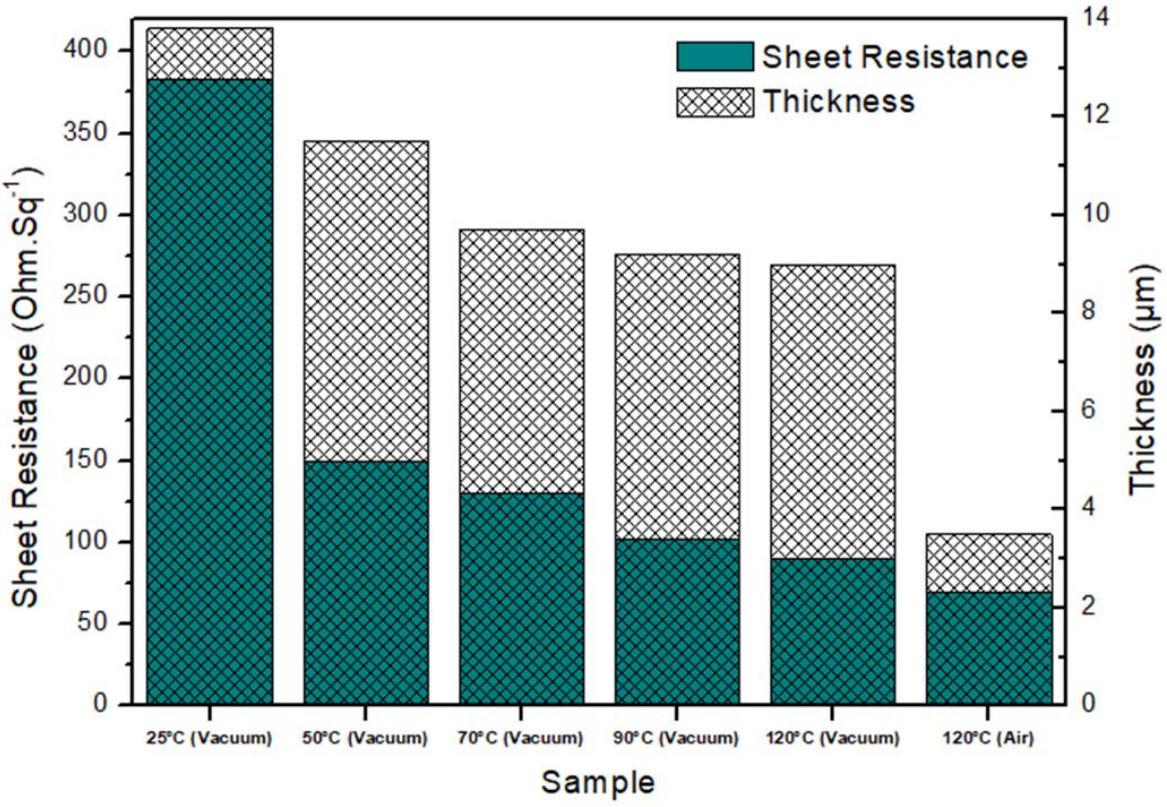

Figure A24: Histogram showing the variation of the Dyenamo Cp film thickness and Sheet resistance annealed for 15 min at different temperatures, under vacuum or in ambient atmosphere

We notice that the sheet resistance is not directly related to the thickness of the film. However, they both decrease when we increase the annealing temperature, and the smallest sheet resistance and thickness are detected for 120°C – air.

Thermogravimetric analysis (TGA) were also elaborated on this commercial carbon paste to verify the evaporation and decomposition of the solvents and additives after annealing. The results for the initial Cp without annealing, the Cp annealed at 60°C and at 120°C for

15 min are presented in Figure A25. We notice that we have to anneal at 120°C to get rid of the solvents inside the carbon paste.

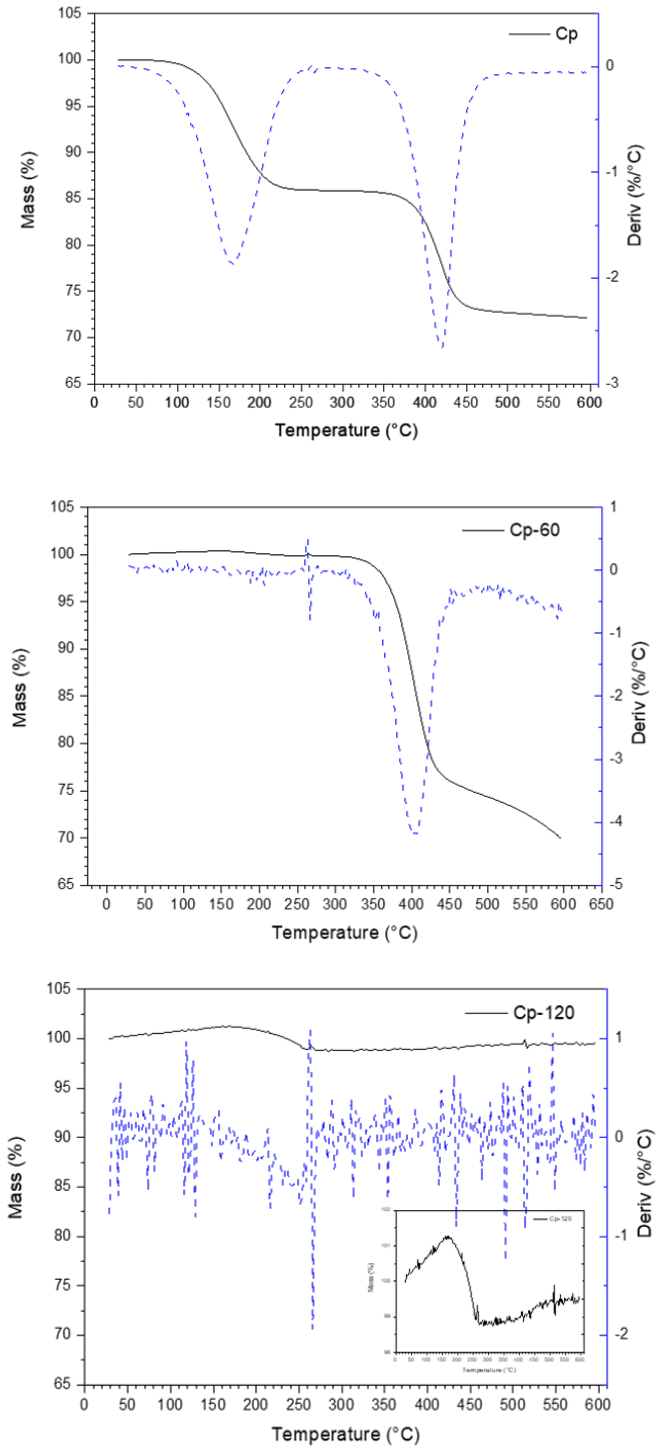

Figure A25: TGA of the Dyenamo carbon paste without annealing Cp, annealed at 60°C Cp-60 and annealed at 120°C Cp-120 (TGA conditions: under vacuum at 10K/min)

We would like to mention that several attempts were considered by our team to elaborate a carbon paste in the lab. The aim was to find a carbon paste compatible with a lower annealing temperature in order to reduce the potential stress which will be applied to the perovskite layer during the Cp annealing step. We tried to use solvent engineering but this

method was hard to elaborate and did not give as good results as expected. However, we were able to develop carbon pastes with different compositions using a formulation close to that of Zhang *et al.*[349]. 2 g carbon black powders (N990 - 280 nm) mixed with 6 g graphite powders (TIMREX different size) in a 30 mL ethyl acetate solution, and then 1 g of 20 nm ZrO_2 nanopowders and 1 g of ethyl cellulose were added into solution, followed by stirring vigorously using ball milling for 2 h at 500 rpm. This formulation was elaborated several times while changing the graphite size (check Table below) and the resistivity was compared to that of the commercial Dyenamo and Solaronix carbon pastes in Figure A26.

	Graphite name	**Graphite size**
P1	KS150	75 µm
P2	KS500	400 µm
P3	KS150-600	500 µm

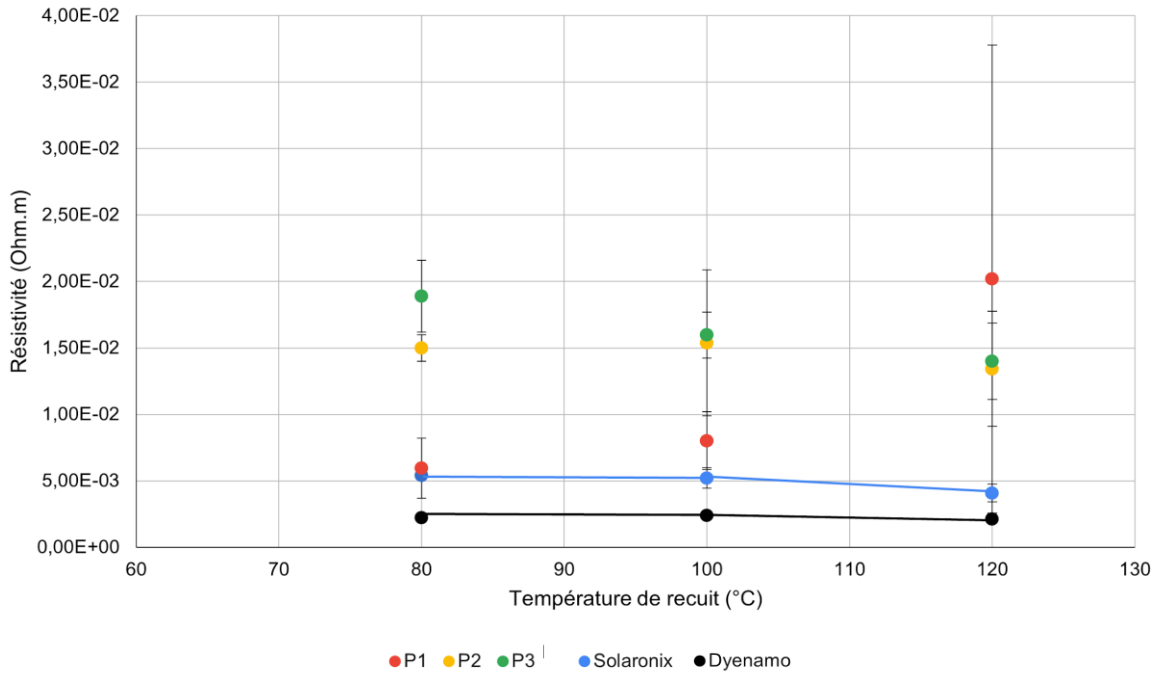

Figure A26: Comparison of the resistivity of the Cp films for the different formulations function of the annealing temperature

The ideal annealing temperature for commercial pastes was found to be 120 °C, whereas it is 80 °C for the paste P1 formulated in the laboratory. Our formulated pastes give good results at low temperature (80 °C) because their solvents are very volatile. Incidentally, in their case, increasing the annealing temperature at 100 or 120°C can be detrimental for some formulations.

Important uncertainties were detected on home-made formulated pastes due to the lack of homogeneity of the solutions. They give higher resistivity than commercial pastes and

are difficult to apply because they dry quickly. However, after a 80°C annealing time, our P1 paste possesses properties very close to commercial ones.

The table below presents the annealing conditions used in the following tests.

Carbon paste	Annealing T°C	Annealing time
P1 - 75 µm	80°C	15 min
P2 - 400 µm	120°C	15 min
P3 - 500 µm	120°C	15 min
Solaronix	120°C	30 min
Dyenamo	120°C	30 min

The three formulated Cp along with the commercial Solaronix and Dyenamo ones were tested in PSCs (ITO/TiO_{2c}/ TiO_{2m}/PK2/P3HT/Cp) and a comparison is presented in Figure A27. The obtained PCEs were much higher using Dyenamo paste, probably due to the lowest resistivity detected previously.

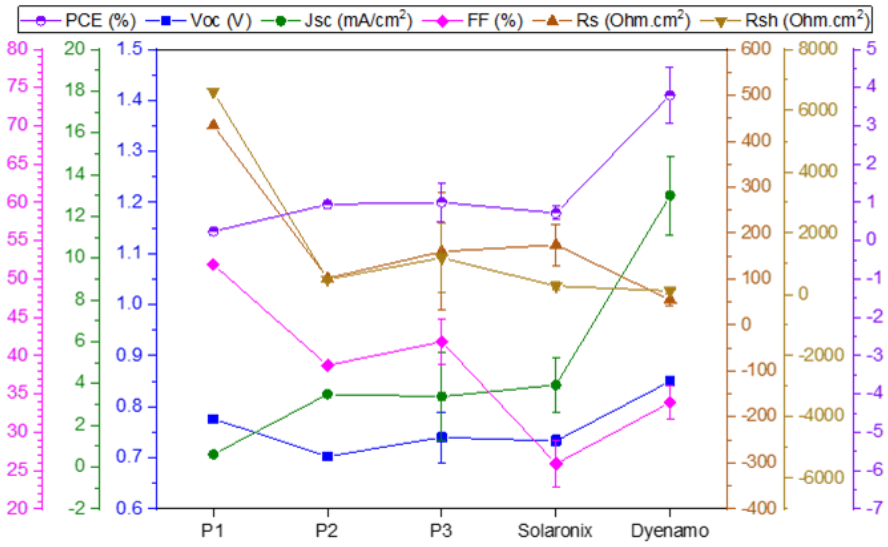

Figure A27: The photovoltaic parameters of the PSCs elaborated using different types of Cp

References

1. El Chaar, L. & El Zein, N. Review of photovoltaic technologies. *Renew. Sustain. energy Rev.* **15**, 2165–2175 (2011).
2. Chamberlain, G. A. Organic solar cells: A review. *Sol. cells* **8**, 47–83 (1983).
3. Garboushian, V., Kinsey, G. S., Stone, K., Crawford, C. & Gordon, R. Performance of Amonix multijunction arrays. in *High and Low Concentrator Systems for Solar Electric Applications IV* vol. 7407 740703 (International Society for Optics and Photonics, 2009).
4. Carella, A., Borbone, F. & Centore, R. Research progress on photosensitizers for DSSC. *Front. Chem.* **6**, 481 (2018).
5. Park, N.-G. Organometal perovskite light absorbers toward a 20% efficiency low-cost solid-state mesoscopic solar cell. *J. Phys. Chem. Lett.* **4**, 2423–2429 (2013).
6. Grätzel, M. The light and shade of perovskite solar cells. *Nat. Mater.* **13**, 838–842 (2014).
7. Xing, G. *et al.* Long-range balanced electron-and hole-transport lengths in organic-inorganic CH3NH3PbI3. *Science (80-.).* **342**, 344–347 (2013).
8. National Renewable Energy Laboratory 2021. https://www.nrel.gov/pv/cell-efficiency.html.
9. Mahmood, K., Sarwar, S. & Mehran, M. T. Current status of electron transport layers in perovskite solar cells: materials and properties. *Rsc Adv.* **7**, 17044–17062 (2017).
10. Berhe, T. A. *et al.* Organometal halide perovskite solar cells: degradation and stability. *Energy Environ. Sci.* **9**, 323–356 (2016).
11. Xu, T., Chen, L., Guo, Z. & Ma, T. Strategic improvement of the long-term stability of perovskite materials and perovskite solar cells. *Phys. Chem. Chem. Phys.* **18**, 27026–27050 (2016).
12. Xu, F., Zhang, T., Li, G. & Zhao, Y. Mixed cation hybrid lead halide perovskites with enhanced performance and stability. *J. Mater. Chem. A* **5**, 11450–11461 (2017).
13. Jacobsson, T. J. *et al.* Exploration of the compositional space for mixed lead halogen perovskites for high efficiency solar cells. *Energy Environ. Sci.* **9**, 1706–1724 (2016).
14. Correa-Baena, J.-P. *et al.* The rapid evolution of highly efficient perovskite solar cells. *Energy Environ. Sci.* **10**, 710–727 (2017).
15. Maniarasu, S. *et al.* Recent advancement in metal cathode and hole-conductor-free perovskite solar cells for low-cost and high stability: A route towards commercialization. *Renew. Sustain. Energy Rev.* **82**, 845–857 (2018).
16. Huang, J. *et al.* Direct conversion of CH 3 NH 3 PbI 3 from electrodeposited PbO for highly efficient planar perovskite solar cells. *Sci. Rep.* **5**, 15889 (2015).
17. Lee, D. S. *et al.* Electrochemical approach for preparing conformal methylammonium lead iodide layer. *Electrochem. commun.* **103**, 120–126 (2019).

18. Koza, J. A., Hill, J. C., Demster, A. C. & Switzer, J. A. Epitaxial electrodeposition of methylammonium lead iodide perovskites. *Chem. Mater.* **28**, 399–405 (2015).

19. Kosta, I., Grande, H. & Tena-Zaera, R. Dimethylformamide-free processing of halide perovskite solar cells from electrodeposited PbI2 precursor films. *Electrochim. Acta* **246**, 1193–1199 (2017).

20. Cui, X.-P. *et al.* Electrodeposition of PbO and its in situ conversion to CH3NH3PbI3 for mesoscopic perovskite solar cells. *Chem. Commun.* **51**, 1457–1460 (2015).

21. Li, W., Yang, J., Jiang, Q., Li, R. & Zhao, L. Electrochemical deposition of PbI2 for perovskite solar cells. *Sol. Energy* **159**, 300–305 (2018).

22. Chen, H., Wei, Z., Zheng, X. & Yang, S. A scalable electrodeposition route to the low-cost, versatile and controllable fabrication of perovskite solar cells. *Nano Energy* **15**, 216–226 (2015).

23. Popov, G., Mattinen, M., Kemell, M. L., Ritala, M. & Leskelä, M. Scalable Route to the Fabrication of CH3NH3PbI3 Perovskite Thin Films by Electrodeposition and Vapor Conversion. *ACS Omega* **1**, 1296–1306 (2016).

24. Abdy, H., Heydari, Z., Aletayeb, A., Kolahdouz, M. & Asl-Soleimani, E. Electrodeposition, solvent engineering, and two-step solution deposition of the perovskite films: morphological and structural study. *J. Mater. Sci. Mater. Electron.* **32**, 12991–12999 (2021).

25. Liu, D. *et al.* Low-voltage room-temperature electrochemical deposition of perovskite films for solar cell devices. *Sol. Energy* **212**, 275–281 (2020).

26. Yadav, J., Liang, Q. & Pan, S. Electrochemical Deposition of Organometallic Halide Perovskite Single-Crystal Particles with Density Gradients and Their Stability, Fluorescence, and Photoelectrochemical Properties. *J. Phys. Chem. C* **124**, 10659–10668 (2020).

27. Heydari, Z. *et al.* A novel approach for preparation of CH 3 NH 3 PbBr 3 via direct transformation of electrodeposited PbO 2 for photodetector application. *J. Mater. Sci. Mater. Electron.* **31**, 154–160 (2020).

28. Charles, U. A., Ibrahim, M. A. & Teridi, M. A. M. Electrodeposition of organic–inorganic tri-halide perovskites solar cell. *J. Power Sources* **378**, 717–731 (2018).

29. Zanca, C., Sunseri, C. & Inguanta, R. Fabrication and characterisation of perovskite thin films for photovoltaic application. in *2018 IEEE 4th International Forum on Research and Technology for Society and Industry (RTSI)* 1–4 (IEEE, 2018).

30. Lv, P. *et al.* The preparation of all-inorganic CsPbI2− xBr1+ x perovskite solar cells based on electrodeposited PbO2 film. *Sol. Energy* **207**, 618–625 (2020).

31. Hill, J. C., Koza, J. A. & Switzer, J. A. Electrodeposition of epitaxial lead iodide and conversion to textured methylammonium lead iodide perovskite. *ACS Appl. Mater. Interfaces* **7**, 26012–26016 (2015).

32. Owusu, P. A. & Asumadu-Sarkodie, S. A review of renewable energy sources, sustainability issues and climate change mitigation. *Cogent Eng.* **3**, 1167990 (2016).

33. Cha, H. & Lee, S. Design and implementation of photovoltaic power conditioning

system using a current based maximum power point tracking. in *2008 IEEE Industry Applications Society Annual Meeting* 1–5 (IEEE, 2008).

34. Kwon, J.-M., Nam, K.-H. & Kwon, B.-H. Photovoltaic power conditioning system with line connection. *IEEE Trans. Ind. Electron.* **53**, 1048–1054 (2006).

35. De Brito, M. A. G., Sampaio, L. P., Junior, L. G. & Canesin, C. A. Research on photovoltaics: review, trends and perspectives. in *XI Brazilian Power Electronics Conference* 531–537 (IEEE, 2011).

36. Lincot, D. The new paradigm of photovoltaics: From powering satellites to powering humanity. *Comptes Rendus Phys.* **18**, 381–390 (2017).

37. Boretti, A., Nayfeh, J. & Al-Maaitah, A. Hydrogen production by solar thermochemical water-splitting cycle via a beam down concentrator. *Front. Energy Res.* **9**, 116 (2021).

38. Yu, J. M. *et al.* High-performance and stable photoelectrochemical water splitting cell with organic-photoactive-layer-based photoanode. *Nat. Commun.* **11**, 1–9 (2020).

39. Grätzel, M. Photoelectrochemical cells. *Nature* **414**, 338 (2001).

40. Parida, B., Iniyan, S. & Goic, R. A review of solar photovoltaic technologies. *Renew. Sustain. energy Rev.* **15**, 1625–1636 (2011).

41. Caillé, A., Al-Moneef, M. & De castro Barnés, F. Survey of Energy Resources. *World Energy Counc.* (2007).

42. Ajayan, J. *et al.* A review of photovoltaic performance of organic/inorganic solar cells for future renewable and sustainable energy technologies. *Superlattices Microstruct.* **143**, 106549 (2020).

43. Newton, D. E. *Solar Energy: A Reference Handbook: A Reference Handbook*. (ABC-CLIO, 2015).

44. Joshi, A. S., Dincer, I. & Reddy, B. V. Performance analysis of photovoltaic systems: a review. *Renew. Sustain. Energy Rev.* **13**, 1884–1897 (2009).

45. Shockley, W. & Queisser, H. J. Detailed balance limit of efficiency of p-n junction solar cells. *J. Appl. Phys.* **32**, 510–519 (1961).

46. Easton, R. L. & Votaw, M. J. Vanguard I IGY satellite (1958 beta). *Rev. Sci. Instrum.* **30**, 70–75 (1959).

47. Badawy, W. A. A review on solar cells from Si-single crystals to porous materials and quantum dots. *J. Adv. Res.* **6**, 123–132 (2015).

48. Moon, M., Alam, M., Rahman, M., Hossain, J. & Ismail, A. B. M. Comparative study of the second generation a-Si: H, CdTe, and CIGS thin-film solar cells. in *Advanced Materials Research* vol. 1154 102–111 (Trans Tech Publ, 2019).

49. Vigil-Galán, O. *et al.* Route towards low cost-high efficiency second generation solar cells: current status and perspectives. *J. Mater. Sci. Mater. Electron.* **26**, 5562–5573 (2015).

50. Frontier, S. Press Release: Solar frontier achieves world record thin-film solar cell

efficiency of 23.35%. (2019).

51. Chopra, K. L., Paulson, P. D. & Dutta, V. Thin-film solar cells: an overview. *Prog. Photovoltaics Res. Appl.* **12**, 69–92 (2004).

52. Green, M. A. Third generation photovoltaics: Ultra-high conversion efficiency at low cost. *Prog. photovoltaics Res. Appl.* **9**, 123–135 (2001).

53. Parisi, M. L. *et al.* Prospective life cycle assessment of third-generation photovoltaics at the pre-industrial scale: A long-term scenario approach. *Renew. Sustain. Energy Rev.* **121**, 109703 (2020).

54. Gutmann, F. & Lyons, L. E. *Organic semiconductors*. (Wiley, 1967).

55. Kallman, H. P. & Silver, M. *Symposium on electrical conductivity in organic solids*. (Interscience Publishers, 1961).

56. Hau, S. K., Yip, H.-L. & Jen, A. K.-Y. A review on the development of the inverted polymer solar cell architecture. *Polym. Rev.* **50**, 474–510 (2010).

57. Etxebarria, I., Ajuria, J. & Pacios, R. Solution-processable polymeric solar cells: A review on materials, strategies and cell architectures to overcome 10%. *Org. Electron.* **19**, 34–60 (2015).

58. Würfel, U. *et al.* A 1 cm2 Organic Solar Cell with 15.2% Certified Efficiency: Detailed Characterization and Identification of Optimization Potential. *Sol. RRL* **5**, 2000802 (2021).

59. O'regan, B. & Grätzel, M. A low-cost, high-efficiency solar cell based on dye-sensitized colloidal TiO 2 films. *Nature* **353**, 737–740 (1991).

60. Mathew, S. *et al.* Dye-sensitized solar cells with 13% efficiency achieved through the molecular engineering of porphyrin sensitizers. *Nat. Chem.* **6**, 242–247 (2014).

61. Gong, J., Sumathy, K., Qiao, Q. & Zhou, Z. Review on dye-sensitized solar cells (DSSCs): Advanced techniques and research trends. *Renew. Sustain. Energy Rev.* **68**, 234–246 (2017).

62. Hashmi, S. G. *et al.* Dye-sensitized solar cells with inkjet-printed dyes. *Energy Environ. Sci.* **9**, 2453–2462 (2016).

63. Mariani, P., Vesce, L. & Di Carlo, A. The role of printing techniques for large-area dye sensitized solar cells. *Semicond. Sci. Technol.* **30**, 104003 (2015).

64. Hashmi, S. G. *et al.* High performance dye-sensitized solar cells with inkjet printed ionic liquid electrolyte. *Nano Energy* **17**, 206–215 (2015).

65. Hashmi, G. *et al.* Review of materials and manufacturing options for large area flexible dye solar cells. *Renew. Sustain. Energy Rev.* **15**, 3717–3732 (2011).

66. Chai, Z. *et al.* High-performance flexible dye-sensitized solar cells by using hierarchical anatase TiO 2 nanowire arrays. *RSC Adv.* **5**, 88052–88058 (2015).

67. Li, B. *et al.* Fabrication of Flexible Dye-Sensitized Solar Cell Modules using Commercially Available Materials. *Energy Technol.* **4**, 536–542 (2016).

68. Yun, M. J., Cha, S. I., Seo, S. H. & Lee, D. Y. Highly flexible dye-sensitized solar cells

produced by sewing textile electrodes on cloth. *Sci. Rep.* **4**, 1–6 (2014).

69. Wang, B. & Kerr, L. L. Dye sensitized solar cells on paper substrates. *Sol. Energy Mater. Sol. Cells* **95**, 2531–2535 (2011).

70. Saifullah, M., Gwak, J. & Yun, J. H. Comprehensive review on material requirements, present status, and future prospects for building-integrated semitransparent photovoltaics (BISTPV). *J. Mater. Chem. A* **4**, 8512–8540 (2016).

71. Vogel, R., Pohl, K. & Weller, H. Sensitization of highly porous, polycrystalline TiO2 electrodes by quantum sized CdS. *Chem. Phys. Lett.* **174**, 241–246 (1990).

72. González-Pedro, V., Xu, X., Mora-Sero, I. & Bisquert, J. Modeling high-efficiency quantum dot sensitized solar cells. *ACS Nano* **4**, 5783–5790 (2010).

73. Jun, H. K., Careem, M. A. & Arof, A. K. Quantum dot-sensitized solar cells—perspective and recent developments: a review of Cd chalcogenide quantum dots as sensitizers. *Renew. Sustain. Energy Rev.* **22**, 148–167 (2013).

74. Yuan, J. *et al.* Metal halide perovskites in quantum dot solar cells: progress and prospects. *Joule* **4**, 1160–1185 (2020).

75. Hao, M. *et al.* Ligand-assisted cation-exchange engineering for high-efficiency colloidal Cs 1− x FA x PbI 3 quantum dot solar cells with reduced phase segregation. *Nat. Energy* **5**, 79–88 (2020).

76. Niu, G., Guo, X. & Wang, L. Review of recent progress in chemical stability of perovskite solar cells. *J. Mater. Chem. A* **3**, 8970–8980 (2015).

77. Roy, P., Sinha, N. K., Tiwari, S. & Khare, A. A review on perovskite solar cells: Evolution of architecture, fabrication techniques, commercialization issues and status. *Sol. Energy* **198**, 665–688 (2020).

78. HUANG, Y., SUN, Q.-D., XU, W., HE, Y. & YIN, W.-J. Halide perovskite materials for solar cells: a theoretical review. *Acta Physico-Chimica Sin.* **33**, 1730–1751 (2017).

79. Wagner, P., Wackers, G., Cardinaletti, I., Manca, J. & Vanacken, J. From colossal magnetoresistance to solar cells: An overview on 66 years of research into perovskites. *Phys. status solidi* **214**, 1700394 (2017).

80. Tschauner, O. *et al.* Discovery of bridgmanite, the most abundant mineral in Earth, in a shocked meteorite. *Science (80-.).* **346**, 1100–1102 (2014).

81. Wasylishen, R. E., Knop, O. & Macdonald, J. B. Cation rotation in methylammonium lead halides. *Solid State Commun.* **56**, 581–582 (1985).

82. Giovanni, D. Optical-Spin dynamics in organic-inorganic hybrid lead halide perovskites.

83. Chen, Y. *et al.* An overview of rare earth coupled lead halide perovskite and its application in photovoltaics and light emitting devices. *Prog. Mater. Sci.* **120**, 100737 (2021).

84. Hong, K., Van Le, Q., Kim, S. Y. & Jang, H. W. Low-dimensional halide perovskites: review and issues. *J. Mater. Chem. C* **6**, 2189–2209 (2018).

85. Passmore, B. S., Wu, J., Manasreh, M. O. & Salamo, G. J. Dual broadband

photodetector based on interband and intersubband transitions in InAs quantum dots embedded in graded InGaAs quantum wells. *Appl. Phys. Lett.* **91**, 233508 (2007).

86. Dou, L. *et al.* Solution-processed hybrid perovskite photodetectors with high detectivity. *Nat. Commun.* **5**, 1–6 (2014).

87. Tang, Z.-K. *et al.* Enhanced optical absorption via cation doping hybrid lead iodine perovskites. *Sci. Rep.* **7**, 1–7 (2017).

88. Green, M. A., Jiang, Y., Soufiani, A. M. & Ho-Baillie, A. Optical properties of photovoltaic organic–inorganic lead halide perovskites. *J. Phys. Chem. Lett.* **6**, 4774–4785 (2015).

89. Dong, Q. *et al.* Electron-hole diffusion lengths> 175 μm in solution-grown CH3NH3PbI3 single crystals. *Science (80-.).* **347**, 967–970 (2015).

90. Chen, Y. *et al.* Extended carrier lifetimes and diffusion in hybrid perovskites revealed by Hall effect and photoconductivity measurements. *Nat. Commun.* **7**, 1–9 (2016).

91. Kiermasch, D., Rieder, P., Tvingstedt, K., Baumann, A. & Dyakonov, V. Improved charge carrier lifetime in planar perovskite solar cells by bromine doping. *Sci. Rep.* **6**, 1–7 (2016).

92. Kim, H.-S. *et al.* Lead Iodide Perovskite Sensitized All-Solid-State Submicron Thin Film Mesoscopic Solar Cell with Efficiency Exceeding 9%. *Sci. Rep.* **2**, 591 (2012).

93. Keav, S., Matam, S. K., Ferri, D. & Weidenkaff, A. Structured perovskite-based catalysts and their application as three-way catalytic converters—a review. *Catalysts* **4**, 226–255 (2014).

94. Parravano, G. Catalytic activity of lanthanum and strontium manganite. *J. Am. Chem. Soc.* **75**, 1497–1498 (1953).

95. Libby, W. F. Promising catalyst for auto exhaust. *Science (80-.).* **171**, 499–500 (1971).

96. Wang, H., Zhang, Q., Qiu, M. & Hu, B. Synthesis and application of perovskite-based photocatalysts in environmental remediation: A review. *J. Mol. Liq.* 116029 (2021).

97. Rupprecht, G. & Bell, R. O. Dielectric constant in paraelectric perovskites. *Phys. Rev.* **135**, A748 (1964).

98. Stylianakis, M. M., Maksudov, T., Panagiotopoulos, A., Kakavelakis, G. & Petridis, K. Inorganic and hybrid perovskite based laser devices: a review. *Materials (Basel).* **12**, 859 (2019).

99. Kim, Y. *et al.* Multicolored organic/inorganic hybrid perovskite light-emitting diodes. *Adv. Mater.* **27**, 1248–1254 (2015).

100. Le, Q. Van, Kim, J. B., Kim, S. Y., Lee, B. & Lee, D. R. Structural investigation of cesium lead halide perovskites for high-efficiency quantum dot light-emitting diodes. *J. Phys. Chem. Lett.* **8**, 4140–4147 (2017).

101. Van Le, Q., Jang, H. W. & Kim, S. Y. Recent advances toward high-efficiency halide

perovskite light-emitting diodes: review and perspective. *Small Methods* **2**, 1700419 (2018).

102. Era, M., Morimoto, S., Tsutsui, T. & Saito, S. Organic-inorganic heterostructure electroluminescent device using a layered perovskite semiconductor (C6H5C2H4NH3) 2PbI4. *Appl. Phys. Lett.* **65**, 676–678 (1994).

103. Fu, Y. *et al.* Broad wavelength tunable robust lasing from single-crystal nanowires of cesium lead halide perovskites (CsPbX3, X= Cl, Br, I). *ACS Nano* **10**, 7963–7972 (2016).

104. Dong, R. *et al.* High-gain and low-driving-voltage photodetectors based on organolead triiodide perovskites. *Adv. Mater.* **27**, 1912–1918 (2015).

105. Hu, X. *et al.* High-performance flexible broadband photodetector based on organolead halide perovskite. *Adv. Funct. Mater.* **24**, 7373–7380 (2014).

106. Wu, T., Pisula, W., Rashid, M. Y. A. & Gao, P. Application of Perovskite-Structured Materials in Field-Effect Transistors. *Adv. Electron. Mater.* **5**, 1900444 (2019).

107. Kojima, A., Teshima, K., Shirai, Y. & Miyasaka, T. Organometal halide perovskites as visible-light sensitizers for photovoltaic cells. *J. Am. Chem. Soc.* **131**, 6050–6051 (2009).

108. Marchini, E., Caramori, S., Bignozzi, C. A. & Carli, S. On the Use of PEDOT as a Catalytic Counter Electrode Material in Dye-Sensitized Solar Cells. *Appl. Sci.* **11**, 3795 (2021).

109. Rao, M. K., Sangeetha, D. N., Selvakumar, M., Sudhakar, Y. N. & Mahesha, M. G. Review on persistent challenges of perovskite solar cells' stability. *Sol. Energy* **218**, 469–491 (2021).

110. Science 342. *Sci. News* 1438–1439 (2013).

111. Nature 504 . *Nat. News Featur.* 357–365 (2013).

112. Kumar, N. S. & Naidu, K. C. B. A review on perovskite solar cells (PSCs), materials and applications. *J. Mater.* (2021).

113. Bellini, E. UNIST, EPFL claim 25.6% efficiency world record for perovskite solar cell. https://www.pv-magazine.com/2021/04/06/unist-epfl-claim-25-6-efficiency-world-record-for-perovskite-solar-cell/.

114. Zhang, Y., Liu, W., Tan, F. & Gu, Y. The essential role of the poly(3-hexylthiophene) hole transport layer in perovskite solar cells. *J. Power Sources* **274**, 1224–1230 (2015).

115. Matebese, F., Taziwa, R. & Mutukwa, D. Progress on the Synthesis and Application of CuSCN Inorganic Hole Transport Material in Perovskite Solar Cells. *Materials (Basel).* **11**, 2592 (2018).

116. Mali, S. S. & Hong, C. K. pin/nip type planar hybrid structure of highly efficient perovskite solar cells towards improved air stability: synthetic strategies and the role of p-type hole transport layer (HTL) and n-type electron transport layer (ETL) metal oxides. *Nanoscale* **8**, 10528–10540 (2016).

117. Tong, X., Lin, F., Wu, J. & Wang, Z. M. High performance perovskite solar cells. *Adv. Sci.* **3**, 1500201 (2016).

118. Xiong, L. *et al.* Review on the application of SnO2 in perovskite solar cells. *Adv. Funct. Mater.* **28**, 1802757 (2018).

119. Jena, A. K., Kulkarni, A. & Miyasaka, T. Halide perovskite photovoltaics: background, status, and future prospects. *Chem. Rev.* **119**, 3036–3103 (2019).

120. Zhao, Y., Nardes, A. M. & Zhu, K. Solid-state mesostructured perovskite CH3NH3PbI3 solar cells: charge transport, recombination, and diffusion length. *J. Phys. Chem. Lett.* **5**, 490–494 (2014).

121. Ermanova, I. *et al.* Crystal engineering approach for fabrication of inverted perovskite solar cell in ambient conditions. *Energies* **14**, 1751 (2021).

122. Min, J. *et al.* Interface Design to Improve the Performance and Stability of Solution-Processed Small-Molecule Conventional Solar Cells. *Adv. Energy Mater.* **4**, 1400816 (2014).

123. Min, J. *et al.* Interface engineering of perovskite hybrid solar cells with solution-processed perylene–diimide heterojunctions toward high performance. *Chem. Mater.* **27**, 227–234 (2015).

124. Qiu, W. *et al.* High efficiency perovskite solar cells using a PCBM/ZnO double electron transport layer and a short air-aging step. *Org. Electron.* **26**, 30–35 (2015).

125. Mali, S. S., Kim, H., Kim, H. H., Shim, S. E. & Hong, C. K. Nanoporous p-type NiOx electrode for pin inverted perovskite solar cell toward air stability. *Mater. Today* **21**, 483–500 (2018).

126. Kwon, S.-N., Yu, J.-H. & Na, S.-I. A systematic approach to ZnO nanoparticle-assisted electron transport bilayer for high efficiency and stable perovskite solar cells. *J. Alloys Compd.* **801**, 277–284 (2019).

127. Zhou, P. *et al.* Efficient and stable mixed perovskite solar cells using P3HT as a hole transporting layer. *J. Mater. Chem. C* **6**, 5733–5737 (2018).

128. Chen, W., Pham, N. D., Wang, H., Jia, B. & Wen, X. Spectroscopic Insight into Efficient and Stable Hole Transfer at the Perovskite/Spiro-OMeTAD Interface with Alternative Additives. *ACS Appl. Mater. Interfaces* **13**, 5752–5761 (2021).

129. Rombach, F. M., Haque, S. A. & Macdonald, T. J. Lessons learned from spiro-OMeTAD and PTAA in perovskite solar cells. *Energy Environ. Sci.* (2021).

130. Jarwal, D. K. *et al.* Fabrication and TCAD validation of ambient air-processed ZnO NRs/CH3NH3PbI3/spiro-OMeTAD solar cells. *Superlattices Microstruct.* **143**, 106540 (2020).

131. Pitchaiya, S. *et al.* A review on the classification of organic/inorganic/carbonaceous hole transporting materials for perovskite solar cell application. *Arab. J. Chem.* **13**, 2526–2557 (2020).

132. Sajid, S. *et al.* Breakthroughs in NiOx-HTMs towards stable, low-cost and efficient perovskite solar cells. *Nano Energy* **51**, 408–424 (2018).

133. Ye, M. *et al.* Recent advances in interfacial engineering of perovskite solar cells. *J. Phys. D. Appl. Phys.* **50**, 373002 (2017).

134. Ku, Z., Rong, Y., Xu, M., Liu, T. & Han, H. Full printable processed mesoscopic CH 3 NH 3 PbI 3/TiO 2 heterojunction solar cells with carbon counter electrode. *Sci. Rep.* **3**, 1–5 (2013).

135. Bogachuk, D. *et al.* Low-temperature carbon-based electrodes in perovskite solar cells. *Energy Environ. Sci.* **13**, 3880–3916 (2020).

136. Hadadian, M., Smått, J.-H. & Correa-Baena, J.-P. The role of carbon-based materials in enhancing the stability of perovskite solar cells. *Energy Environ. Sci.* **13**, 1377–1407 (2020).

137. Fagiolari, L. & Bella, F. Carbon-based materials for stable, cheaper and large-scale processable perovskite solar cells. *Energy Environ. Sci.* **12**, 3437–3472 (2019).

138. Zhang, F. *et al.* Structure engineering of hole–conductor free perovskite-based solar cells with low-temperature-processed commercial carbon paste as cathode. *ACS Appl. Mater. Interfaces* **6**, 16140–16146 (2014).

139. Calabrò, E. *et al.* Easy Strategy to Enhance Thermal Stability of Planar PSCs by Perovskite Defect Passivation and Low-Temperature Carbon-Based Electrode. *ACS Appl. Mater. Interfaces* **12**, 32536–32547 (2020).

140. Ono, L. K., Juarez-Perez, E. J. & Qi, Y. Progress on perovskite materials and solar cells with mixed cations and halide anions. *ACS Appl. Mater. Interfaces* **9**, 30197–30246 (2017).

141. Kour, R. *et al.* Potential substitutes for replacement of lead in perovskite solar cells: A review. *Glob. Challenges* **3**, 1900050 (2019).

142. Snaith, H. J. Perovskites: the emergence of a new era for low-cost, high-efficiency solar cells. *J. Phys. Chem. Lett.* **4**, 3623–3630 (2013).

143. Burschka, J. *et al.* Sequential deposition as a route to high-performance perovskite-sensitized solar cells. *Nature* **499**, 316–319 (2013).

144. Lee, M. M., Teuscher, J., Miyasaka, T., Murakami, T. N. & Snaith, H. J. Efficient hybrid solar cells based on meso-superstructured organometal halide perovskites. *Science (80-.).* **338**, 643–647 (2012).

145. Liu, M., Johnston, M. B. & Snaith, H. J. Efficient planar heterojunction perovskite solar cells by vapour deposition. *Nature* **501**, 395–398 (2013).

146. Luo, S. & Daoud, W. A. Recent progress in organic–inorganic halide perovskite solar cells: mechanisms and material design. *J. Mater. Chem. A* **3**, 8992–9010 (2015).

147. Ye, M., Hong, X., Zhang, F. & Liu, X. Recent advancements in perovskite solar cells: flexibility, stability and large scale. *J. Mater. Chem. A* **4**, 6755–6771 (2016).

148. Kazim, S., Nazeeruddin, M. K., Grätzel, M. & Ahmad, S. Perovskite as light harvester: a game changer in photovoltaics. *Angew. Chemie Int. Ed.* **53**, 2812–2824 (2014).

149. Dai, Z. *et al.* Interfacial toughening with self-assembled monolayers enhances perovskite solar cell reliability. *Science (80-.).* **372**, 618–622 (2021).

150. Akman, E., Shalan, A. E., Sadegh, F. & Akin, S. Moisture-Resistant FAPbI3 Perovskite Solar Cell with 22.25% Power Conversion Efficiency through Pentafluorobenzyl Phosphonic Acid Passivation. *ChemSusChem* **14**, 1176–1183 (2021).

151. Quarti, C., De Angelis, F. & Beljonne, D. Influence of surface termination on the energy level alignment at the CH3NH3PbI3 perovskite/C60 interface. *Chem. Mater.* **29**, 958–968 (2017).

152. Brenner, T. M., Egger, D. A., Kronik, L., Hodes, G. & Cahen, D. Hybrid organic—inorganic perovskites: low-cost semiconductors with intriguing charge-transport properties. *Nat. Rev. Mater.* **1**, 1–16 (2016).

153. Shirayama, M. *et al.* Optical transitions in hybrid perovskite solar cells: ellipsometry, density functional theory, and quantum efficiency analyses for CH 3 NH 3 PbI 3. *Phys. Rev. Appl.* **5**, 14012 (2016).

154. Yin, W.-J., Yang, J.-H., Kang, J., Yan, Y. & Wei, S.-H. Halide perovskite materials for solar cells: a theoretical review. *J. Mater. Chem. A* **3**, 8926–8942 (2015).

155. Chen, Q. *et al.* Under the spotlight: The organic–inorganic hybrid halide perovskite for optoelectronic applications. *Nano Today* **10**, 355–396 (2015).

156. Carignano, M. A. *et al.* A close examination of the structure and dynamics of HC (NH 2) 2 PbI 3 by MD simulations and group theory. *Phys. Chem. Chem. Phys.* **18**, 27109–27118 (2016).

157. Hakamata, T. *et al.* The nature of free-carrier transport in organometal halide perovskites. *Sci. Rep.* **6**, 1–6 (2016).

158. Bergmann, V. W. *et al.* Local time-dependent charging in a perovskite solar cell. *ACS Appl. Mater. Interfaces* **8**, 19402–19409 (2016).

159. Leyden, M. R., Jiang, Y. & Qi, Y. Chemical vapor deposition grown formamidinium perovskite solar modules with high steady state power and thermal stability. *J. Mater. Chem. A* **4**, 13125–13132 (2016).

160. Sutton, R. J. *et al.* Bandgap-tunable cesium lead halide perovskites with high thermal stability for efficient solar cells. *Adv. Energy Mater.* **6**, 1502458 (2016).

161. Lee, J., Seol, D., Cho, A. & Park, N. High-efficiency perovskite solar cells based on the black polymorph of HC (NH2) 2PbI3. *Adv. Mater.* **26**, 4991–4998 (2014).

162. Lee, J. *et al.* Formamidinium and cesium hybridization for photo-and moisture-stable perovskite solar cell. *Adv. Energy Mater.* **5**, 1501310 (2015).

163. Lee, J.-W., Kim, H.-S. & Park, N.-G. APbI 3 (A= CH 3 NH 3 and HC (NH 2) 2) Perovskite Solar Cells: From Sensitization to Planar Heterojunction. in *Organic-Inorganic Halide Perovskite Photovoltaics* 223–253 (Springer, 2016).

164. Zhou, Y., Yang, M., Pang, S., Zhu, K. & Padture, N. P. Exceptional morphology-preserving evolution of formamidinium lead triiodide perovskite thin films via organic-cation displacement. *J. Am. Chem. Soc.* **138**, 5535–5538 (2016).

165. Stoumpos, C. C., Malliakas, C. D. & Kanatzidis, M. G. Semiconducting tin and lead iodide perovskites with organic cations: phase transitions, high mobilities, and near-infrared photoluminescent properties. *Inorg. Chem.* **52**, 9019–9038 (2013).

166. Li, Z. *et al.* Stabilizing perovskite structures by tuning tolerance factor: formation of formamidinium and cesium lead iodide solid-state alloys. *Chem. Mater.* **28**, 284–292 (2016).

167. Pellet, N. *et al.* Mixed-organic-cation Perovskite photovoltaics for enhanced solar-light harvesting. *Angew. chemie* **126**, 3215–3221 (2014).

168. Aharon, S., Dymshits, A., Rotem, A. & Etgar, L. Temperature dependence of hole conductor free formamidinium lead iodide perovskite based solar cells. *J. Mater. Chem. A* **3**, 9171–9178 (2015).

169. Salado, M., Calio, L., Berger, R., Kazim, S. & Ahmad, S. Influence of the mixed organic cation ratio in lead iodide based perovskite on the performance of solar cells. *Phys. Chem. Chem. Phys.* **18**, 27148–27157 (2016).

170. Li, G. *et al.* Ion-Exchange-Induced 2D–3D Conversion of HMA1− xFAxPbI3Cl Perovskite into a High-Quality MA1− xFAxPbI3 Perovskite. *Angew. Chemie Int. Ed.* **55**, 13460–13464 (2016).

171. Huang, Y. *et al.* The intrinsic properties of FA (1− x) MA x PbI 3 perovskite single crystals. *J. Mater. Chem. A* **5**, 8537–8544 (2017).

172. Zhu, T., Zheng, D., Rager, M.-N. & Pauporté, T. The Stabilization of Formamidinium Lead Tri-Iodide Perovskite through a Methylammonium-Based Additive for High-Efficiency Solar Cells. *Sol. RRL* **4**, 2000348 (2020).

173. Liu, J. *et al.* High-Quality Mixed-Organic-Cation Perovskites from a Phase-Pure Non-stoichiometric Intermediate (FAI) 1− x-PbI2 for Solar Cells. *Adv. Mater.* **27**, 4918–4923 (2015).

174. Chen, C.-C. *et al.* Improving the efficiency of inverted mixed-organic-cation perovskite absorber based photovoltaics by tailing the surface roughness of PEDOT: PSS thin film. *Sol. Energy* **134**, 445–451 (2016).

175. Deng, Y., Dong, Q., Bi, C., Yuan, Y. & Huang, J. Air-Stable, Efficient Mixed-Cation Perovskite Solar Cells with Cu Electrode by Scalable Fabrication of Active Layer. *Adv. Energy Mater.* **6**, 1600372 (2016).

176. Kim, J., Kim, H. P., Teridi, M. A. M., bin Mohd Yusoff, A. R. & Jang, J. Bandgap tuning of mixed organic cation utilizing chemical vapor deposition process. *Sci. Rep.* **6**, 1–11 (2016).

177. Chen, J. *et al.* Mixed-Organic-Cation (FA) x (MA) 1–x PbI3 Planar Perovskite Solar Cells with 16.48% Efficiency via a Low-Pressure Vapor-Assisted Solution Process. *ACS Appl. Mater. Interfaces* **9**, 2449–2458 (2017).

178. Binek, A., Hanusch, F. C., Docampo, P. & Bein, T. Stabilization of the trigonal high-temperature phase of formamidinium lead iodide. *J. Phys. Chem. Lett.* **6**, 1249–1253 (2015).

179. Weber, O. J., Charles, B. & Weller, M. T. Phase behaviour and composition in the formamidinium–methylammonium hybrid lead iodide perovskite solid solution. *J. Mater. Chem. A* **4**, 15375–15382 (2016).

180. Zhou, Y. *et al.* Doping and alloying for improved perovskite solar cells. *J. Mater.*

Chem. A **4**, 17623–17635 (2016).

181. Spalla, M. *et al.* Influence of Chloride/Iodide Ratio in MAPbI3-xClx Perovskite Solar Devices: Case of Low Temperature Processable AZO Sub-Layer. *Energies* **13**, 1927 (2020).

182. Gao, P., Grätzel, M. & Nazeeruddin, M. K. Organohalide lead perovskites for photovoltaic applications. *Energy Environ. Sci.* **7**, 2448–2463 (2014).

183. Pham, N. D. *et al.* Enhanced perovskite electronic properties via a modified lead (ii) chloride Lewis acid–base adduct and their effect in high-efficiency perovskite solar cells. *J. Mater. Chem. A* **5**, 5195–5203 (2017).

184. Xu, F., Zhang, T., Li, G. & Zhao, Y. Synergetic Effect of Chloride Doping and CH3NH3PbCl3 on CH3NH3PbI3− xClx Perovskite-Based Solar Cells. *ChemSusChem* **10**, 2365–2369 (2017).

185. Kim, M. *et al.* Methylammonium chloride induces intermediate phase stabilization for efficient perovskite solar cells. *Joule* **3**, 2179–2192 (2019).

186. Stranks, S. D. & Snaith, H. J. Metal-halide perovskites for photovoltaic and light-emitting devices. *Nat. Nanotechnol.* **10**, 391 (2015).

187. Binek, A. *et al.* Control of perovskite crystal growth by methylammonium lead chloride templating. *Chem. Asian J.* **11**, 1199–1204 (2016).

188. Yang, B. *et al.* Deciphering halogen competition in organometallic halide perovskite growth. *J. Am. Chem. Soc.* **138**, 5028–5035 (2016).

189. Fan, L. *et al.* Elucidating the role of chlorine in perovskite solar cells. *J. Mater. Chem. A* **5**, 7423–7432 (2017).

190. Unger, E. L. *et al.* Chloride in lead chloride-derived organo-metal halides for perovskite-absorber solar cells. *Chem. Mater.* **26**, 7158–7165 (2014).

191. Colella, S. *et al.* MAPbI3-xCl x mixed halide perovskite for hybrid solar cells: the role of chloride as dopant on the transport and structural properties. *Chem. Mater.* **25**, 4613–4618 (2013).

192. Dualeh, A. *et al.* Effect of annealing temperature on film morphology of organic–inorganic hybrid pervoskite solid-state solar cells. *Adv. Funct. Mater.* **24**, 3250–3258 (2014).

193. Cojocaru, L. *et al.* Determination of Chloride Content in Planar CH3NH3PbI3− x Cl x Solar Cells by Chemical Analysis. *Chem. Lett.* **44**, 1089–1091 (2015).

194. Pool, V. L., Gold-Parker, A., McGehee, M. D. & Toney, M. F. Chlorine in PbCl2-derived hybrid-perovskite solar absorbers. *Chem. Mater.* **27**, 7240–7243 (2015).

195. Li, Y. *et al.* High-Performance Planar Solar Cells Based On CH3NH3PbI3-xClx Perovskites with Determined Chlorine Mole Fraction. *Adv. Funct. Mater.* **25**, 4867–4873 (2015).

196. Zhang, H. *et al.* Controlled substitution of chlorine for iodine in single-crystal nanofibers of mixed perovskite MAPbI3–xClx. *Small* **12**, 3780–3787 (2016).

197. Luo, D. *et al.* Cubic structure of the mixed halide perovskite CH 3 NH 3 PbI 3− x Cl x

via thermal annealing. *RSC Adv.* **5**, 85480–85485 (2015).

198. Li, G., Zhang, T. & Zhao, Y. Hydrochloric acid accelerated formation of planar CH 3 NH 3 PbI 3 perovskite with high humidity tolerance. *J. Mater. Chem. A* **3**, 19674–19678 (2015).

199. Pan, J. *et al.* Room-temperature, Hydrochloride-assisted, one-step deposition for highly efficient and air-stable perovskite solar cells. *Adv. Mater.* **28**, 8309–8314 (2016).

200. Chen, Y., Zhao, Y. & Liang, Z. Non-thermal annealing fabrication of efficient planar perovskite solar cells with inclusion of NH4Cl. *Chem. Mater.* **27**, 1448–1451 (2015).

201. Chen, Y., Zhao, Y. & Liang, Z. Nonvolatile chlorinated additives adversely influence $CH_3NH_3PbI_3$ based planar solar cells. *J. Mater. Chem. Chem.* (2015).

202. Sun, C. *et al.* Phosphonium Halides as Both Processing Additives and Interfacial Modifiers for High Performance Planar-Heterojunction Perovskite Solar Cells. *Small* **11**, 3344–3350 (2015).

203. Noh, J. H., Im, S. H., Heo, J. H., Mandal, T. N. & Seok, S. Il. Chemical management for colorful, efficient, and stable inorganic–organic hybrid nanostructured solar cells. *Nano Lett.* **13**, 1764–1769 (2013).

204. Jeon, N. J. *et al.* Solvent engineering for high-performance inorganic--organic hybrid perovskite solar cells. *Nat. Mater.* **13**, 897 (2014).

205. Brivio, F., Caetano, C. & Walsh, A. Thermodynamic origin of photoinstability in the CH3NH3Pb (I1–x Br x) 3 hybrid halide perovskite alloy. *J. Phys. Chem. Lett.* **7**, 1083–1087 (2016).

206. Misra, R. K. *et al.* Effect of halide composition on the photochemical stability of perovskite photovoltaic materials. *arXiv Prepr. arXiv1603.08683* (2016).

207. Rehman, W. *et al.* Charge-carrier dynamics and mobilities in formamidinium lead mixed-halide perovskites. *Adv. Mater.* **27**, 7938–7944 (2015).

208. Eperon, G. E. *et al.* Formamidinium lead trihalide: a broadly tunable perovskite for efficient planar heterojunction solar cells. *Energy Environ. Sci.* **7**, 982–988 (2014).

209. Jeon, N. J. *et al.* Compositional engineering of perovskite materials for high-performance solar cells. *Nature* **517**, 476–480 (2015).

210. Yang, W. S. *et al.* High-performance photovoltaic perovskite layers fabricated through intramolecular exchange. *Science (80-.).* **348**, 1234–1237 (2015).

211. Niu, G., Yu, H., Li, J., Wang, D. & Wang, L. Controlled orientation of perovskite films through mixed cations toward high performance perovskite solar cells. *Nano Energy* **27**, 87–94 (2016).

212. Yi, C. *et al.* Entropic stabilization of mixed A-cation ABX 3 metal halide perovskites for high performance perovskite solar cells. *Energy Environ. Sci.* **9**, 656–662 (2016).

213. Saliba, M. *et al.* Cesium-containing triple cation perovskite solar cells: improved stability, reproducibility and high efficiency. *Energy Environ. Sci.* **9**, 1989–1997 (2016).

214. Saliba, M. *et al.* Incorporation of rubidium cations into perovskite solar cells improves photovoltaic performance. *Science (80-.).* **354**, 206–209 (2016).

215. Lu, H., Guo, X., Yang, C. & Li, S. Tailoring perovskite compounds for broadband light absorption. in *IOP Conference Series: Materials Science and Engineering* vol. 303 12002 (IOP Publishing, 2018).

216. Gardner, K. L. *et al.* Nonhazardous solvent systems for processing perovskite photovoltaics. *Adv. Energy Mater.* **6**, 1600386 (2016).

217. Hendriks, K. H. *et al.* 2-Methoxyethanol as a new solvent for processing methylammonium lead halide perovskite solar cells. *J. Mater. Chem. A* **5**, 2346–2354 (2017).

218. Noel, N. K. *et al.* A low viscosity, low boiling point, clean solvent system for the rapid crystallisation of highly specular perovskite films. *Energy Environ. Sci.* **10**, 145–152 (2017).

219. Yang, Y. *et al.* Bi-functional additive engineering for high-performance perovskite solar cells with reduced trap density. *J. Mater. Chem. A* **7**, 6450–6458 (2019).

220. WS, J. N. J. N. J. H. Y. Kim YC Ryu S. Seo J. Seok S. II. *Nature* **517**, 476 (2015).

221. Sun, X. *et al.* Mixed-solvent-vapor annealing of perovskite for photovoltaic device efficiency enhancement. *Nano Energy* **28**, 417–425 (2016).

222. Eperon, G. E., Burlakov, V. M., Docampo, P., Goriely, A. & Snaith, H. J. Morphological control for high performance, solution-processed planar heterojunction perovskite solar cells. *Adv. Funct. Mater.* **24**, 151–157 (2014).

223. Liang, K., Mitzi, D. B. & Prikas, M. T. Synthesis and Characterization of Organic–Inorganic Perovskite Thin Films Prepared Using a Versatile Two-Step Dipping Technique. *Chem. Mater.* **10**, 403–411 (1998).

224. Huang, F., Li, M., Siffalovic, P., Cao, G. & Tian, J. From scalable solution fabrication of perovskite films towards commercialization of solar cells. *Energy Environ. Sci.* **12**, 518–549 (2019).

225. Im, J.-H., Jang, I.-H., Pellet, N., Grätzel, M. & Park, N.-G. Growth of CH3NH3PbI3 cuboids with controlled size for high-efficiency perovskite solar cells. *Nat. Nanotechnol.* **9**, 927–932 (2014).

226. Wu, Y. *et al.* Retarding the crystallization of PbI 2 for highly reproducible planar-structured perovskite solar cells via sequential deposition. *Energy Environ. Sci.* **7**, 2934–2938 (2014).

227. Zhou, Y. *et al.* Growth control of compact CH 3 NH 3 PbI 3 thin films via enhanced solid-state precursor reaction for efficient planar perovskite solar cells. *J. Mater. Chem. A* **3**, 9249–9256 (2015).

228. Mei, A. *et al.* A hole-conductor–free, fully printable mesoscopic perovskite solar cell with high stability. *Science (80-.).* **345**, 295–298 (2014).

229. Ahn, N. *et al.* Highly reproducible perovskite solar cells with average efficiency of 18.3% and best efficiency of 19.7% fabricated via Lewis base adduct of lead (II) iodide. *J. Am. Chem. Soc.* **137**, 8696–8699 (2015).

230. Chen, Q. *et al.* Planar heterojunction perovskite solar cells via vapor-assisted solution process. *J. Am. Chem. Soc.* **136**, 622–625 (2014).

231. Feng, J. *et al.* High-throughput large-area vacuum deposition for high-performance formamidine-based perovskite solar cells. *Energy Environ. Sci.* **14**, 3035–3043 (2021).

232. Nie, W. *et al.* High-efficiency solution-processed perovskite solar cells with millimeter-scale grains. *Science (80-.).* **347**, 522–525 (2015).

233. Hu, Y. *et al.* Stable large-area (10× 10 cm2) printable mesoscopic perovskite module exceeding 10% efficiency. *Sol. Rrl* **1**, 1600019 (2017).

234. Peng, X. *et al.* Perovskite and organic solar cells fabricated by inkjet printing: progress and prospects. *Adv. Funct. Mater.* **27**, 1703704 (2017).

235. Gao, B. & Meng, J. Flexible CH3NH3PbI3 perovskite solar cells with high stability based on all inkjet printing. *Sol. Energy* **230**, 598–604 (2021).

236. Wang, D. *et al.* Improvement on the performance of perovskite solar cells by doctor-blade coating under ambient condition with hole-transporting material optimization. *J. Energy Chem.* **38**, 207–213 (2019).

237. Deng, Y. *et al.* Scalable fabrication of efficient organolead trihalide perovskite solar cells with doctor-bladed active layers. *Energy Environ. Sci.* **8**, 1544–1550 (2015).

238. Deng, Y., Wang, Q., Yuan, Y. & Huang, J. Vividly colorful hybrid perovskite solar cells by doctor-blade coating with perovskite photonic nanostructures. *Mater. Horizons* **2**, 578–583 (2015).

239. Back, H. *et al.* Interfacial modification of hole transport layers for efficient large-area perovskite solar cells achieved via blade-coating. *Sol. Energy Mater. Sol. Cells* **144**, 309–315 (2016).

240. Razza, S. *et al.* Perovskite solar cells and large area modules (100 cm2) based on an air flow-assisted PbI2 blade coating deposition process. *J. Power Sources* **277**, 286–291 (2015).

241. Di Giacomo, F. *et al.* Up-scalable sheet-to-sheet production of high efficiency perovskite module and solar cells on 6-in. substrate using slot die coating. *Sol. Energy Mater. Sol. Cells* **181**, 53–59 (2018).

242. Xiao, Z. *et al.* Solvent annealing of perovskite-induced crystal growth for photovoltaic-device efficiency enhancement. *Adv. Mater.* **26**, 6503–6509 (2014).

243. Xiao, Y., Han, G., Wu, J. & Lin, J.-Y. Efficient bifacial perovskite solar cell based on a highly transparent poly (3, 4-ethylenedioxythiophene) as the p-type hole-transporting material. *J. Power Sources* **306**, 171–177 (2016).

244. Wang, X. *et al.* Electrochemical deposition of CsPbBr3 perovskite for photovoltaic devices with robust ambient stability. *ACS Appl. Mater. Interfaces* **12**, 50455–50463 (2020).

245. Wang, Y., Gao, C., Wang, X., Liu, H. & Shen, W. Controllable Electrochemical Deposition and Theoretical Understanding of Conformal Perovskite on Textured Silicon towards Efficient Perovskite/Silicon Tandem Solar Cells. *J. Phys. Chem. C*

125, 2875–2883 (2021).

246. Gozalzadeh, S., Nasirpouri, F. & Seok, S. Il. Towards environmental friendly multi-step processing of efficient mixed-cation mixed halide perovskite solar cells from chemically bath deposited lead sulphide. *Sci. Rep.* **11**, 1–11 (2021).

247. Azarhoosh, P., McKechnie, S., Frost, J. M., Walsh, A. & Van Schilfgaarde, M. Research Update: Relativistic origin of slow electron-hole recombination in hybrid halide perovskite solar cells. *Apl Mater.* **4**, 91501 (2016).

248. Nature News Features. **Nature 504**, 357–365 (2013).

249. Science News. **Science 34**, 1438–1439 (2013).

250. Zhao, D. *et al.* Four-Terminal All-Perovskite Tandem Solar Cells Achieving Power Conversion Efficiencies Exceeding 23%. *ACS Energy Lett.* **3**, 305–306 (2018).

251. Seok, S. Il, Grätzel, M. & Park, N.-G. Methodologies toward Highly Efficient Perovskite Solar Cells. *Small* **14**, 1704177 (2018).

252. Xiao, Z. *et al.* Efficient, high yield perovskite photovoltaic devices grown by interdiffusion of solution-processed precursor stacking layers. *Energy Environ. Sci.* **7**, 2619–2623 (2014).

253. Zardetto, V. *et al.* Atomic layer deposition for perovskite solar cells: research status, opportunities and challenges. *Sustain. Energy Fuels* **1**, 30–55 (2017).

254. Daideche, K. Élaboration électrochimique des films minces de SnO2: effets des conditions d'électrodéposition. (Université Ferhat Abbas Setif, 2018).

255. Lee, J., Varela, H., Uhm, S. & Tak, Y. Electrodeposition of PbO2 onto Au and Ti substrates. *Electrochem. commun.* **2**, 646–652 (2000).

256. Devilliers, D. & Mahé, E. Modified titanium electrodes: Application to Ti/TiO2/PbO2 dimensionally stable anodes. *Electrochim. Acta* **55**, 8207–8214 (2010).

257. Wang, Z. *et al.* Additive-modulated evolution of HC (NH2) 2PbI3 black polymorph for mesoscopic perovskite solar cells. *Chem. Mater.* **27**, 7149–7155 (2015).

258. Jiang, F. *et al.* Synergistic Effect of PbI2 Passivation and Chlorine Inclusion Yielding High Open-Circuit Voltage Exceeding 1.15 V in Both Mesoscopic and Inverted Planar CH3NH3PbI3 (Cl)-Based Perovskite Solar Cells. *Adv. Funct. Mater.* **26**, 8119–8127 (2016).

259. Oku, T. Crystal structures of CH3NH3PbI3 and related perovskite compounds used for solar cells. *Sol. Cells-New Approaches Rev.* **1**, (2015).

260. Brivio, F. *et al.* Lattice dynamics and vibrational spectra of the orthorhombic, tetragonal, and cubic phases of methylammonium lead iodide. *Phys. Rev. B* **92**, 144308 (2015).

261. Liu, F. *et al.* Is excess PbI2 beneficial for perovskite solar cell performance? *Adv. Energy Mater.* **6**, 1502206 (2016).

262. Chen, Q. *et al.* Controllable self-induced passivation of hybrid lead iodide perovskites toward high performance solar cells. *Nano Lett.* **14**, 4158–4163 (2014).

263. Jacobsson, T. J. *et al.* Unreacted PbI2 as a double-edged sword for enhancing the performance of perovskite solar cells. *J. Am. Chem. Soc.* **138**, 10331–10343 (2016).

264. Wang, H. *et al.* Adverse effects of excess residual PbI2 on photovoltaic performance, charge separation, and trap-state properties in mesoporous structured perovskite solar cells. *Chem. Eur. J.* **23**, 3986–3992 (2017).

265. Park, B. *et al.* Enhanced crystallinity in organic–inorganic lead halide perovskites on mesoporous TiO2 via disorder–order phase transition. *Chem. Mater.* **26**, 4466–4471 (2014).

266. Hu, M., Bi, C., Yuan, Y., Bai, Y. & Huang, J. Stabilized wide bandgap MAPbBrxI3–x perovskite by enhanced grain size and improved crystallinity. *Adv. Sci.* **3**, 1500301 (2016).

267. Nie, W. *et al.* Critical role of interface and crystallinity on the performance and photostability of perovskite solar cell on nickel oxide. *Adv. Mater.* **30**, 1703879 (2018).

268. Yu, N., Gao, L., Zhao, S. & Wang, Z. Electrodeposited PbO2 thin film as positive electrode in PbO2/AC hybrid capacitor. *Electrochim. Acta* **54**, 3835–3841 (2009).

269. Bing, J., Huang, S. & Ho-Baillie, A. W. Y. A review on halide perovskite film formation by sequential solution processing for solar cell applications. *Energy Technol.* **8**, 1901114 (2020).

270. Tian, Y. & Scheblykin, I. G. Artifacts in absorption measurements of organometal halide perovskite materials: what are the real spectra? *J. Phys. Chem. Lett.* **6**, 3466–3470 (2015).

271. Park, N.-G. Perovskite solar cells: an emerging photovoltaic technology. *Mater. Today* **18**, 65–72 (2015).

272. Assadi, M. K., Bakhoda, S., Saidur, R. & Hanaei, H. Recent progress in perovskite solar cells. *Renew. Sustain. Energy Rev.* **81**, 2812–2822 (2018).

273. Sarritzu, V. *et al.* Direct or indirect bandgap in hybrid lead halide perovskites? *Adv. Opt. Mater.* **6**, 1701254 (2018).

274. Von Behren, J., Van Buuren, T., Zacharias, M., Chimowitz, E. H. & Fauchet, P. M. Quantum confinement in nanoscale silicon: The correlation of size with bandgap and luminescence. *Solid State Commun.* **105**, 317–322 (1998).

275. Combessis, A., Mazel, C., Maugin, M. & Flandin, L. Optical density as a probe of carbon nanotubes dispersion in polymers. *J. Appl. Polym. Sci.* **130**, 1778–1786 (2013).

276. Zhang, X., Shen, J.-X., Wang, W. & Van de Walle, C. G. First-principles analysis of radiative recombination in lead-halide perovskites. *ACS Energy Lett.* **3**, 2329–2334 (2018).

277. Planes, E., Spalla, M., Juillard, S., Perrin, L. & Flandin, L. Absolute Quantification of Photo-/Electroluminescence Imaging for Solar Cells: Definition and Application to Organic and Perovskite Devices. *ACS Appl. Electron. Mater.* **1**, 2489–2501 (2019).

278. Kaienburg, P. *et al.* How contact layers control shunting losses from pinholes in

thin-film solar cells. *J. Phys. Chem. C* **122**, 27263–27272 (2018).

279. Chueh, C.-C., Li, C.-Z. & Jen, A. K.-Y. Recent progress and perspective in solution-processed Interfacial materials for efficient and stable polymer and organometal perovskite solar cells. *Energy Environ. Sci.* **8**, 1160–1189 (2015).

280. Chae, J., Dong, Q., Huang, J. & Centrone, A. Chloride incorporation process in CH3NH3PbI3–x Cl x perovskites via nanoscale bandgap maps. *Nano Lett.* **15**, 8114–8121 (2015).

281. Yu, H. *et al.* The role of chlorine in the formation process of "CH3NH3PbI3-xClx" perovskite. *Adv. Funct. Mater.* **24**, 7102–7108 (2014).

282. Jamshaid, A. *et al.* Atomic-scale Insight into Enhanced Surface Stability of Methylammonium Lead Iodide Perovskite by Controlled Deposition of Lead Chloride. *Energy Environ. Sci.* (2021).

283. Hieulle, J. *et al.* Unraveling the impact of halide mixing on perovskite stability. *J. Am. Chem. Soc.* **141**, 3515–3523 (2019).

284. Maculan, G. *et al.* CH3NH3PbCl3 single crystals: inverse temperature crystallization and visible-blind UV-photodetector. *J. Phys. Chem. Lett.* **6**, 3781–3786 (2015).

285. Isikgor, F. H., Li, B., Zhu, H., Xu, Q. & Ouyang, J. High performance planar perovskite solar cells with a perovskite of mixed organic cations and mixed halides, MA 1− x FA x PbI 3− y Cl y. *J. Mater. Chem. A* **4**, 12543–12553 (2016).

286. Mosconi, E., Amat, A., Nazeeruddin, M. K., Grätzel, M. & De Angelis, F. First-principles modeling of mixed halide organometal perovskites for photovoltaic applications. *J. Phys. Chem. C* **117**, 13902–13913 (2013).

287. Mu, C., Pan, J., Feng, S., Li, Q. & Xu, D. Quantitative doping of chlorine in formamidinium lead trihalide (FAPbI3− xClx) for planar heterojunction perovskite solar cells. *Adv. Energy Mater.* **7**, 1601297 (2017).

288. Odysseas Kosmatos, K. *et al.* Methylammonium Chloride: A Key Additive for Highly Efficient, Stable, and Up-Scalable Perovskite Solar Cells. *Energy Environ. Mater.* **2**, 79–92 (2019).

289. Planes, E. *et al.* Degradation Mechanisms in a Mixed Cations and Anions Perovskite Solar Cell: Mitigation Effect of the Gold Electrode. *ACS Appl. Energy Mater.* (2021).

290. Kirchartz, T., Márquez, J. A., Stolterfoht, M. & Unold, T. Photoluminescence-based characterization of halide perovskites for photovoltaics. *Adv. energy Mater.* **10**, 1904134 (2020).

291. Thomson, S. Observing Phase Transitions in a Halide Perovskite Using Temperature Dependent Photoluminescence Spectroscopy. *Edinburgh Instuments Ltd* **AN**, 45 (2018).

292. Tavakoli, M. M. *et al.* Controllable perovskite crystallization via antisolvent technique using chloride additives for highly efficient planar perovskite solar cells. *Adv. Energy Mater.* **9**, 1803587 (2019).

293. Stranks, S. D. *et al.* Electron-hole diffusion lengths exceeding 1 micrometer in an organometal trihalide perovskite absorber. *Science (80-.).* **342**, 341–344 (2013).

294. Xie, F. X., Su, H., Mao, J., Wong, K. S. & Choy, W. C. H. Evolution of diffusion length and trap state induced by chloride in perovskite solar cell. *J. Phys. Chem. C* **120**, 21248–21253 (2016).

295. Zhong, Y., Tada, A., Izawa, S., Hashimoto, K. & Tajima, K. Enhancement of VOC without loss of JSC in organic solar cells by modification of donor/acceptor interfaces. *Adv. Energy Mater.* **4**, 1301332 (2014).

296. Chaudhary, B. *et al.* Mixed-dimensional naphthylmethylammonium-methylammonium lead iodide perovskites with improved thermal stability. *Sci. Rep.* **10**, 1–11 (2020).

297. Merdasa, A. *et al.* Super-resolution luminescence microspectroscopy reveals the mechanism of photoinduced degradation in CH3NH3PbI3 perovskite nanocrystals. *J. Phys. Chem. C* **120**, 10711–10719 (2016).

298. Jošt, M., Kegelmann, L., Korte, L. & Albrecht, S. Monolithic perovskite tandem solar cells: A review of the present status and advanced characterization methods toward 30% efficiency. *Adv. Energy Mater.* **10**, 1904102 (2020).

299. Tabuchi, Y., Asai, K., Rikukawa, M., Sanui, K. & Ishigure, K. Preparation and characterization of natural lower dimensional layered perovskite-type compounds. *J. Phys. Chem. Solids* **61**, 837–845 (2000).

300. Liu, G. *et al.* Two regimes of bandgap red shift and partial ambient retention in pressure-treated two-dimensional perovskites. *ACS Energy Lett.* **2**, 2518–2524 (2017).

301. Hong, D., Li, J., Wan, S., Scheblykin, I. G. & Tian, Y. Red-shifted photoluminescence from crystal edges due to carrier redistribution and reabsorption in lead triiodide perovskites. *J. Phys. Chem. C* **123**, 12521–12526 (2019).

302. Kong, W. *et al.* Characterization of an abnormal photoluminescence behavior upon crystal-phase transition of perovskite CH 3 NH 3 PbI 3. *Phys. Chem. Chem. Phys.* **17**, 16405–16411 (2015).

303. Milot, R. L., Eperon, G. E., Snaith, H. J., Johnston, M. B. & Herz, L. M. Temperature-dependent charge-carrier dynamics in CH3NH3PbI3 perovskite thin films. *Adv. Funct. Mater.* **25**, 6218–6227 (2015).

304. Wu, K. *et al.* Temperature-dependent excitonic photoluminescence of hybrid organometal halide perovskite films. *Phys. Chem. Chem. Phys.* **16**, 22476–22481 (2014).

305. Misra, R. K. *et al.* Temperature-and component-dependent degradation of perovskite photovoltaic materials under concentrated sunlight. *J. Phys. Chem. Lett.* **6**, 326–330 (2015).

306. Christians, J. A., Miranda Herrera, P. A. & Kamat, P. V. Transformation of the excited state and photovoltaic efficiency of CH3NH3PbI3 perovskite upon controlled exposure to humidified air. *J. Am. Chem. Soc.* **137**, 1530–1538 (2015).

307. Yamada, Y. *et al.* Dynamic optical properties of CH3NH3PbI3 single crystals as revealed by one-and two-photon excited photoluminescence measurements. *J. Am. Chem. Soc.* **137**, 10456–10459 (2015).

308. Wu, B. *et al.* Discerning the surface and bulk recombination kinetics of organic–inorganic halide perovskite single crystals. *Adv. Energy Mater.* **6**, 1600551 (2016).

309. Zhao, Y., Nardes, A. M. & Zhu, K. Mesoporous perovskite solar cells: material composition, charge-carrier dynamics, and device characteristics. *Faraday Discuss.* **176**, 301–312 (2015).

310. Hanusch, F. C. *et al.* Efficient planar heterojunction perovskite solar cells based on formamidinium lead bromide. *J. Phys. Chem. Lett.* **5**, 2791–2795 (2014).

311. Smecca, E. *et al.* Stability of solution-processed MAPbI 3 and FAPbI 3 layers. *Phys. Chem. Chem. Phys.* **18**, 13413–13422 (2016).

312. Singh, R., Parashar, M., Sandhu, S., Yoo, K. & Lee, J.-J. The effects of crystal structure on the photovoltaic performance of perovskite solar cells under ambient indoor illumination. *Sol. Energy* **220**, 43–50 (2021).

313. Zhumekenov, A. A. *et al.* Formamidinium lead halide perovskite crystals with unprecedented long carrier dynamics and diffusion length. *ACS Energy Lett.* **1**, 32–37 (2016).

314. Yang, Z. *et al.* Effects of formamidinium and bromide ion substitution in methylammonium lead triiodide toward high-performance perovskite solar cells. *Nano Energy* **22**, 328–337 (2016).

315. Bi, C., Yuan, Y., Fang, Y. & Huang, J. Low-temperature fabrication of efficient wide-bandgap organolead trihalide perovskite solar cells. *Adv. Energy Mater.* **5**, 1401616 (2015).

316. Liu, D., Zhou, W., Tang, H., Fu, P. & Ning, Z. Supersaturation controlled growth of MAFAPbI 3 perovskite film for high efficiency solar cells. *Sci. China Chem.* **61**, 1278–1284 (2018).

317. Targhi, F. F., Jalili, Y. S. & Kanjouri, F. MAPbI3 and FAPbI3 perovskites as solar cells: Case study on structural, electrical and optical properties. *Results Phys.* **10**, 616–627 (2018).

318. Glaser, T. *et al.* Infrared spectroscopic study of vibrational modes in methylammonium lead halide perovskites. *J. Phys. Chem. Lett.* **6**, 2913–2918 (2015).

319. Huo, B. *et al.* Amino-mediated anchoring of FAPbBr3 perovskite quantum dots on silica spheres for efficient visible light photocatalytic NO removal. *Chem. Eng. J.* **406**, 126740 (2021).

320. Lim, J. W. *et al.* Unprecedentedly high indoor performance (efficiency> 34%) of perovskite photovoltaics with controlled bromine doping. *Nano Energy* **75**, 104984 (2020).

321. Arora, N. *et al.* Intrinsic and extrinsic stability of formamidinium lead bromide perovskite solar cells yielding high photovoltage. *Nano Lett.* **16**, 7155–7162 (2016).

322. Codaro, E. N. & Vilche, J. R. A kinetic study of the electroformation of PbO2 on Pb electrodes in sulphuric acid solutions. *Electrochim. Acta* **42**, 549–555 (1997).

323. Bao, Q., Liu, X., Braun, S. & Fahlman, M. Oxygen-and water-based degradation in [6, 6]-phenyl-C61-butyric acid methyl ester (PCBM) films. *Adv. Energy Mater.* **4**,

1301272 (2014).

324. Bi, C. *et al.* Non-wetting surface-driven high-aspect-ratio crystalline grain growth for efficient hybrid perovskite solar cells. *Nat. Commun.* **6**, 1–7 (2015).

325. Ummadisingu, A., Meloni, S., Mattoni, A., Tress, W. & Grätzel, M. Crystal-size-induced band gap tuning in perovskite films. *Angew. Chemie* **133**, 21538–21546 (2021).

326. Spalla, M. *et al.* Effect of the Hole Transporting/Active Layer Interface on the Perovskite Solar Cell Stability. *ACS Appl. Energy Mater.* **3**, 3282–3292 (2020).

327. Meng, L., You, J., Guo, T.-F. & Yang, Y. Recent advances in the inverted planar structure of perovskite solar cells. *Acc. Chem. Res.* **49**, 155–165 (2016).

328. Saliba, M. *et al.* How to Make over 20% Efficient Perovskite Solar Cells in Regular (n–i–p) and Inverted (p–i–n) Architectures. *Chem. Mater.* **30**, 4193–4201 (2018).

329. Lemercier, T., Perrin, L., Planès, E., Berson, S. & Flandin, L. A Comparison of the Structure and Properties of Opaque and Semi-Transparent NIP/PIN-Type Scalable Perovskite Solar Cells. *Energies* **13**, 3794 (2020).

330. Lemercier, T., Perrin, L., Berson, S., Flandin, L. & Planes, E. Innovative PIN-type perovskite solar cells with 17% efficiency: processing and characterization. *Mater. Adv.* (2021).

331. Do Kim, H., Miyamoto, Y., Kubota, H., Yamanari, T. & Ohkita, H. Open-circuit voltage loss in CH3NH3SnI3 perovskite solar cells. *Chem. Lett.* **46**, 253–256 (2017).

332. Ren, A. *et al.* Efficient perovskite solar modules with minimized nonradiative recombination and local carrier transport losses. *Joule* **4**, 1263–1277 (2020).

333. Spalla, M. Stabilité intrinsèque des cellules solaires pérovskites: impact de la formulation de la couche active et des couches de transport de charges. (Université Grenoble Alpes, 2019).

334. Hashmi, S. G. *et al.* Air processed inkjet infiltrated carbon based printed perovskite solar cells with high stability and reproducibility. *Adv. Mater. Technol.* **2**, 1600183 (2017).

335. Anuratha, K. S. *et al.* Electrodeposition of nanostructured TiO2 thin film as an efficient bifunctional layer for perovskite solar cells. *Electrochim. Acta* **295**, 662–667 (2019).

336. Su, T., Hsieh, T. & Wei, T. Electrodeposited TiO2 Film with Mossy Nanostructure for Efficient Compact Layer in Scaffold-Type Perovskite Solar Cell. *Sol. RRL* **2**, 1700120 (2018).

337. El-Etre, A. Y. & Reda, S. M. Characterization of nanocrystalline SnO2 thin film fabricated by electrodeposition method for dye-sensitized solar cell application. *Appl. Surf. Sci.* **256**, 6601–6606 (2010).

338. Chen, J.-Y., Chueh, C.-C., Zhu, Z., Chen, W.-C. & Jen, A. K.-Y. Low-temperature electrodeposited crystalline SnO2 as an efficient electron-transporting layer for conventional perovskite solar cells. *Sol. energy Mater. Sol. cells* **164**, 47–55 (2017).

339. Chappaz-Gillot, C. *et al.* Polymer solar cells with electrodeposited CuSCN nanowires

as new efficient hole transporting layer. *Sol. energy Mater. Sol. cells* **120**, 163–167 (2014).

340. Ye, S. *et al.* CuSCN-based inverted planar perovskite solar cell with an average PCE of 15.6%. *Nano Lett.* **15**, 3723–3728 (2015).

341. Ren, Z., Zhang, X., Li, H., Sun, X. & Yan, S. A facile way to fabricate anisotropic P3HT films by combining epitaxy and electrochemical deposition. *Chem. Commun.* **52**, 10972–10975 (2016).

342. Ratcliff, E. L., Jenkins, J. L., Nebesny, K. & Armstrong, N. R. Electrodeposited,"textured" poly (3-hexyl-thiophene)(e-p3ht) films for photovoltaic applications. *Chem. Mater.* **20**, 5796–5806 (2008).

343. He, Y., Guo, W., Pei, M. & Zhang, G. Electrosyntheses of free-standing poly (thiophene-3-acetic acid) film in mixed electrolytes of boron trifluoride diethyl etherate and trifluoroacetic acid. *Chinese J. Polym. Sci.* **30**, 537–547 (2012).

344. Pelicano, C. M. & Yanagi, H. Effect of rubrene: P3HT bilayer on photovoltaic performance of perovskite solar cells with electrodeposited ZnO nanorods. *J. energy Chem.* **27**, 455–462 (2018).

345. Burgos, A., Schrebler, R., Cáceres, G., Dalchiele, E. & Gómez, H. Electrodeposition of ZnO nanorods as electron transport layer in a mixed halide perovskite solar cell. *Int. J. Electrochem. Sci* **13**, 6577–6583 (2018).

346. Hyde, M. E., Jacobs, R. M. J. & Compton, R. G. An AFM Study of the Correlation of Lead Dioxide Electrocatalytic Activity with Observed Morphology. *J. Phys. Chem. B* **108**, 6381–6390 (2004).

347. Solaronix. Ti-Nanoxide T600/SC. https://shop.solaronix.com/titania-pastes/spin-coating-specials/ti-nanoxide-t600-sc.html.

348. Li, B. *et al.* Insights into the hole transport properties of LiTFSI-doped spiro-OMeTAD films through impedance spectroscopy. *J. Appl. Phys.* **128**, 85501 (2020).

349. Zhang, L. *et al.* The effect of carbon counter electrodes on fully printable mesoscopic perovskite solar cells. *J. Mater. Chem. A* **3**, 9165–9170 (2015).

Cellules solaires pérovskites réalisées par électrodéposition

Récemment, les pérovskites aux halogénures ont suscité un intérêt substantiel dans le domaine du photovoltaïque. Cependant, la méthode la plus utilisée pour déposer la couche active de pérovskite est l'enduction centrifuge, qui présente de nombreuses contraintes telles qu'une couverture de surface limitée, un prix de production élevé, une non-homogénéité, une cristallinité de pérovskite indéfinie, une mauvaise stabilité et nécessite un atmosphère inerte. Des méthodes alternatives doivent être explorées, telles que l'électrodéposition qui pourrait résoudre les inconvénients mentionnés. Dans ce travail, différents types de pérovskites ont été développées par électrodéposition, en étudiant l'impact des différents paramètres de dépôt sur leur structure et améliorant leur stabilité par rapport à celles déposées par enduction centrifuge . Une approche innovante a été atteinte en électrodéposant différentes pérovskites mixtes $MAPbI_{3-x}Cl_x$ et $MA_{1-y}FA_yPbI_{3-x}Cl_x$, et en élaborant une cellule solaire de structure inverse p-i-n à base de $MAPbI_3$ électrodéposé. Cependant, une architecture de cellule solaire optimisée doit être trouvée, correspondant à la pérovskite électrodéposée, pour améliorer encore l'efficacité.

Mots clés : Pérovskite, électrodéposition, cellules solaires pérovskites

Development of Perovskite Solar Cells Using Electrodeposition

In the last decade, halide perovskites have drawn substantial interest in the fields of photovoltaic. However, the most used method to deposit perovskite active layer is spin coating, which presents many constraints such as limited surface coverage, high production price, non-homogeneity, undefined perovskite crystallinity, poor stability and must be elaborated under inert atmosphere. Alternative methods must be explored, such as electrodeposition since it solves the as-mentioned disadvantages. In this work, we were able to develop different types of perovskites using electrodeposition, understand the impact of the different deposition parameters on their structure, and improve their stability comparing to the spin-coated ones. An innovative approach was reached by electrodepositing different mixed perovskites $MAPbI_{3-x}Cl_x$ and $MA_{1-y}FA_yPbI_{3-x}Cl_x$, and fabricating a p-i-n solar device using electrodeposited $MAPbI_3$. However, an optimized solar cell architecture must be found, corresponding to the electrodeposited perovskite, to further enhance the efficiency.

Keywords: perovskite, electrodeposition, perovskite solar cells